Intermediate Reynolds Number Free-Surface Flows

Thesis by
David Stewart Dandy

in Partial Fulfillment of the Requirements
for the Degree of
Doctor of Philosophy

California Institute of Technology
Pasadena, California
1987
(Submitted May 14, 1987)

To Sonia, my wife

And to my parents

Acknowledgment

I would like to thank my research advisor Professor L. Gary Leal. His confidence in my abilities has enabled me to achieve more than I would have ever thought possible.

My thanks to Ken Reardon, a great housemate and friend. I would also like to thank the other members of the Leal research group. Most of the fluid mechanics I have learned in the past several years has come out of conversations with this group. Greg Ryskin was instrumental in getting me on my numerical feet in my studies of droplets. Ed Ascoli's knowledge of mathematics, and interest in fluid mechanics has led to some very interesting collaborations. Tony Geller, keenly aware of swim coach transgressions, helped me a great deal to understand the physics behind the equations. The two office mates, Jim Stoos and Howard Stone, have also been invaluable. I have to also mention In Seok Kang, a first-class numericist and theorist, who helped find so many of the algebraic mistakes that I am prone to.

Mostly, I want to thank my wife, Sonia Maria Kreidenweis-Dandy, without whose love I could not have done this thesis.

Abstract

The buoyancy driven motion of a deformable viscous drop at intermediate Reynolds numbers has been studied using numerical techniques. The motion was assumed to be steady and rectilinear, and a pseudo-implicit method was used to solve the Navier-Stokes equations. Cases for a variety of values of the Reynolds number, Weber number, viscosity ratio and density ratio have been considered. The calculations reveal that the shape of the drop is most heavily dependent on the Weber number, attaining spheroidal capped shapes at $O(1)$ Reynolds numbers, and flattened ellipsoidal shapes at higher Reynolds numbers. Two mechanisms are observed for vorticity production at the interface of the drop—curvature and the no-slip condition—and the no-slip mechanism is a more efficient source of vorticity. When there is sufficient vorticity produced, a detached closed streamline wake forms at the back of the drop, in contrast to the attached wakes seen on inviscid bubbles and solid particles.

To further explore the role of vorticity production in wake formation, numerical computations were done on flow past inviscid bubbles of fixed shape. It was found that attached recirculating wakes existed at intermediate Reynolds numbers and these wakes could not be predicted by either low or high Reynolds number asymptotic theories. The numerical results indicate that the mechanism responsible for flow separation at modest Reynolds numbers may be different than that present at high Reynolds numbers.

Because of the inherent difficulties in solving the Navier-Stokes equations using successive approximation schemes, and to investigate the behavior of solutions of these equations on the dimensionless parameters, a Newton's method scheme has been developed and tested successfully on the steady buoyancy driven motion of an inviscid bubble; an arc length continuation method has also been implemented. Calculations indicate that the scheme achieves quadratic convergence.

Last, a numerical technique has been developed for the study of the creeping

motion of drops and particles in the presence of a rigid plane boundary. This method is based upon the distribution of point forces on the surface of the body and the use of a Green's function to obtain the unknown velocity and stress on the body surface, without having to consider the rigid boundary.

Table of Contents

Chapter I

Buoyancy-driven motion of a deformable drop through a quiescent liquid at intermediate Reynolds numbers

The text of Chapter I consists of an article which has been submitted for publication in the *Journal of Fluid Mechanics*

Buoyancy-driven motion of a deformable drop through a quiescent liquid at intermediate Reynolds numbers.

D.S. Dandy and L.G. Leal

Department of Chemical Engineering
California Institute of Technology
Pasadena, California 91125

Abstract

Numerical solutions have been obtained for steady streaming flow past an axisymmetrc drop over a wide range of Reynolds numbers ($0.005 \leq Re \leq 250$), Weber numbers ($0.005 \leq We \leq 14$), viscosity ratios ($0.001 \leq \lambda \leq 1000$), and density ratios ($0.001 \leq \varsigma \leq 100$). Our results indicate that at lower Reynolds numbers the shape of the drop tends toward a spherical cap shape with increasing We, but at higher Re the body becomes more disk-shaped with increasing We. Unlike the recirculating wake behind an inviscid bubble or solid particle, the eddy behind a drop is detached from the interface. The size of the eddy and the separation distance from the drop depend on the four dimensionless parameters of the problem. The motion of the fluid inside the drop is seen to control the behavior of the external flow near the body, and even for cases when λ and $\varsigma \ll 1$ (a "real" bubble), a recirculating wake remains unattached.

I. Introduction

The bouyancy-driven motion of drops and bubbles plays a critical role in many areas of the chemical engineering industry. Such diverse processes as liquid-liquid extraction, flotation, sedimentation, and combustion all rely on the dispersion of one fluid phase in another. As a consequence, a great deal of experimental work has been done to study the buoyancy-driven motion of bubbles, drops, and particles (Clift *et al* (1978) provides a thorough survey of both theoretical and experimental work), and approximate theoretical solutions have been obtained for drops and bubbles in the limit of very small deformation at either high (Moore 1959, 1963, 1965; Harper and Moore 1968; Parlange 1970; Harper 1972) or low (Taylor and Acrivos 1964; Brignell 1973) Reynolds number. Until recently, however, the motion of drops and bubbles at intermediate Reynolds numbers, or with a finite degree of deformation, had not been studied theoretically due to the lack of effective methods for dealing with the unknown shape of the free-surface. Within the last few years, however, Ryskin and Leal (1984) and Christov and Volkov (1985) have obtained numerical solutions for the steady rise of a deformable inviscid bubble, without intrinsic restriction on the bubble shape. Ryskin and Leal's solutions encompass Reynolds and Weber numbers in the ranges $1 \leq We \leq 20$ and $1 \leq Re \leq 200$, and show a dramatic variety of shapes and flows. The present paper presents a numerical study of the corresponding motion of a viscous drop.

The intermediate Reynolds number range is of particular interest because of unusual flow features that have been observed experimentally, but not duplicated via either the low or high Reynolds number asymptotic analyses. Specifically, Garner and Tayeban (1960), and LeClair (1970) have observed a steady recirculating wake behind a drop, but with the eddy *detached* from the drop surface. Later, Rivkind and Ryskin (1976) carried out a series of calculations for flow past spherical liquid drops and also found that a detached wake could exist for a wide range of viscosity ratios. However, their results were only for spheri-

cal shapes, and the later numerical study of deformed bubble shapes showed that deformation was critical to an understanding of wake structures at finite Reynolds number.

The experimental observation of a detached recirculating wake is not predicted via the existing asymptotic solutions for droplet motion. The Hadamard-Rybczinski solution for low Re indicates a single fore-aft symmetric internal vortex and an external flowfield which is free of any recirculating wake at the rear of the drop. For high Reynolds number, Harper and Moore (1968) carried out a boundary layer analysis similar to an earlier work on inviscid bubbles (1963, 1965), and found that as $Re \longrightarrow \infty$ the $O(1)$ solution outside a spherical drop was potential flow and inside was Hill's spherical vortex. Again, this solution does not exhibit a recirculating wake.

A similar difference between results at large, but finite Re, and asymptotic solutions for $Re \longrightarrow \infty$ was reported in the earlier study of inviscid bubbles by Ryskin and Leal (1984). The numerical solutions and existing experiments showed the presence of an attached recirculating wake at finite Reynolds numbers, while Moore's boundary-layer theory predicted no separation, except in a region of size $O(Re^{-1/6})$ near the rear stagnation point, for the limit $Re \longrightarrow \infty$. Later, Dandy and Leal (1986) demonstrated that the recirculating wake behind an inviscid bubble was strictly a finite Reynolds number phenomenon which disappeared with increasing Reynolds number, and speculated that the recirculating flow was a consequence of vorticity accumulation due to inefficient transport of vorticity downstream of the bubble at intermediate Reynolds numbers. If the presence of a detached wake were confirmed for viscous drops by the present numerical solutions, taking proper account of the drop shape, this would provide strong evidence in support of the vorticity transport mechanism suggested for existence of recirculating wakes at intermediate Reynolds number in our earlier study. Clearly, a detached recirculating zone could not result from flow separation at the boundary.

The goals of the present work are broadly to study the solution behavior—flowfield and drop shape—as a function of the four dimensionless parameters of the problem: the Reynolds number Re, Weber number We, viscosity ratio λ, and density ratio ς. Because of the extremely large number of combinations of these four parameters, we show results only for selected ranges of the dimensionless parameters, selected to demonstrate important qualitative features of the problem. Results for a large number of additional cases in the ranges $0 \leq Re \leq 350$, $0.05 \leq We \leq 14$, $0.01 \leq \lambda \leq 1000$ and $0.01 \leq \varsigma \leq 2000$ are included in the appendix to Chapter I.

To facilitate the study of this problem, we employ the boundary-fitted orthogonal curvilinear coordinate grid generation technique of Ryskin and Leal (1983). It is not necessary to describe the method here except to note that since it is boundary-fitted, the free surface of the droplet corresponds to a coordinate line in the computational domain, thereby avoiding the problems associated with interpolation between node points to provide approximate boundary conditions. Further, there are two routes that are available when using this grid generation technique. The first is called the strong constraint method and is very useful when used in conjunction with free-boundary problems. The second is referred to as the weak constraint method, and this method is useful when it is necessary to specify the positions of nodal points on the boundary. In this work we have used the strong constraint method to generate the outer coordinate grid and the weak constraint method to generate the grid inside the drop. The reasons for this will be discussed shortly.

II. Problem statement

In this section we will discuss the formulation of the problem and the method of solution. We consider a viscous droplet that is assumed to undergo a steady rectilinear motion, due to the action of gravity, through an outer quiescent liquid. The drop phase is characterized by a constant viscosity $\hat{\mu}$ and density $\hat{\rho}$ (quantities associated with the drop fluid will be denoted by a $\hat{}$). Likewise, the outer, or continuous phase is represented by μ and ρ. The interface between the two liquids is assumed to be completely described by a single constant parameter, the interfacial tension γ. As shown in Fig. 1, the geometry of the system is represented by cylindrical coordinates (z, σ, ϕ). We assume that the drop shape and flowfield are both axisymmetric; therefore, all quantities are independent of ϕ. The flow fields inside and outside the drop, as well as the drop shape, will be determined using a finite difference numerical scheme that is a generalization of the method of Ryskin and Leal (1984).

a. Grid generation

In order to utilize finite difference methods, it is necessary to define a coordinate grid, upon which the governing equations can be discretized. For reasons discussed elsewhere (Ryskin and Leal 1984; Dandy and Leal 1986) we have chosen to use an orthogonal boundary-fitted coordinate grid that is generated numerically. Because of axisymmetry, the grid generation problem takes the form of numerically constructing a discrete set of mapping functions $z(\xi, \eta)$ and $\sigma(\xi, \eta)$, both inside and outside the drop. Briefly, to generate the exterior coordinate system, we use the strong constaint method of Ryskin and Leal (1983, 1984), which amounts to solving the covariant Laplace equations for z and σ on a unit square in the (ξ, η) curvilinear coordinate system. The drop surface corresponds to the coordinate line $\xi = 1$, while infinity in the outer domain is $\xi = 0$. It is necessary to also generate a coordinate grid inside the drop, and for this inner problem the coordinate system is spherical in nature, with the

point $(\hat{z},\hat{\sigma}) = (0,0)$ corresponding to $\xi = 0$. After mapping, the computational domain for both phases will always be a unit square in (ξ,η).

One difficulty which arises in unbounded flow problems is the treatment of conditions at infinity. The two choices available are to either truncate the (z,σ) domain at some distance from the body, or to perform a coordinate inversion. Grosch and Orszag (1977) compared solutions obtained using coordinate inversion to those obtained via domain truncation for a variety of unbounded domain problems, including Burger's equation, and concluded that mapping will yield more accurate solutions than those obtained with truncation, provided that the solution being sought vanishes rapidly or approaches constant values at infinity. For the present study, we follow Ryskin and Leal (1984) and use a conformal coordinate inversion of the outer domain:

$$z + i\sigma = \frac{1}{z^* - i\sigma^*}, \tag{1}$$

which preserves the orthogonality of the coordinate grid. Thus, rather than map the outer (z,σ) domain directly to the (ξ,η) computational domain, the conformal mapping was used to transform the *infinite* (z,σ) domain to an auxiliary *finite* domain (z^*,σ^*), which was then mapped to a unit square in the (ξ,η) domain using the numerically generated orthogonal mapping technique. Since the domain inside the drop is finite, it is not necessary to carry out the coordinate inversion; the variables $(\hat{z},\hat{\sigma})$ are mapped directly onto the (ξ,η) computational domain.

Because of the inherently interesting flow structures which arise at the rear of the drops at larger values of the Reynolds number and Weber number, it is advantageous to use the strong constraint method to generate the coordinate grid in the continuous phase (Ryskin and Leal 1984). By using the strong constraint method, one can control grid spacing via the distortion function, denoted by $f(\xi,\eta)$. Again, we follow Ryskin and Leal (1984), and choose $f(\xi,\eta) = \pi\xi\big(1 - \alpha\cos\pi\eta\big)$, where $0 \le \alpha < 1$, which results in a grid that is finer at the rear of the drop (near $\eta = 0$) than at the front, and also finer near the

drop surface ($\xi = 1$) than at infinity.

There is one critical difference in the mapping problem for the bubble, which requires only one coordinate map external to the bubble surface, and the present problem, which requires both an internal and external coordinate map. Namely, if we are to avoid large errors in applying boundary conditions at the drop surface, it is necessary that the two coordinate grids, inside and outside the drop, must match up exactly at the free-surface. In order to insure that this is true, the strong constraint method is used in the outer phase and the weak constraint method is used in the inner phase. In the weak constraint method, complete boundary correspondence is prescribed (similar to other grid generation techniques; see Thompson *et al* 1985), and because of this the distortion function $f(\xi, \eta)$ *cannot* be specified. The advantage in using the weak constraint method in conjunction with the strong constraint method is that the solution of the strong constraint mapping, namely the position of the free surface $\big(z(1,\eta), \sigma(1,\eta)\big)$, is used as the boundary condition for the weak constraint method. That is, the strong constraint method generates the grid in the outer domain, with the position of the interface found as part of the solution, and then the weak constraint method is used to generate a grid inside the drop which matches exactly at the interface.

b. Governing equations

The equations governing the fluid motion and the shape of the drop are the steady state Navier-Stokes equations and associated boundary conditions, which we choose to state with respect to a frame of reference that is fixed on the drop. In the present work, these equations and boundary conditions are nondimensionalized using the radius a of an undeformed drop of volume $\frac{4}{3}\pi a^3$ as the characteristic length scale, the uniform streaming velocity at infinity U_∞ as a characteristic velocity, and $\frac{1}{2}\rho U_\infty^2$ as the pressure scale. The dimensionless

equations then take the form

$$\hat{\mathbf{u}} \cdot \nabla \hat{\mathbf{u}} = -\frac{1}{2\zeta} \nabla \hat{p} + \frac{a}{U_\infty^2} g\, \mathbf{e}_g + \frac{2\lambda}{\zeta\, Re} \nabla^2 \hat{\mathbf{u}} \tag{2a}$$

$$\nabla \cdot \hat{\mathbf{u}} = 0 \tag{2b}$$

and

$$\mathbf{u} \cdot \nabla \mathbf{u} = -\frac{1}{2} \nabla p + \frac{a}{U_\infty^2} g\, \mathbf{e}_g + \frac{2}{Re} \nabla^2 \mathbf{u} \tag{3a}$$

$$\nabla \cdot \mathbf{u} = 0. \tag{3b}$$

There are three dimensionless groups appearing in these equations: the Reynolds number $Re = 2\rho a U_\infty / \mu$, the density ratio $\zeta = \hat{\rho}/\rho$ and the viscosity ratio $\lambda = \hat{\mu}/\mu$. The boundary condition at infinity is

$$\mathbf{u} \longrightarrow \mathbf{e}_z \qquad \text{as } \|\mathbf{x}\| \longrightarrow \infty. \tag{4a}$$

At the drop interface we require continuity of velocity

$$\hat{\mathbf{u}} = \mathbf{u}, \tag{4b}$$

continuity of stress

$$\mathbf{n} \cdot (\mathbf{T} - \hat{\mathbf{T}}) = \frac{4}{We} (\nabla \cdot \mathbf{n})\, \mathbf{n}, \tag{4c}$$

and the kinematic condition

$$\mathbf{n} \cdot \hat{\mathbf{u}} = \mathbf{n} \cdot \mathbf{u} = 0. \tag{4d}$$

A fourth dimensionless group which appears in the boundary conditions is the Weber number $We = 2\rho a U_\infty^2 / \gamma$.

Due to the axisymmetry of the problem, it is convenient to use a stream-function vorticity formulation rather than the primitive variables $\mathbf{u}$ and p. To recast the problem, we first take the curl of Eqs. (2a) and (3a) to obtain an

equation in terms of vorticity $\omega\, e_\phi$ and velocity. Then we define the velocities in the general curvilinear coordinate system using the streamfunction ψ:

$$u_\xi = -\frac{1}{\sigma h_\eta}\frac{\partial \psi}{\partial \eta}$$

$$u_\eta = \frac{1}{\sigma h_\xi}\frac{\partial \psi}{\partial \xi},$$

and substitute these into the velocity-vorticity formulation to obtain

$$\mathcal{L}^2(\hat{\omega}\hat{\sigma}) - \frac{\lambda\, Re}{2\zeta \hat{h}_\xi \hat{h}_\eta}\left[\frac{\hat{u}_\xi}{\hat{h}_\xi}\frac{\partial}{\partial \xi}\left(\frac{\hat{\omega}}{\hat{\sigma}}\right) + \frac{\hat{u}_\eta}{\hat{h}_\eta}\frac{\partial}{\partial \eta}\left(\frac{\hat{\omega}}{\hat{\sigma}}\right)\right] = 0 \tag{5a}$$

$$\mathcal{L}^2\hat{\psi} + \hat{\omega} = 0 \tag{5b}$$

and

$$\mathcal{L}^2(\omega\sigma) - \frac{1}{2}\frac{Re}{h_\xi h_\eta}\left[\frac{u_\xi}{h_\xi}\frac{\partial}{\partial \xi}\left(\frac{\omega}{\sigma}\right) + \frac{u_\eta}{h_\eta}\frac{\partial}{\partial \eta}\left(\frac{\omega}{\sigma}\right)\right] = 0 \tag{6a}$$

$$\mathcal{L}^2\psi + \omega = 0, \tag{6b}$$

where

$$\mathcal{L}^2 \equiv \frac{1}{h_\xi h_\eta}\left[\frac{\partial}{\partial \xi}\left(\frac{f}{\sigma}\frac{\partial}{\partial \xi}\right) + \frac{\partial}{\partial \eta}\left(\frac{1}{f\sigma}\frac{\partial}{\partial \eta}\right)\right]$$

The scale factors of the coordinate system are

$$h_\xi = \left[\left(\frac{\partial z}{\partial \xi}\right)^2 + \left(\frac{\partial \sigma}{\partial \xi}\right)^2\right]^{\frac{1}{2}}$$

$$h_\eta = \left[\left(\frac{\partial z}{\partial \eta}\right)^2 + \left(\frac{\partial \sigma}{\partial \eta}\right)^2\right]^{\frac{1}{2}}$$

and the distortion function is

$$f = \frac{h_\eta}{h_\xi}.$$

The geometric factors $\mathcal{L}^2$, h_ξ,and h_η in each phase are defined in terms of the appropriate coordinate variables.

At large distances from the body the velocity asymptotically approaches the uniform streaming flow $\psi_2 \sim \frac{1}{2}\sigma^2$. To remove this singularity in the

streamfunction we define a modified streamfunction by subtracting off a function which has the same asymptotic behavior at large distances and satisfies homogenous conditions at the other three boundaries. The modified streamfunction is $\psi^* = \psi - \frac{1}{2}\sigma^2(1-\xi^3)$. The subtracted term is the potential flow solution for a spherical bubble, but it has no simple physical meaning for a drop of arbitrary shape. From the Oseen solution (Proudman and Pearson 1957) we know that ψ^* is bounded at infinity, and because this point is a singular point of the differential equation, boundedness is a sufficient condition for solution (Morse and Feshbach 1953).

The boundary conditions corresponding to Eqs. (5) and (6) are: along the lines of symmetry,

$$\omega,\ \psi^*,\ \hat{\omega},\ \hat{\psi} = 0 \qquad \text{at } \eta = 0,\ 1 \tag{7a}$$

at infinity,

$$\psi^*,\ \omega = 0 \qquad \text{at } \xi = 0 \tag{7b}$$

and at the center of the drop,

$$\hat{\psi},\ \hat{\omega} = 0 \qquad \text{at } \xi = 0. \tag{7c}$$

At the surface of the drop,

$$\hat{\psi} = \psi^* = 0 \qquad \text{at } \xi = 1, \tag{7d}$$

because of zero normal velocity. The tangential stress balance takes the form

$$\lambda\,\hat{\omega}_s - \omega_s = 2\,\kappa_\eta\,(\lambda\,\hat{u}_\eta - u_\eta)\Big|_{\xi=1}, \tag{7e}$$

where $\omega_s \equiv \omega(1,\eta)$ and $\hat{\omega}_s \equiv \hat{\omega}(1,\eta)$. Finally, the normal stress balance is

$$\hat{p} - p + \frac{8}{Re}\left[\frac{\lambda}{\hat{\sigma}\hat{h}_\eta}\,\frac{\partial}{\partial\eta}(\hat{\sigma}\hat{u}_\eta) - \frac{1}{\sigma h_\eta}\,\frac{\partial}{\partial\eta}(\sigma u_\eta)\right] = \frac{4}{We}(\kappa_\eta + \kappa_\phi)\Big|_{\xi=1}, \tag{7f}$$

where the difference in pressure is given by

$$\hat{p} - p = -\frac{3}{4}C_D z - \varsigma \hat{u}_\eta^2 + u_\eta^2 + \frac{4}{Re}\left[\lambda \int \frac{\hat{f}}{\hat{\sigma}}\frac{\partial}{\partial \xi}(\hat{\sigma}\hat{\omega})\, d\eta + \int \frac{f}{\sigma}\frac{\partial}{\partial \xi}(\sigma\omega)\, d\eta\right] + C_1\Big|_{\xi=1},$$

where C_1 is a constant of integration, and normal curvatures are

$$\kappa_\eta = \frac{1}{h_\eta^3}\left(\frac{\partial z}{\partial \eta}\frac{\partial^2 \sigma}{\partial \eta^2} - \frac{\partial^2 z}{\partial \eta^2}\frac{\partial \sigma}{\partial \eta}\right)\Big|_{\xi=1}$$

and

$$\kappa_\phi = -\frac{1}{\sigma h_\xi}\frac{\partial \sigma}{\partial \xi}\Big|_{\xi=1}.$$

The incorporation of these boundary conditions into the numerical computations will be discussed in the next section.

c. Details of the numerical scheme

The numerical scheme used to solve the partial differential equations is the ADI method of Peacemann and Rachford (1955). An artificial time dependence is imbedded in Eqs. (5a), (5b), and the Laplace equations governing the mapping, and the PDE's are approximated using second-order centered finite differences (see, for example, Ryskin and Leal 1984). Although Eqs. (5a) and (5b) are coupled, and the two mapping equations are coupled through the distortion function f, each set of equations is solved successively rather than simultaneously at each iteration, or, time step.

The homogeneous Dirichlet conditions (7a)-(7d) do not introduce any additional terms in the tridagonal system generated by applying ADI and further, they are strong conditions in the sense that they "tie down" the values of the unknown vorticity at three of the four boundaries of the domain. The remaining two boundary conditions—the tangential and normal stress balances—must somehow be used to specify the three remaining unknown quantities: the interface shape, $\hat{\omega}(1,\eta)$ and $\omega(1,\eta)$. For application as a boundary condition, it is

not sufficient to use Eq. (7e) as written; the numerical scheme requires explicit values for $\hat{\omega}_s$ and ω_s. Instead, we use an approach based on a method developed by Dorodnitsyn and Meller (1968) and Israeli (1970), and described elsewhere (Ryskin 1980). Briefly, the facts that (1) the vorticity street is proportional to the velocity difference and (2) until numerical convergence $\hat{u}_\eta(1,\eta) \neq u_\eta(1,\eta)$ are both used in an iterative process to explicitly specify both $\hat{\omega}(1,\eta)$ and $\omega(1,\eta)$ at each ADI step. That is, until continuity of tangential velocity is satisfied, the local vorticity is adjusted proportionally to the magnitude of the velocity jump, which itself is proportional to the corresponding vortex sheet at the surface. The diffusion and convection of vorticity leads to a smoothing of the velocity discontinuity. Eqs. (7a)-(7e) are sufficient to obtain solutions to the flow equations for ψ^*, $\hat{\psi}$, ω and $\hat{\omega}$. The position of the interface is then updated using the normal stress balance, Eq. (7f), in a manner analogous to Ryskin and Leal (1984).

All calculations were done on a CRAY XM-P/24. To insure that the code ran as fast as possible, it was written efficiently and vectorized wherever possible. In fact, with the exception of one loop in the entire program, all of the inner loops vectorized. Even though the solution of the tridiagonal system arising from the ADI scheme is recursive in nature, it is possible to reverse the order of the loops and thus make the inner loop vectorizable. Due to the extreme underrelaxation needed in employing the normal stress balance to move the interface, a fairly large number of iterations were required, particularly at the larger Weber numbers. The number of iterations needed was usually in the range 1000-7500, and the corresponding CPU time required on the CRAY was roughly 15 to 120 seconds. There were two criteria which had to be met for convergence: the maximum norm of the relative difference between the inner and outer velocities and the maximum norm of the absolute error in evaluating Eq. (7f) both had to be less than 10^{-3}. We found that if these two convergence criteria were satisfied, the governing equations were also satisfied to within acceptable tolerances.

Solutions were obtained by choosing values for λ, ς, Re and We and march-

ing along one of the parameter branches while holding the other three fixed. In this manner, the solution at a particular set of parameter values was used as the initial guess for an incremental change in one of the four parameters.

To explore solution behavior as a function of the parameter space, we divided the problem up into three parts. First, we examine the effect of changing the Reynolds number and Weber number (as would happen if the diameter of the undeformed drop were changed) while holding the fluid properties λ and ς fixed. Second, the viscosity ratio λ and the density ratio ς are varied independently while Re and We were held fixed. Last, solutions for low Re (< 1) and high Re (> 100) are obtained for fixed We, λ, and ς so that the numerical results could be compared to the asymptotic solutions for high and low Reynolds number.

III. Results and discussion

a. Numerical results

In order to illustrate the effects of variations in Re and We, we choose a series of solutions with the density ratio and viscosity ratio fixed at $\varsigma = 0.91$ and $\lambda = 4$, respectively. These values are rather arbitrary, though representative of values of $O(1)$, but picked with the general aim of having a drop viscosity high enough to expose interesting flow behavior (recirculating wakes) at moderate Reynolds where solution accuracy is not an issue. Results obtained at other values of λ and ς (specifically, for ς, λ pairs (0.01, 0.001), (0.91, 10), (4, 0.5) and other isolated values) show that the qualitative dependence of drop shape on Re and We, illustrated below, was invariant to λ and ς. In general, the flowfields for the ς, λ pairs were also similar. At the lower values of ς and λ, the drop acts more like a bubble, that is, with nearly zero shear stress at the interface and a higher level of deformation than for other values of ς and λ.

Figs. 2 and 3 show results for shape and flowfield at Reynolds numbers of 2 and 10 for the values of λ and ς mentioned above, and several values of We. Table I contains the corresponding values of the drag coefficient. (Values of C_D for all solutions presented in this chapter are displayed in Table I.) For fixed values of λ, ς, and Re, the shapes shown in Fig. 2 become more deformed with increasing We (or, decreasing surface tension), tending towards a spherical cap shape at the higher values of the Weber number. The streamfunction plots in Fig. 3 show that at the lower values of Re the external flow, moving from left to right, induces the motion of a single, primary vortex inside the drop. The results for shape and external flow are qualitatively similar to those found by Ryskin and Leal for gas bubbles at the same values of Reynolds number and Weber number. However, at any particular Re and We the drop is less deformed than the bubble, due to the fact that the drop viscosity $\hat{\mu}$, and the inertia of the inner fluid (proportional to the density $\hat{\rho}$) both act to reduce deformation. Fluid inside the drop near the front stagnation point is caused to move because

of the motion of the fluid outside of the drop. The inner fluid will tend to move all the way to the rear stagnation point not only because of the outer fluid, but also because it has inertia of its own. Thus, the fluid being "driven" to the rear counteracts to some extent the external stagnation pressure at the rear of the drop. There are two opposing forces at the rear of the drop: internal inertia forcing the surface outward and stagnation pressure pushing the surface inwards.

In addition to the streamlines, we also show the corresponding vorticity fields in Fig. 3 for $Re = 10$. The values of vorticity are largest near the top of the drop, where curvature is the highest, and smallest on the axes of symmetry, where the value is zero. Because of the orientation of our coordinate system, all values of vorticity shown, for example in $Re = 10$, $We = 0.5$ are negative. For small values of Re and We, such as $Re = 0.5$, $We = 0.5$ (shown in the appendix), the internal streamlines resemble Hill's spherical vortex, that is, a fore-aft symmetric recirculating ring, and the vorticity is a function of $\hat{\sigma}$ only, so that lines of constant vorticity are horizontal. As the Reynolds number is increased, for example to 10 as in Fig. 3, the internal vortex is gradually shifted towards the front of the drop. The lines of constant vorticity then deform in the interior, bending upwards as they approach the surface at the rear of the drop. When the drop becomes sufficiently deformed, at $We = 4$, a region of positive vorticity appears, both inside and outside, at the rear of the drop.

For bubbles and solid particles, the appearance of a region of oppositely-signed vorticity signals the beginning of flow separation. Further, the η (or, θ) position on the surface where $\omega_s = 0$ coincides with the separation point. In the first three illustrations in Fig. 4 (a, b and c) we demonstrate this phenomenon for a void. (We define a void as $\lambda \longrightarrow 0$ and $\varsigma \longrightarrow 0$.) These three figures represent results calculated for flow past an oblate ellipsoid of revolution at three different Reynolds numbers: 20, 90 and 180, respectively. For the shape shown in Fig. 4, at $Re = 20$ there is no recirculating wake present and the vorticity has the same

sign everywhere (negative). When Re has reached 90, an attached recirculating wake has formed, and it can be seen in Fig. 4b that there is now a small region of positive vorticity at the rear of the bubble. Finally, in Fig. 4c, at $Re = 180$ the eddy has disappeared and the vorticity is once again negative everywhere in the domain. To see why $\omega_s = 0$ marks the separation point for a bubble, we must examine the tangential stress balance:

$$\omega - 2\kappa_\eta u_\eta = 0.$$

The necessary and sufficient condition for separation on a bubble is $u_\eta = 0$, and from the tangential stress balance, we see that this is equivalent to $\omega_s = 0$, provided that the curvature κ_η is finite.

For a solid (which we regard as $\lambda \longrightarrow \infty$), a separation point is also identified by $\omega_s = 0$, and a region of positive vorticity, although significantly larger than that for a bubble of similar curvature, is also present at the rear of the body. An example of this vorticity pattern is shown in Fig. 4d, where we show the result for $Re = 100$. Fornberg (1980) displays results for streaming flow past a solid cylinder for Reynolds numbers in the range $2 \leq Re \leq 300$. The region of positive vorticity does not form behind the cylinder until separation first occurs, about $Re = 10$. This region appears to gradually increase in size with increasing Reynolds number. The necessary and sufficient condition that separation occur from a solid is that the tangential stress (or, "skin friction") goes to zero. This condition requires that $\partial u_\eta / \partial \xi = 0$ and this, in turn, is equivalent to stating that $\omega_s = 0$ (because $\partial u_\xi / \partial \eta \equiv 0$ on the surface).

In Fig. 3, however, we have seen that a region of positive vorticity forms behind the drop *without* any accompanying flow separation once the drop becomes sufficiently deformed. As we will show below, this positive vorticity cannot be solely an artifact of increased surface curvature or of the condition $\lambda > 1$, although these can certainly be contributing factors to the size of this region. Instead, we offer the following explanation, which is based on arguments in Lighthill (1986, pp. 75-79). The base of the argument is the supposition that

the layer near the drop surface containing the vorticity generated at the interface can be regarded as a vortex sheet. The strength of this vortex sheet is fixed by knowing the drag on the body, and the value of the vorticity at each point on the surface is then set by requiring the total vortex strength be constant. Assume that a point B exists on the surface of a ficticious drop near, but not at, the rear stagnation point. Also assume that a point A exists on the surface of this same drop, slightly upstream of B. Since the tangential velocity of the interface is decreasing as the rear stagnation point is approached, convection removes vorticity from the vicinity of B at a rate much smaller than at which the vorticity from A is replacing it. The total strength of the vortex sheet must remain unchanged, and as a consequence new vorticity of opposite sign is generated at the drop surface at a rate greater than can be compensated for by vorticity diffusion from within the "boundary layer". That is, if negative vorticity is being produced at point A, point B will begin to produce positive vorticity in amounts greater than can be cancelled out by negative vorticity transported from upstream. As mentioned above, for a void or a solid, the appearance of positive vorticity on the surface is equivalent to flow separation, and the actual mechanism for production of positive vorticity is flow reversal. It is easy to see this effect on a void from the tangential stress balance shown above—a change in sign of velocity must be accompanied by change in sign of vorticity, assuming curvature does not change sign. For the drop, however, the mechanism is not quite so obvious since a region of positive vorticity appears without any flow reversal; it is necessary to examine which quantities determine the vorticty, and how they can lead to a change in sign of vorticity. On the surface of a drop of fixed shape (that is, a surface with zero normal velocity) the vorticity is defined to be

$$\omega_s = \kappa_\eta u_\eta - \frac{1}{h_\xi}\frac{\partial u_\eta}{\partial \xi}.$$

The sign of this equation arises because the outer coordinate system is left-handed. If neither the curvature nor the velocity at the surface change sign, the

first term on the right hand side will be negative. The derivative $\partial u_\eta / \partial \xi$ is also negative, so ω will be negative as long as the magnitude of the first term exceeds that of the second. Thus, positive vorticity can occur if the normal derivative of u_η is large enough for the second term to dominate the first, or if u_η changes sign. Even before the appearance of a recirculating wake, accumulation of vorticity, both inside and outside, at the rear of the drop causes a distortion of the velocity field, making the velocity gradient large enough for the vorticity to be positive.

In their numerical solution for steady flow past viscous spherical drops, Rivkind and Ryskin (1976) display a series of results at $Re = 100$ for $1 \leq \lambda \leq 100$. At $\lambda = 1$ there is no recirculating wake, but there is again a region of positive vorticity at the rear of the drop. The fact that Rivkind and Ryskin found this same effect for spherical drops when $\lambda = 1$ indicates that neither a vorticity jump at the surface (as would exist for $\lambda > 1$) nor a region of locally large surface curvature (as could exist for $We > 1$ if the drop were allowed to deform) is requisite for the existence of a region of oppositely-signed vorticity in the flow domain.

Similar shapes have been calculated in this work for Reynolds numbers below approximately 60 for the values of viscosity ratio λ and density ratio ς used in the calculations (see the Appendix). However, for $Re \gtrsim 60$ the flow and the shape of the drop change dramatically.

The flow changes to the extent that recirculating wakes begin to appear behind the drops, which are $O(1)$ in size with respect to the body. This effect is well represented in Fig. 5a, where the flowfield for $Re = 60$ is shown for several values of We. For smaller values of We the curvature of the drop is too low to produce a sufficient accumulation of vorticity at the rear and thus lead to a recirculating wake. But as the curvature grows with We, more vorticity is produced at the interface than can be carried away by convection, and a recirculating wake forms. Figure 5a is a good demonstration of the appearance and growth of a recirculating wake as the surface curvature increases with We.

At $We = 0.5$, although the shape is nearly spherical, there is enough vorticity produced due to the no-slip condition that an eddy is beginning to form at the rear. We can also see at this Weber number that a modestly sized region of positive vorticity has formed. As the Weber number, and thus deformation, increases, the recirculating wake becomes larger, as does the inner and outer regions of positive vorticity.

Figure 5b shows another example, at $Re = 100$. Not surprisingly, in both of these examples deformation increases with We, but whereas the stagnation pressure at the rear of the drop caused an indentation to occur there at the lower Reynolds numbers, the stagnation pressure at the *front* of the drop begins to dominate for $Re \gtrsim 100$. The result is that the front of the drop becomes flattened at the higher Weber numbers. The present solutions were obtained assuming the drop and the flow to be steady and axisymmetric. With this constraint, the solutions shown in Fig. 5 were obtained via a quasi-time-dependent algorithm, even though it is well known from experimental observation that drops and bubbles for $Re \gtrsim 100$ do not assume a steady shape or motion for $4 \lesssim We \lesssim 20$. Rather, in this range of Re and We, both bubbles and drops move in a transitory wobbling manner (and thus attain non-axisymmetric time-dependent shapes), and it is not until $We \gtrsim 30$ that they become spherical caps and the motion of a drop again becomes steady. Although the steady axisymmetric calculations that were obtained for this paper cannot capture the three dimensional transient behavior exhibited at intermediate values of We, the steady solutions may nevertheless provide important qualitative insights and serve as the basis for future investigations of the stability of the rise trajectory. It may also be noted that solutions in the unstable regime at a given Re and We were the same, whether attained by fixing the Weber number at some intermediate value and increasing the Reynolds number, or fixing Re at some large $O(100)$ value and increasing the Weber number.

The most striking flow feature of Fig. 5 for both $Re = 60$ and 100 is the

detached recirculating wake; this wake appears behind the droplet and increases in size with increasing We (that is, increasing surface curvature and therefore increasing surface vorticity). This detached wake for the liquid drop is is marked contrast to the well known attached wakes which exist on voids (Ryskin and Leal 1984; Miksis *et al* 1981), and solid particles (Taneda 1956; Nisi and Porter 1923; Kalra and Uhlherr 1971). However, as noted earlier, unattached wakes have been observed experimentally and predicted numerically for streaming flow past viscous spherical drops (Garner and Tayeban 1960; Rivkind and Ryskin 1976; LeClair 1970). Although the drop shape for a given Re and We has less surface curvature than a void for the same Re and We, an eddy can still form because vorticity is also generated via the no-slip condition at the interface. Indeed, the maximum surface vorticity for both $Re = 60$ and 100 has a value of approximately 7 when a closed streamline wake first appears, and this value is similar to the maximum surface vorticity when a closed streamline wake appears for both the void and a solid sphere at similar Reynolds numbers. We shall have more to say on this later.

The closed streamline wakes of Fig. 5 are represented schematically in Fig. 6a. The external fluid moving towards the drop along the upstream axis of symmetry continues all the way around the drop to the rear axis of symmetry before moving around the outside of the detached eddy. Inside the drop there is a single recirculating vortex. As Fig. 6b shows, the situation for a void is markedly different (see, for example, Ryskin and Leal 1984); if a wake exists behind a void, it is attached to the void "surface", and the motion of the fluid in the wake causes the fluid at the surface in the wake region to move upwards, or towards the front of the void. When separation first occurs on a bubble, the surface vorticity changes sign and becomes positive at a point near the rear axis of symmetry. As the attached eddy grows larger, the point where the surface vorticity changes sign moves along the surface further from the rear axis, creating a section of the body surface with positive values of ω_s. The fluid elements

at the surface moving from the front of the bubble to the rear meet the upwardly moving fluid elements from the rear at the separation point, and the fluid subsequently departs the bubble surface. Figure 6c shows one possible sketch of the flow that would occur if the recirculating wake were attached for a drop. In the drop, very close to the interface, the fluid is moving in a clockwise direction, toward the rear stagnation point, while the outer fluid in the main recirculating region of the wake is moving in the opposite direction. Thus, the velocity changes sign in an extremely small distance, and even though the velocities in this region are not large, the resulting shear would nonetheless be high (based upon the magnitude of the velocity in the rear region and the length scale over which the velocity changes sign), certainly an energetically unlikely situation for the drop to be in. The detached configuration in Fig. 6a, is one way to avoid this problem and is, in fact, the observed configuration in all of our calculations.

It is interesting to note that a similar situation can occur in a cavity flow (Kang and Chang 1982): under certain conditions, steady flow in a channel over a cavity will cause the formation of two eddies in the cavity, both rotating in the same direction (see Fig. 3b of Kang and Chang). Because the velocities of the closest points of the two eddies are opposite in sign—a situation analogous to Fig. 6c—the eddies maintain as wide a gap as possible between them.

There are of course, other multi-eddy configurations with attached recirculating wakes that also avoid the problem illustrated in Fig. 6c. The simplest of these is the structure sketched in Fig. 6d. In fact, a configuration a double internal vortex has been observed in numerical calculations (Rivkind and Ryskin 1976; LeClair 1972), and experiments (Pruppacher and Beard 1970), but only for $Re \gg 1$ and $\varsigma \gg \lambda \gg 1$, which corresponds roughly to a mercury droplet or even a water droplet falling through air. The present results indicate that the detached wake similar to Fig. 6a is observed in all other cases where there is a recirculating wake.

As mentioned above, the onset of separation for a void or solid is denoted by

a change of sign in ω_s, and the situation is markedly different for a drop because positive vorticity is observed without the accompanying flow detachment from the surface. When a recirculating wake does appear, it is detached, and thus there is no flow separation although there is a region of positive vorticity. A necessary and sufficient condition for flow detachment to occur on a drop is for $u_\eta = \hat{u}_\eta = 0$ at a point other than $\eta = 0$ or 1. As we can see from Eq. 7e, for arbitrary λ, this condition is equivalent to $\lambda\hat{\omega}_s - \omega_s = 0$ or $\omega_s = \hat{\omega}_s = 0$. However, we find that for all $\lambda \neq 1$ the vorticity jump across interface is nonzero at every point on the interface for $0 < \eta < 1$, and ω_s and $\hat{\omega}_s$ are not zero at the same point except for $\lambda = 1$. The reverse is not always true, however. If $\lambda = 1$, we can have $\omega_s = \hat{\omega}_s = 0$ at a point and still not have flow separation, and Eq. (7e) will still be satisfied. With this in mind, by looking at the tangential stress balance, Eq. (7e), we can see that a change in sign of ω_s and/or $\hat{\omega}_s$ does not violate or contradict the tangential stress balance, whether or not a *detached* recirculating wake is present. If there is no flow separation, then u_η will have the same sign everywhere on the surface, and thus the right hand side of Eq. (7e) will always be positive or negative, depending on whether λ is greater or less than 1. Then, as long as the left hand side, $(\lambda\hat{\omega} - \omega)$, does not change sign, the tangential stress balance is satisfied. Indeed, we have found in all of our calculations that the left hand side of Eq. (7e) does not change sign for any choice of λ.

All of the results discussed so far were obtained by varying We with the other parameters held fixed. Here, we consider the effect of viscosity ratio on the shape and flowfield. In Fig. 7 we present results for the case $Re = 100$, $We = 4$, $\varsigma = 0.91$ and $1 \leq \lambda \leq 1000$. One consequence of increasing λ is a decrease in deformation of the drop due to the rising resistance of the drop to deforming forces, and we have found that for all choices of Re, We, and ς the change in curvature was weakly dependent to changes in viscosity ratio, but that curvature always decreased with increasing λ. A more dramatic effect

of increasing λ is that the wake becomes larger in size, in proportion to the increase in vorticity produced at the surface as the no-slip condition becomes a more effective source of vorticity. We have seen that there are two mechanisms for producing vorticity at the surface of the drop: curvature and the no-slip condition. The results in Fig. 7 demonstrate that the no-slip mechanism is a more efficient source of vorticity than curvature at this Re, We and ς because as λ increases, the curvature source decreases due to the slight decrease in curvature and dramatic decrease in surface velocity, while the no-slip mechanism increases.

Also, as the viscosity ratio becomes larger, the strength of the flow inside the drop becomes correspondingly smaller, and the wake moves in closer to the body. Indeed, we find that $\|u_\eta\|_\infty \propto \lambda^{-1}$ at the surface $\xi = 1$. When the viscosity ratio λ is $O(1)$, the velocity at the surface of the drop is the same magnitude at the characteristic velocity, U_∞. However, as λ rises the surface velocity falls, and the flow inside the drop becomes weaker. Therefore, the wake exists in a detached state because it is forced to do so by the internal flow, and this provides further evidence that the phenomena observed arise as a consequence of the interaction of two viscous liquids. The flowfields in Fig. 7 show that at the lower viscosity ratios the wake is not only smaller than at the higher λ's (since less vorticity is being produced at the interface), but it is also farther away from the body due to the strength of the flow inside the drop. Based upon these observations it's not surprising that an attached wake can only occur on a droplet when $\lambda \gg 1$.

From Fig. 7 it is not possible to see that the wakes at the highest viscosity ratios $\lambda = 100$ and $\lambda = 1000$ are actually detached, but this is easily demonstrated by examining the signs of the velocity at the surface. The limit $\lambda \longrightarrow \infty$ can be regarded as a solid particle and the wake behind such a body will be attached (see, for example, Masliyah 1970; Nakamura 1976). The calculations here show that as λ increases the wake moves closer to the drop, but up to $\lambda = 1000$, it is still not attached. We therefore hypothesize that for the value

of the density ratio $\varsigma = 0.91$, the wake will only become attached in the limit $\lambda \longrightarrow \infty$, and that this limit is singular insofar as wake attachment is concerned.

Although Re was held fixed to obain the results shown in Fig. 7, the interior Reynolds number decreased as λ increased. To investigate the effect of fixed inner *and* outer Reynolds numbers, we did a series of calculations for $Re = 100$ and $We = 4$ at various values of ς and λ, holding their ratio fixed at 0.25 (i.e., $\varsigma/\lambda = 0.25$, and thus the inner Reynolds number was 25). The results of these calculations, shown in Fig. 8, demonstrate that the interior Reynolds number does not appear to play a significant role in the qualitative or quantitative features of the flow field. As λ and ς are both increased, the solutions look very similar to those in Fig. 7, where ς was fixed. We see that as λ and ς are increased, the shape becomes less deformed, and surface velocity slows down, in proportion to λ^{-1}, and the wake grows larger and moves closer to the rear of the drop. The conclusion from these results is that not only does the internal Reynolds number appear to play a small role in determining the flowfield but also that the density ratio ς plays a similarly small role. In Fig. 9 we show results for $Re = 100$, $We = 4$, $\lambda = 1$ and two values of ς: 0.1 and 0.01. Together with the first result in Fig. 7, for $\varsigma = 0.91$, we see that an almost two order of magnitude change in density ratio produces only a slight change in shape and flowfield, leading us to conclude that ς does indeed only have a slight effect on the problem. This is not really surprising since ς appears in the boundary conditions in only the pressure, whereas the viscosity ratio λ appears appears in the viscous terms in both the tangential and normal stress balances. This observation has been confirmed by other numerical computations, particularly those of Rivkind and Ryskin (1976).

b. Comparison with experiment

A generalized graphical correlation exists (Clift, Grace, and Weber, Fig. 2.5

1978) for drop and bubble shape in terms of the Eötvös, or Bond number,

$$Eo = \frac{4a^2 g \Delta\rho}{\gamma}$$

the Morton, or M-group number,

$$M = \frac{g \mu^4 \Delta\rho}{\rho^2 \gamma^3}$$

and the Reynolds number. These two dimensionless groups Eo and M can be rewritten in terms of our parameters as

$$Eo = \frac{3}{4} C_D We$$

and

$$M = \frac{3}{4} C_D \frac{We^3}{Re^4}.$$

For the case $Re = 2$ shown in Fig. 2, the Eötvös and Morton numbers lie in the ranges $5.2 \leq Eo \leq 160$ and $8.2 \times 10^{-2} \leq M \leq 2.0 \times 10^3$. From Fig. 2.5 of Clift *et al* it can be seen that the motion and shape of the drop at this Reynolds number are both steady for the entire spectrum of Weber numbers. At the lower Weber numbers, the shape is nearly spherical, and for $We \gtrsim 5$ the shapes tend to dimpled ellipsiodal caps, which is exactly what is shown in Fig. 2a. For $Re = 10$ (Fig. 3) the behavior is very similar, except that the drop shapes lie more in the ellipsiodal range, also tending towards ellipsiodal caps at larger Weber numbers. From the graph in Clift *et al* one predicts that if the Weber number is further increased the shape will be skirted. In our calculations at $Re = 2$ and 10, we stopped at $We = 14$ and 10 because the shapes became sufficiently distorted that it was difficult to generate an interior mapping with high resolution near the interface $\xi = 1$. At these high Weber numbers, the solution process was very unstable and extremely small time steps and relaxation parameters were needed, increasing the computational cost to unacceptable levels.

In the graphical correlation (Clift, Grace and Weber 1978) there are three general regimes. Two of these are steady, and they represent spherical and

spherical/ellipsiodal cap shapes. The spherical regime corresponds to the entire range of Reynolds numbers (up to several hundred in the chart) for sufficiently low Weber numbers. In Fig. 1 of Wellek *et al* (1966), photographs over the range $91 \leq Re \leq 369$ are presented, with steady shapes ranging from nearly-spherical to ellipsoidal. In Fig. 2 of Hendrix *et al*, photographs of drops are shown for the range $80 \leq Re \leq 215$. Also shown are the gross structures, but not the fine details, of the closed streamline wakes. The shapes are all nearly spherical and, with the exception of the high Re case, all are steady. Unfortunately, neither Wellek *et al* nor Hendrix *et al* cite interfacial tension data, so it is not possible to explicitly state the We range. However, for both papers, the systems were immiscible organic/water mixtures for which interfacial tensions are large (Handbook of Chemistry and Physics 1980) and it is therefore a reasonable guess that $We = o(1)$.

The capped shapes also occur over the entire range of Reynolds numbers, but only for the highest Weber numbers. Shoemaker and Marc de Chazal (1968) present an excellent series of dimpled shapes for 2-butanone in glycerol, for $20.4 \leq Re \leq 75.2$ and $50.4 \leq We \leq 342$. For this system, $\varsigma = 0.691$ and $\lambda = 0.00482$. All shapes and flowfields are steady and axisymmetric except for the highest value of Re and We, where there is a "ragged skirt attached to perimeter of a rising spherical cap drop. ... Not axially symmetric because of vortex shedding." At intermediate values of We the shapes are ellipsiodal, tending to unsteady wobbling motion for $Re \gtrsim 100$. Although direct comparison with these unsteady shapes is not possible, disk-like shapes are known to exist at the onset of the wobbling instability. Satapathy and Smith (1960) break down the shape and flow regimes as a function of Reynolds number, based on numerous experiments they performed. The authors do not even list the fluids used in the dispersed phase, so one can only speculate from their figures only that interfacial tensions were high, as with Wellek *et al* and Hendrix *et al*. Satapathy and Smith found that for $Re < 4$ the shapes are spherical and

the flowfield is nearly fore-aft symmetric. For $4 < Re < 10$, a single ring vortex forms at the rear of the drop, and the drag is higher than would be expected for a sphere; the shape is ellipsoidal, with a slight flattening in the rear. From $10 < Re < 45$ the recirculating wake increases in length and the deformation is markedly ellipsoidal. Above $Re = 45$, Satapathy and Smith observe a transition to unsteady flowfield and motion, characterized by vortex shedding. Without knowing values for any of the dimensionless groups other than Re, it is difficult to quantitatively compare the work of Satapathy and Smith with other experimental work mentioned above, or with the numerical results of the present work. However, we can see that the gross features of the present work—that is, flowfield and shape—compare favorably with the steady cases found in these experimental papers. At low Weber numbers, the shapes of the drops are spheroidal (nearly spherical and elliptical) and at higher values of We the shape tends to a spherical or ellipsoidal cap. At intermediate values of Re, the shape is ellipsoidal in nature, and appreciably sized recirculating wakes form at the rear of the drop. While the length of the wake can be up to two body-lengths in size, the width never exceeds that of the drop.

Thorsen *et al* (1968) performed a series of experiments to obtain the terminal velocities of carefully purified organic/water systems. Their aim was to obtain results for both the steady and oscillating regimes. In Fig. 13 of Thorsen *et al*, a comparison is made with the earlier work of Hu and Kintner (1955). Hu and Kintner correlated their data for organic drops falling in water by means of a physical property group and the Weber number (Fig. 3 of Hu and Kintner). They found that all of their data fell onto a single curve, including data taken from solid spheres, and concluded (wrongly) that spherical liquid droplets behave like solid spheres for $Re < 300$. Thorsen *et al* use the same correlation as Hu and Kintner and demonstrate that liquid drops do indeed behave differently than solid particles, and attribute the results of Hu and Kintner to surfactants. We have superposed our numerical results on Fig. 13 of Thorsen *et al*, and these

are shown in Fig. 10. The solid symbols represent experimental results obtained by Thorsen *et al* using a surface active agent, while the light symbols are for pure fluids. It is obvious that our results lie among those of the pure liquid systems.

c. Comparison with theory

Moore (1963, 1965) carried out boundary layer analyses for high Reynolds number flow past spherical and oblate ellipsoidal inviscid bubbles, that is, bodies of fixed shape having a pure slip surface. Moore's results showed that the $O(1)$ solution for the flow was the potential flow solution and consequently that a recirculating eddy did *not* exist for bubbles in the limit $Re \longrightarrow \infty$. The numerical calculations of Ryskin and Leal (1984) and Dandy and Leal (1986), on the other hand, demonstrated that closed streamline wakes do exist at moderate Re, $O(100)$, and only disappear for an ellipsoidal void in the limit $Re \gg 1$. Similarly, for a spherical liquid drop, Harper and Moore (1968) showed that the limiting solution for $Re \longrightarrow \infty$ in the outer fluid was the potential flow solution, and the $O(1)$ solution for the flow inside the drop was Hill's spherical vortex, except for a thin boundary layer existing near the drop interface and along the line of symmetry inside the drop. Again, all the vorticity leaving the body surface was predicted to be confined within an infinitesimally thin wake extending to infinity. On the other hand, our present results for free-surface drops show that recirculating wakes appear behind drops at finite values of the Reynolds number (exceeding some critical value for each λ) provided that the drop is sufficiently deformed, the necessary degree of deformation again depending upon λ. Other workers have found via numerical calculation (Rivkind and Ryskin 1976) that recirculating wakes also exist behind spherical liquid drops at moderate Reynolds numbers ($Re = O(100)$) so long as $\lambda > 1$. It is therefore clear that the existence of a recirculating wake must be attributed to some mechanism which is present at moderate Reynolds numbers for *both* drops and bubbles, and either absent or secondary at high Re. As discussed in Dandy and

Leal (1986) these recirculating wake regions appear to exist as a consequence of vorticity accumulation due to the relative inefficiency behind the bubble or drop of convective transport of vorticity at modest Reynolds numbers. The main difference between the bubbles considered in our earlier work, and the viscous drop studied here, is that vorticity is generated both as a consequence of surface curvature (as for the bubble) and the "no-slip" condition so that sufficient vorticity to produce a recirculating wake can be achieved with less deformation. Further, since the presence of the unattached recirculating wake obviously has nothing to do with detachment of the *boundary* fluid for the case of the liquid drops, it would be very surprising indeed if boundary layer theory were able to accurately predict the flow behavior observed in this work or in Rivkind and Ryskin (1976). Thus, if the asymptotic structure of Harper and Moore (1968) is to provide an adequate description of the flowfield it can only be for larger $Re \gg 1$.

To investigate the effect of the Reynolds number on the flowfields at large Re, a series of calculations were done for $We = 1$, $\varsigma = 0.91$, $\lambda = 2.5$ and $150 \leq Re \leq 350$. The idea was to choose a value of We and λ such that the rate of vorticity production might be small enough that convective transport could sweep the vorticity away (and thus "dissipate" the recirculating flow) at finite Re so that a transition toward the asymptotic structure might be evident numerically. In using second order centered finite differences there is an upper bound on Re for which (reliable) solutions may be obtained, which in turn depends on the cell Reynolds number (or, a Reynolds number based on the discretization). Thus, a fine mesh will increase the Reynolds number at which a reliable solution can be found. With the discretization used (61x61 mesh, inside and out), and the nearly spherical shapes arising from $We = 1$, we had no trouble finding apparently reliable solutions up to $Re = 400$. Figure 11 shows the flow behavior as Re is increased: the recirculating wake first appears at a Reynolds number of approximately 60, grows to a maximum length at roughly

$Re = 180$, and then completely disappears by the time the Reynolds number reaches 350. Note that as the eddy shrinks in size the vortex inside the drop becomes more fore-aft symmetric, that is, closer to Hill's vortex. Comparison of C_D between our numerical solutions and the analytical work of Harper and Moore can be found in Table II for a variety of Reynolds numbers.

Another interesting aspect of the solutions shown in Fig. 11 is that for $Re \gtrsim 100$ the drop shape is relatively insensitive to Reynolds number. A similar insensitivity to Re was also observed by Ryskin and Leal in their work on deformable voids. Had the shape not been so insensitive to Re, that is, had deformation increased with increasing Reynolds number as was true for lower Reynolds numbers, then it probably would not have been possible to determine anything about the correspondece between the results of this work and those of Harper and Moore. A great deal of care was taken to insure that the numerical results are accurate, and that they do not depend on either numerical parameters or the method used. A much more detailed discussion of the accuracy of the numerical scheme is given in an earlier paper (Dandy and Leal 1986). Of course, the results for other values of We, λ and ς will be different in detail from those exhibited here, but we expect that the same qualitiative behavior would be manifested at sufficiently large Re in all cases.

Another point of interest is the Reynolds number dependence of wake structure and its dependence on λ, i.e., on the relative mix of vorticity production by the boundary curvature and no-slip. Theory predicts that in the limit $\lambda \longrightarrow \infty$, the maximum surface vorticity becomes proportional to the square root of the Reynolds number for $Re \gg 1$, that is, $\omega_m \propto Re^{1/2}$, and in this case, a separated flow with recirculating wake exists even in the limit $Re \longrightarrow \infty$, as predicted by boundary-layer theory. On the other hand, for $\lambda = 0$, $\omega_m \longrightarrow$ constant as $Re \longrightarrow \infty$ for a body of fixed shape, and we showed in an earlier paper that the recirculating wake then disappears for sufficiently large Re and is not predicted either by boundary-layer analysis. The solutions for a viscous drop, considered

here, provide the basis for understanding and examining the transition process where vorticity is produced by some combination of no-slip and boundary curvature. In Fig. 12 we display numerical results from the present work for ω_m at fixed $We = 0.5$, $\varsigma = 0.91$ and several different Reynolds numbers: 100, 150, 200 and 250. The upper solid line is $\omega \equiv Re^{1/2}$ and it is apparent that as λ increases, ω_m tends toward a $Re^{1/2}$ dependence. The lower solid line is a plot of numerically calculated values of ω_m as a function of Re, for a void of fixed shape, taken from Dandy and Leal (1986). It is apparent for the void that ω_m asymptotes to a constant as $Re \longrightarrow \infty$. The fact that convection of vorticity downstream becomes increasingly efficient for increasing Re, while the rate of production asymptotes to a constant value in this case, may explain the disappearance of the recirculating wake for increasing Re (as shown by Dandy and Leal). Similarly, for $\lambda = O(1)$ the magnitude of vorticity ω_m for large Re increases much more slowly with Re than for a solid, and thus may account for the disappearance of the recirculating wake with increase of Re in these cases.

As a check on our numerical results at higher values of Re, we compare drag coefficients calculated in this work against those of Rivkind and Ryskin (1976) who present a correlation for calculating the drag on a viscous spherical drop, as a function of Re and λ:

$$C_D = \frac{1}{\lambda+1}\left[\lambda\left(\frac{24}{Re} + \frac{4}{Re^{1/3}}\right) + \frac{14.9}{Re^{0.78}}\right] \tag{8}$$

We have computed solutions for $We = 0.5$ and $\varsigma = 0.91$ and a range of Reynolds numbers $0.5 \leq Re \leq 300$ at three values of the viscosity ratio: 1.33, 2.5 and 4; some of these solutions are shown in Fig. 11, the rest are in the Appendix. We chose $We = 0.5$ so the drops would be nearly spherical. We also computed solutions for a solid spherical particle. The results of all of these numerical calculations are compared with the correlation of Rivkind and Ryskin in Fig. 13. The symbols correspond to our numerical results and the lines to the correlation.

At lower Reynolds numbers (< 1), numerical results are a great deal easier to obtain, and the shapes and flowfields are simpler than at the higher Reynolds

numbers. A comparison of a result for $Re = 0.5$, $We = 0.5$, $\varsigma = 0.91$ and $\lambda = 4$ with that of Taylor and Acrivos (1964) is shown in Fig. 14, where the solid line indicates the result from this work and the dashed line is the result of Taylor and Acrivos. The agreement between the two shapes is pretty good, especially considering that the work by Taylor and Acrivos is an asymptotic analysis which takes into account the first effects of inertia and non-sphericity. In other words, it is implied that Re, $We \ll 1$. The drag coefficients compare favorably, with Taylor and Acrivos yielding $C_D = 48.4$, and the numerical results from this work give $C_D = 48.7$.

IV. Conclusions

The problem solved here demonstrates the viability of a finite difference technique in conjunction with the grid generation technique of Ryskin and Leal (1983) for the solution of two-fluid free-boundary problems. In the past 15 years a tremendous amount of work has been put into different methods of generating both orthogonal and nonorthogonal coordinate grids (for a review of this work, see Eiseman 1985; Thompson *et al* 1986), so that there is now a very versatile collection of grid generation techniques available, and no fundamental difficulty in applying finite difference techniques to complicated (and unknown) domains. As far as we know, however, very little prior work has been done using *either* finite difference or finite element techniques on a two-fluid free surface boundary problem at finite Reynolds number. In effect, our numerical technique enables us to perform experiments that would be difficult to carry out in the laboratory: for example, we have the ability to independently vary the four dimensionless parameters that are present in this problem.

Although the detached recirculating wake structure is not new in the fluid mechanics literature, it is nevertheless quite novel and its appearance is impossible to understand on the basis of concepts of separation from boundary-layer theory. Indeed, as we have demonstrated, the existence of closed streamline wakes

behind bubbles and drops is strictly a finite Reynolds number phenomenon. For a fixed Reynolds number and Weber number, the drop shape became slightly more distorted with decreasing density ratio or viscosity ratio. If a recirculating wake was present, it grew in size when λ was increased, and moved closer to the rear of the drop due to the slowing of the interior flow. The range of shapes that were observed in this work for $0.5 \lesssim Re \lesssim 300$ and $0.5 \lesssim We \lesssim 15$ were all in agreement with the predictions of the graphical correlation in Clift *et al* and with experimental observation.

Acknowledgements

All computations were carried out on Boeing Computer Services' CRAY X-MP/24, and the authors wish to acknowledge the expert help and courtesy shown by Boeing employees Horst Simon and David Dodson.

This work was supported by grants from the Fluid Mechanics Program and the Office of Advanced Scientific Computing at the National Science Foundation.

Re	*We*	λ	ζ	C_D
0.5	0.5	1.33	0.91	42.3
	1			42.5
	2			42.6
	4			42.8
2	0.5	4		13.92
	1			14.05
	2			14.20
	4			14.38
	6			14.52
	8			14.71
	10			14.95
	12			15.09
	14			15.23
5	1	1.33		5.80
	2			5.88
	4			6.12
10	0.5	4		3.96
	1			4.01
	2			4.10
	4			4.28
	6			4.42
	8			4.88
20	1	100	10000	2.72
	2			2.74
	4			2.80
	6			2.85
40	0.5	4	0.91	1.62
60				1.27
	2			1.31
	4			1.43
	6			1.65
	8			1.85

Table I. Drag coefficients in present work

Re	We	λ	ζ	C_D
60	2	0.5	0.91	0.890
		10		1.30
		1	0.1	0.998
	0.5	0.01	0.001	0.589
	4	1	2	1.15
		1.33	0.91	1.22
	6	10		1.51
80	0.5	4		1.08
100	1	2		0.856
	4	1		0.919
		2		0.990
		4		1.10
		10		1.21
		50		1.28
		100		1.29
		500		1.29
		1000		1.30
		∞		1.31
		200	100	1.29
		200	500	1.29
		200	2000	1.31
		2	0.5	1.02
		4	0.85	1.11
		8	2	1.18
		16	4	1.24
		32	8	1.27
		50	20	1.28
		1	0.002	0.854
			0.01	0.856
			0.02	0.859
			0.1	0.867
			0.2	0.875
			0.25	0.880
			0.5	0.889
			2	0.911
	0.5	4	0.91	0.958
	2			1.00
	4			1.098
	6			1.214
	8			1.298

Table I (continued)

Re	We	λ	ζ	C_D
100	0.5	4	0.91	0.958
	2			1.00
	4			1.098
	6			1.214
	8			1.298
150	1			0.78
200				0.68
250				0.61
275				0.58
300				0.56
350				0.51

Table I (continued)

Re	C_D	
	Harper and Moore	Present Work
100	- 0.4854	0.912
150	0.3142	0.726
200	0.5192	0.633
250	0.5692	0.570
300	0.5686	0.565
350	0.5502	0.554
400	0.5256	-

Table II. Comparison between analytical results of Harper and Moore (1968) and Present work, for λ=2.5 and ζ=0.91.

The formula for C_D in Harper and Moore is

$$C_D = \frac{48}{Re}\left\{1 + \frac{3}{2V} + \frac{\log Re}{Re^{1/2}}\frac{\lambda_b^2(1+V')}{V^2}C_1 + \frac{\lambda_b(1+V')}{Re^{1/2}V}\left[\frac{\lambda_b(1+V')}{V}C_2 + \left(1+\frac{3}{2V}\right)C_3\right]\right\},$$

where

$$V = \mu/\hat{\mu} = 0.4$$

$$V' = (\zeta\lambda)^{-1/2} = 0.66332$$

$$\lambda_b = \frac{2V+3}{2V'+3} = 0.878278$$

$$C_1 \simeq 0.120775$$

$$C_2 \simeq 7.099424$$

$$C_3 \simeq -8.745213$$

References

Brignell, A.S. 1973 *Q. J. Mech. Appl. Maths.* **26**, 99-107.

Clift, R., Grace, J.R., and Weber, M.E. 1978 *Bubbles, Drops, and Particles.* Academic Press.

Christov, C.I. and Volkov, P.K. 1985 *J. Fluid Mech.* **158**, 341-364.

Dandy, D.S. and Leal, L.G. 1986 *Phys. Fluids* **29**, 1360.

Dorodnitsyn, A.A. and Meller, N.A. 1968 *U.S.S.R. Comput. Math. and Math. Phys.* **8**, 205-217.

Eiseman, P.R. 1985 *Ann. Rev. Fluid Mech.* **17**, 487-522.

Fornberg, B. 1980 *J. Fluid Mech* **98**, 819-855.

Garner, F.H. and Tayeban, M. 1960 *Anales. Real. Soc., Espan. Fis. Quim.* **B56** No. 5.

Grosch, C.E. and Orszag, S.A. 1977 *J. Comput. Phys.* **25**, 273.

Haas, U., Schmidt-Traub, H., and Brauer, H. 1972 *Chem.-Ing.-Tech.* **44**, 1060-1068.

Harper, J.F. 1972 *Adv. Appl. Mech.* **12**, 59-129.

Harper, J.F. and Moore, D.W. 1968 *J. Fluid Mech.* **32**, 367-391.

Hendrix, C.D., Dave, S.B. and Johnson, H.F. 1967 *AIChE J.* **13**, 1072-1077.

Hu, S. and Kintner, R.C. 1955 *AIChE J.* **1**, 42-48.

Israeli, M. 1970 *Stud. Appl. Math.* **49**, 327-349.

Kalra, T.R. and Uhlherr, P.H.T. 1971 *Aust. Conf. Hydraul. Fluid Mech., 4th, Melbourne.*

Kang, I.S. and Chang, H.N. 1982 *Int. J. Heat Mass Transfer* **25**, 1167-1181.

LeClair, B.P. 1970 PhD Thesis, McMaster Univ., Hamilton, Ontario.

LeClair, B.P., Hamielec, A.E., Pruppacher, H.R., and Hall, W.D. 1972 *J. Atmos. Sci.* **29**, 728-740.

Lighthill, J. 1986 *An Informal Introduction to Theoretical Fluid Mechanics*, Clarendon Press, Oxford.

Masliyah, J.H. 1970 PhD Thesis, Univ. of British Columbia, Vancouver.

Miksis, M., Vanden-Broeck, J.-M., and Keller, J.B. 1981 *J. Fluid Mech.* **108**, 89-100.

Moore, D.W. 1959 *J. Fluid Mech.* **6**, 113-130.

Moore, D.W. 1963 *J. Fluid Mech.* **16**, 161-176.

Moore, D.W. 1965 *J. Fluid Mech.* **23**, 749-766.

Morse, P.M. and Feshbach, H. 1953 *Methods of Theoretical Physics.* McGraw-Hill.

Nakamura, I. 1976 *Phys. Fluids* **19**, 5-8.

Nisi, H. and Porter, A.W. 1923 *Philos. Mag.* **46**, 754-768.

Parlange, J.-Y. 1970 *Acta Mechanica* **9**, 323-328.

Peacemann, D.W. and Rachford, H.H. 1955 *J. Soc. Indust. Appl. Math.* **3**, 28.

Proudman, I. and Pearson, J.R. 1957 *J. Fluid Mech.* **2**, 237.

Pruppacher, H.R. and Beard, K.V. 1970 *Q. J. R. Meteorol. Soc.* **96**, 247-256.

Rivkind, V.Y. and Ryskin, G. 1976 *Fluid Dyn.* **11**, 5-12.

Ryskin, G. 1980 *J. Fluid Mech.* **99**, 513-529.

Ryskin, G. and Leal, L.G. 1983 *J. Comput. Phys.* **50**, 71-100.

Ryskin, G. and Leal L.G. 1984 *J. Fluid Mech.* **148**, 1-17.

Ryskin, G. and Leal, L.G. 1984 *J. Fluid Mech.* **148**, 19-35.

Satapathy, R. and Smith, W. 1960 *J. Fluid Mech.* **10**, 561-570.

Shoemaker, P.D. and Marc de Chazal L.E. 1968 *Chem. Engng. Sci.* **24**, 795-798.

Taneda, S. 1956 *J. Phys. Soc. Jpn.* **11**, 1104.

Taylor, T.D. and Acrivos, A. 1964 *J. Fluid Mech.* **18**, 466-476.

Thompson, J.F., Warsi, Z.U.A., and Mastin, C.W. 1985 *Numerical Grid Generation: Foundations and Applications.* Elsevier.

Thorsen, G., Stordalen, R.M. and Terjesen, S.G. 1968 *Chem. Engng. Sci.* **23**, 413-426.

Wellek, R.M., Agrawal, A.K. and Skelland, A.H.P. 1966 *AIChE J.* **12**, 854-862.

Figure captions

Figure 1: Schematic sketch of the problem.

Figure 2: (a) Shape of drop as a function of We for $Re = 2$, $\varsigma = 0.909$, and $\lambda = 4$. (b) The corresponding flowfields; $|\psi| \geq 10^{-3}$.

Figure 3: Vorticity lines and streamlines for several values of We for $Re = 10$, $\varsigma = 0.909$, and $\lambda = 4$; $|\psi| \geq 10^{-3}$ and $|\omega| \geq 10^{-2}$.

Figure 4: Streamfunction $|\psi| \geq 10^{-3}$ and vorticity $|\omega| \geq 10^{-2}$ plots showing detail of rear of (a) void with $Re = 20$, (b) void with $Re = 90$, (c) void with $Re = 180$ and (d) solid with $Re = 100$.

Figure 5: Streamfunction $|\psi| \geq 10^{-3}$ and vorticity $|\omega| \geq 10^{-2}$ plots for $\lambda = 4$ and $\varsigma = 0.91$ as a function of We for (a) $Re = 60$ and (b) $Re = 100$.

Figure 6: (a) Schematic of the flowfield (with arrows indicating the direction of flow) for the case of a detached wake behind a liquid drop. (b) Schematic for the flowfield for a gas bubble. (c) Hypothetical flowfield for liquid drop with attached wake. (d) Schematic of the flowfield for liquid drop with attached wake and secondary interior recirculating vortex.

Figure 7: Streamfunction $|\psi| \geq 10^{-3}$ and vorticity $|\omega| \geq 10^{-2}$ plots for $Re = 100$, $We = 4$ and $\varsigma = 0.91$ as a function of λ. For the last plot, $\lambda = 1000$, the inner streamfunction and vorticity values are $|\hat{\psi}| \geq 10^{-5}$ and $|\hat{\omega}| \geq 10^{-4}$.

Figure 8: Streamfunction $|\psi| \geq 10^{-3}$ and vorticity $|\omega| \geq 10^{-2}$ plots for $Re = 100$ and $We = 4$ as a function of $\varsigma/\lambda = 0.25$.

Figure 9: Streamfunction $|\psi| \geq 10^{-3}$ and vorticity $|\omega| \geq 10^{-2}$ plots for $Re = 100$, $We = 4$ and $\lambda = 1$ as a function of ς.

Figure 10: Comparison of selected numerical results with experimental observations of Thorsen *et al* (1968): (A) $We = 1$, $\lambda = 2.5$, $\varsigma = 0.91$, $Re =$

100, 150, 200, 250, 300, 350; (B) $Re = 100, We = 1, \lambda = 2, \varsigma = 0.5$; (C) $Re = 100, We = 0.5, \lambda = 1, \varsigma = 0.02$; (D) $Re = 60, We = 0.5, \lambda = 4, \varsigma = 0.91$; (E) $Re = 60, We = 1, \lambda = 0.01, \varsigma = 0.001$; (F) $Re = 80, We = 0.5, \lambda = 4, \varsigma = 0.91$.

Figure 11: The flowfield as a function of Re for $We = 100$, $\varsigma = 0.909$, and $\lambda = 2.5$.

Figure 12: Plot of maximum surface vorticity ω_m versus Re for several values of the viscosity ratio. The upper solid line is $\omega = Re^{1/2}$ and the lower line is calculated values of ω_m for a void of fixed shape.

Figure 13: Comparison of C_D between numerical results of current work and correlation of Rivkind and Ryskin (1976).

Figure 14: Comparison between numerical results of this work and asymptotic analysis of Taylor and Acrivos (1964) for $Re = 0.5$, $We = 0.5$, $\varsigma = 0.909$, and $\lambda = 4$.

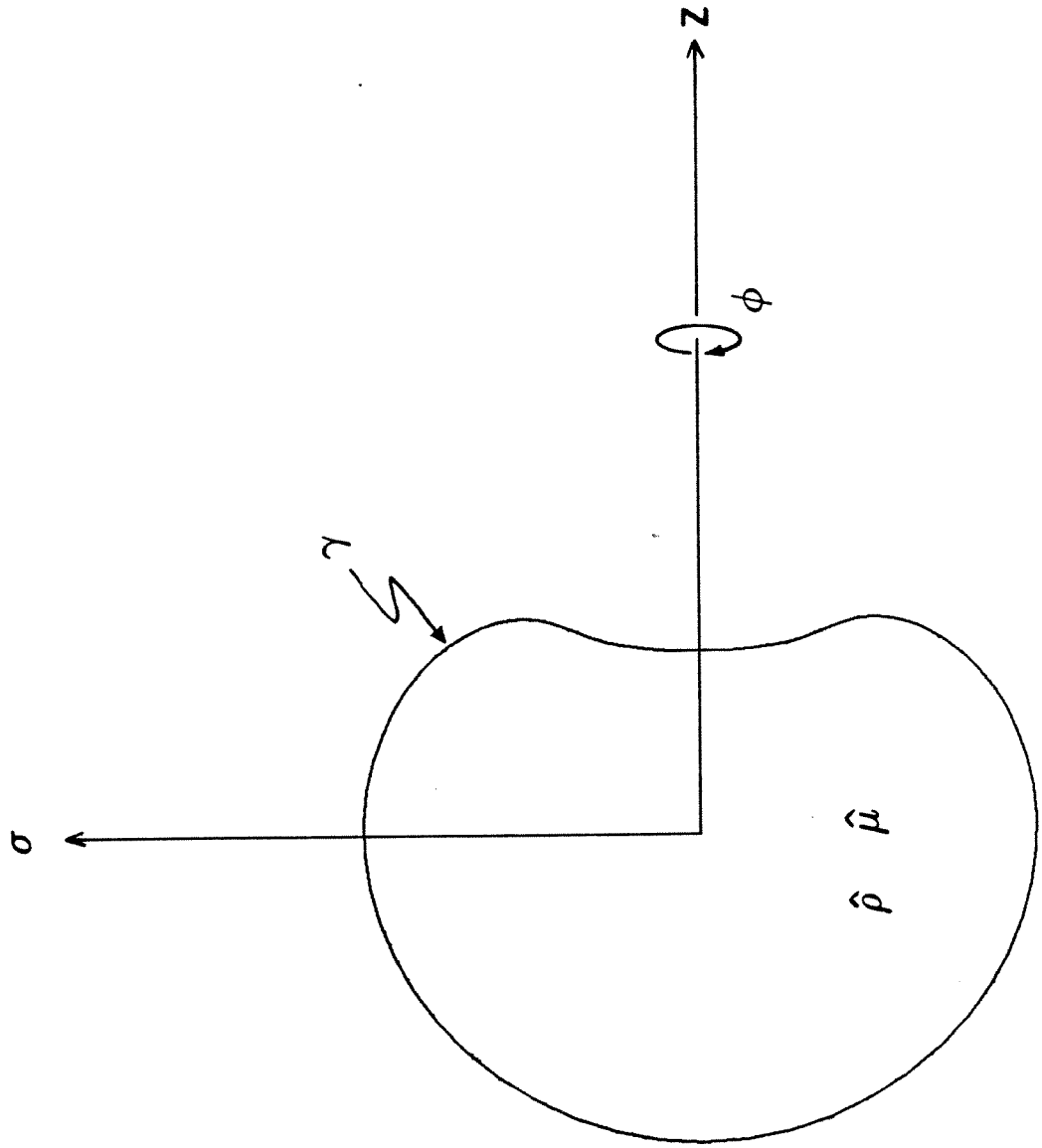

Figure 1.

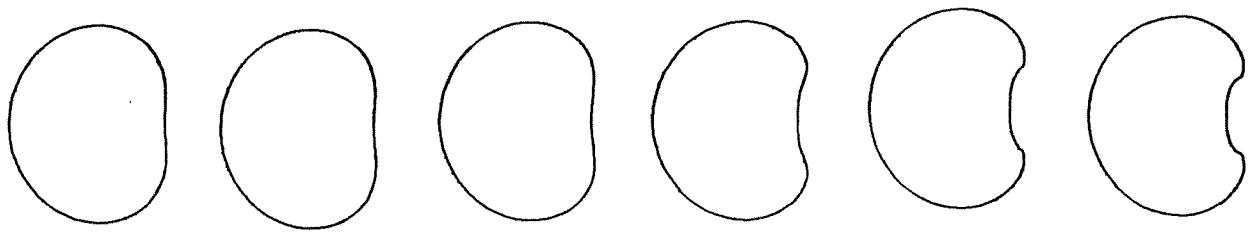

$We =$ 4 6 8 10 12 14

$Re = 2 \qquad \lambda = 4 \qquad \varsigma = 0.909$

Figure 2a.

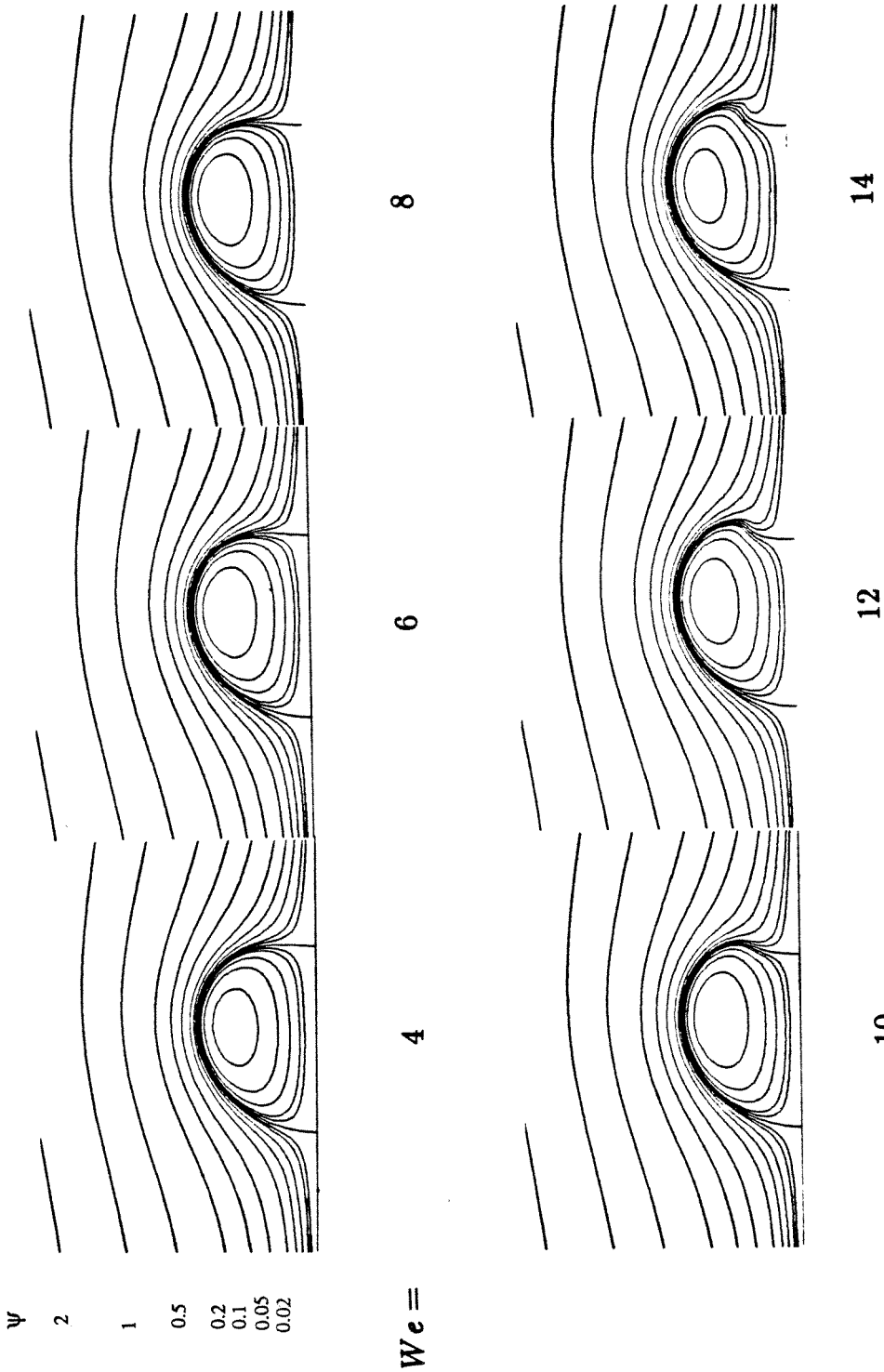

$Re = 2 \qquad \lambda = 4 \qquad \varsigma = 0.909$

Figure 2b.

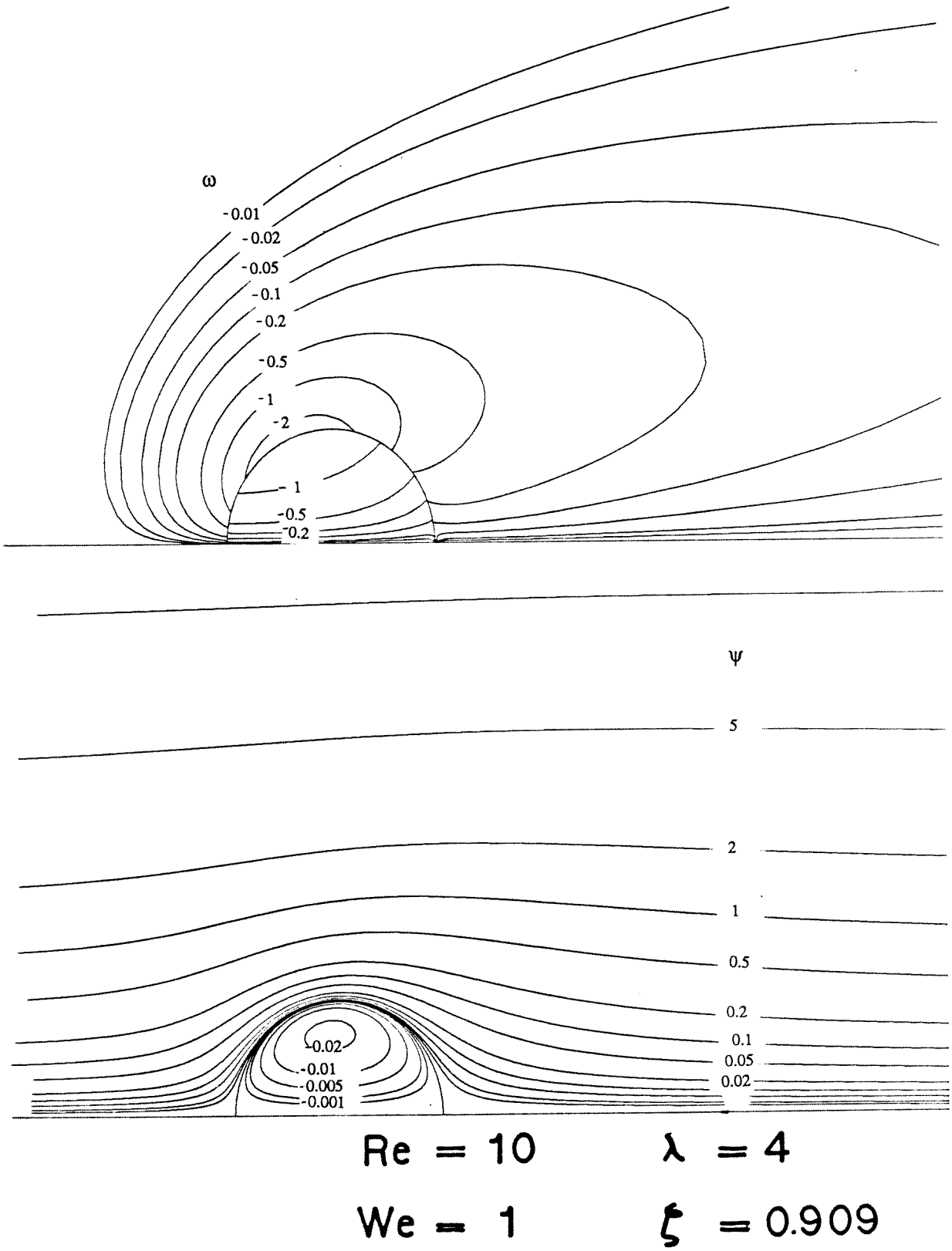
ω
-0.01
-0.02
-0.05
-0.1
-0.2
-0.5
-1
-2
-1
-0.5
-0.2
ψ
5
2
1
0.5
0.2
0.1
0.05
0.02
-0.02
-0.01
-0.005
-0.001
Re = 10
λ = 4
We = 1
ζ = 0.909

Figure 3

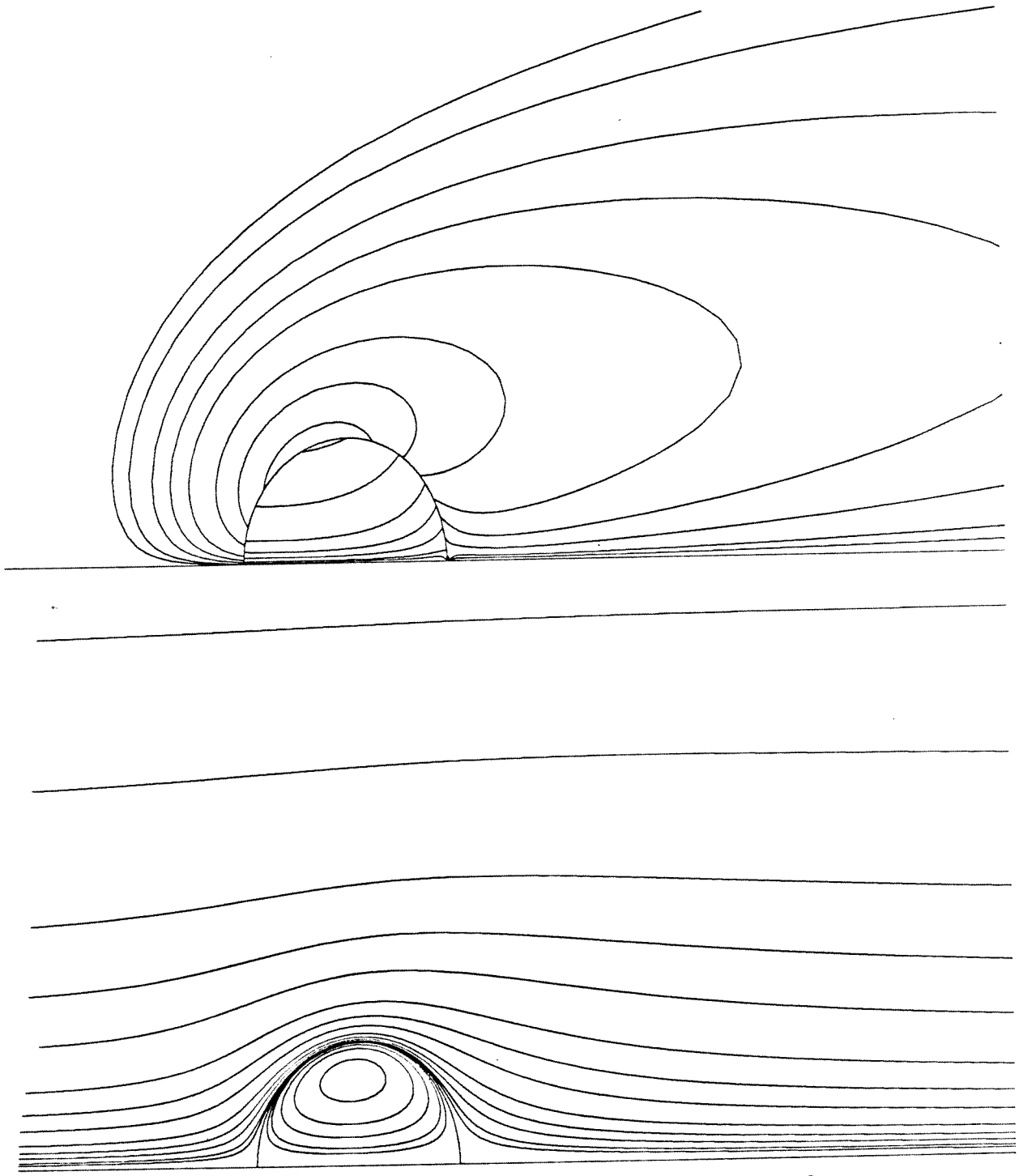

Figure 3 (continued)

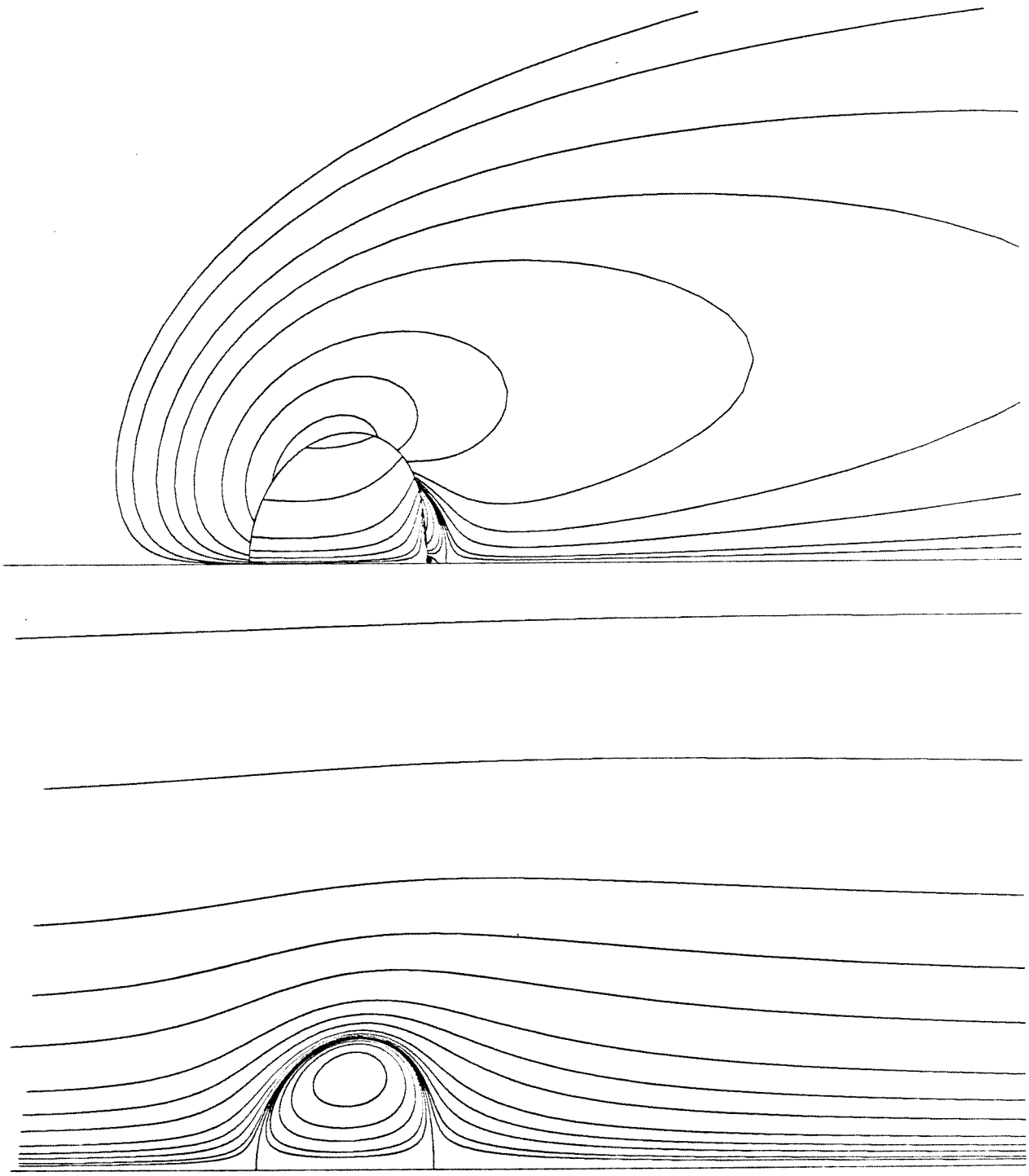

Figure 3 (continued)

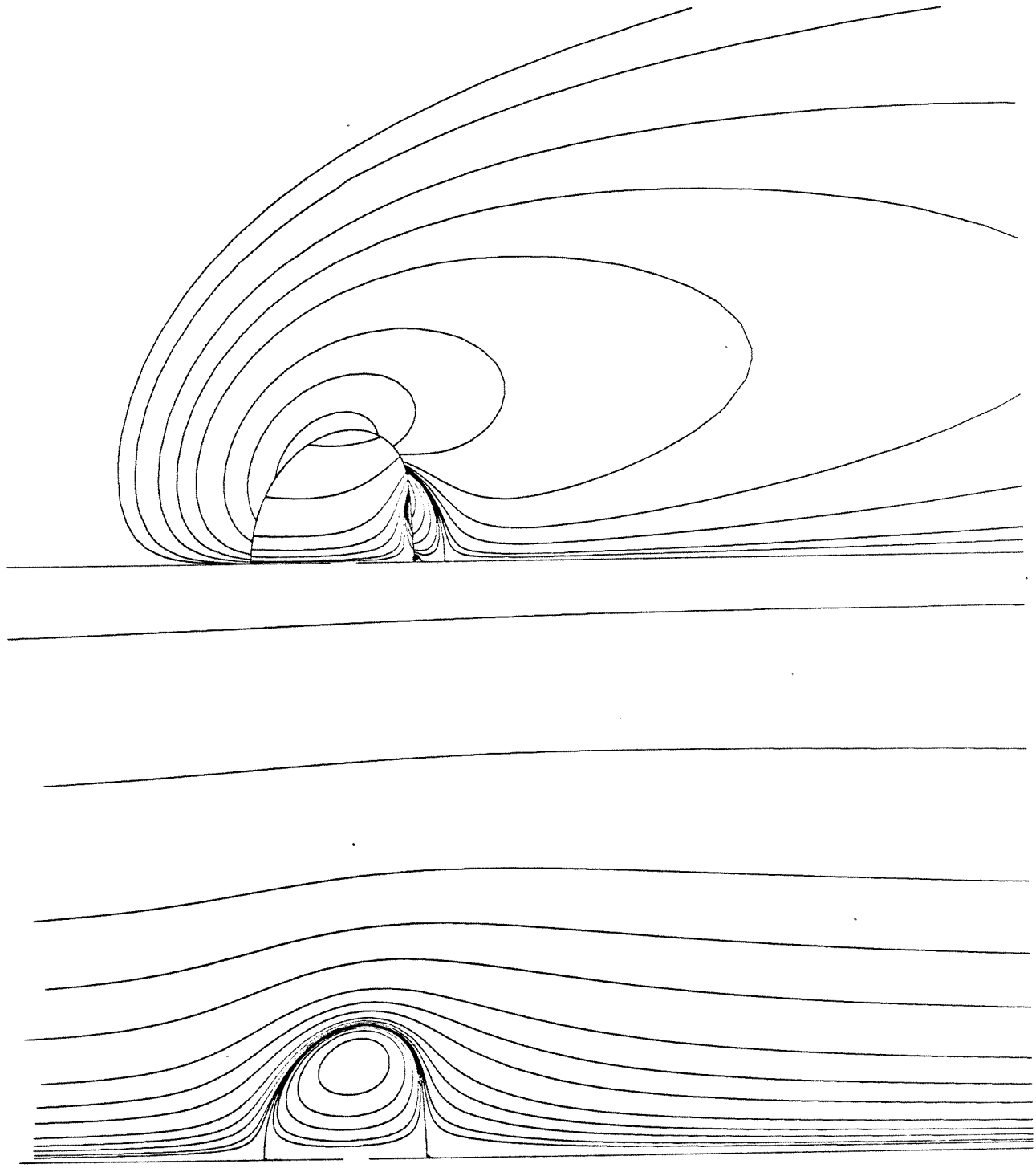

Figure 3 (continued)

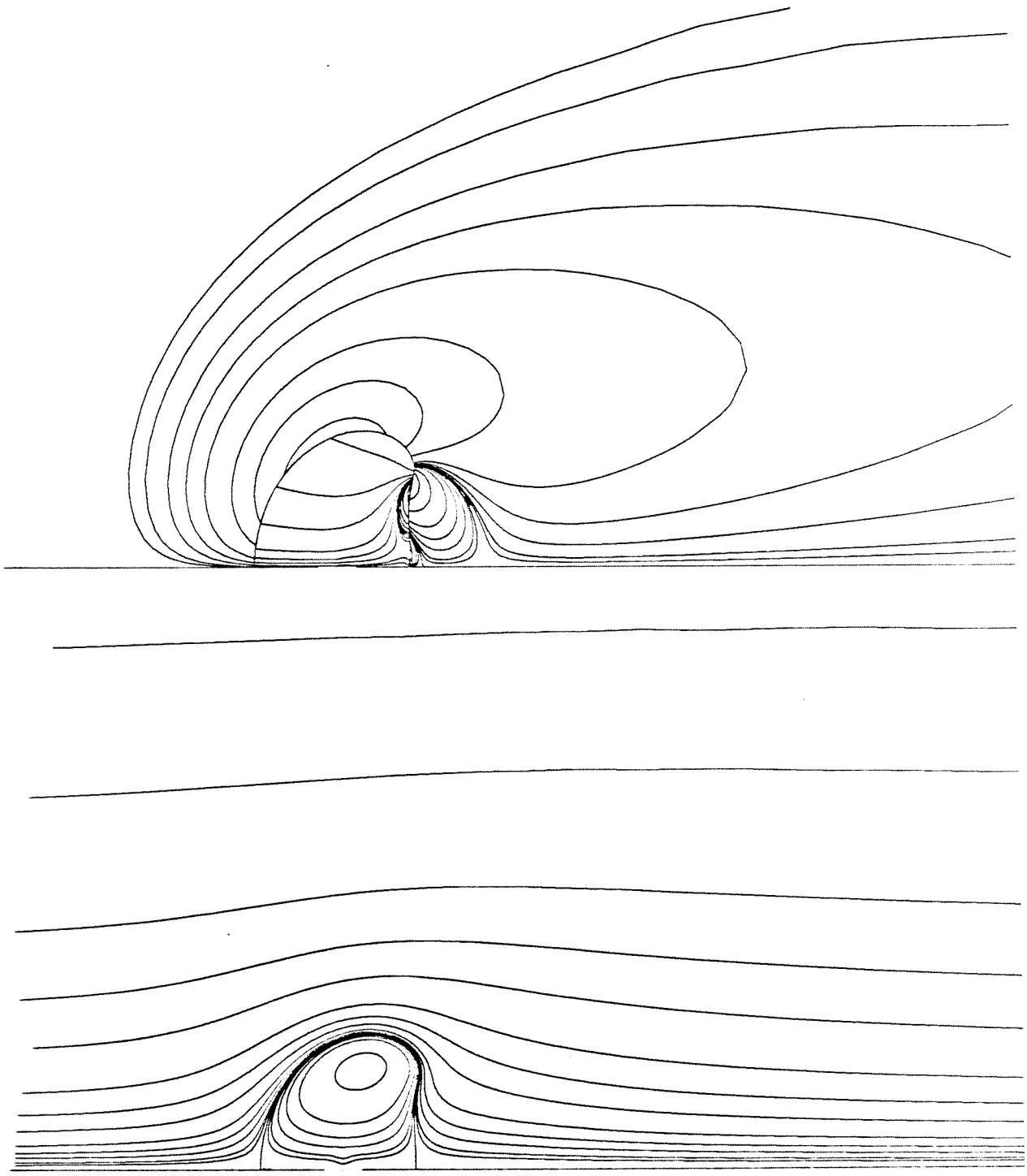

Figure 3 (continued)

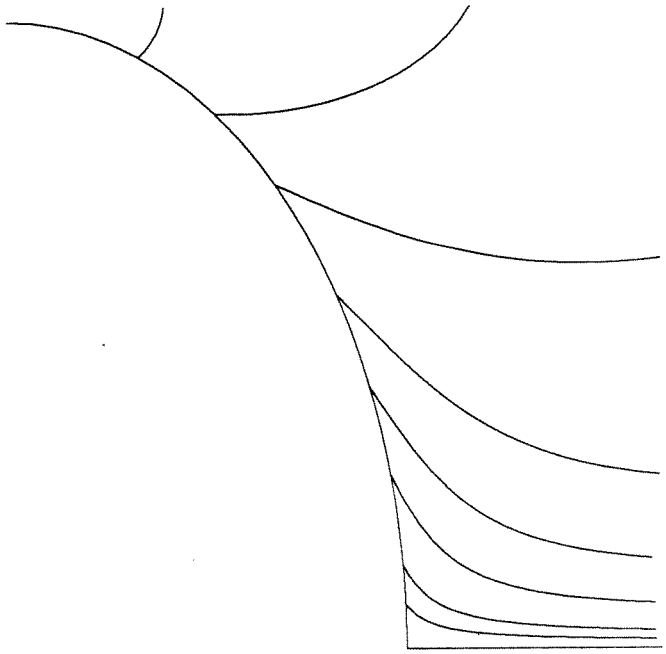

Re = 20

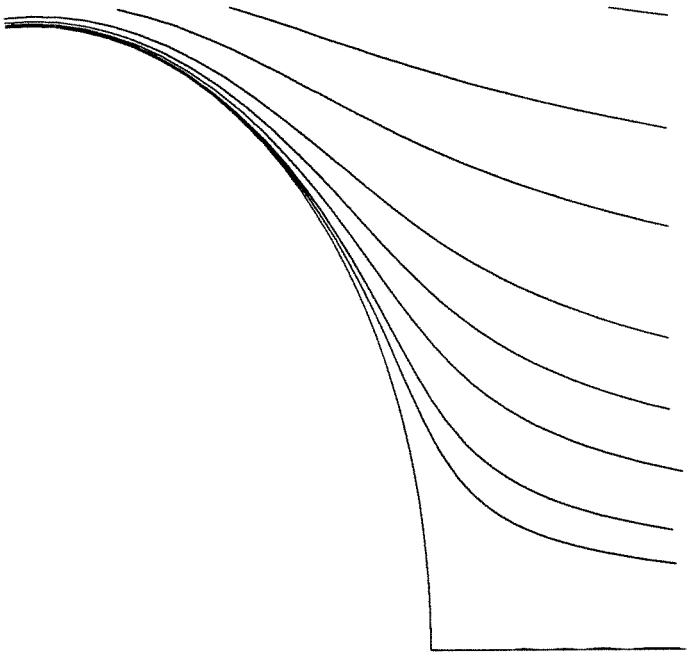

Figure 4a

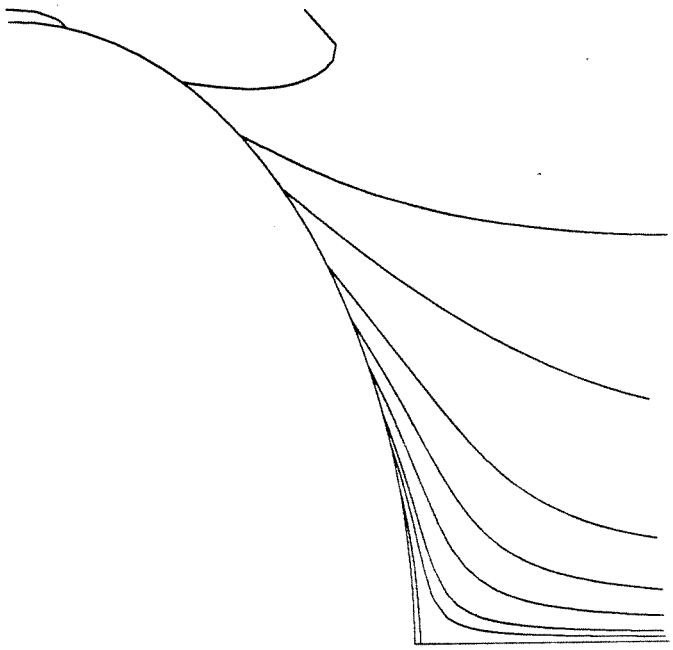

Re = 90

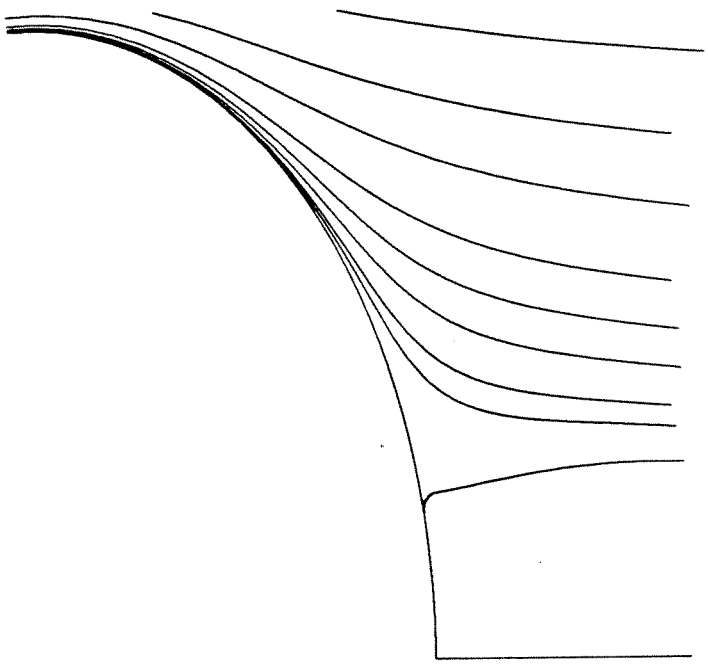

Figure 4b

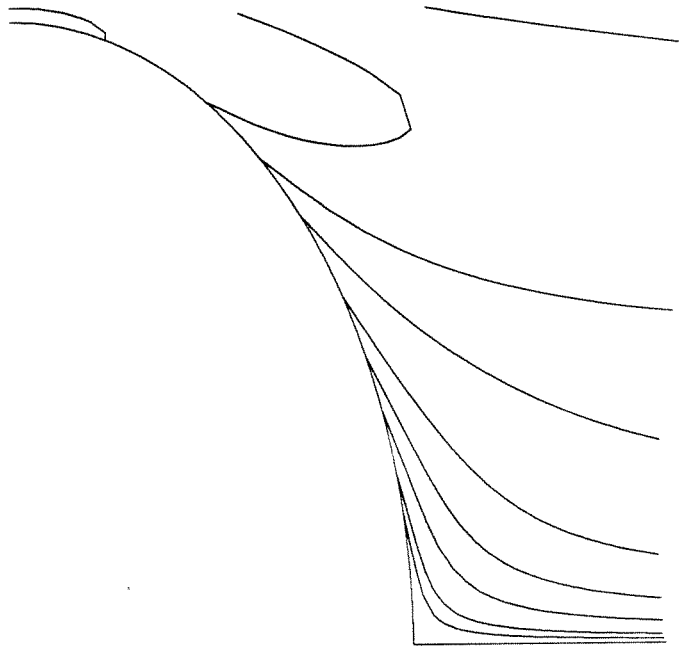

Re = 180

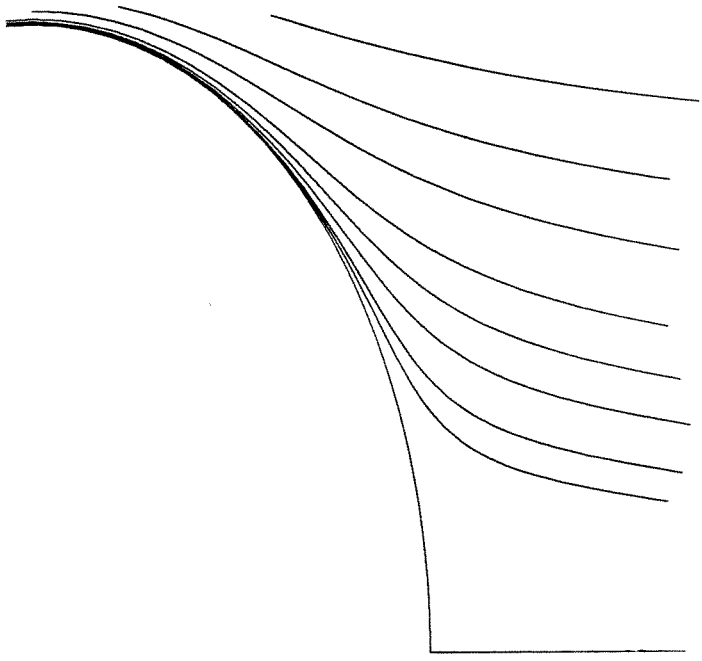

Figure 4c

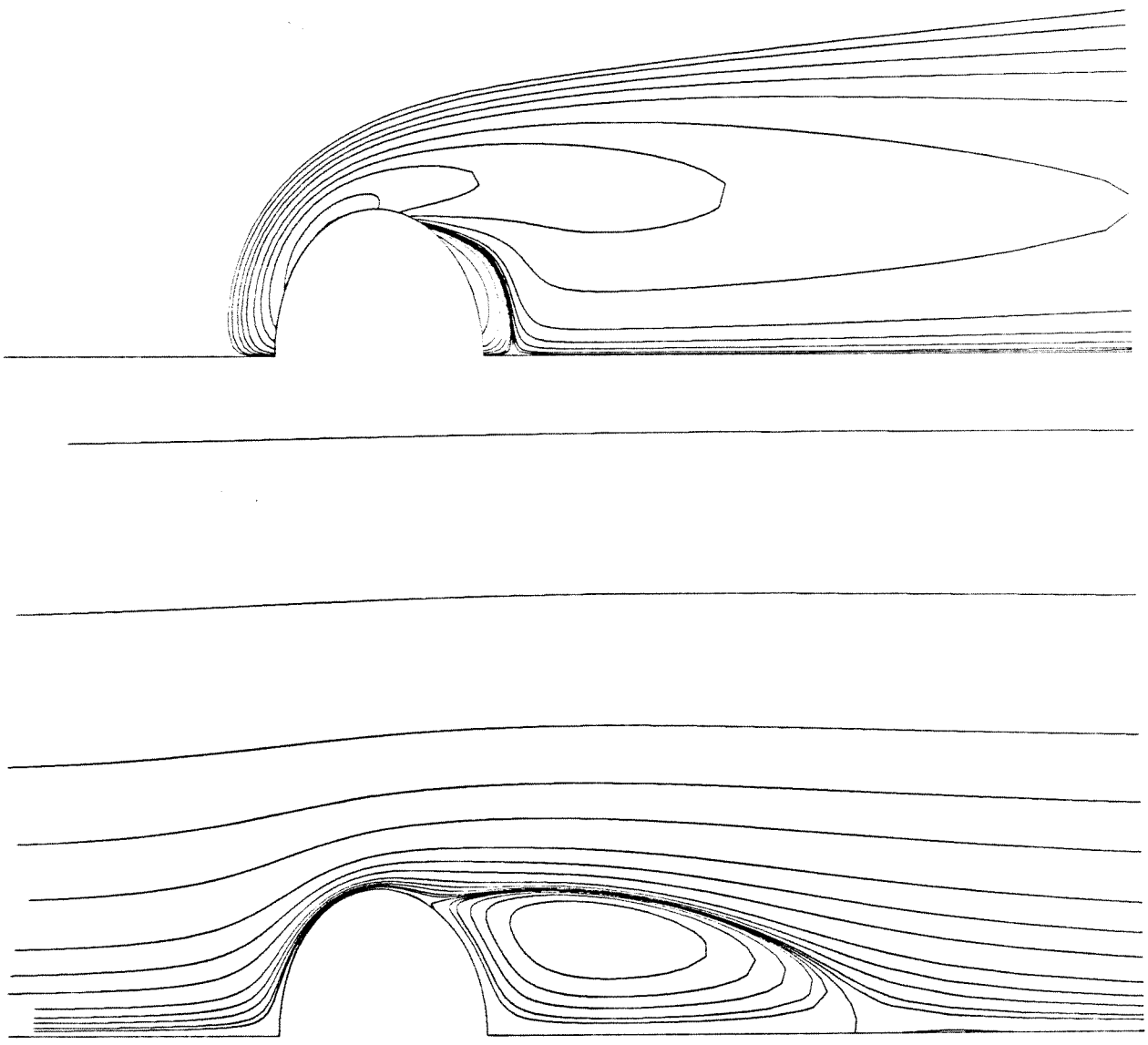

Re = 100 $\lambda = \infty$

We = 4 $\zeta = 0.909$

Figure 4d

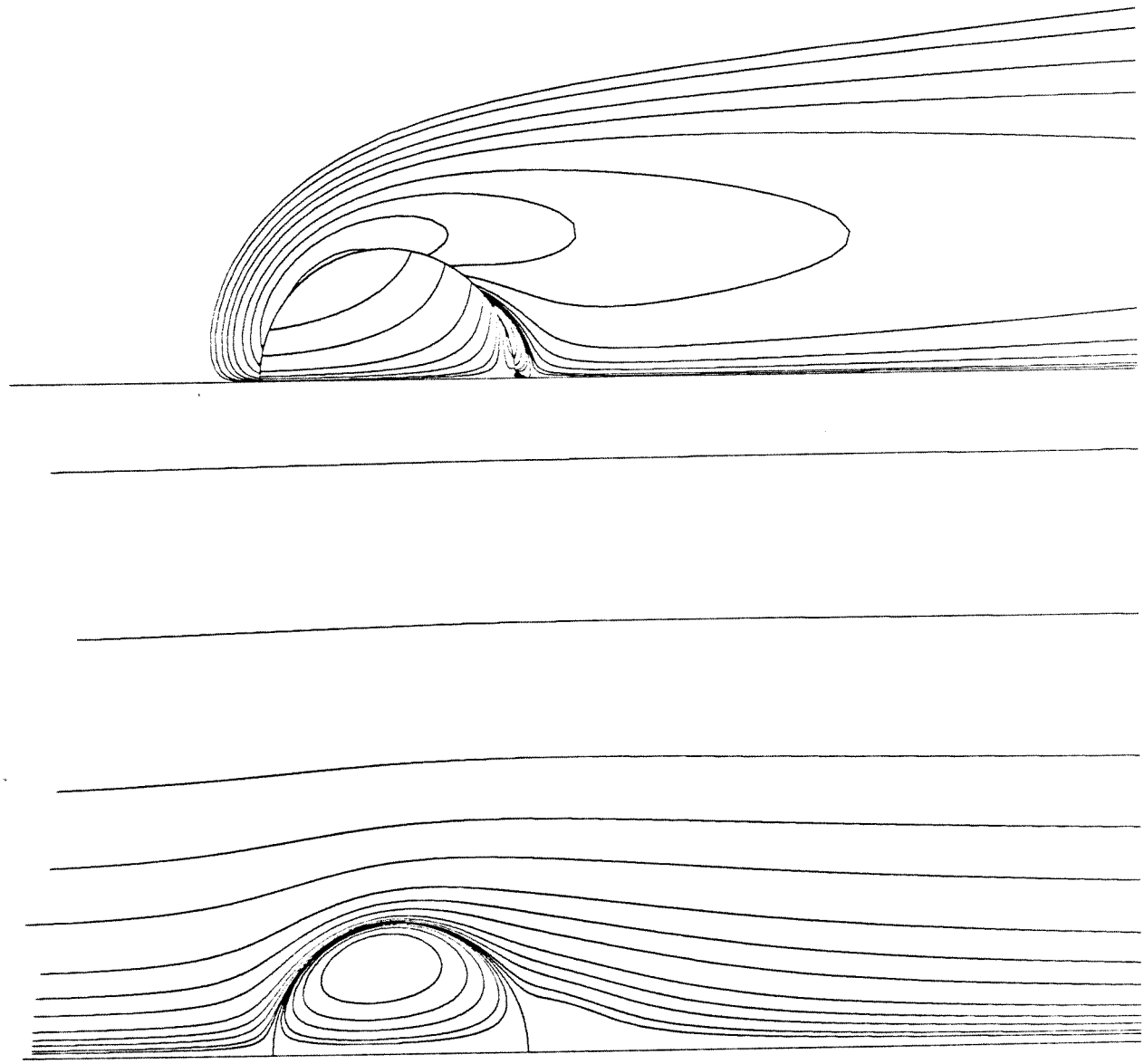

Re = 60 λ = 4

We = 0.5 ξ = 0.909

Figure 5a

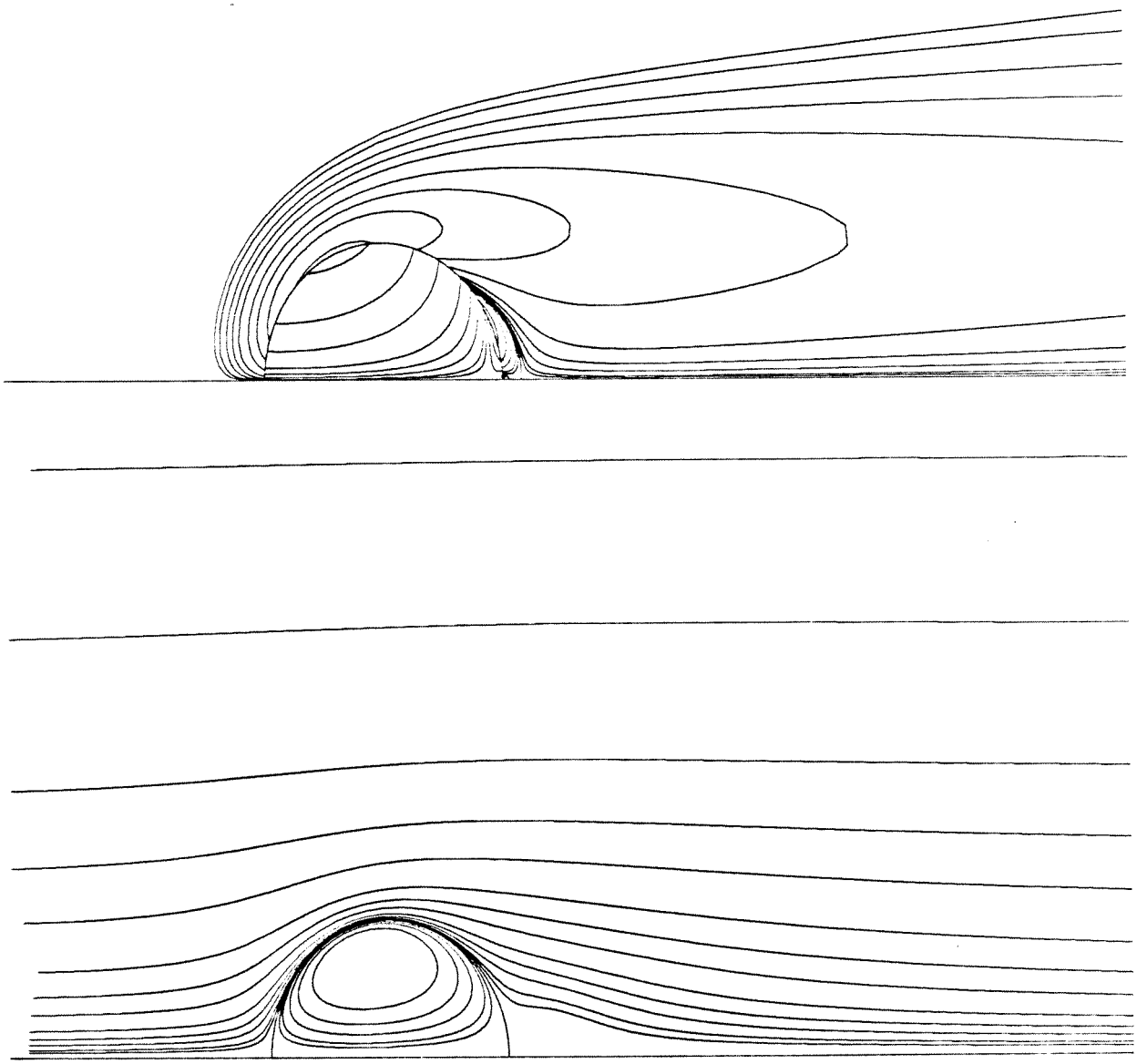

Figure 5a (continued)

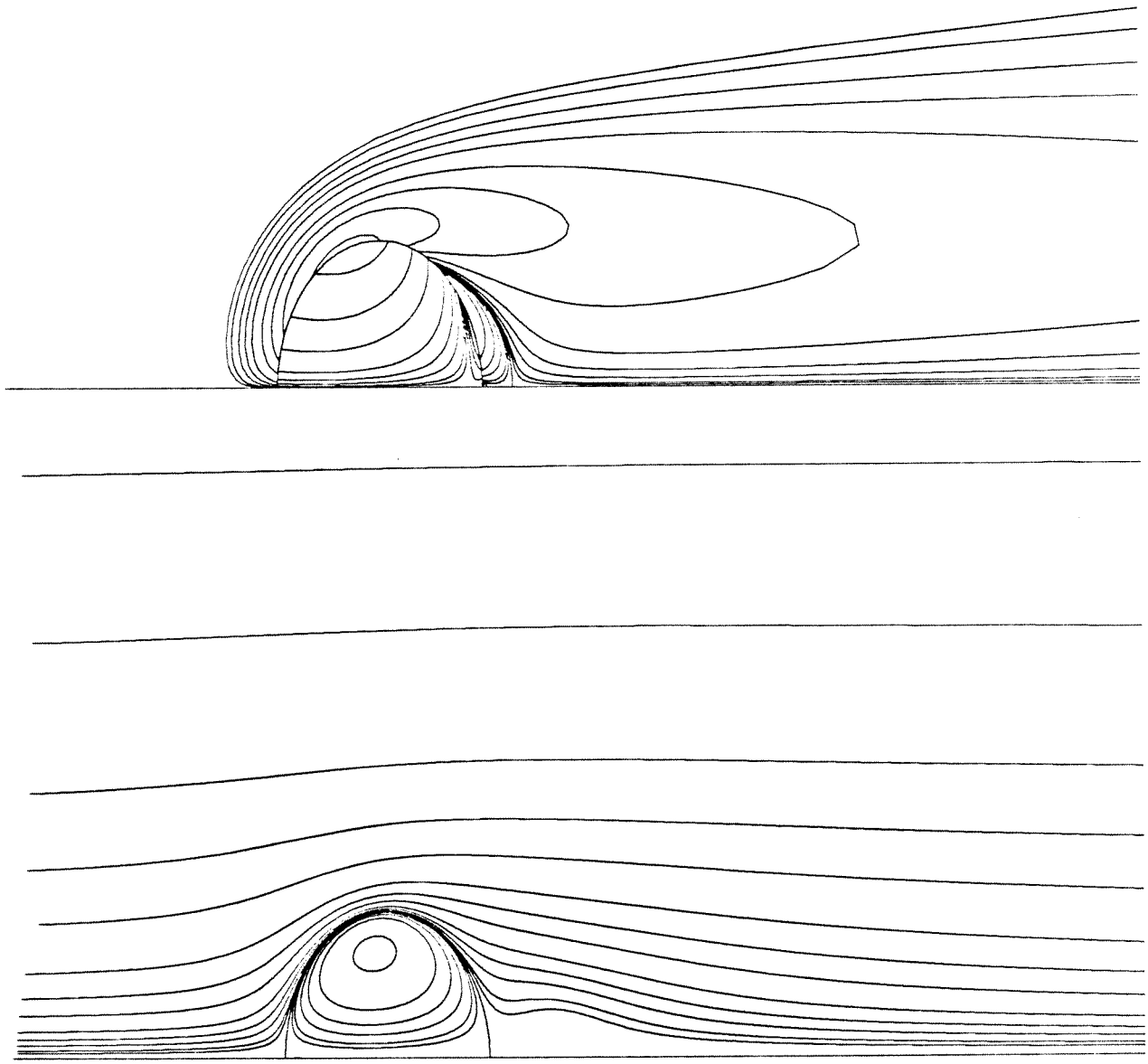

Figure 5a (continued)

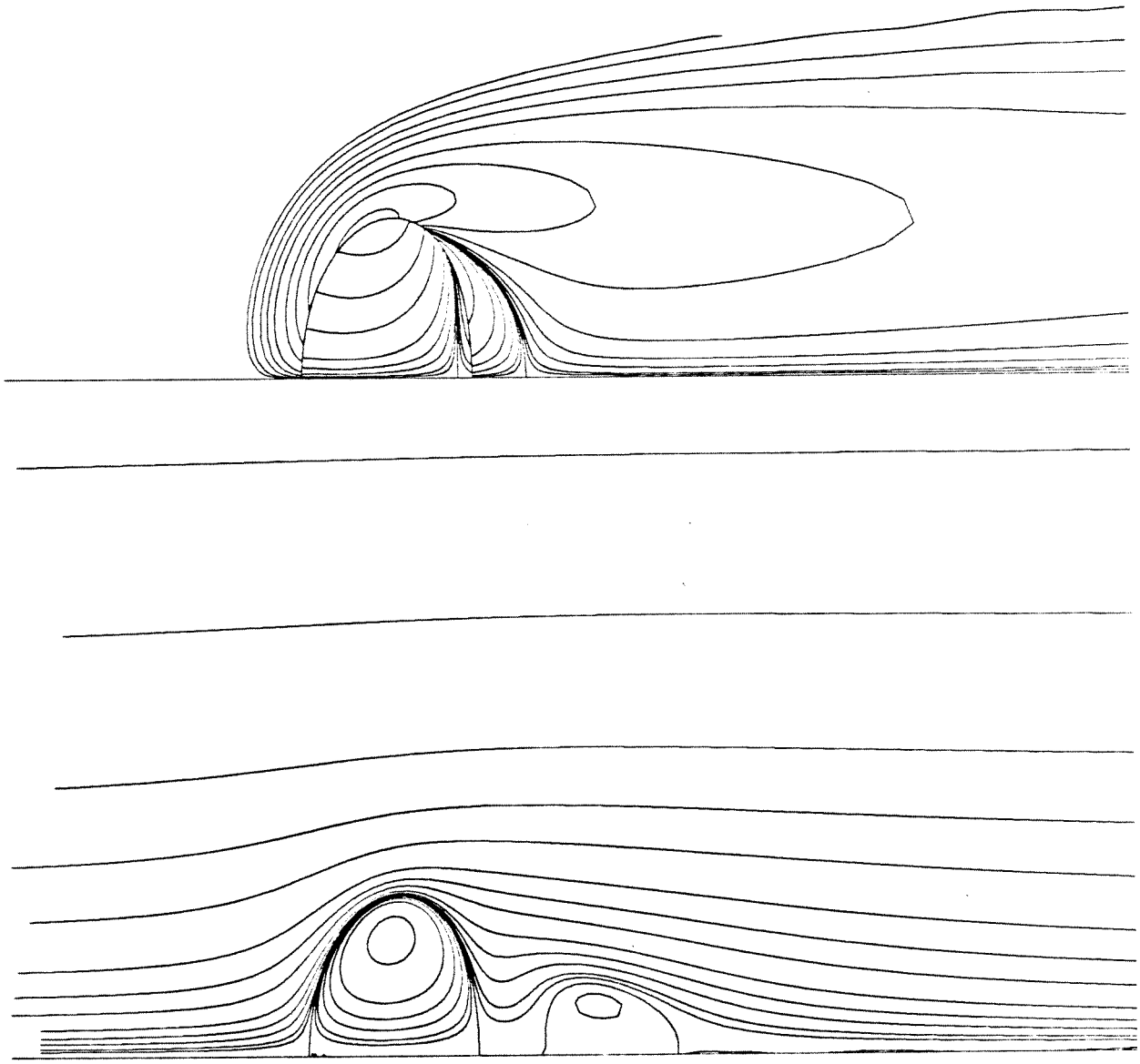

Figure 5a (continued)

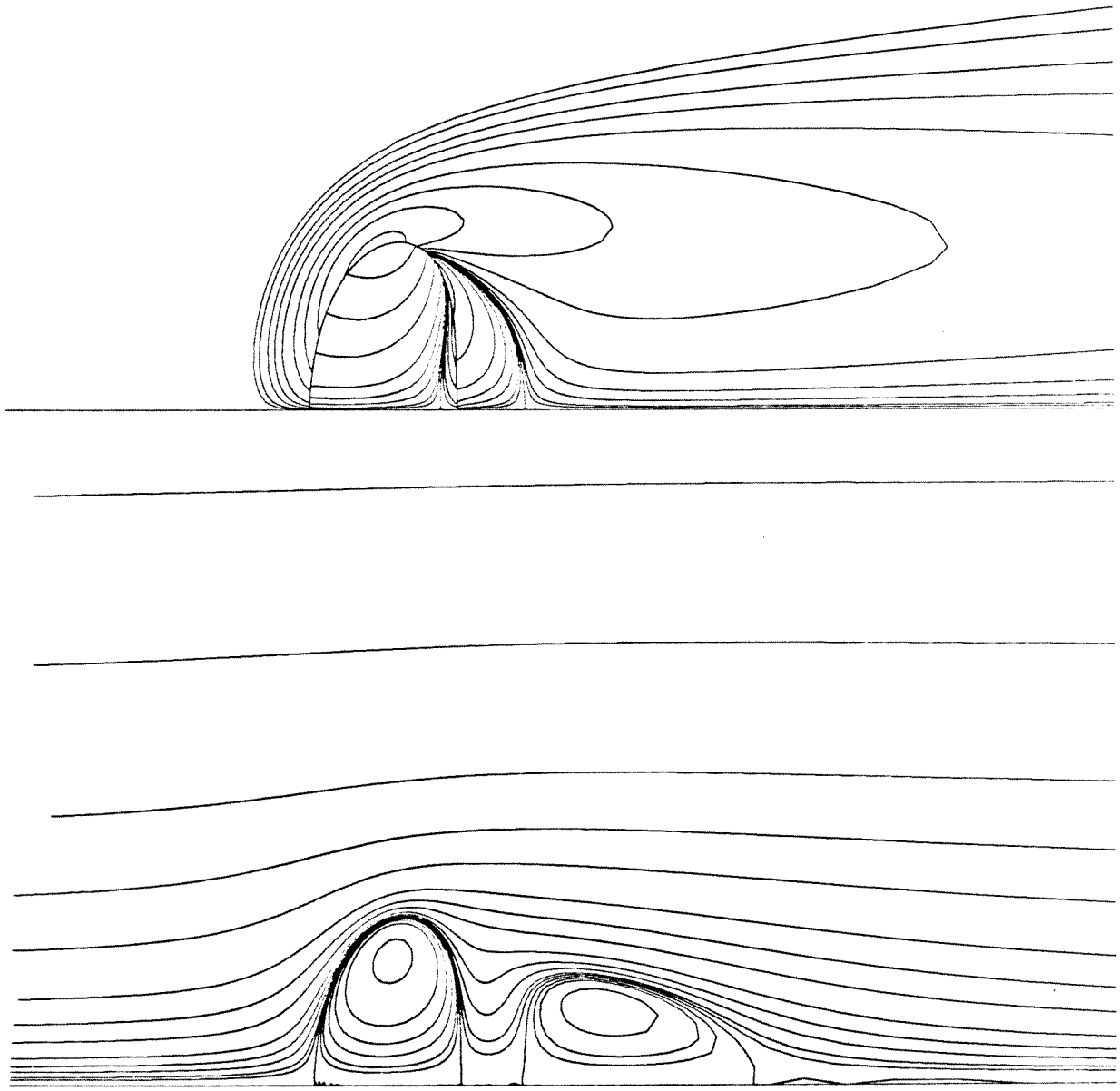

Figure 5a (continued)

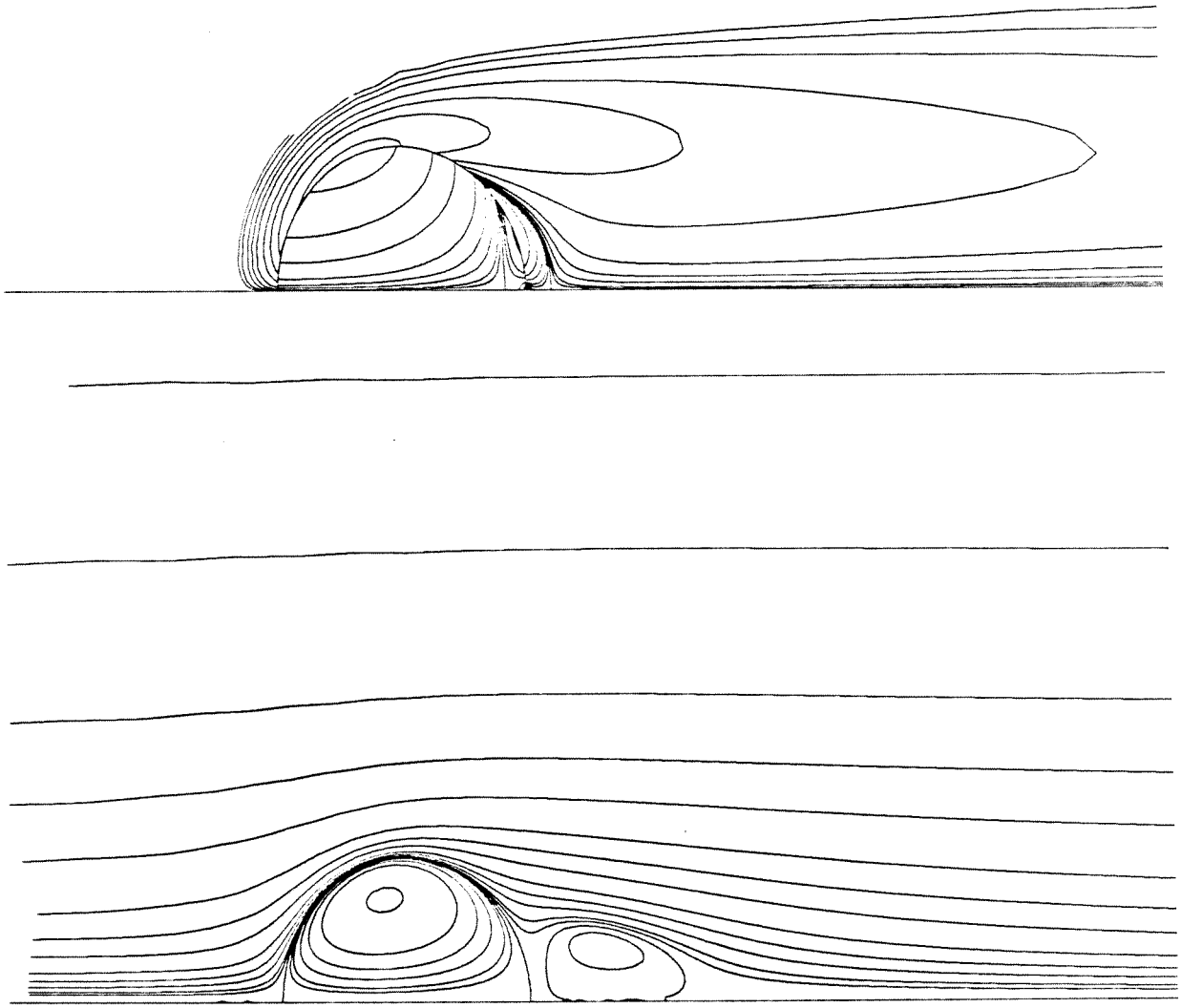

Re = 100 λ = 4

We = 2 ξ = 0.909

Figure 5b

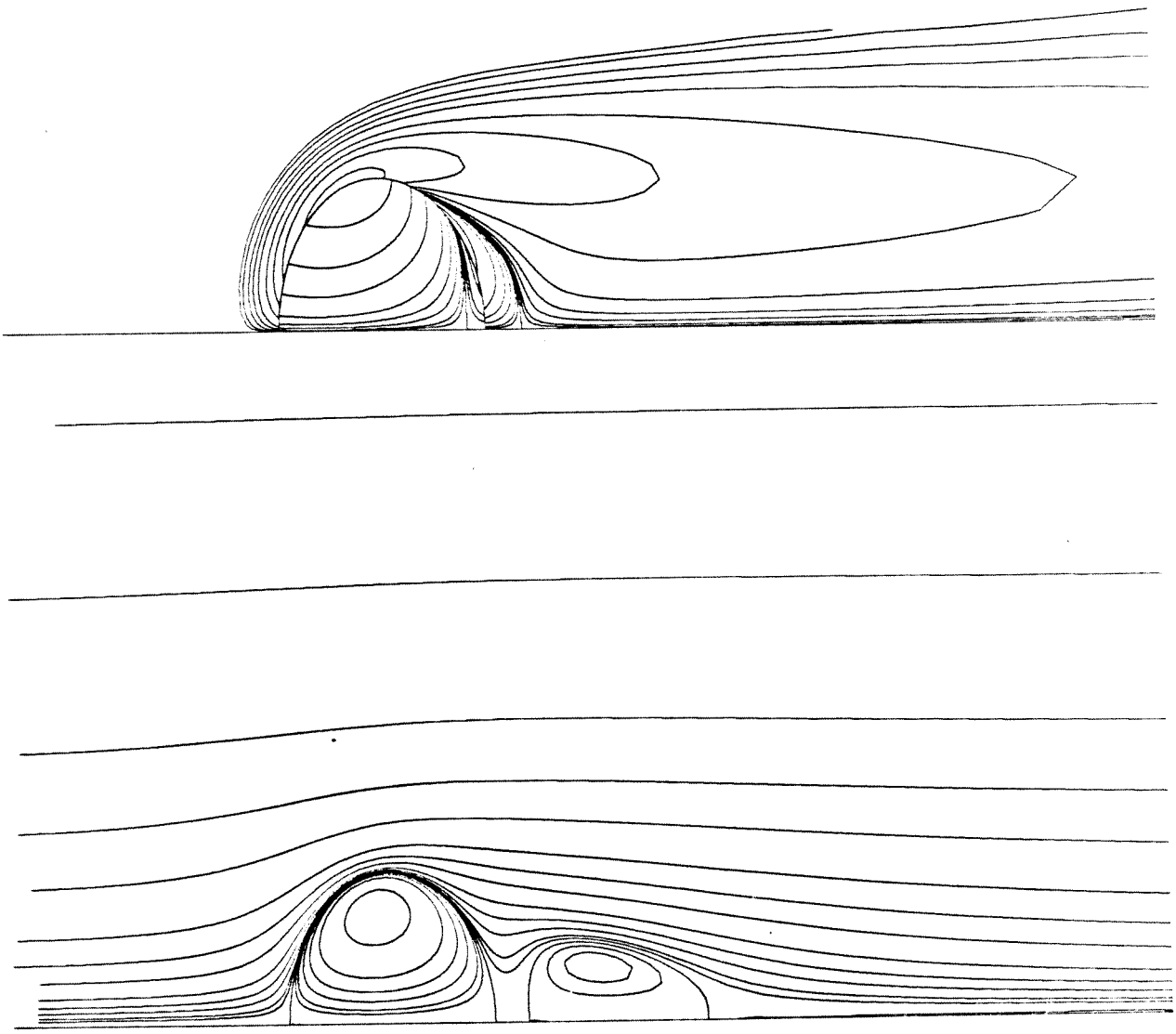

Figure 5b (continued)

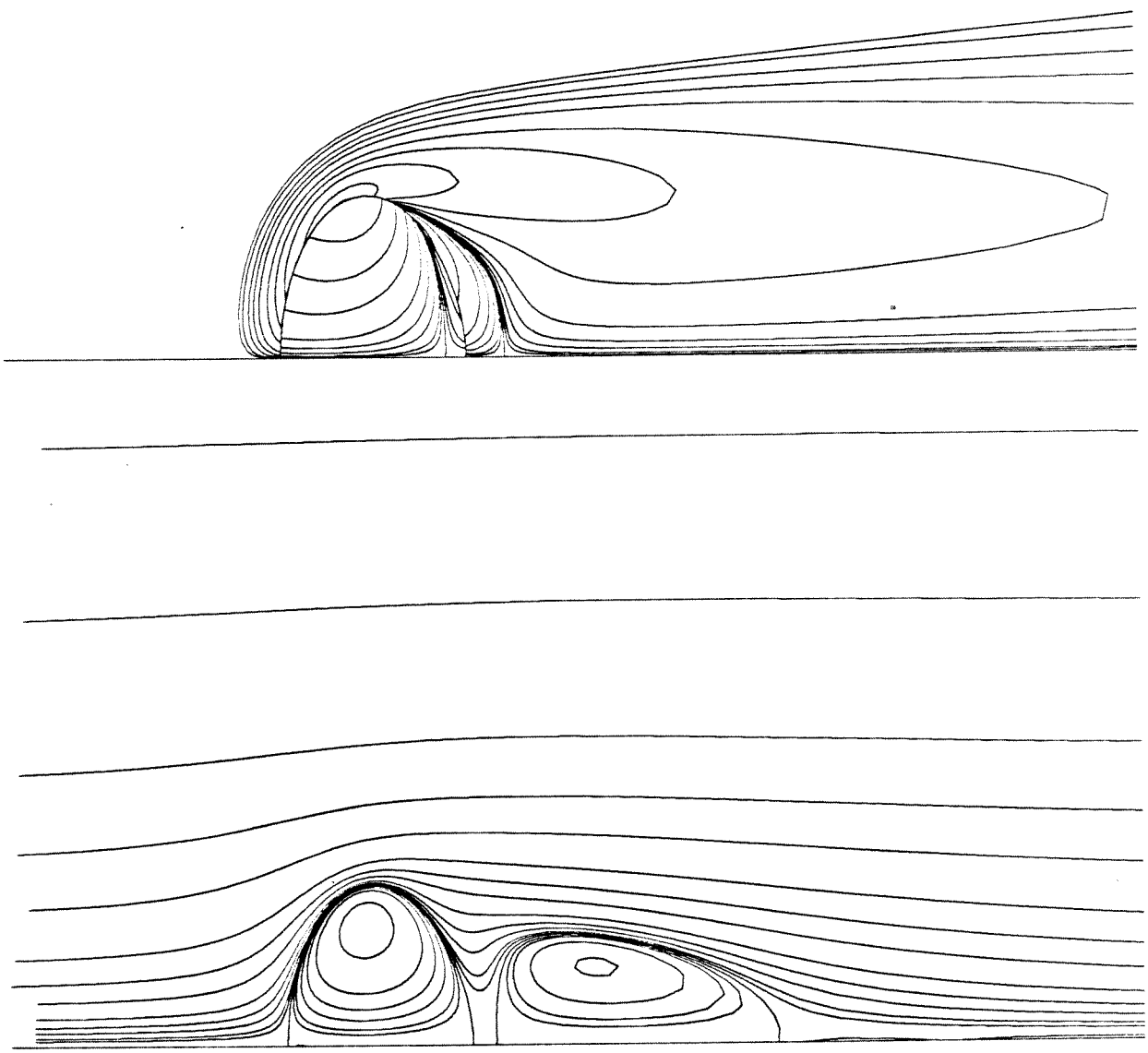

Figure 5b (continued)

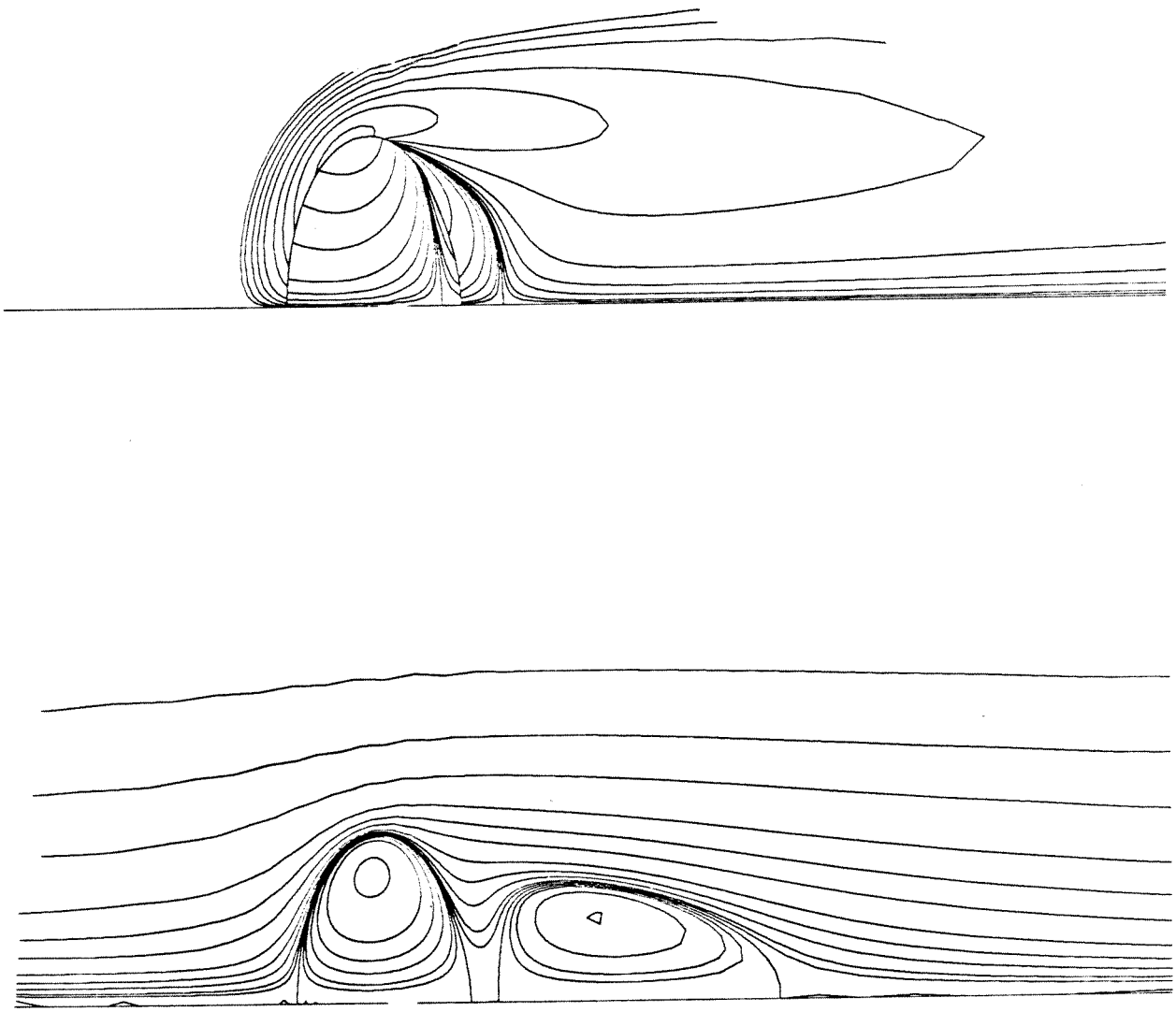

Figure 5b (continued)

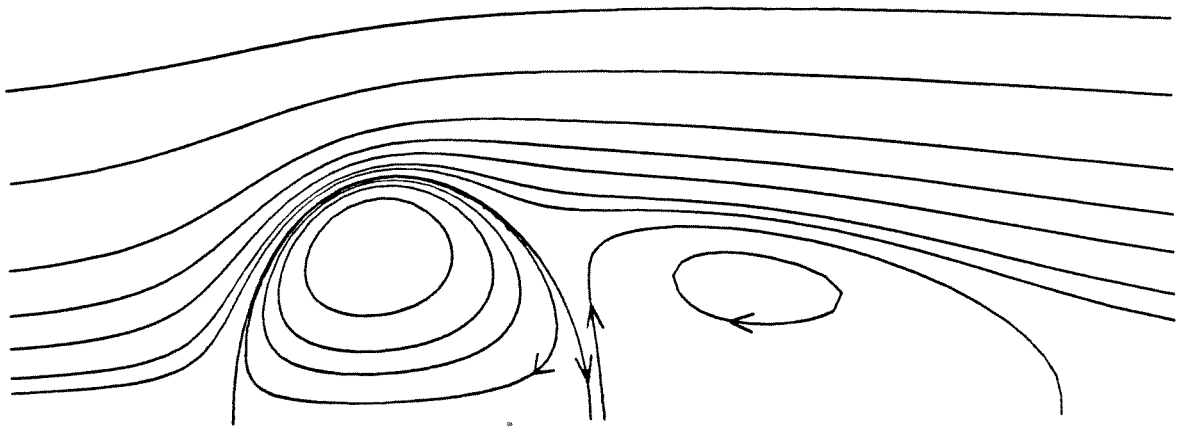

(a)

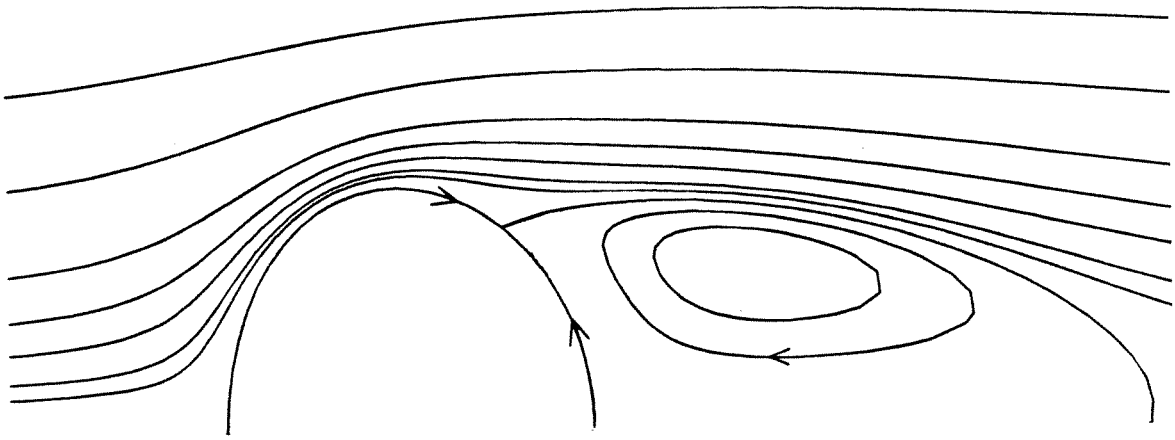

(b)

Figure 6

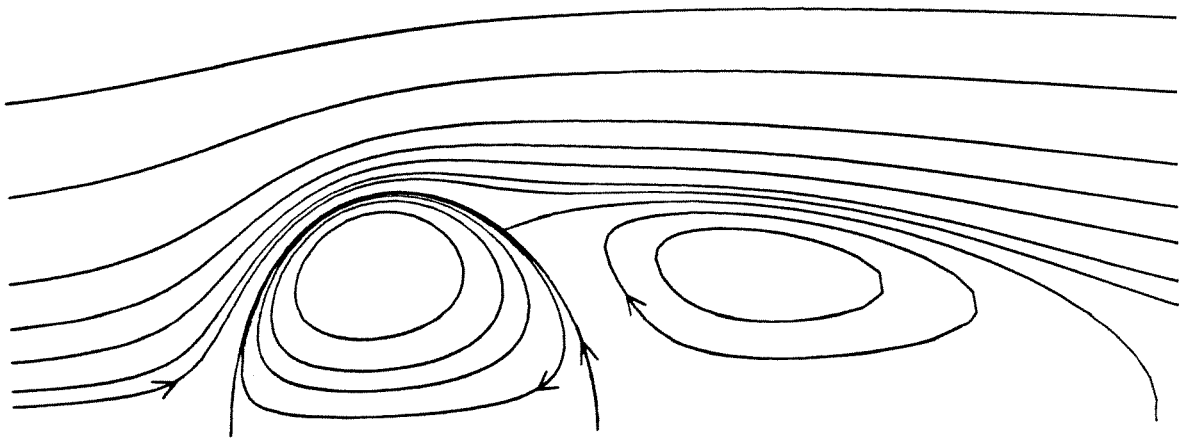

(c)

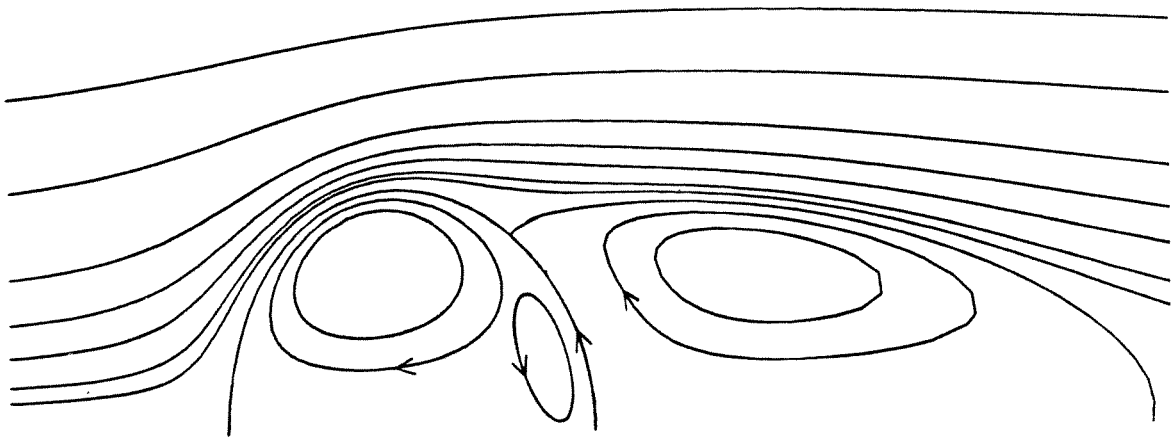

(d)

Figure 6 (continued)

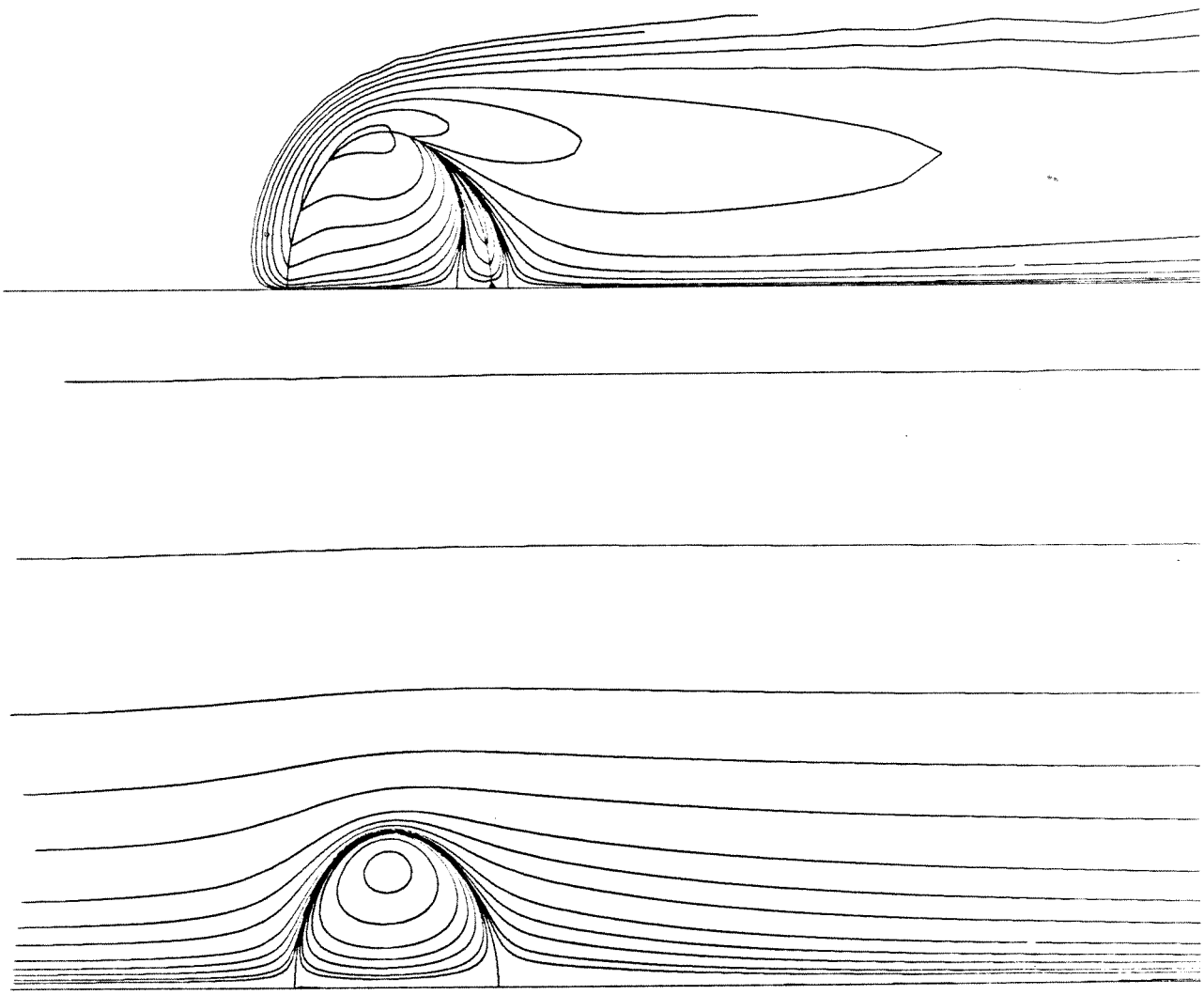

Figure 7

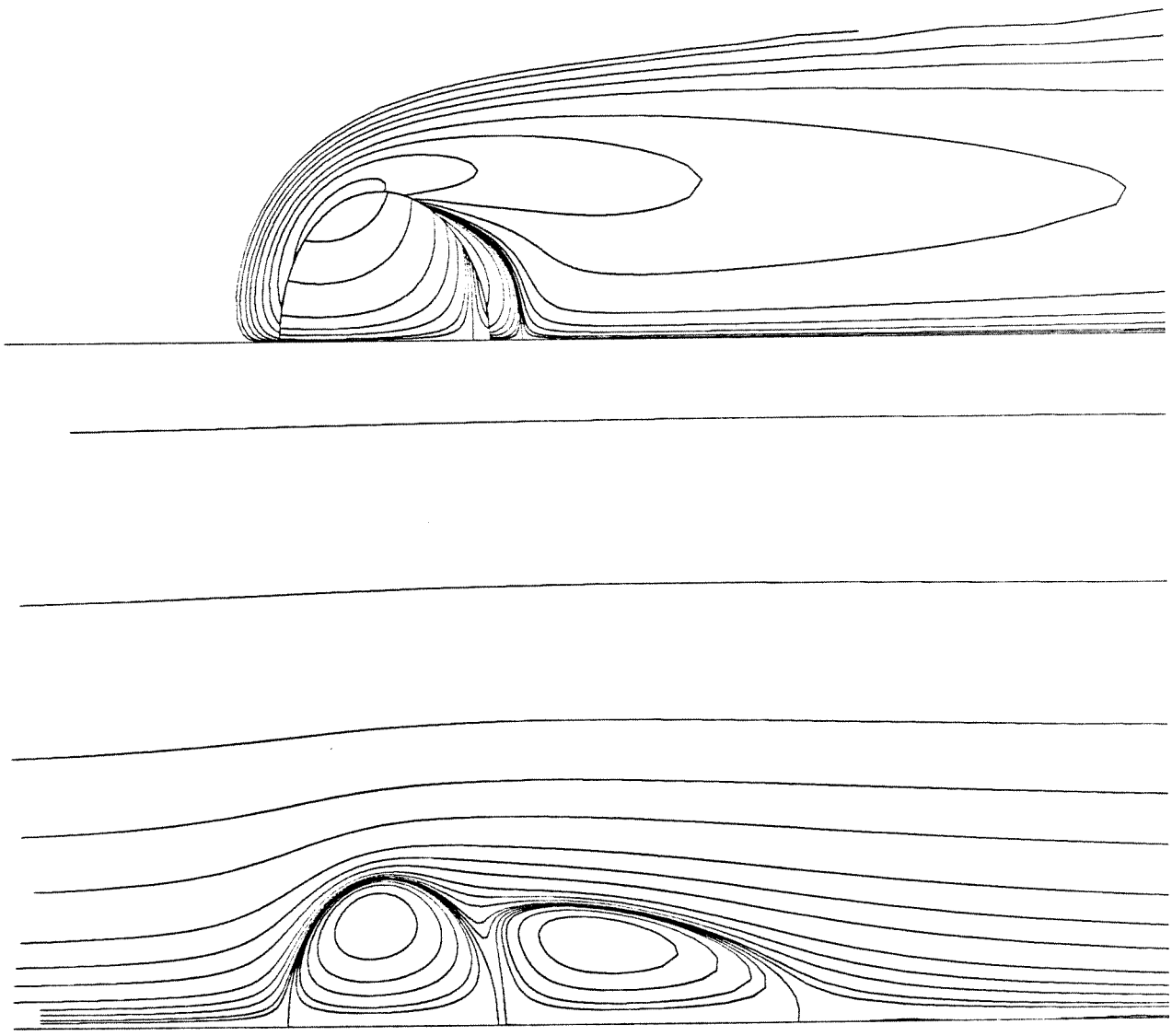

Re = 100 λ = 10

We = 4 ζ = 0.909

Figure 7 (continued)

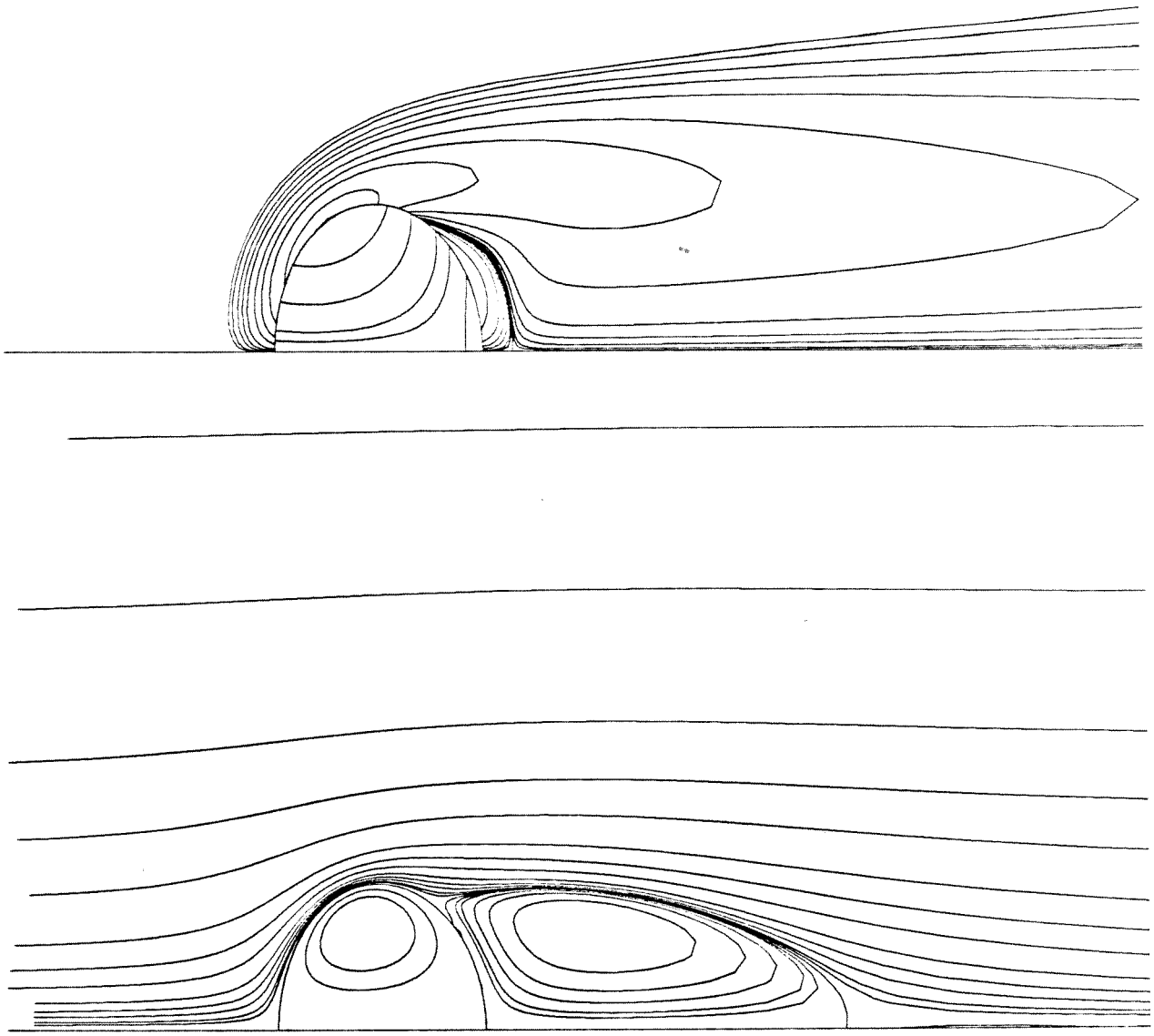

Re = 100 $\lambda = 100$

We = 4 $\zeta = 0.909$

Figure 7 (continued)

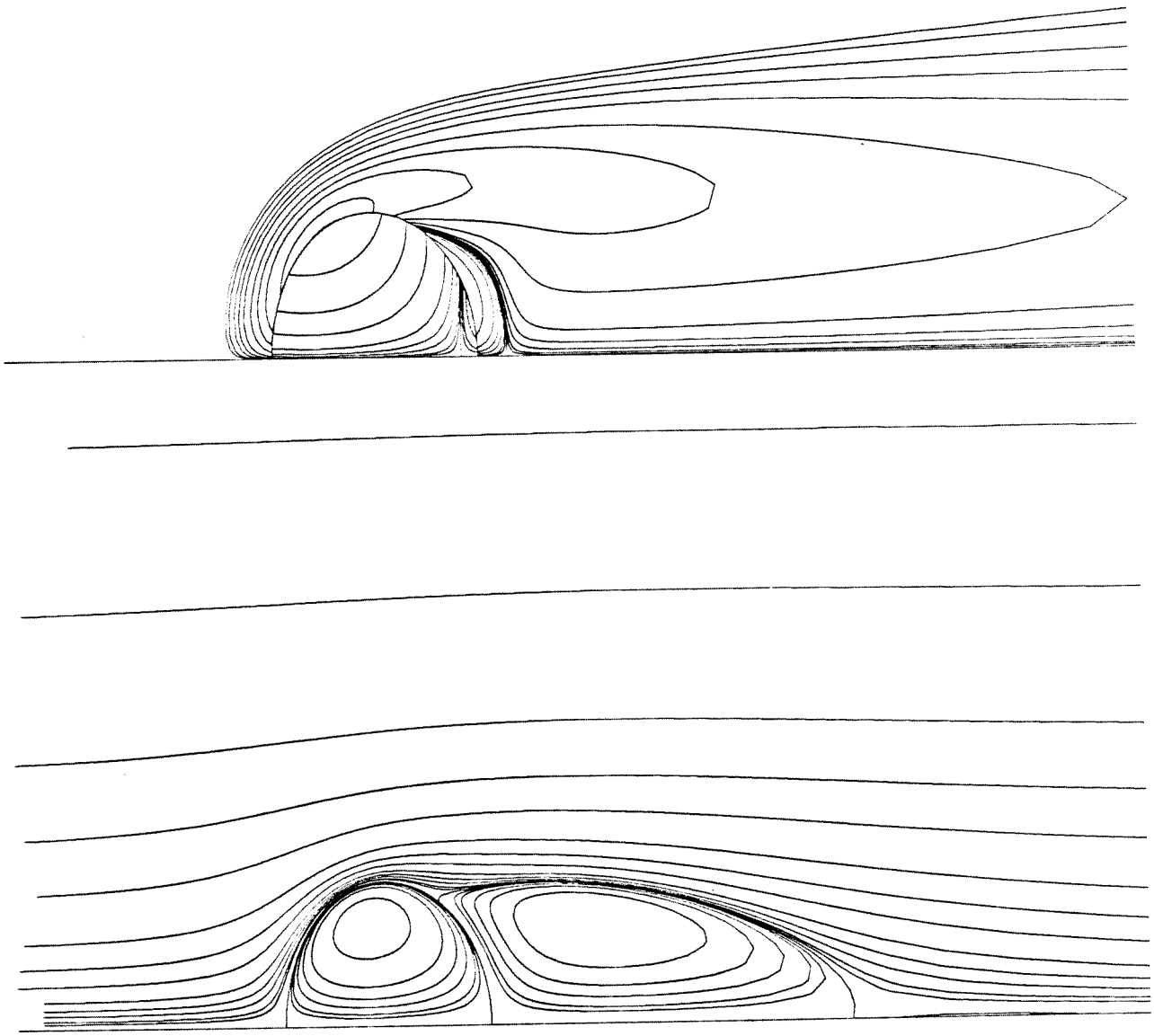

Figure 7 (continued)

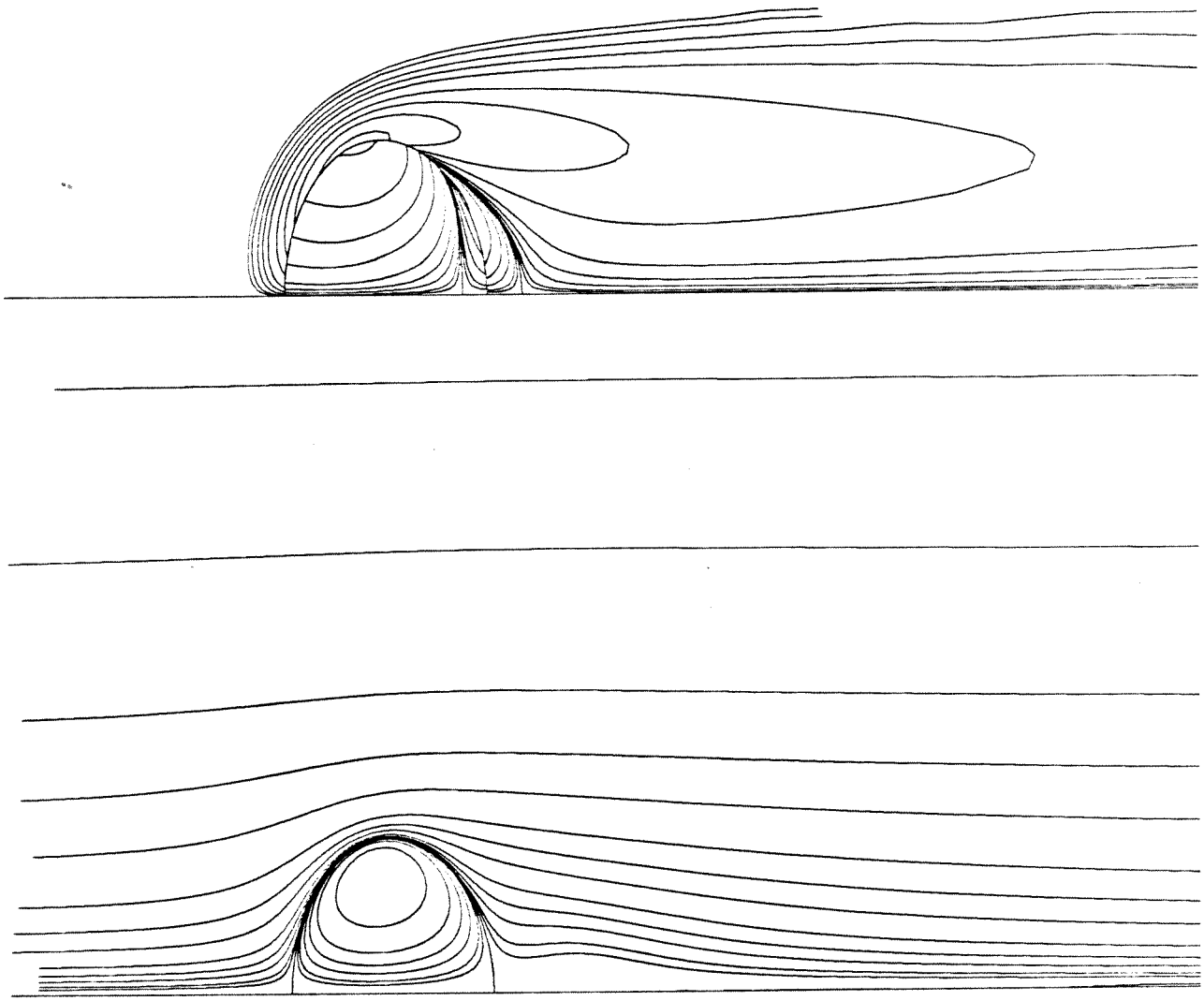

$Re = 100 \qquad \lambda = 2$

$We = 4 \qquad \zeta = 0.5$

Figure 8

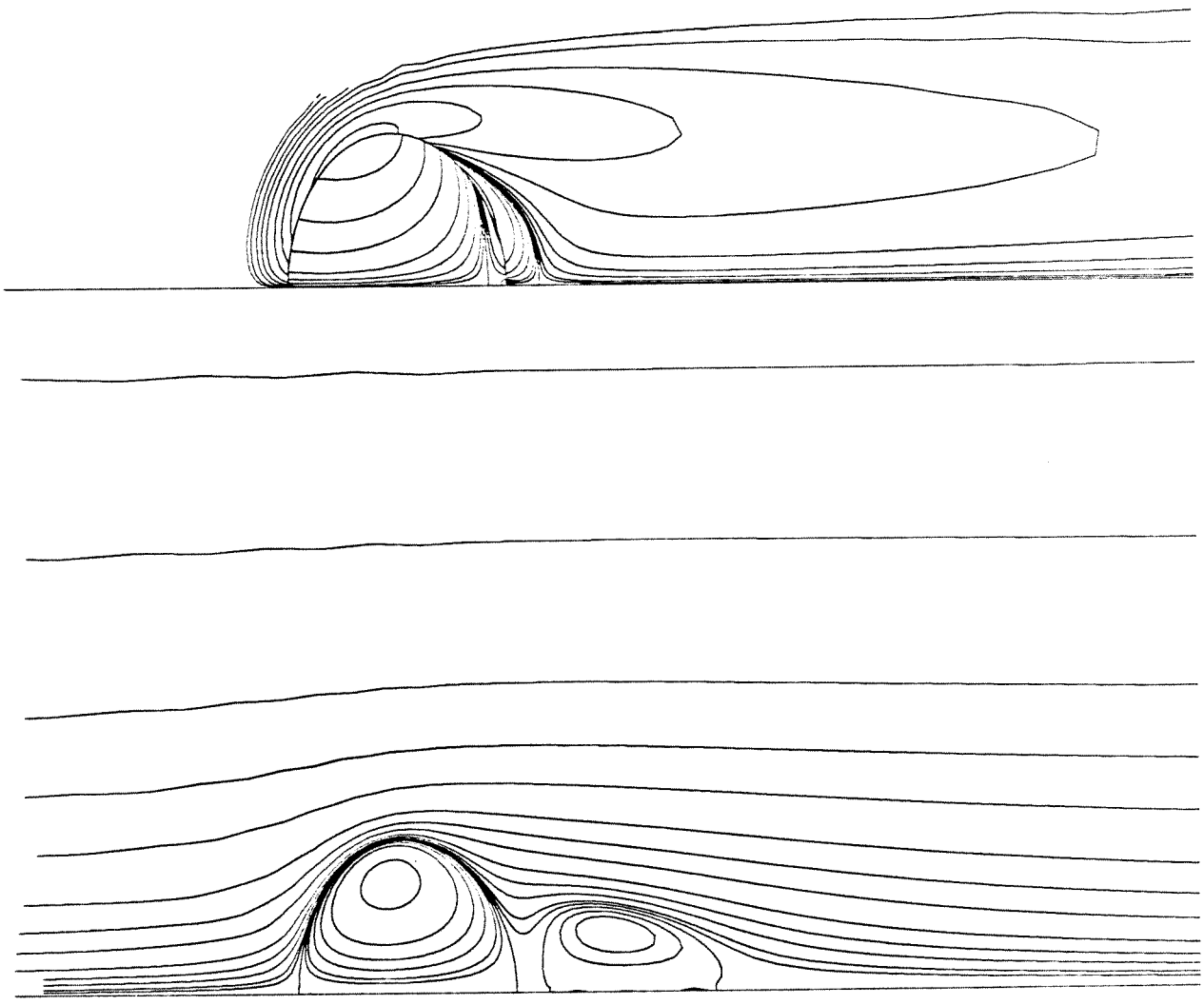

Figure 8 (continued)

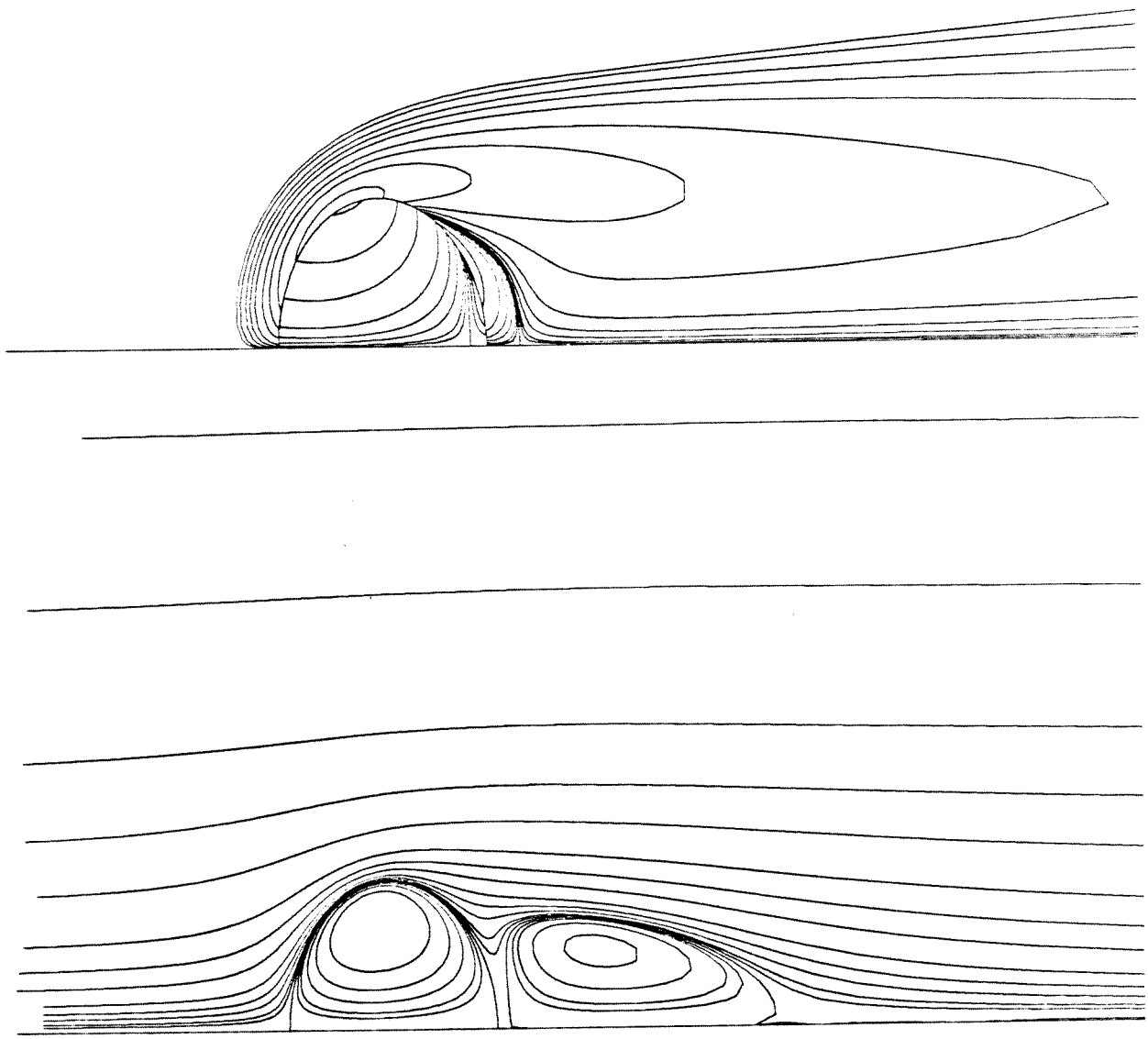

Figure 8 (continued)

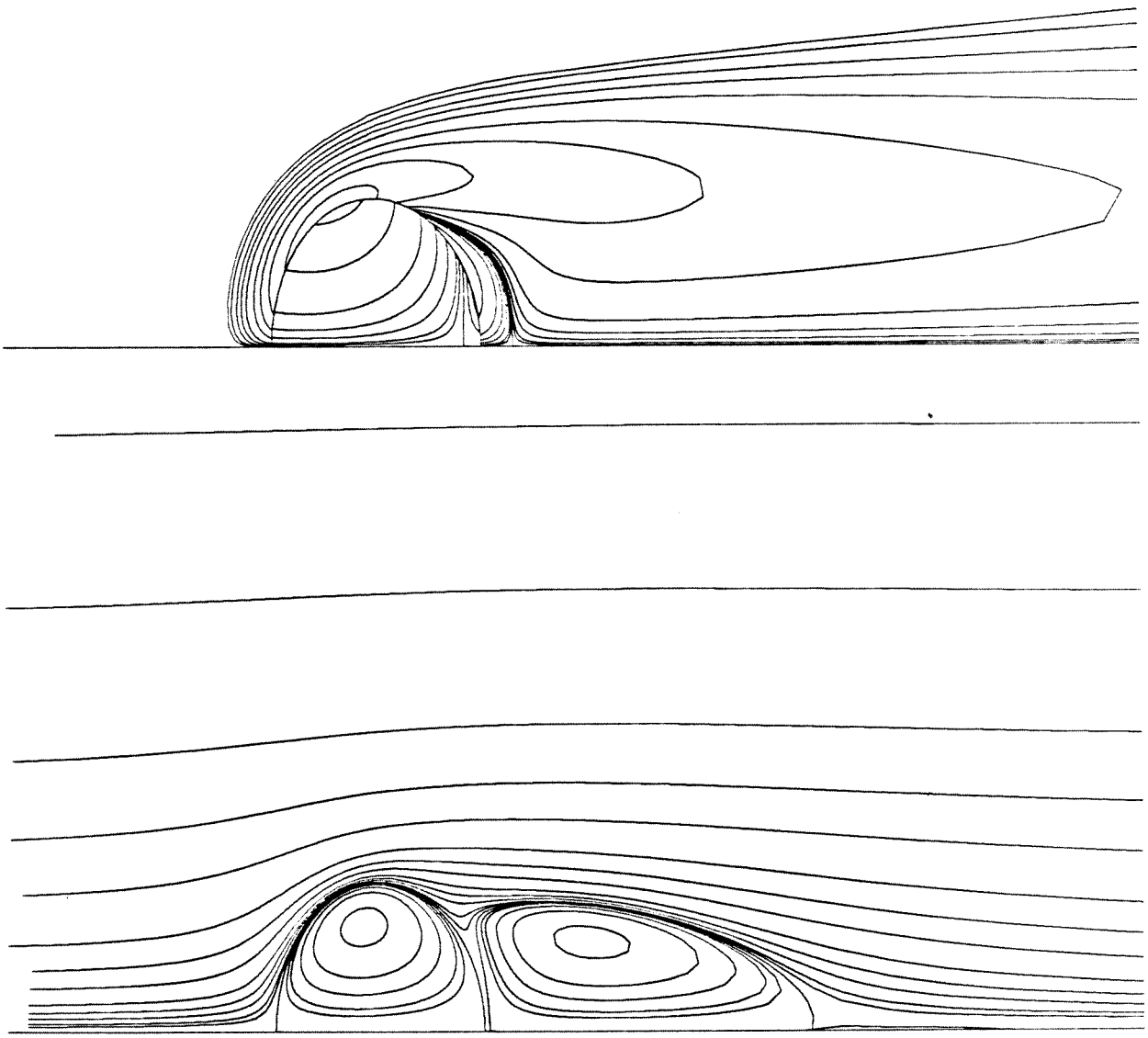

Figure 8 (continued)

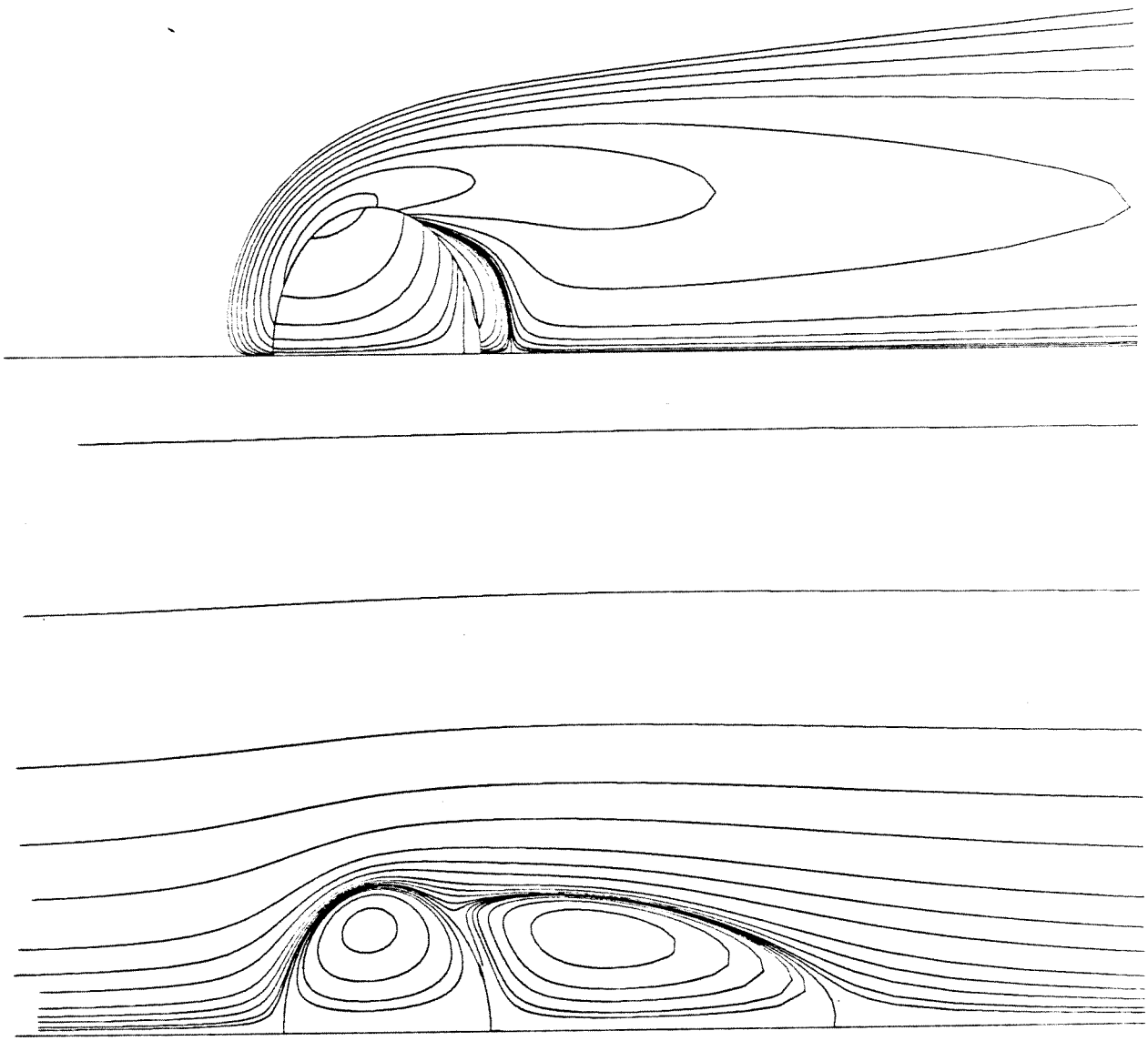

$Re = 100 \qquad \lambda = 32$

$We = 4 \qquad \zeta = 8$

Figure 8 (continued)

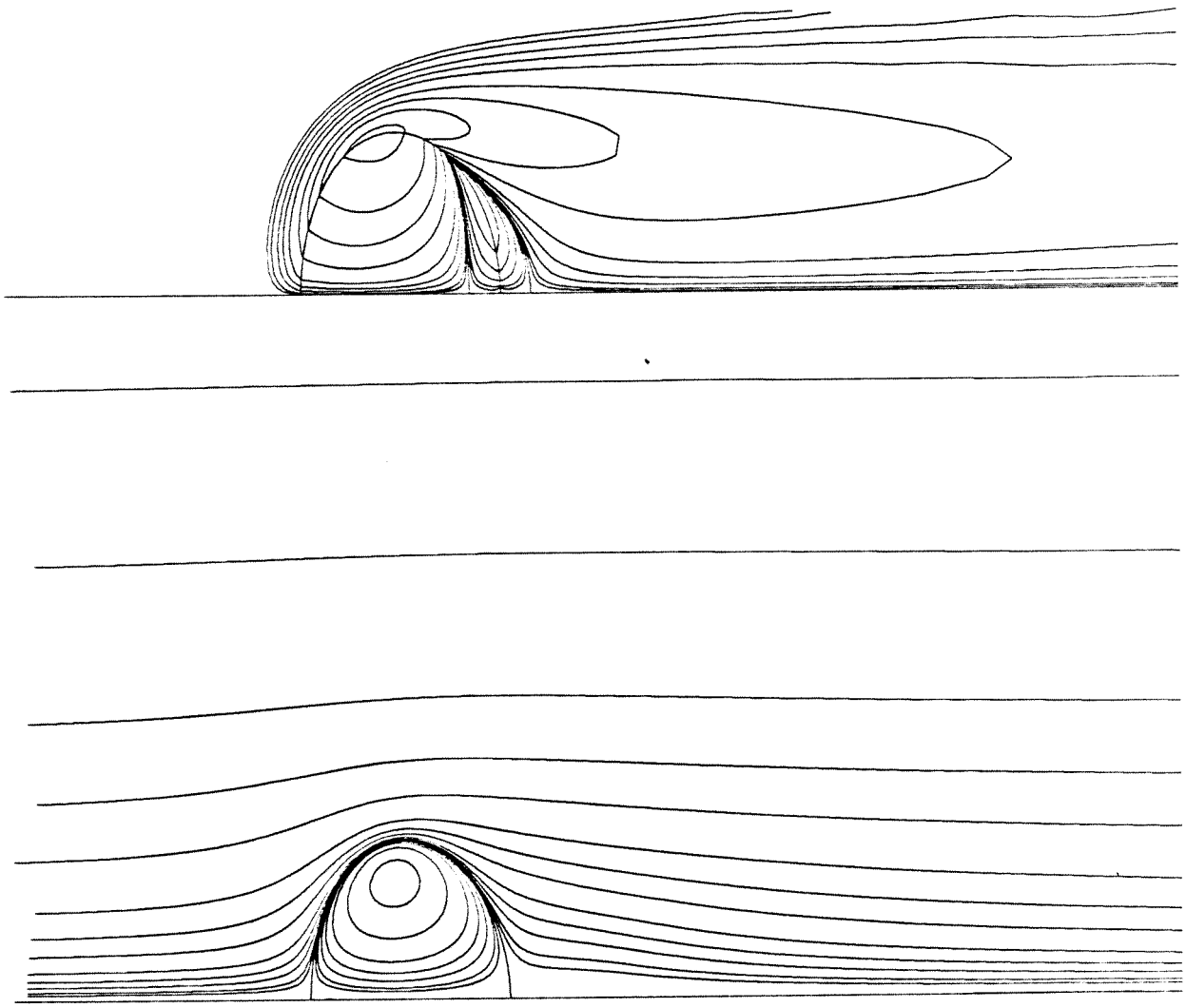

Figure 9

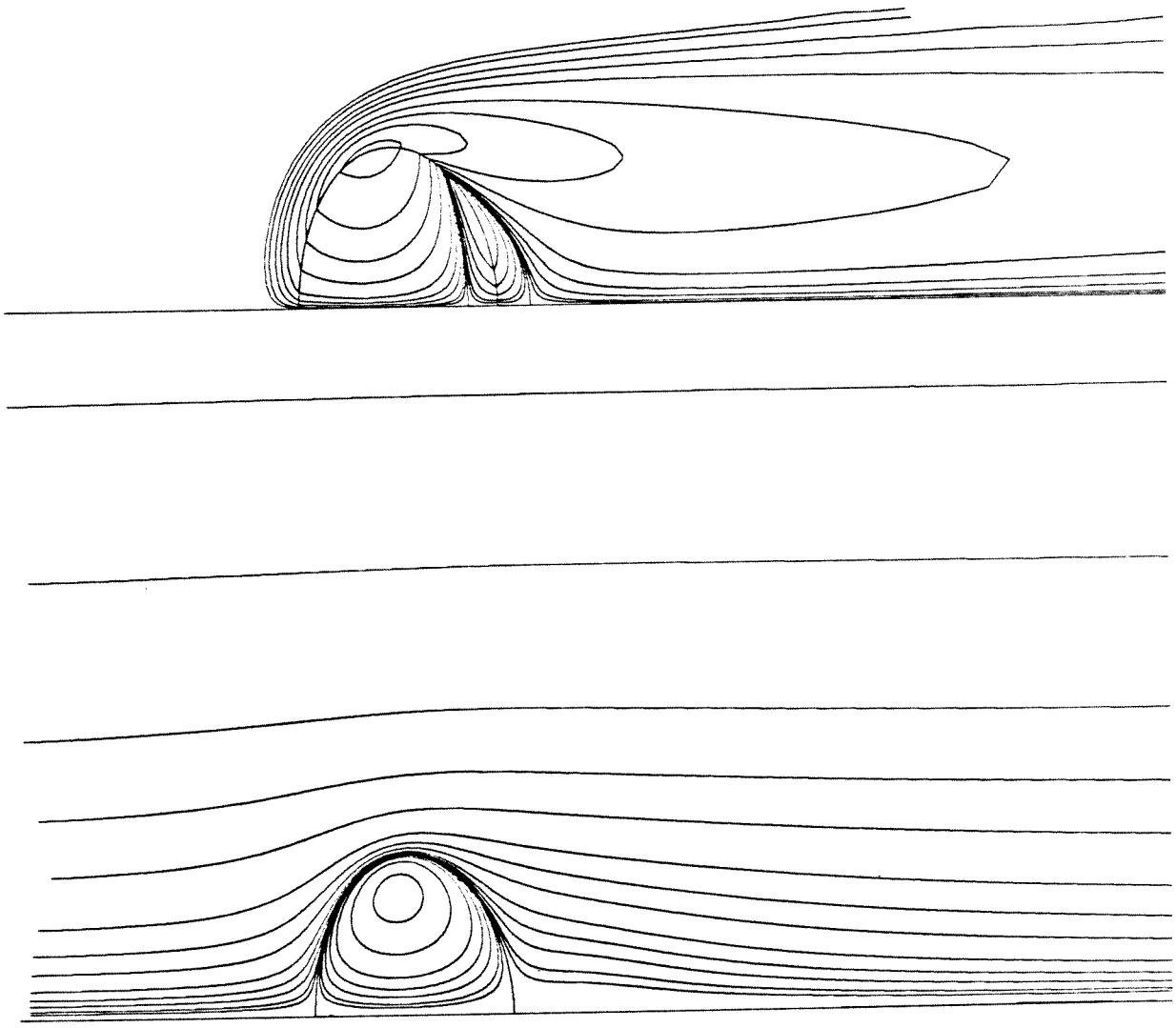

$Re = 100$ $\lambda = 1$

$We = 4$ $\zeta = 0.01$

Figure 9 (continued)

(Fig. 13, Thorsen, Stordalen, and Terjensen, *Chem. Eng. Sci.* 23 , 1968)

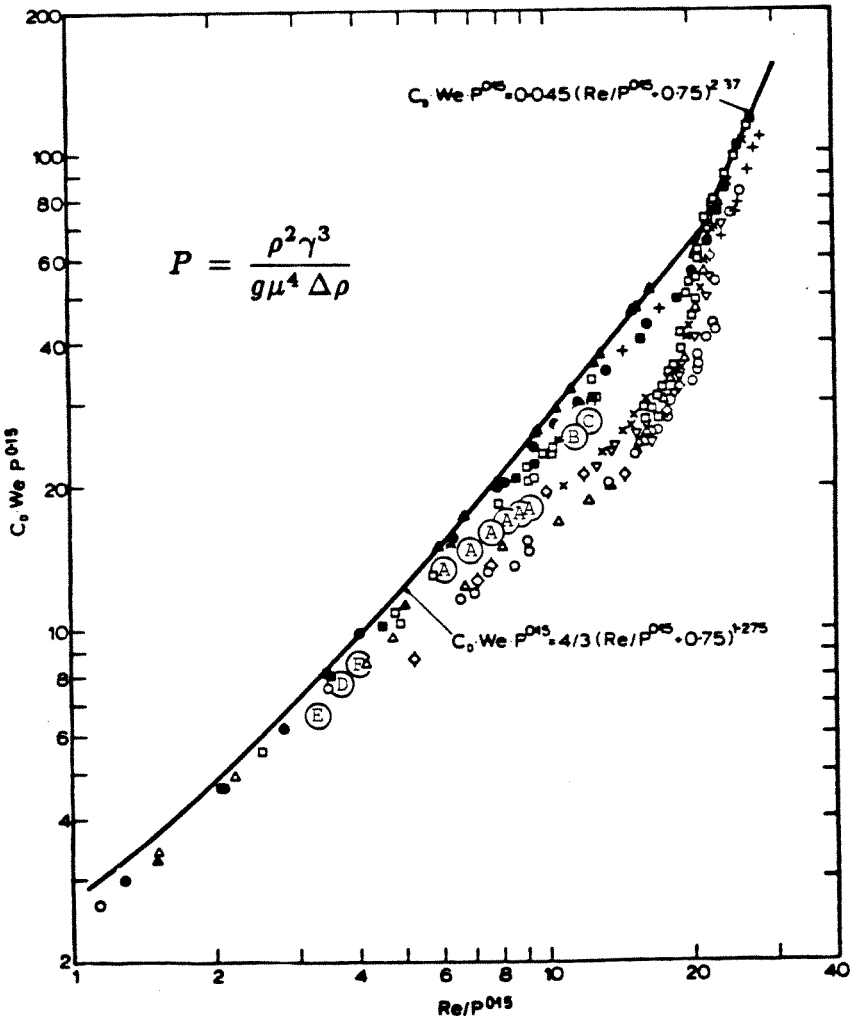

Figure 10

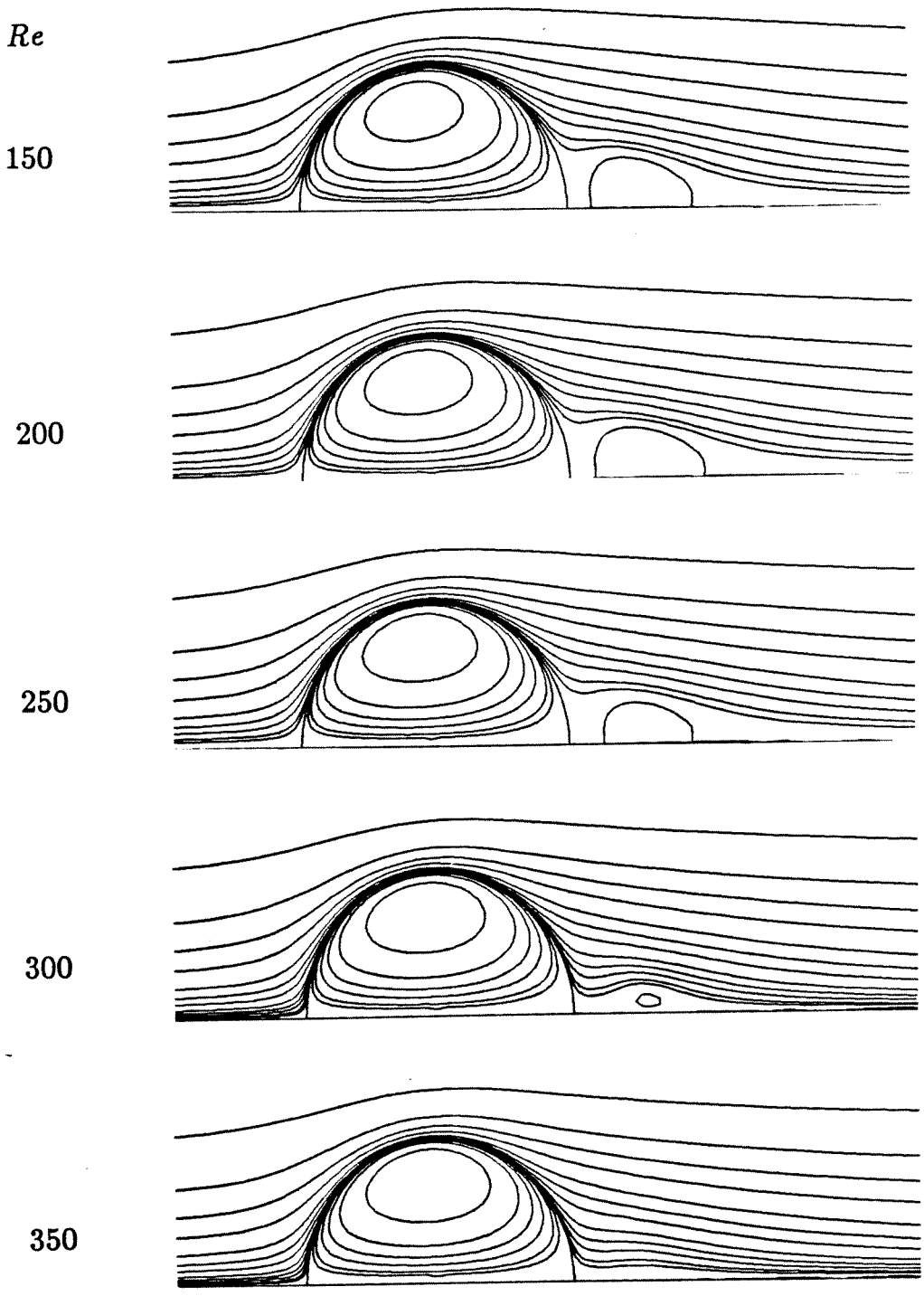

$We = 1 \qquad \varsigma = 0.91 \qquad \lambda = 2.5$

Figure 11

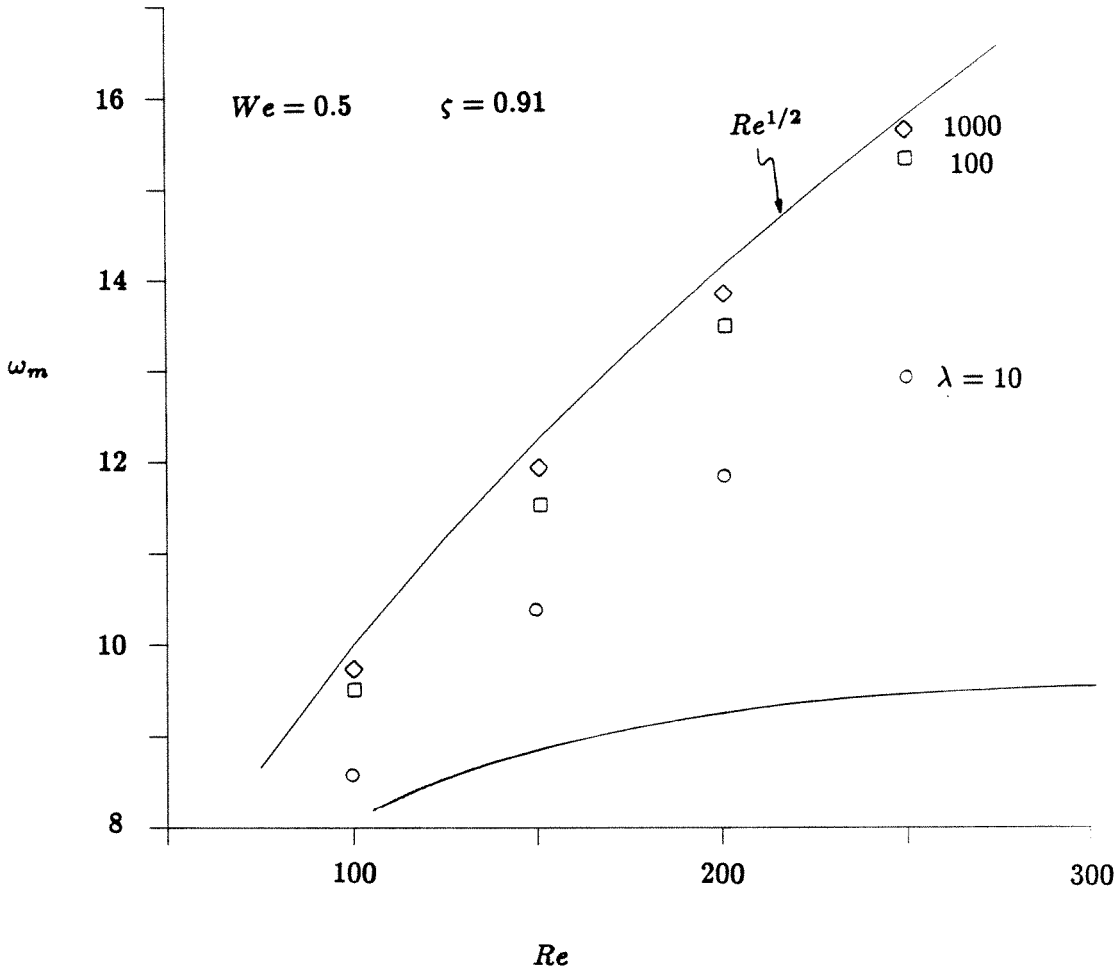
$We = 0.5$
$\varsigma = 0.91$
$Re^{1/2}$
1000
100
$\lambda = 10$
ω_m
16
14
12
10
8
100
200
300
Re

Figure 12

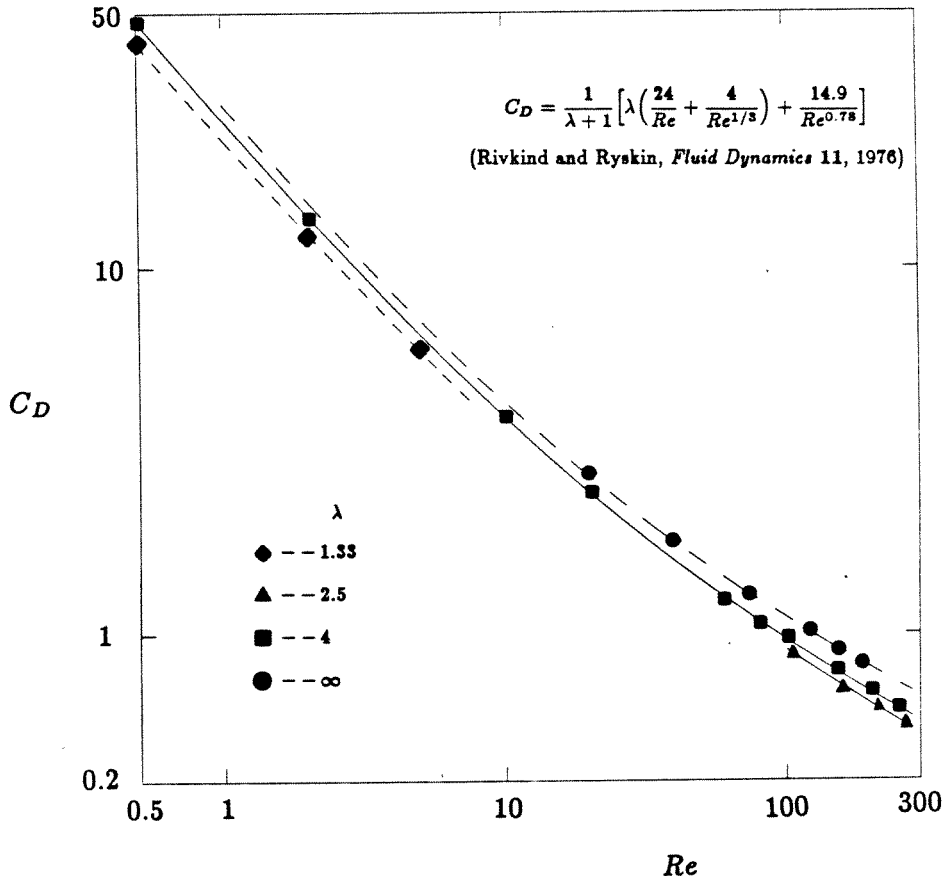
50
10
1
0.2
C_D
0.5
1
10
100
300
Re
$C_D = \frac{1}{\lambda+1}\left[\lambda\left(\frac{24}{Re} + \frac{4}{Re^{1/3}}\right) + \frac{14.9}{Re^{0.78}}\right]$
(Rivkind and Ryskin, *Fluid Dynamics* 11, 1976)
λ
1.33
2.5
4
∞

Figure 13

$Re = 0.5$ $We = 0.5$ $\varsigma = 0.91$ $\lambda = 4$

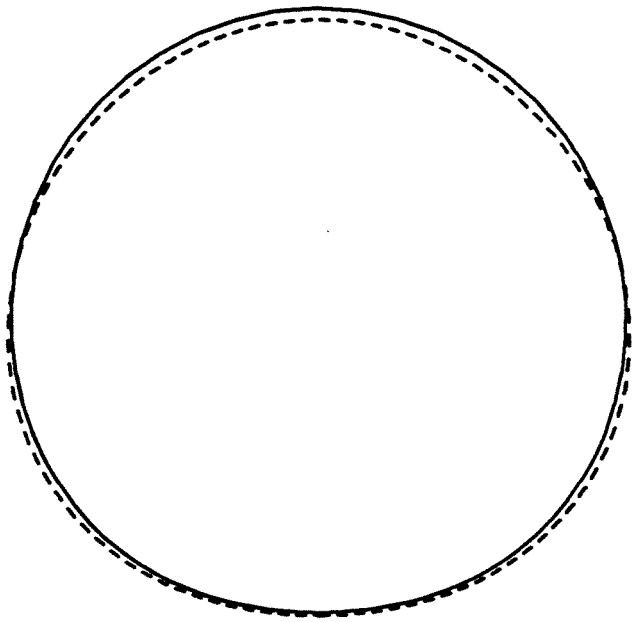

Taylor & Acrivos: $C_D = 48.4$

Present Work: $C_D = 48.7$

Figure 14

Appendix: Additional figures

The following figures are results that, although inherently interesting, are similar in qualitative nature to results presented in the main body of this Chapter. The figures are loosely arranged by Reynolds number.

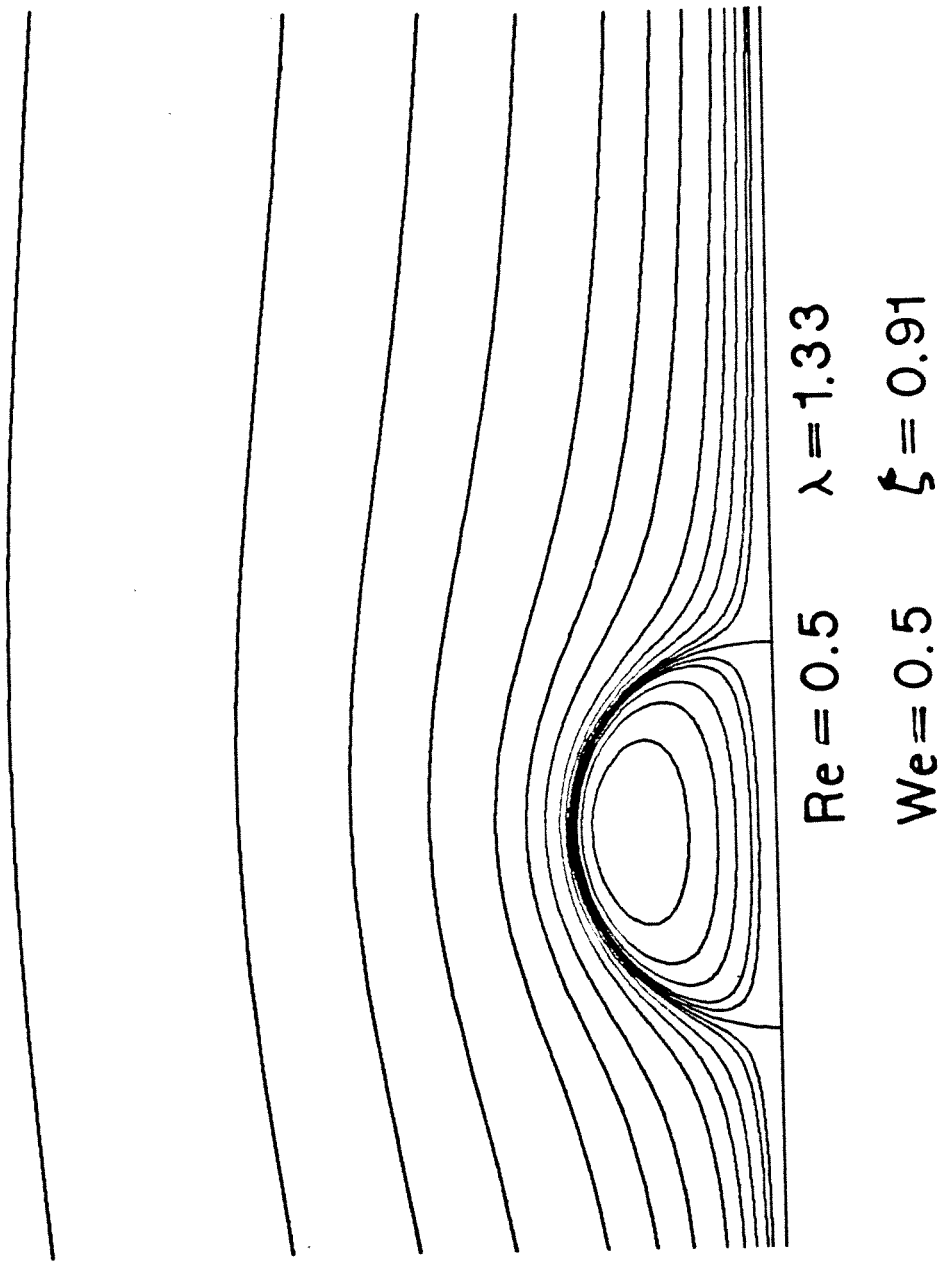
Re = 0.5
We = 0.5
λ = 1.33
ζ = 0.91

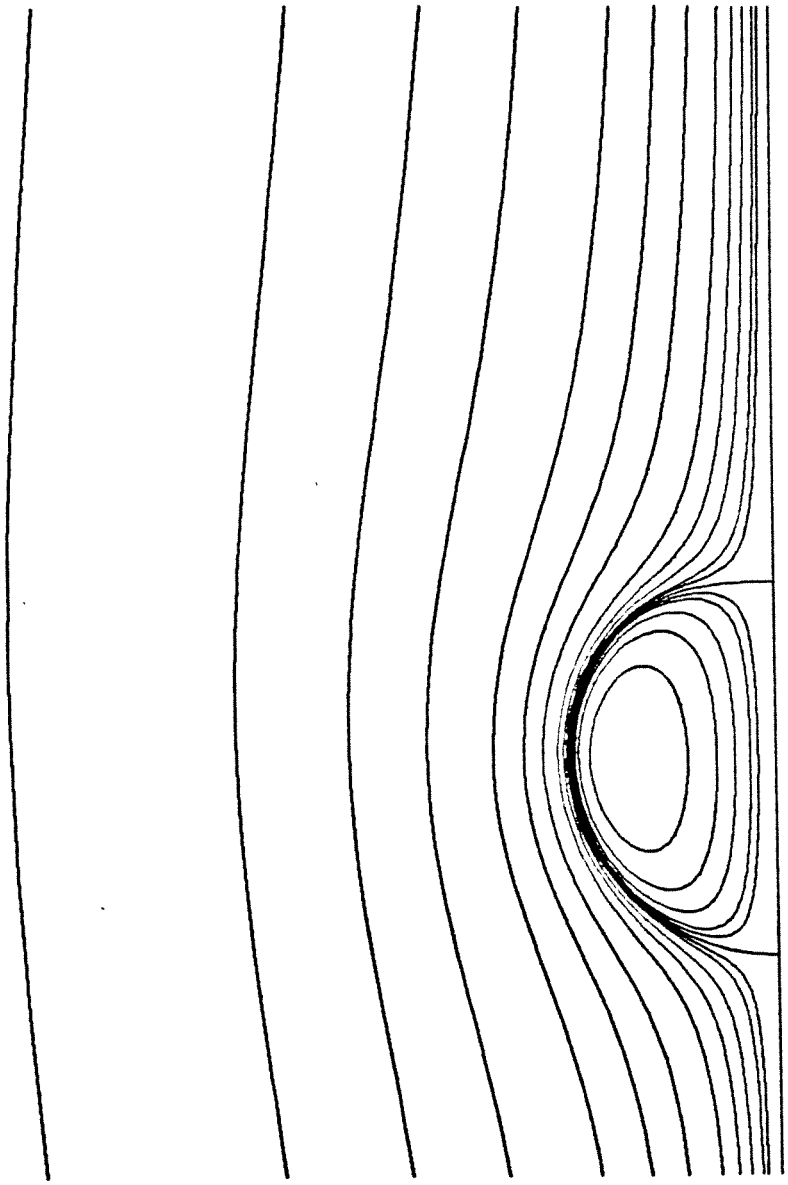
Re = 0.5
λ = 1.33
We = 1
ξ = 0.91

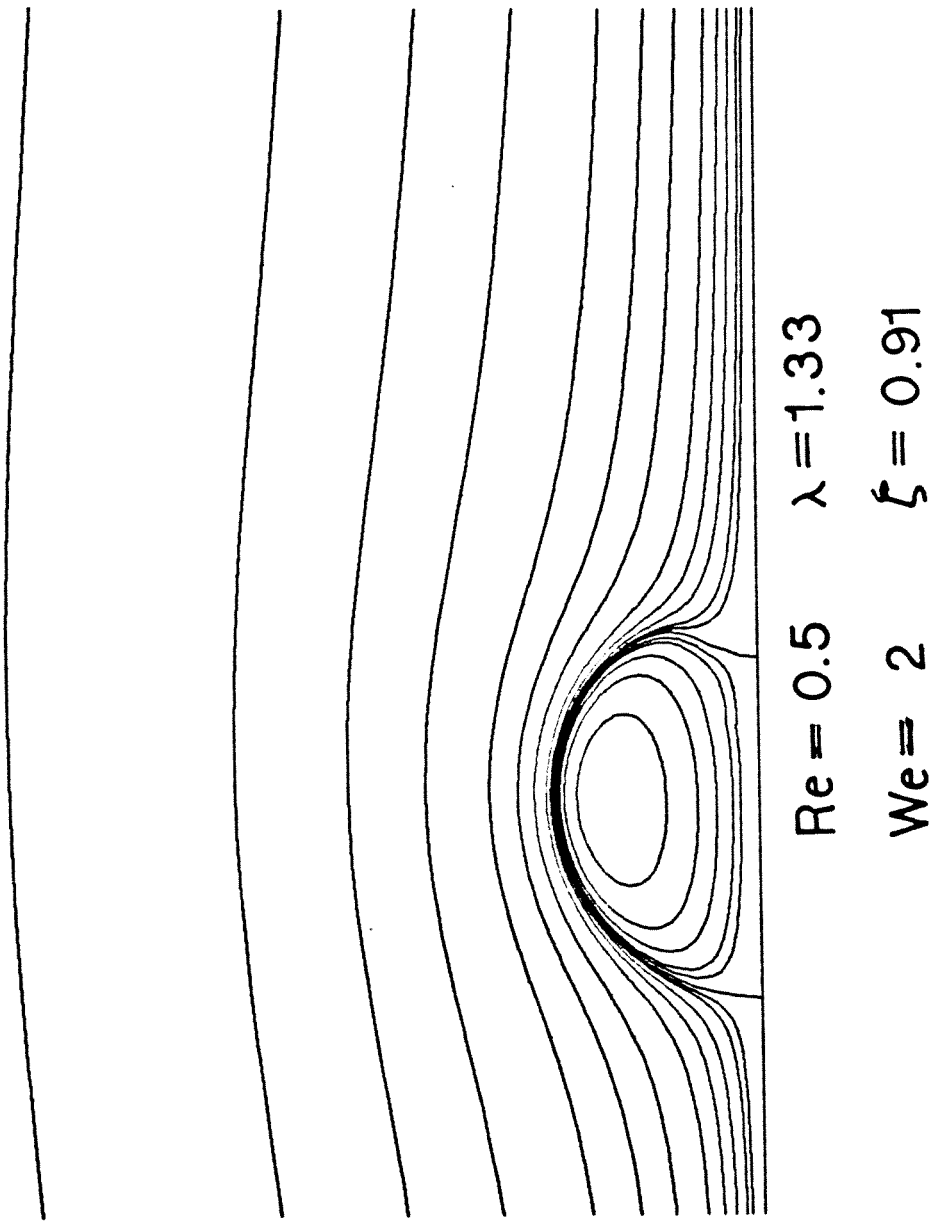
Re = 0.5
λ = 1.33
We = 2
ξ = 0.91

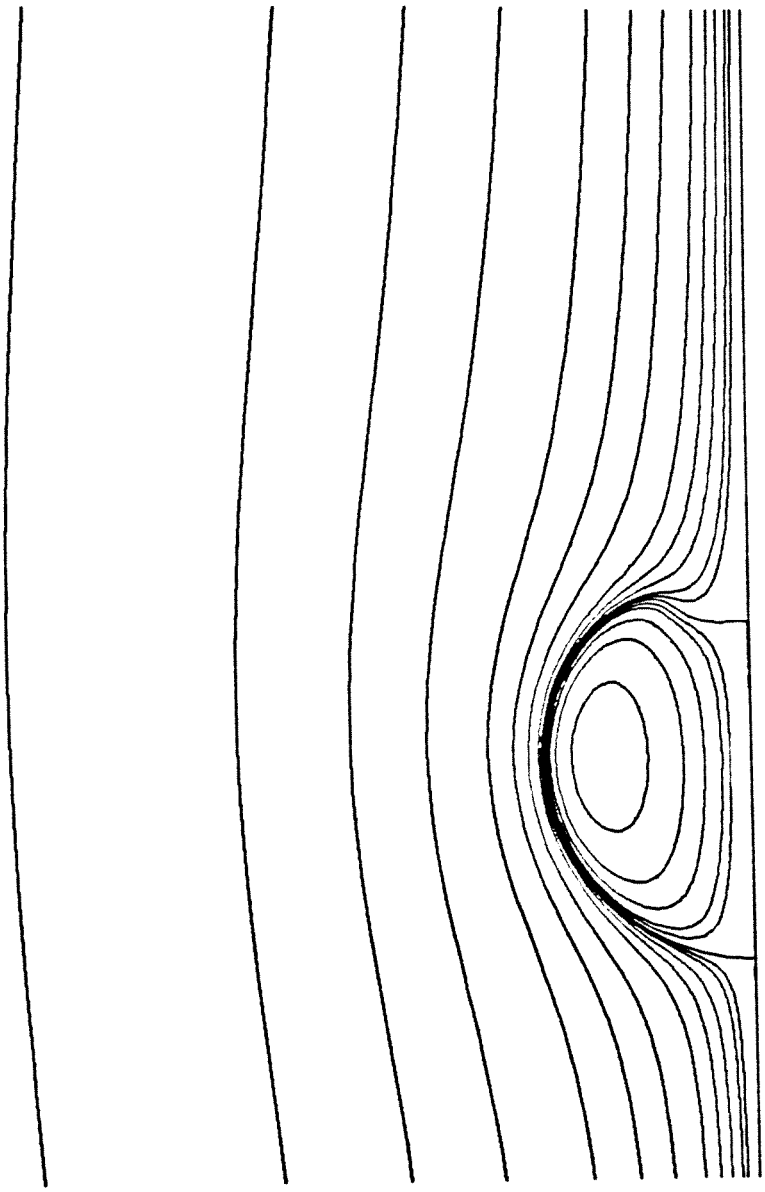
Re = 0.5
λ = 1.33
We = 4
ξ = 0.91

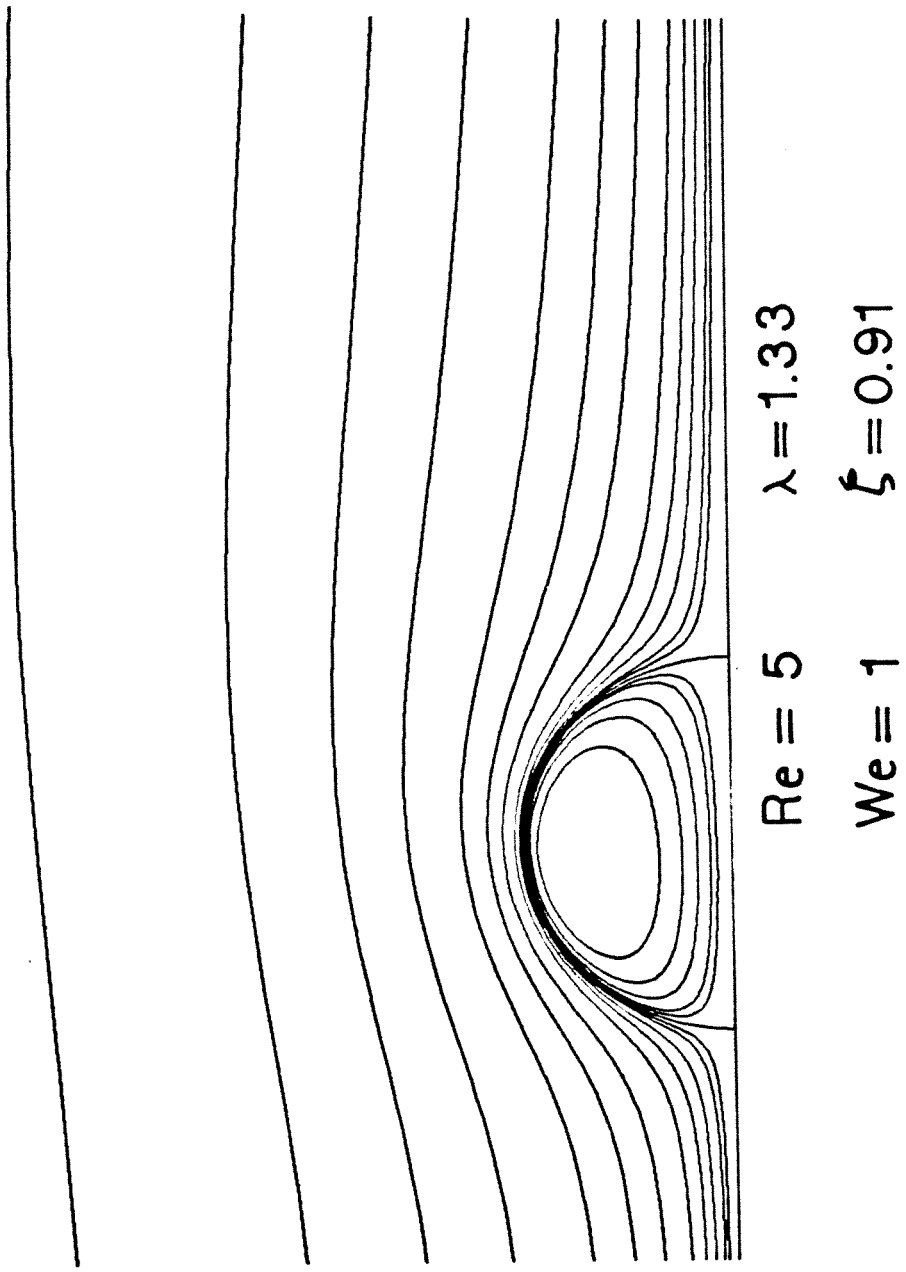
Re = 5
We = 1
λ=1.33
ξ=0.91

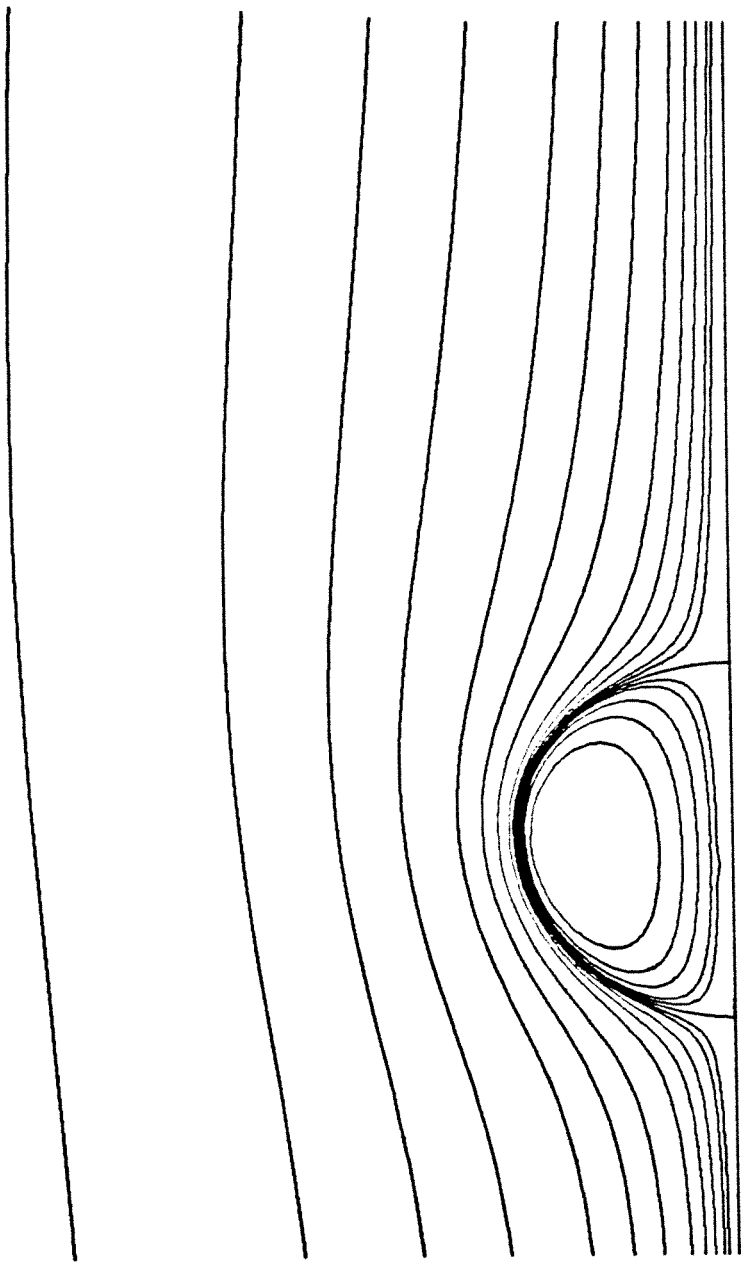
Re = 5
λ = 1.33
We = 2
ζ = 0.91

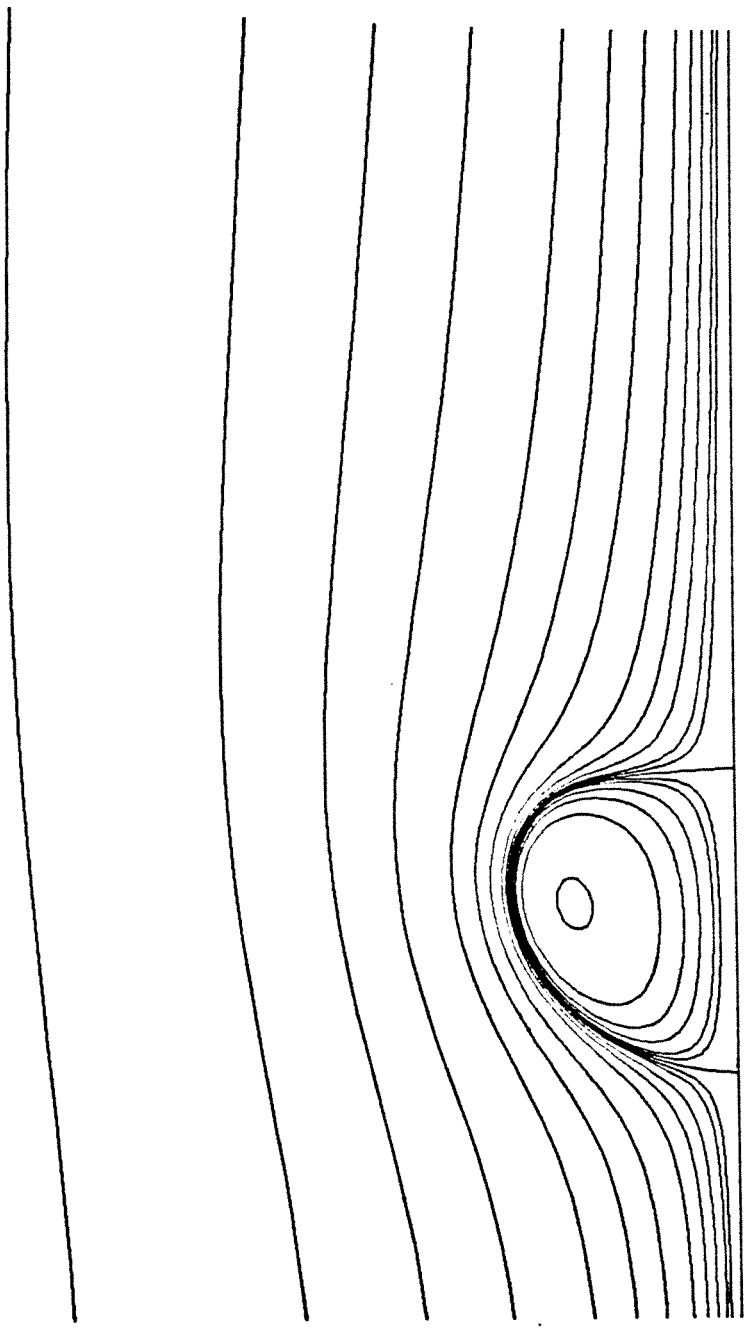
Re = 5
λ = 1.33
We = 4
ζ = 0.91

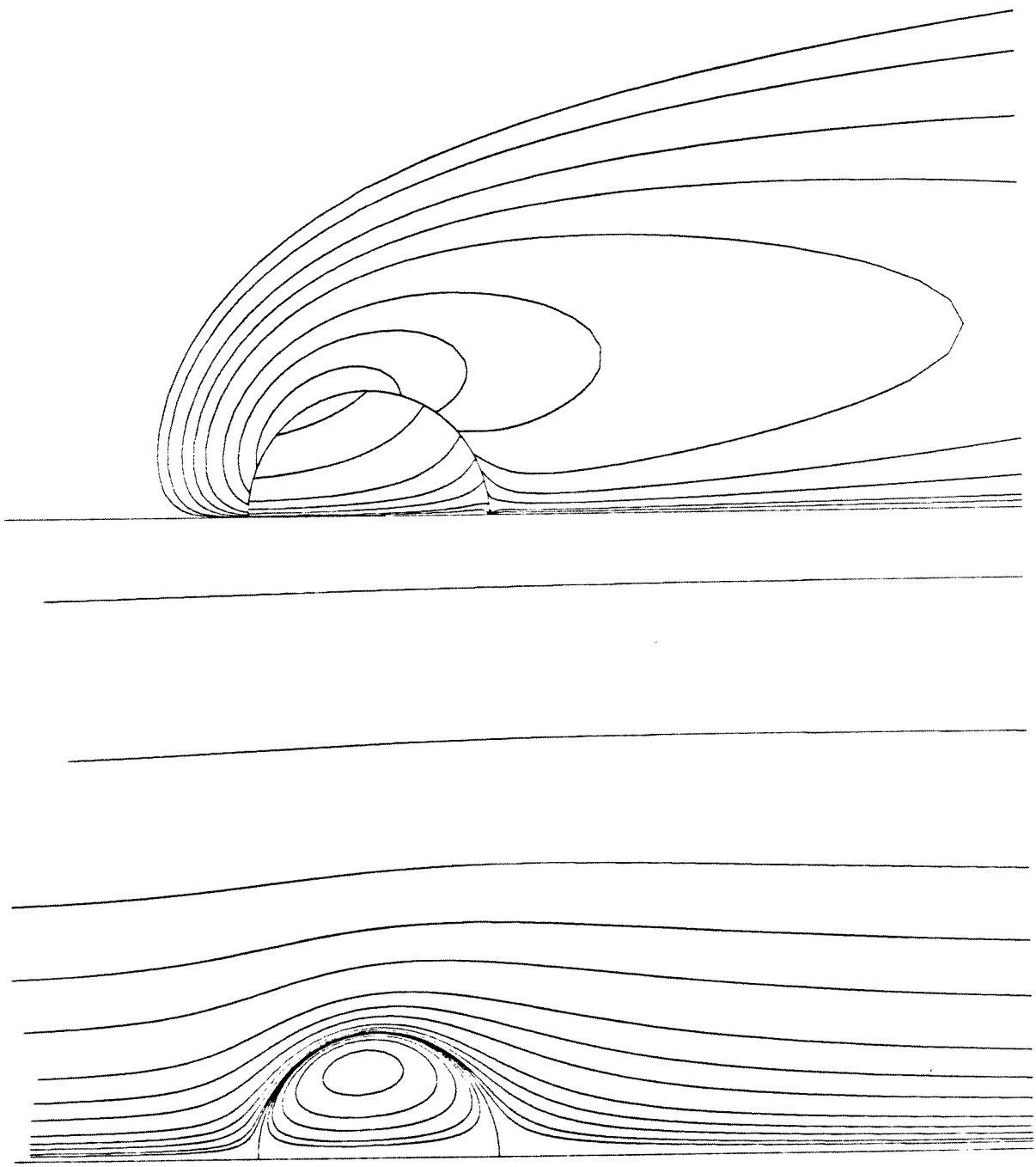

Re = 20 λ = 4

We = 0.5 ζ = 0.91

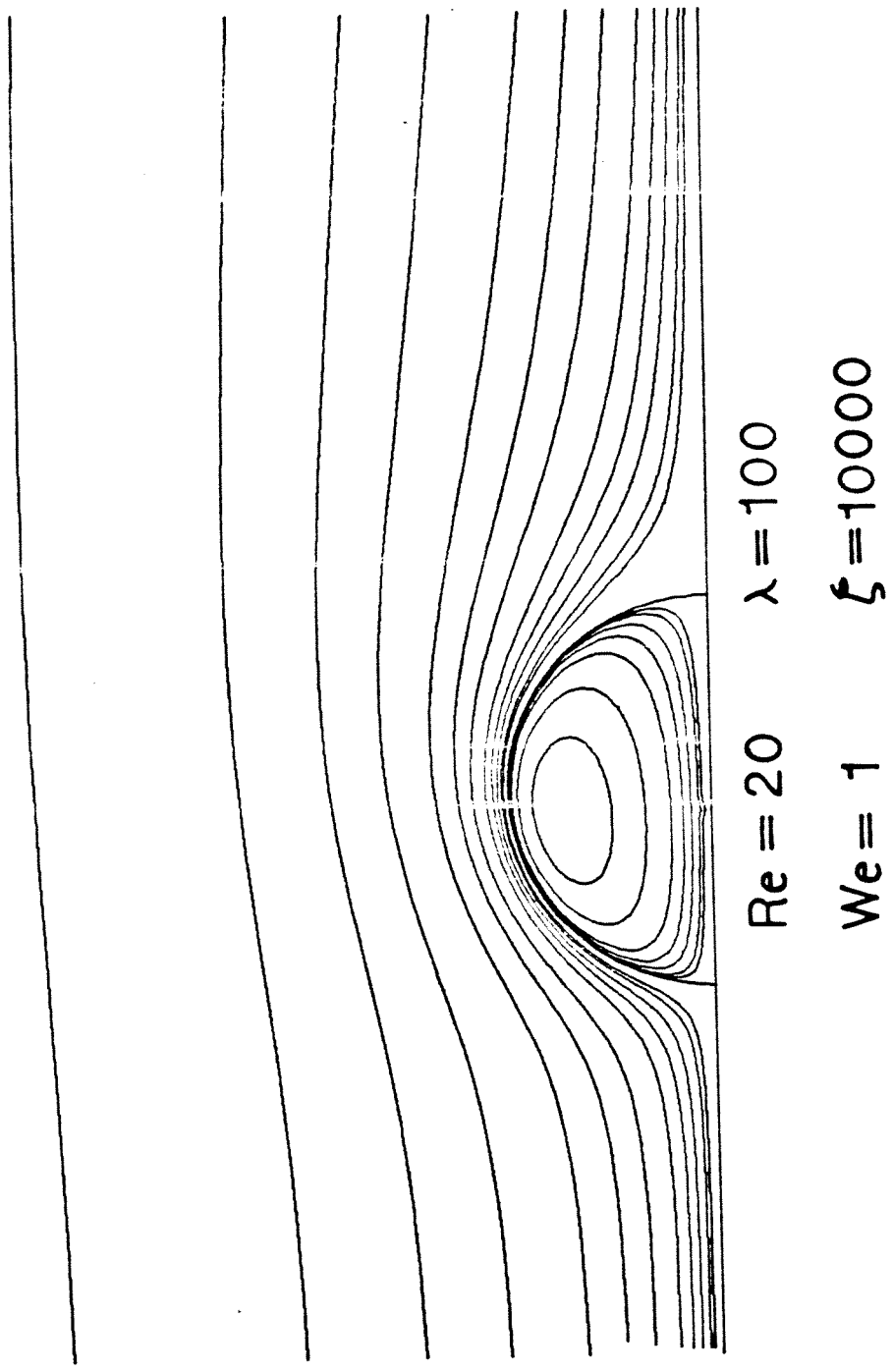
Re = 20
λ = 100
We = 1
ζ = 10000

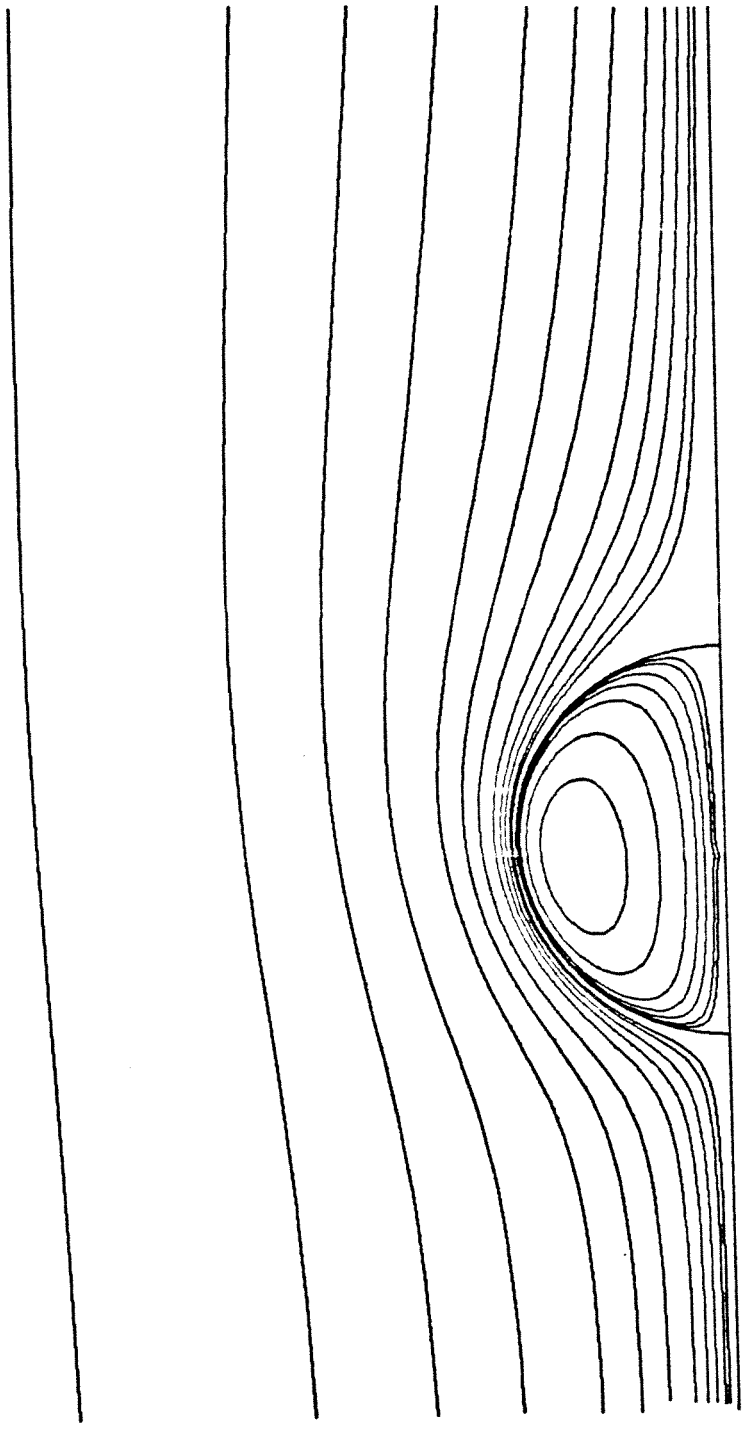
Re = 20
λ = 100
We = 2
ξ = 10000

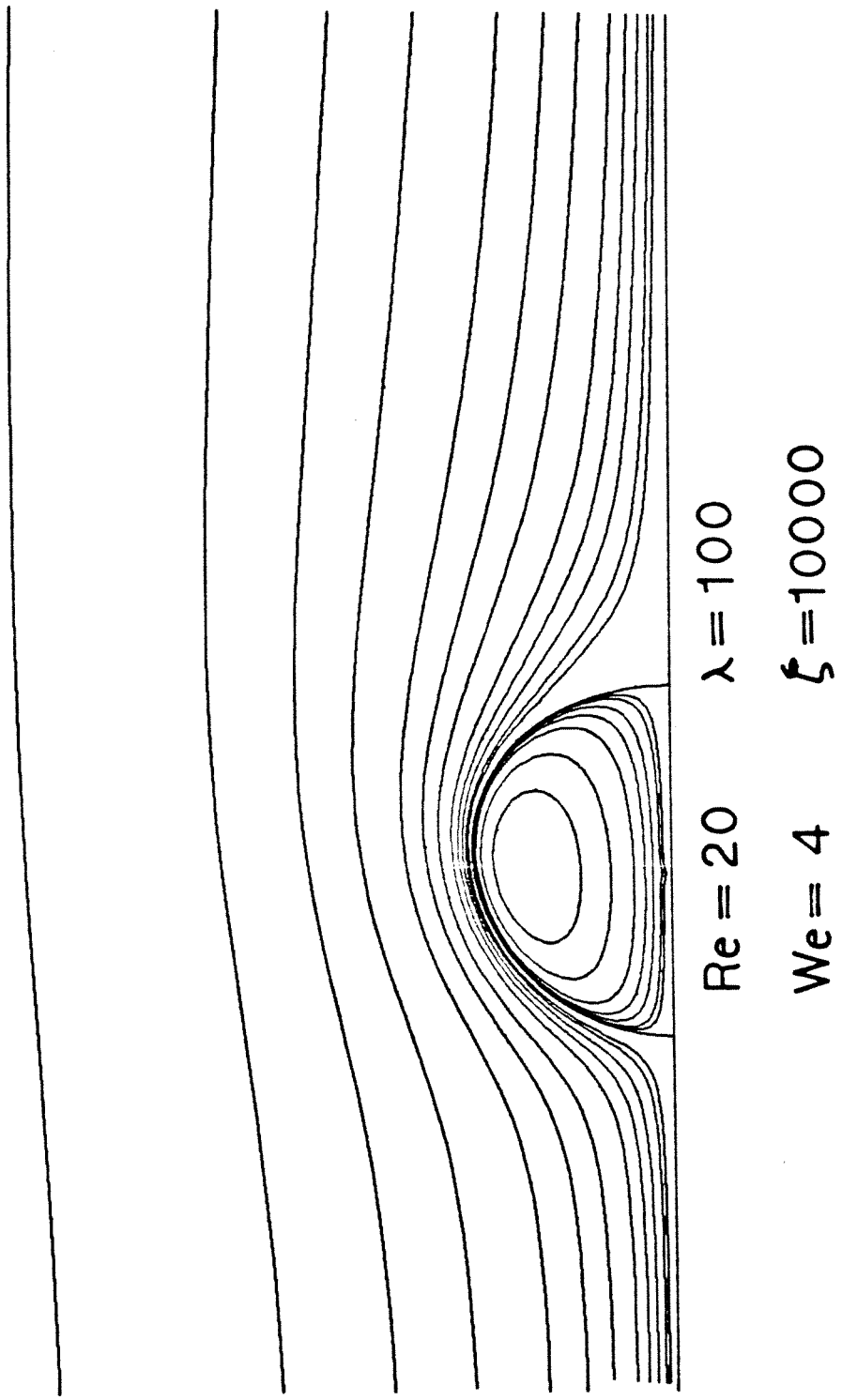
Re = 20
λ = 100
We = 4
ζ = 10000

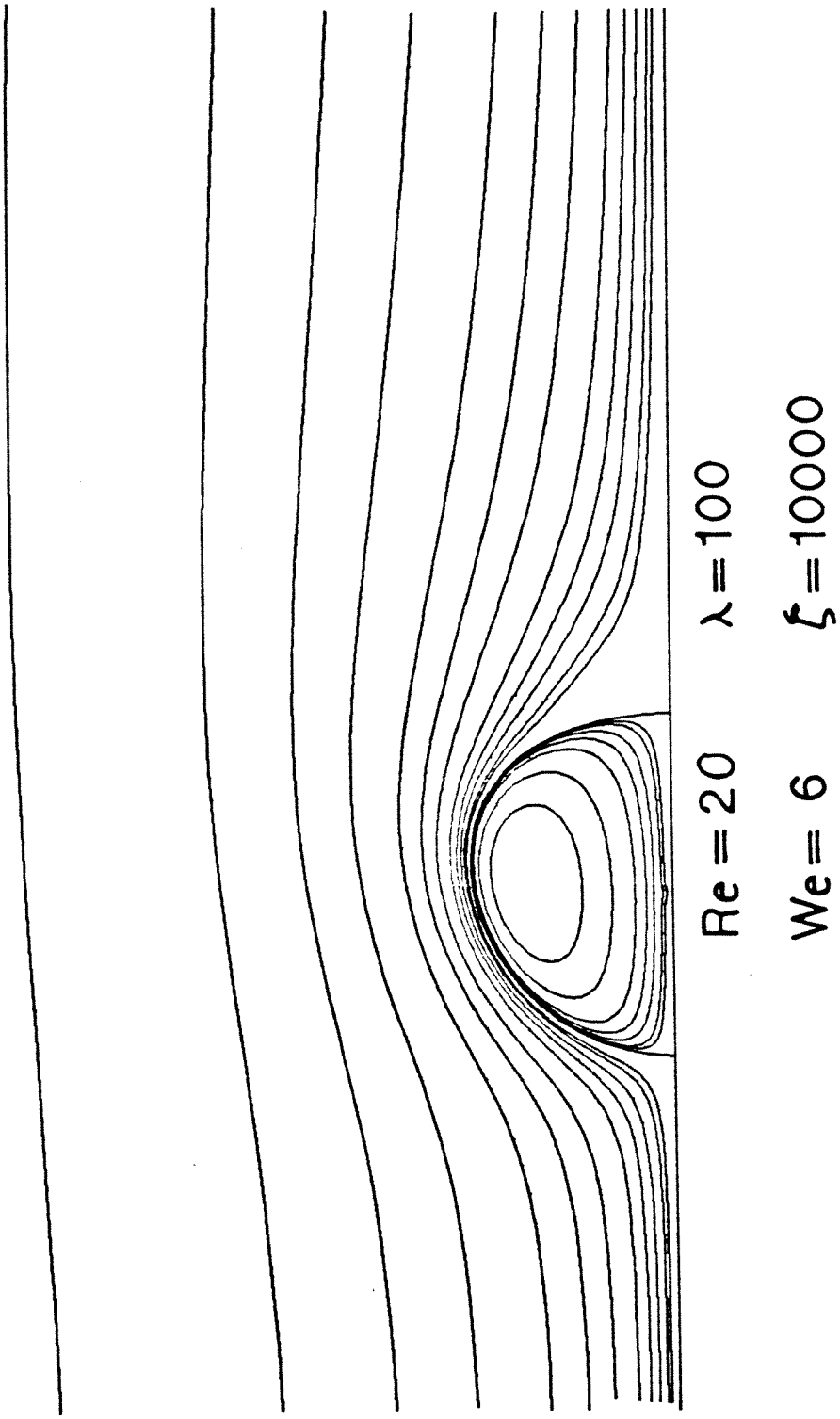
Re = 20
λ = 100
We = 6
ζ = 10000

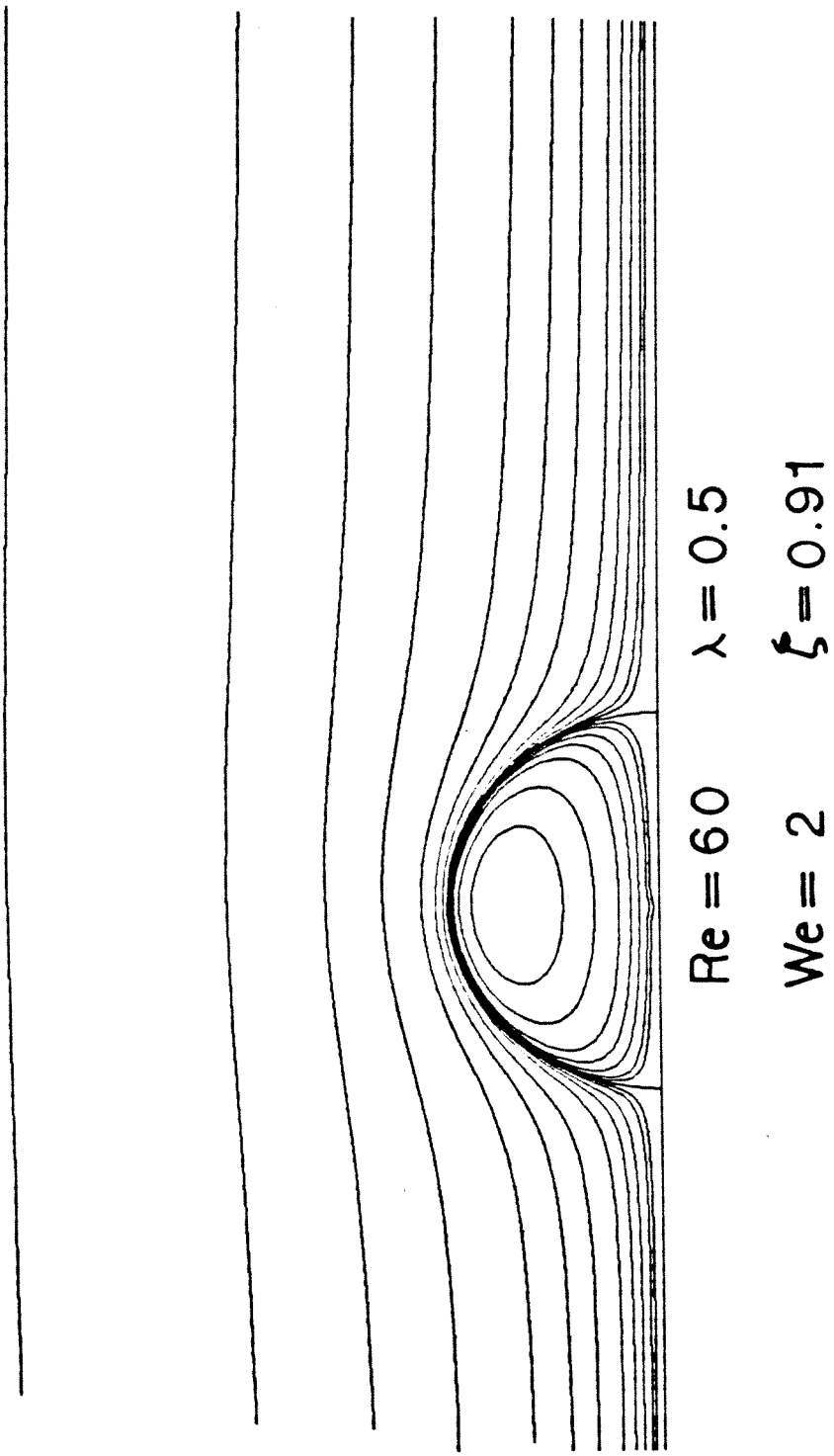
Re = 60
λ = 0.5
We = 2
ζ = 0.91

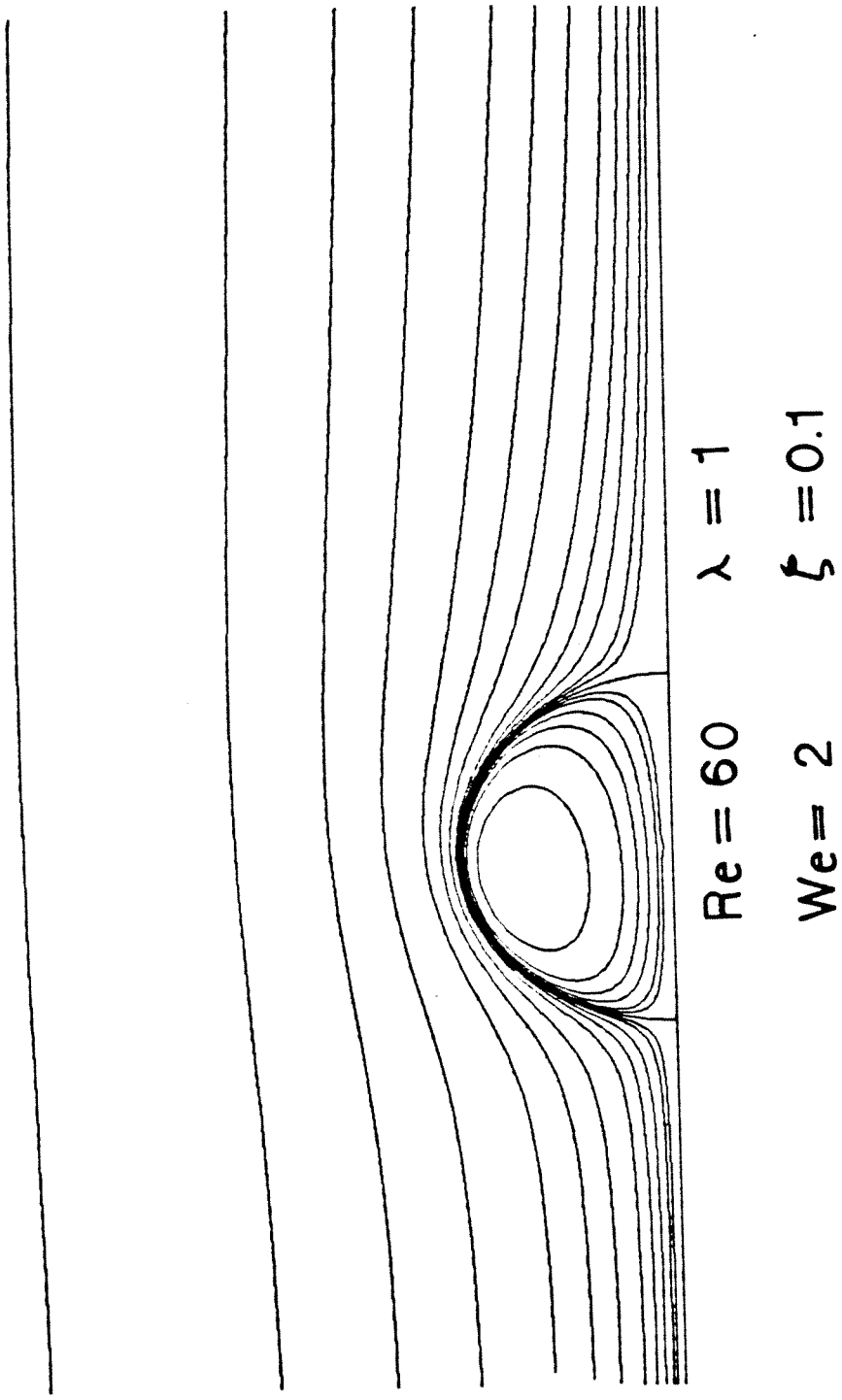
Re = 60
λ = 1
We = 2
ζ = 0.1

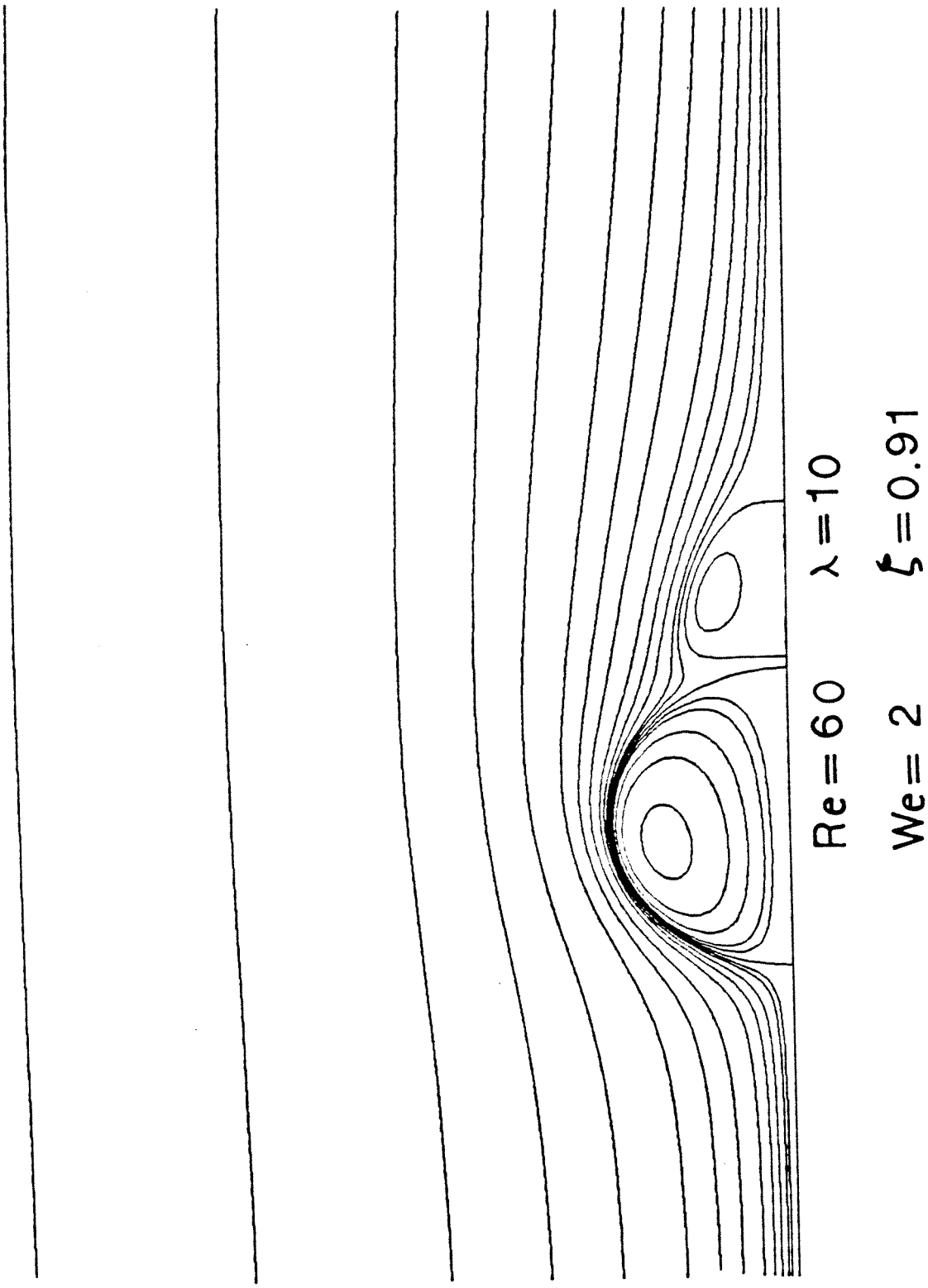
Re=60 λ=10
We= 2 ζ=0.91

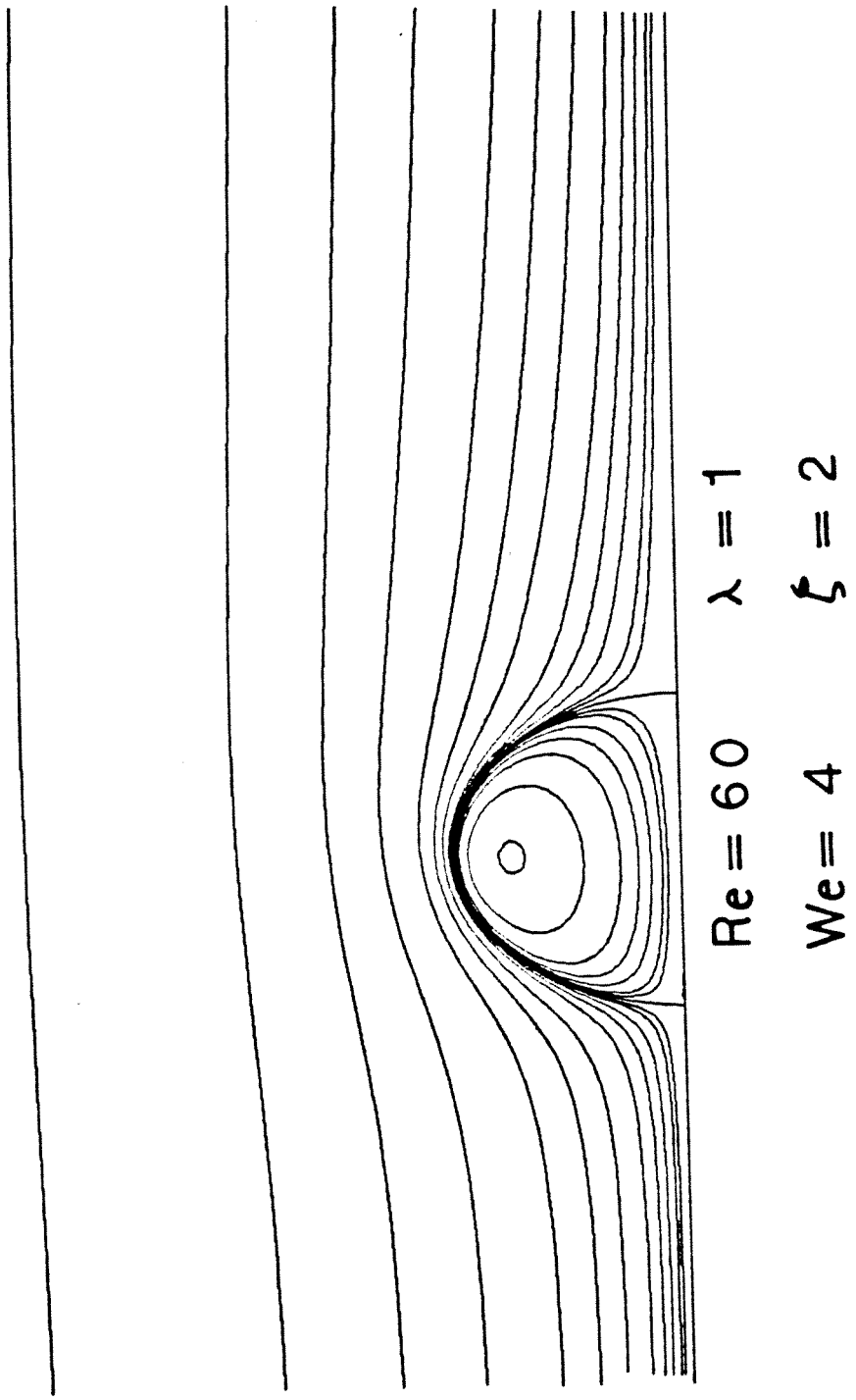
Re = 60 λ = 1
We = 4 ζ = 2

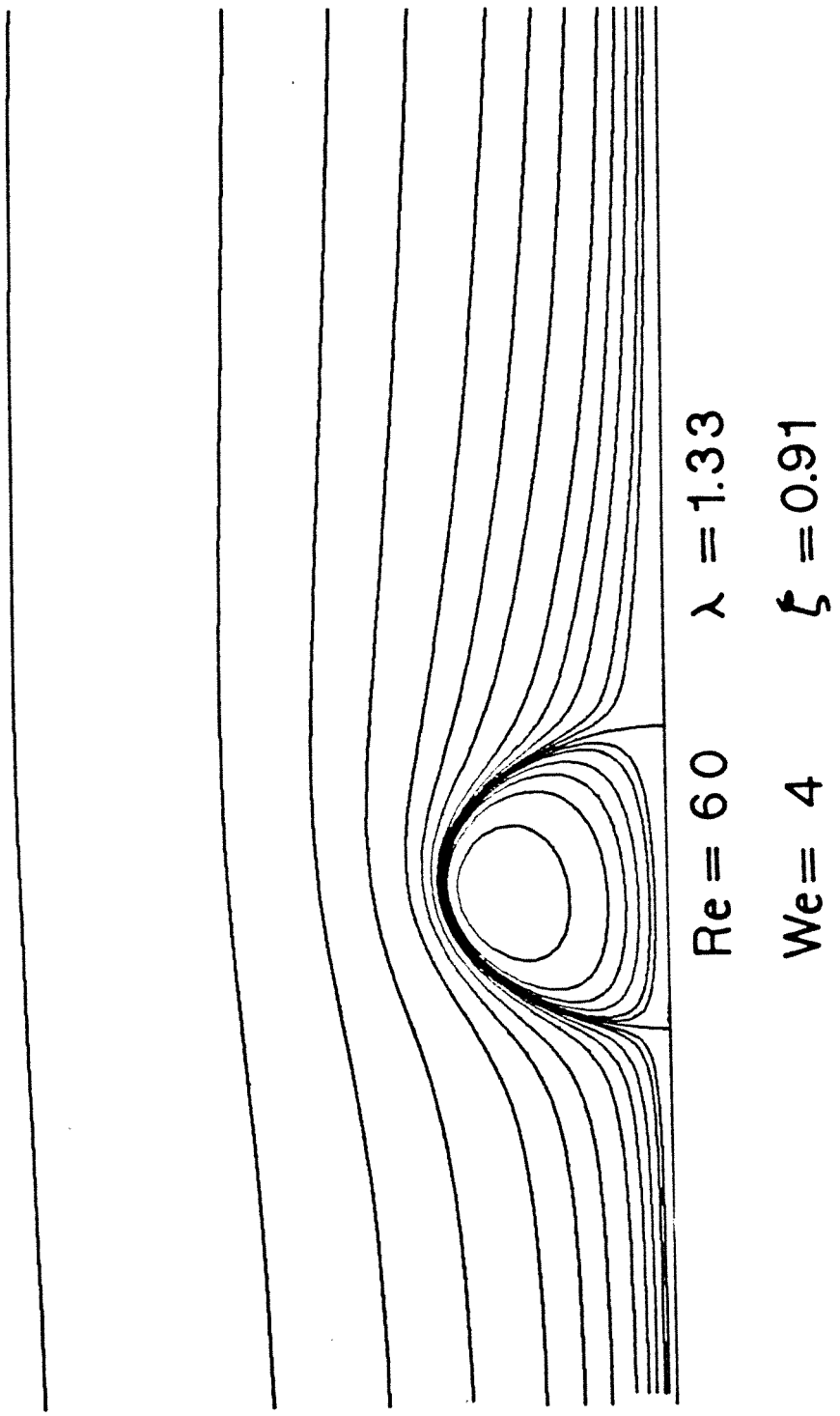
Re = 60
λ = 1.33
We = 4
ζ = 0.91

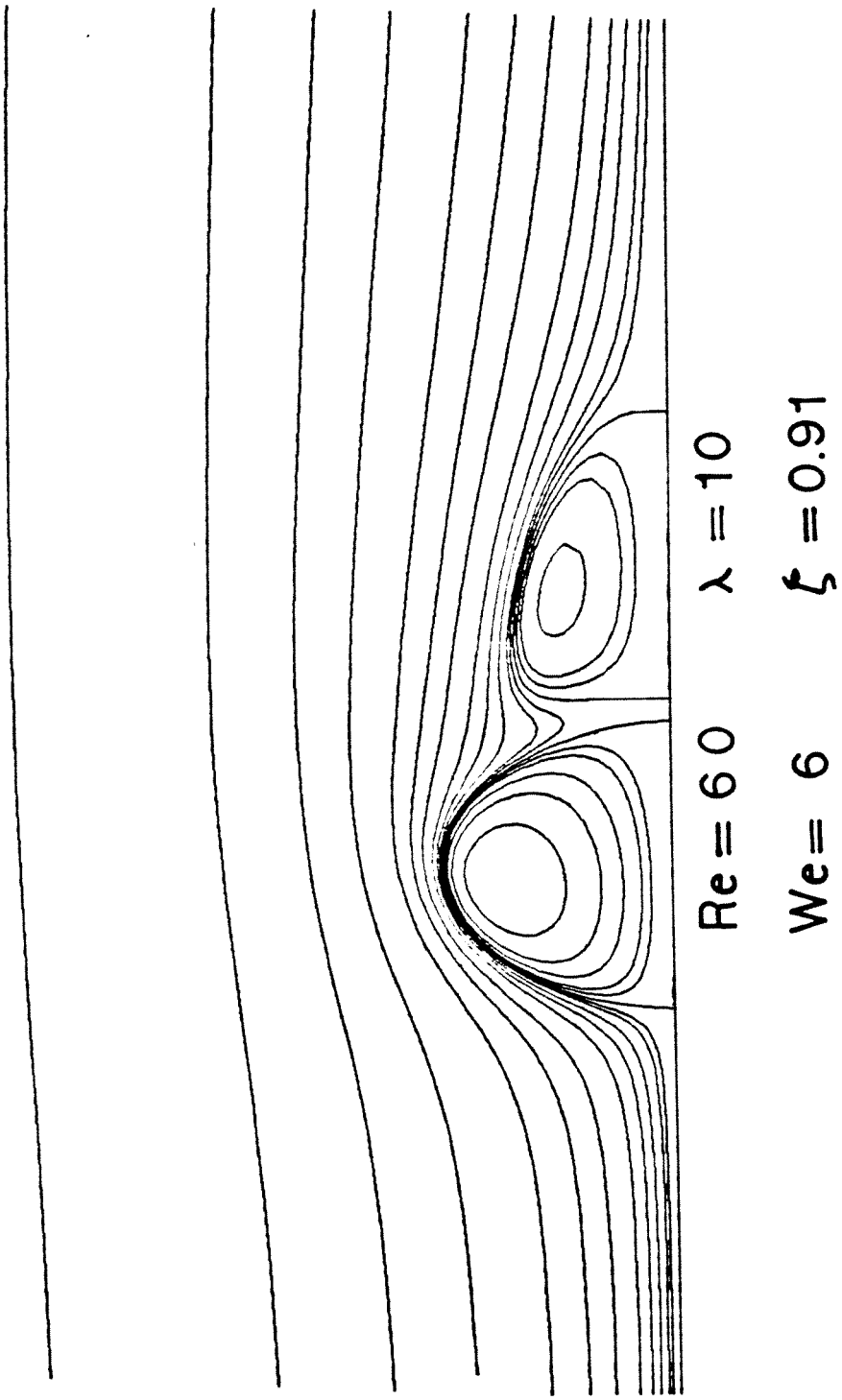
Re = 60
We = 6
λ = 10
ξ = 0.91

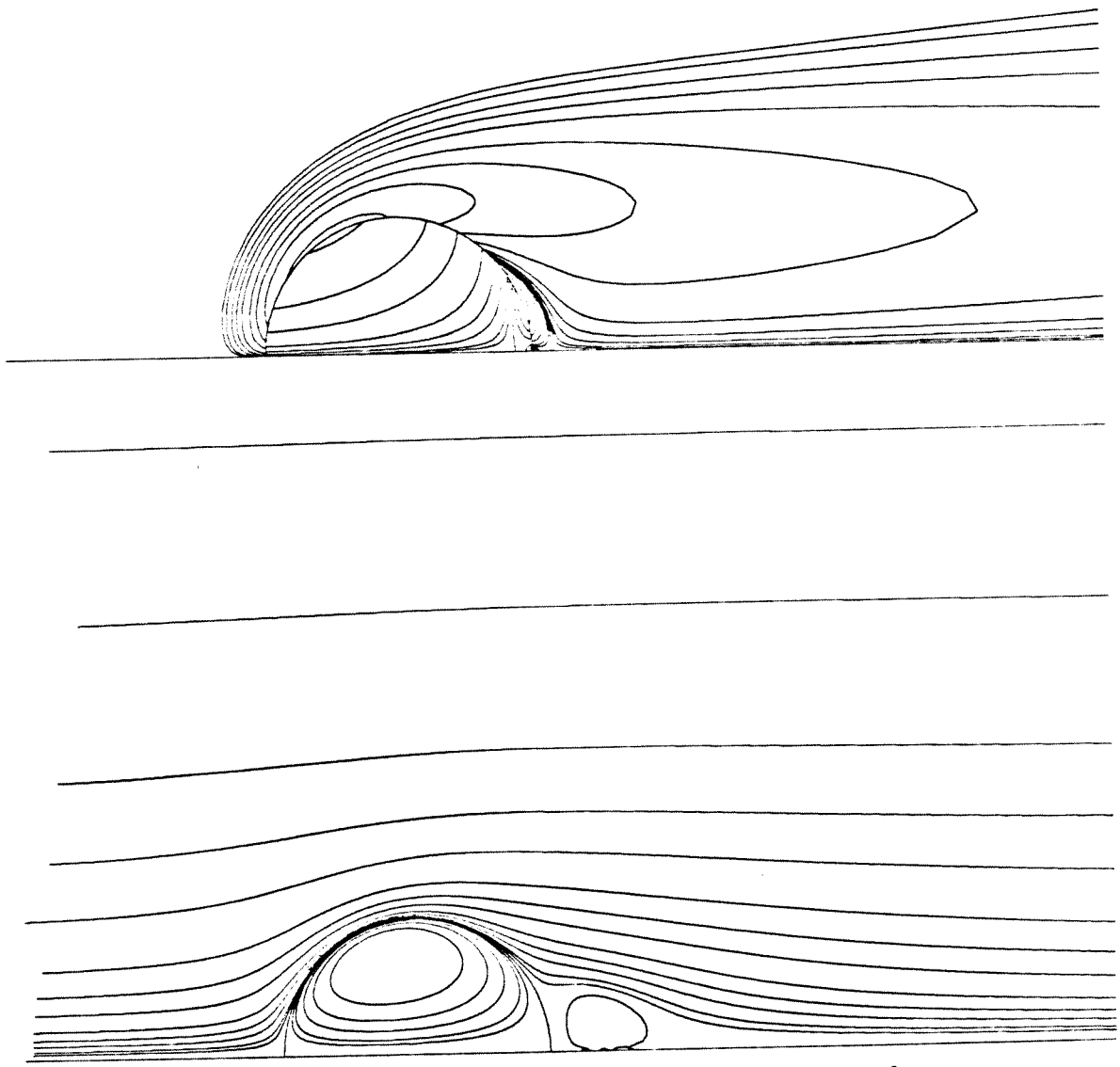

Re = 80 λ = 4

We = 0.5 ζ = 0.909

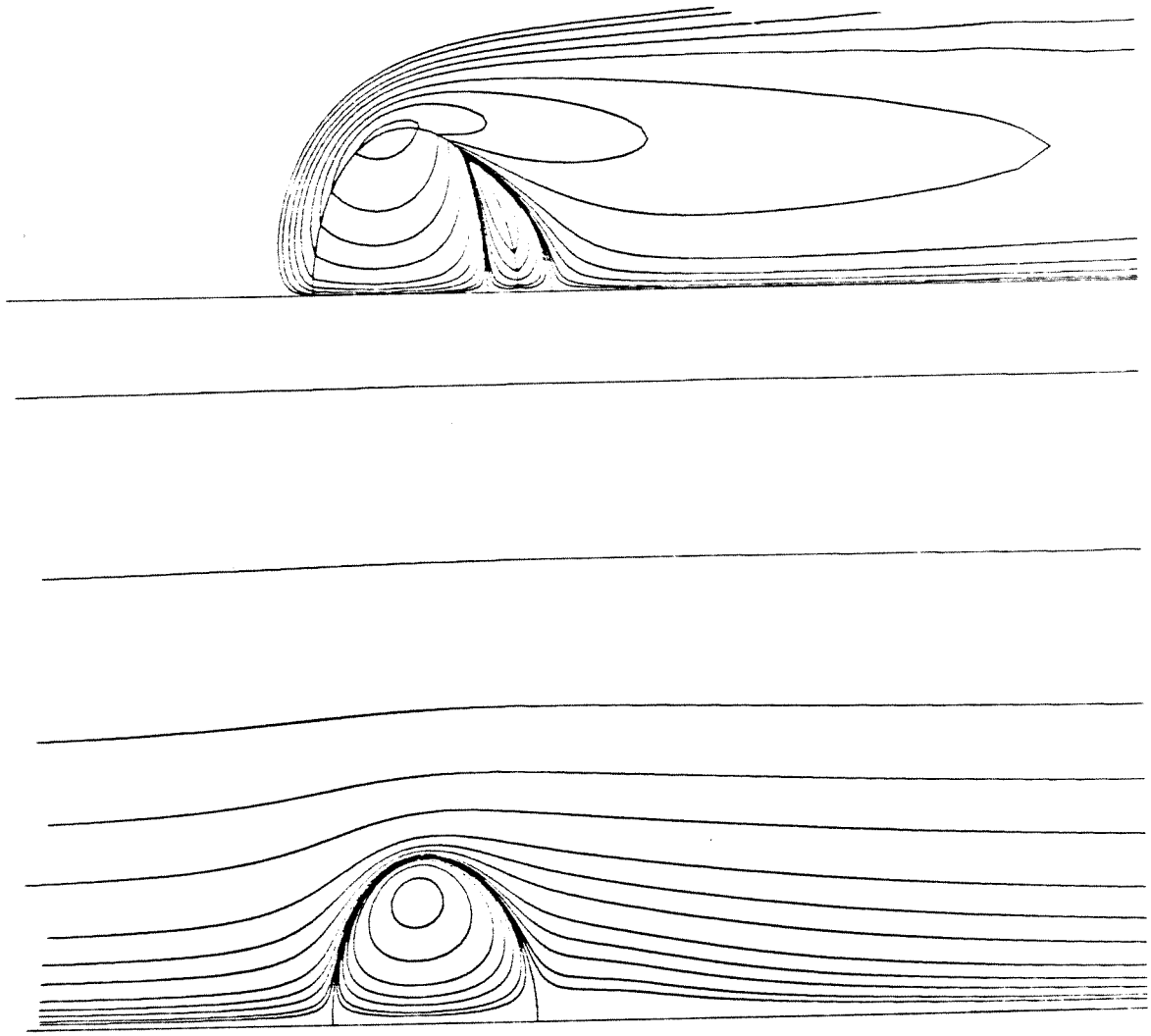

$Re = 100$ $\lambda = 1$

$We = 4$ $\zeta = 0.002$

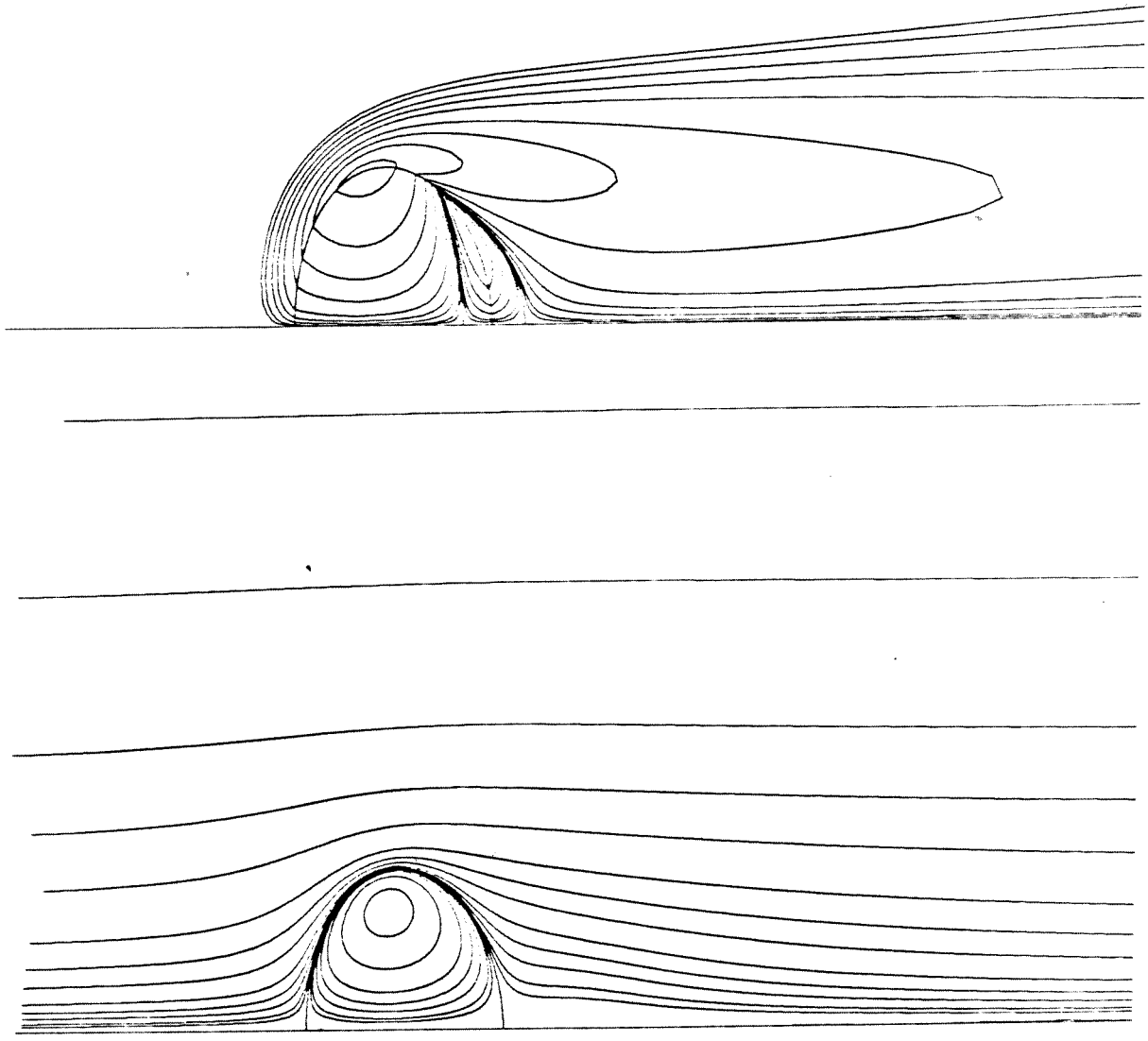

$Re = 100$ $\lambda = 1$

$We = 4$ $\zeta = 0.02$

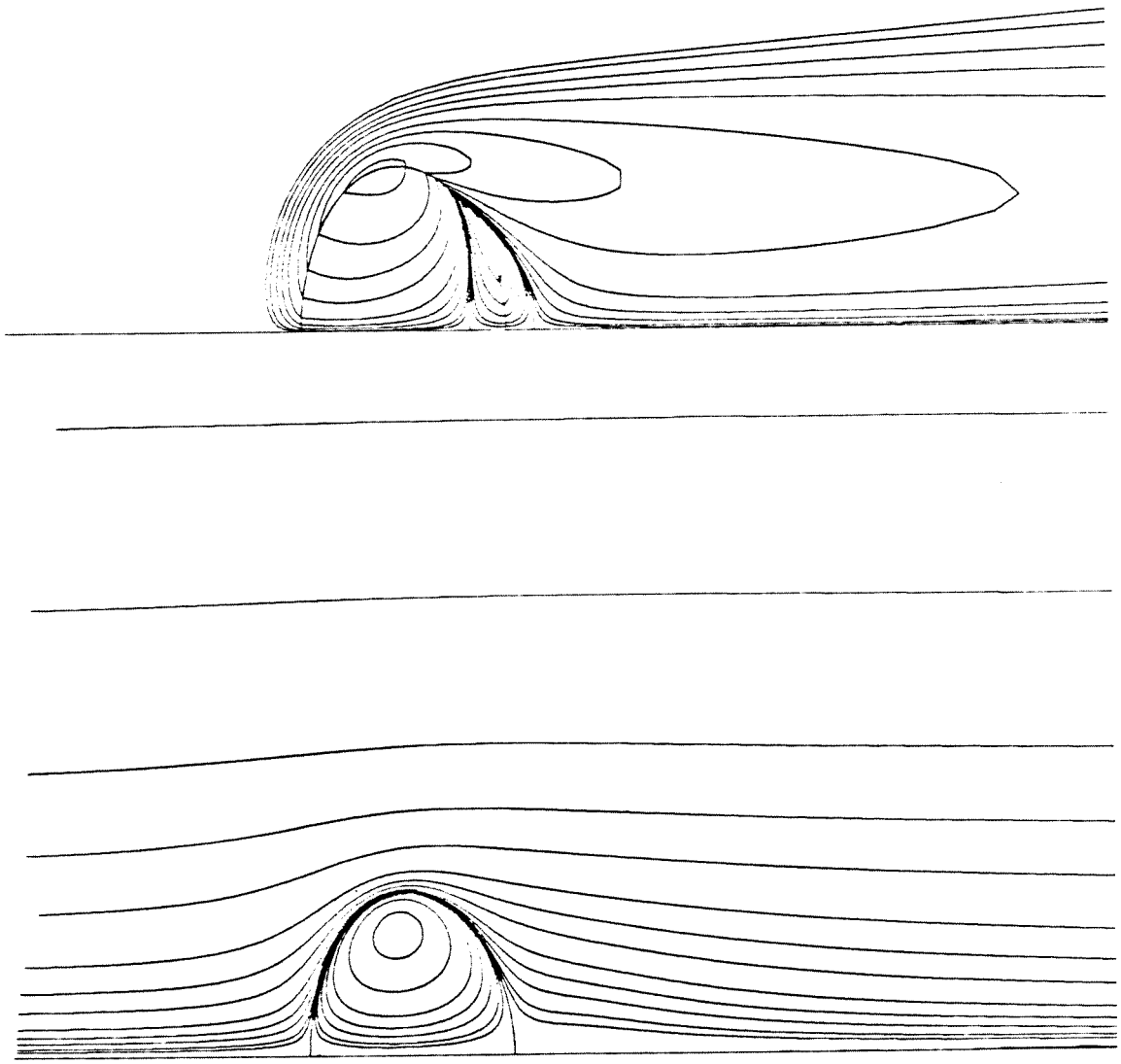

$Re = 100$ $\lambda = 1$

$We = 4$ $\zeta = 0.25$

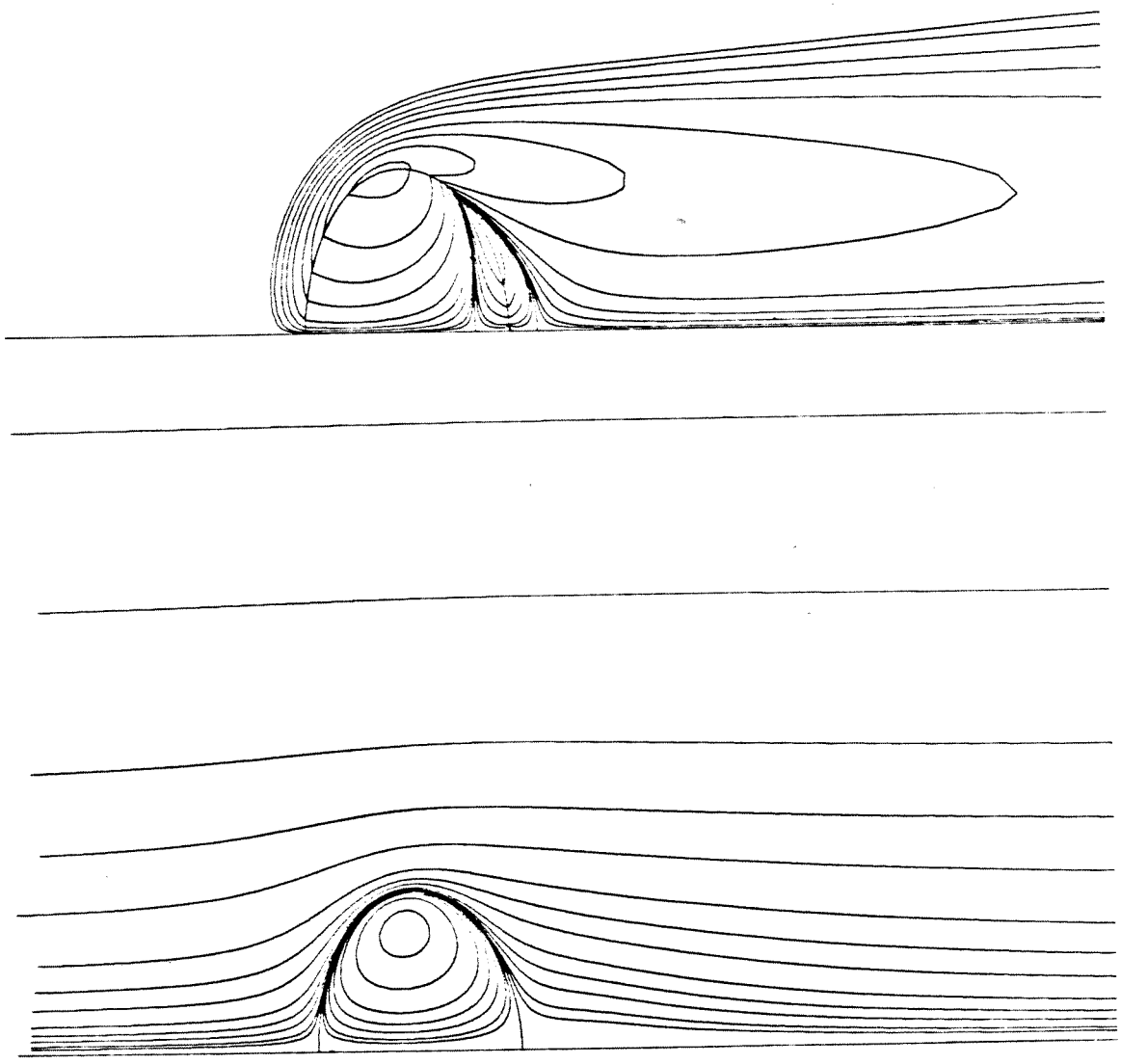

$Re = 100$ $\lambda = 1$

$We = 4$ $\xi = 0.2$

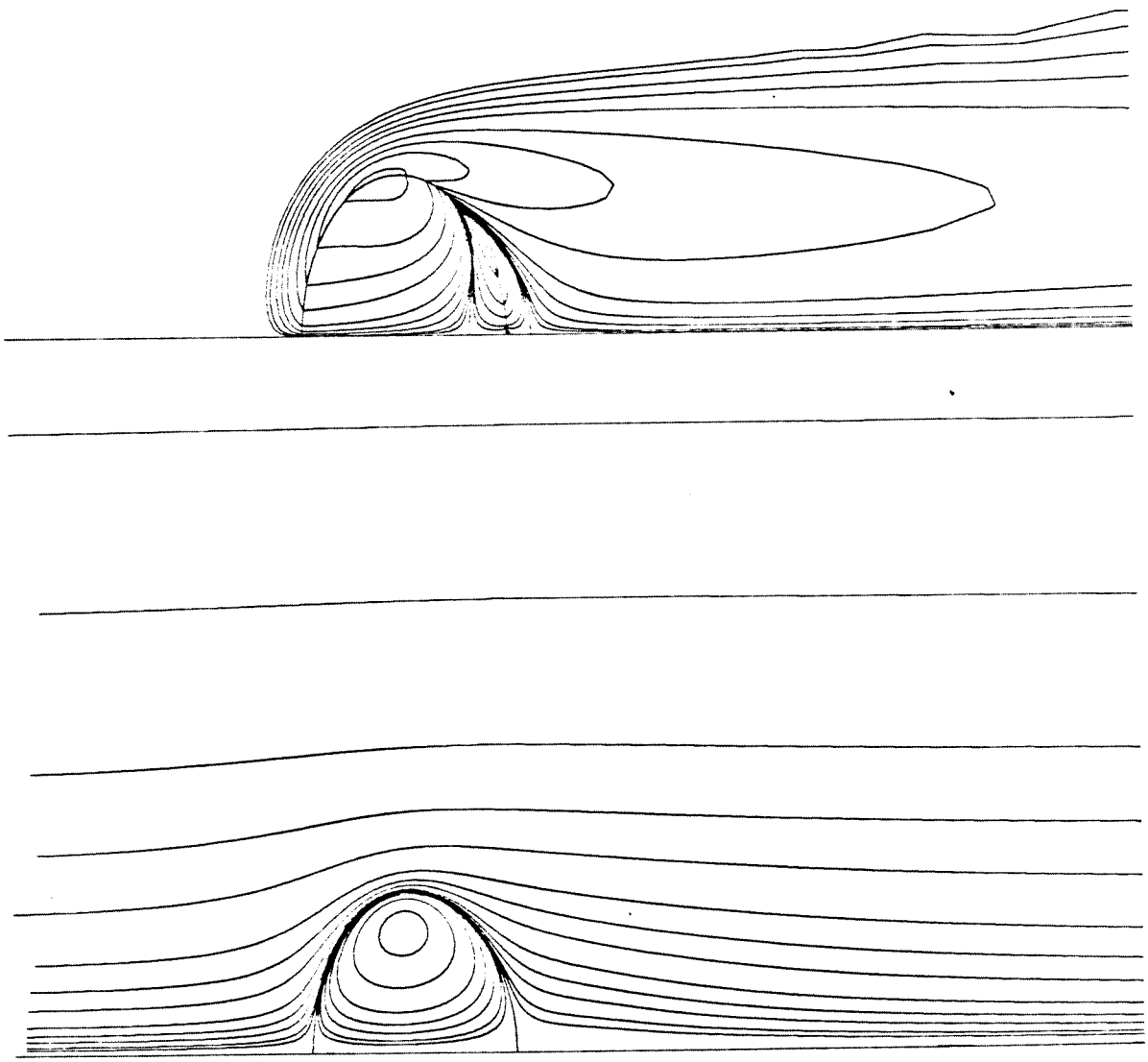

Re = 100 λ = 1

We = 4 ζ = 0.5

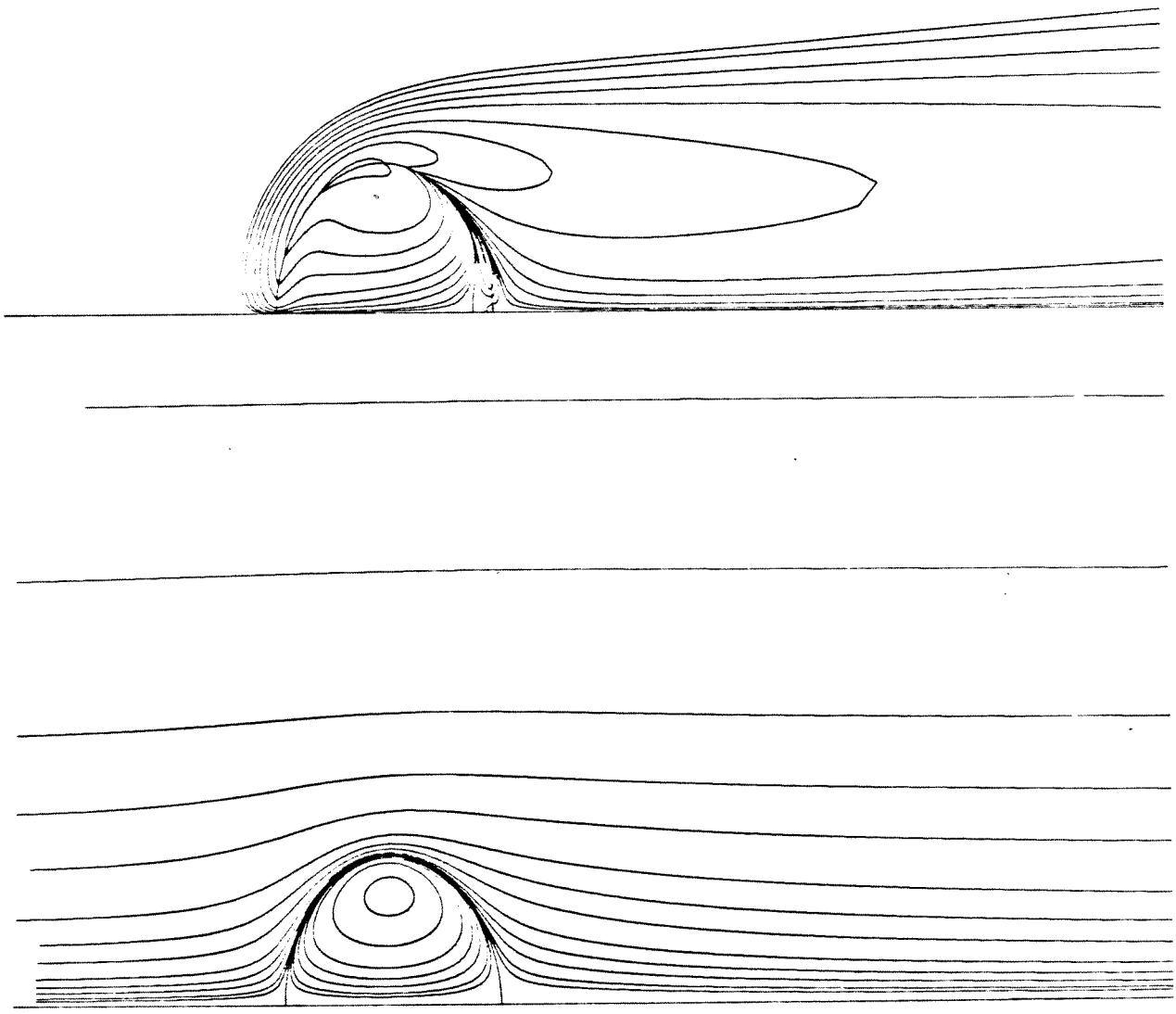

$Re = 100$ $\lambda = 1$

$We = 4$ $\zeta = 2$

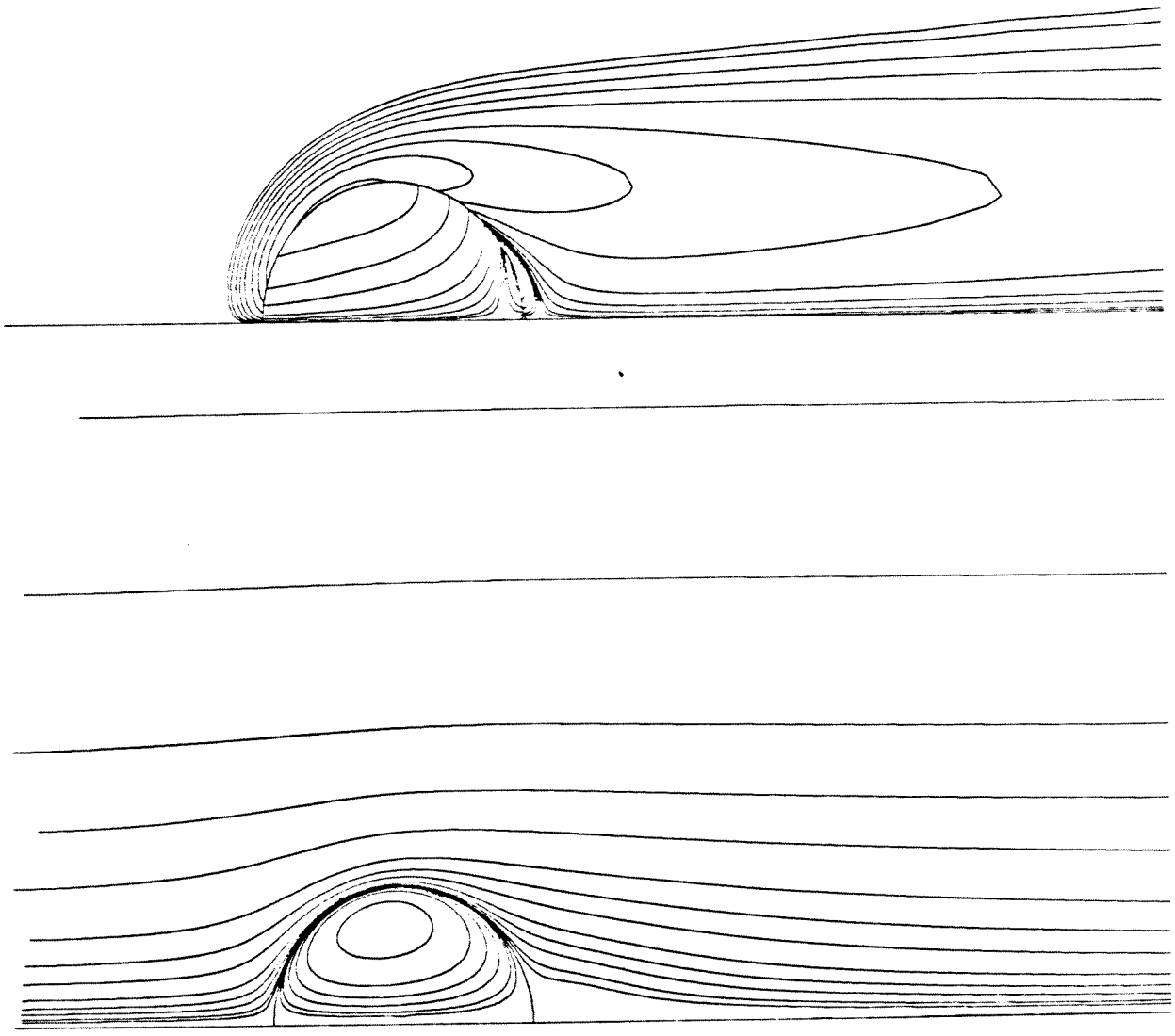

$Re = 100$ $\lambda = 2$

$We = 1$ $\zeta = 0.909$

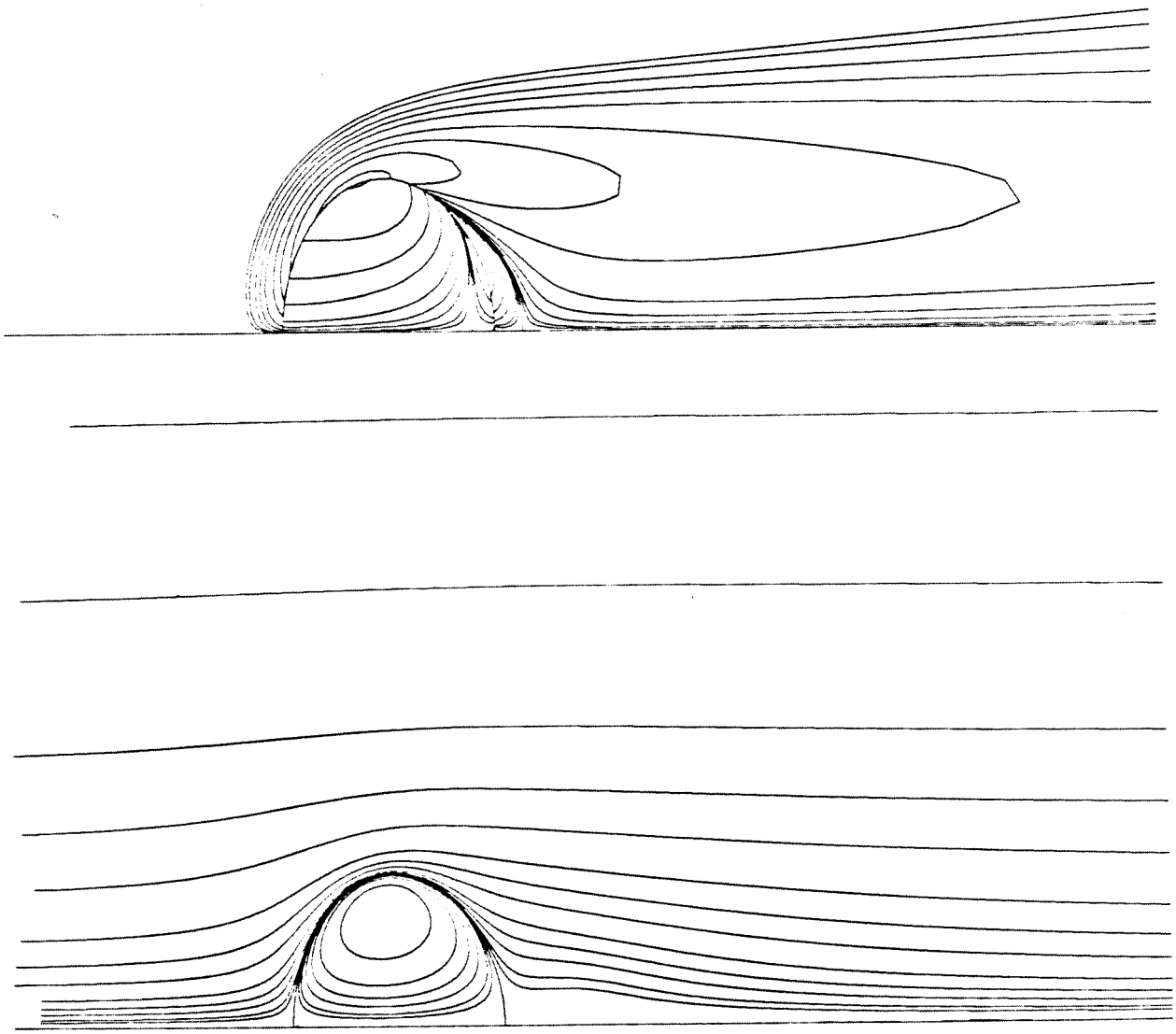

Re = 100 $\lambda = 2$

We = 4 $\zeta = 0.909$

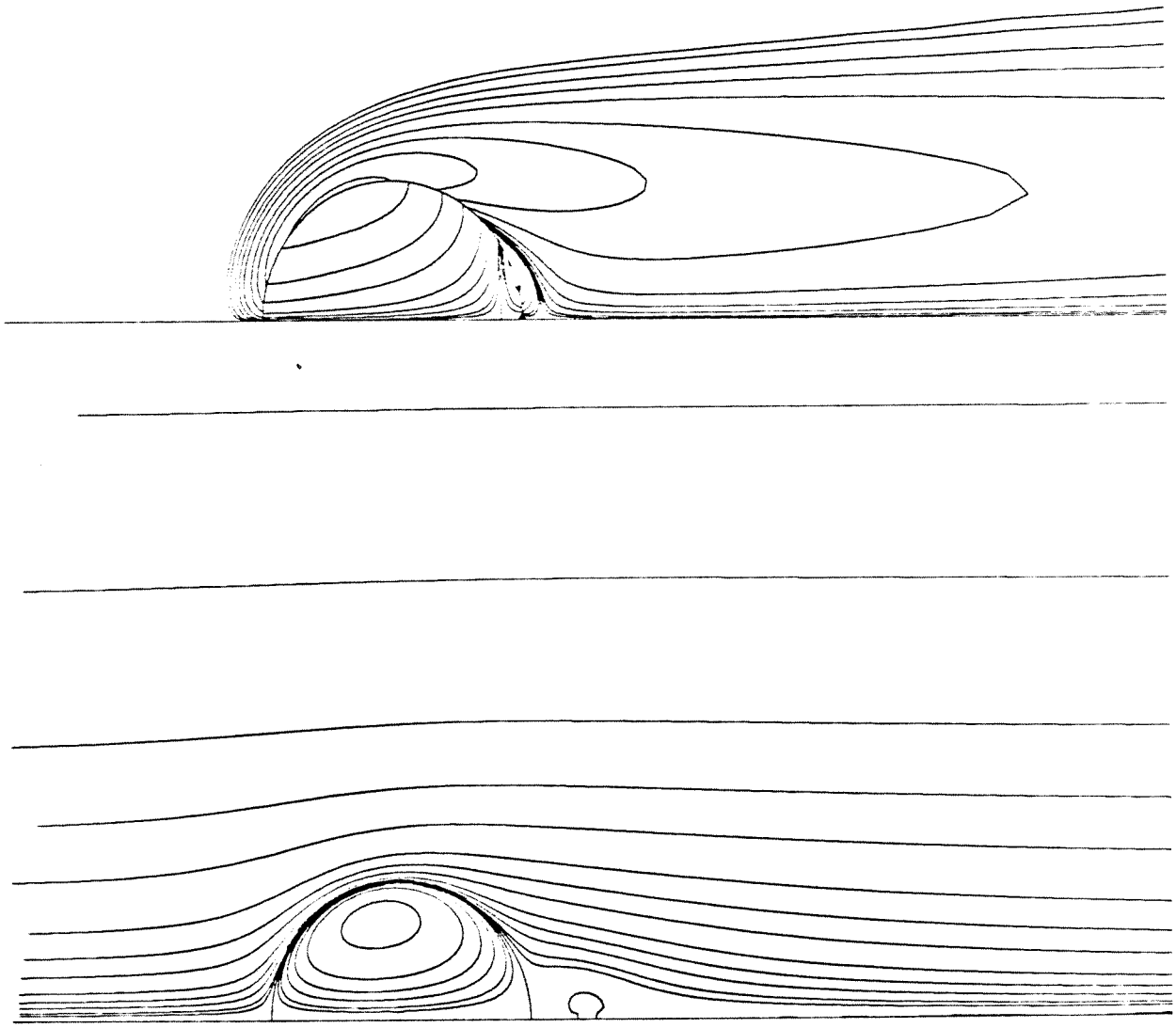

Re = 100 λ = 2.5

We = 1 ζ = 0.909

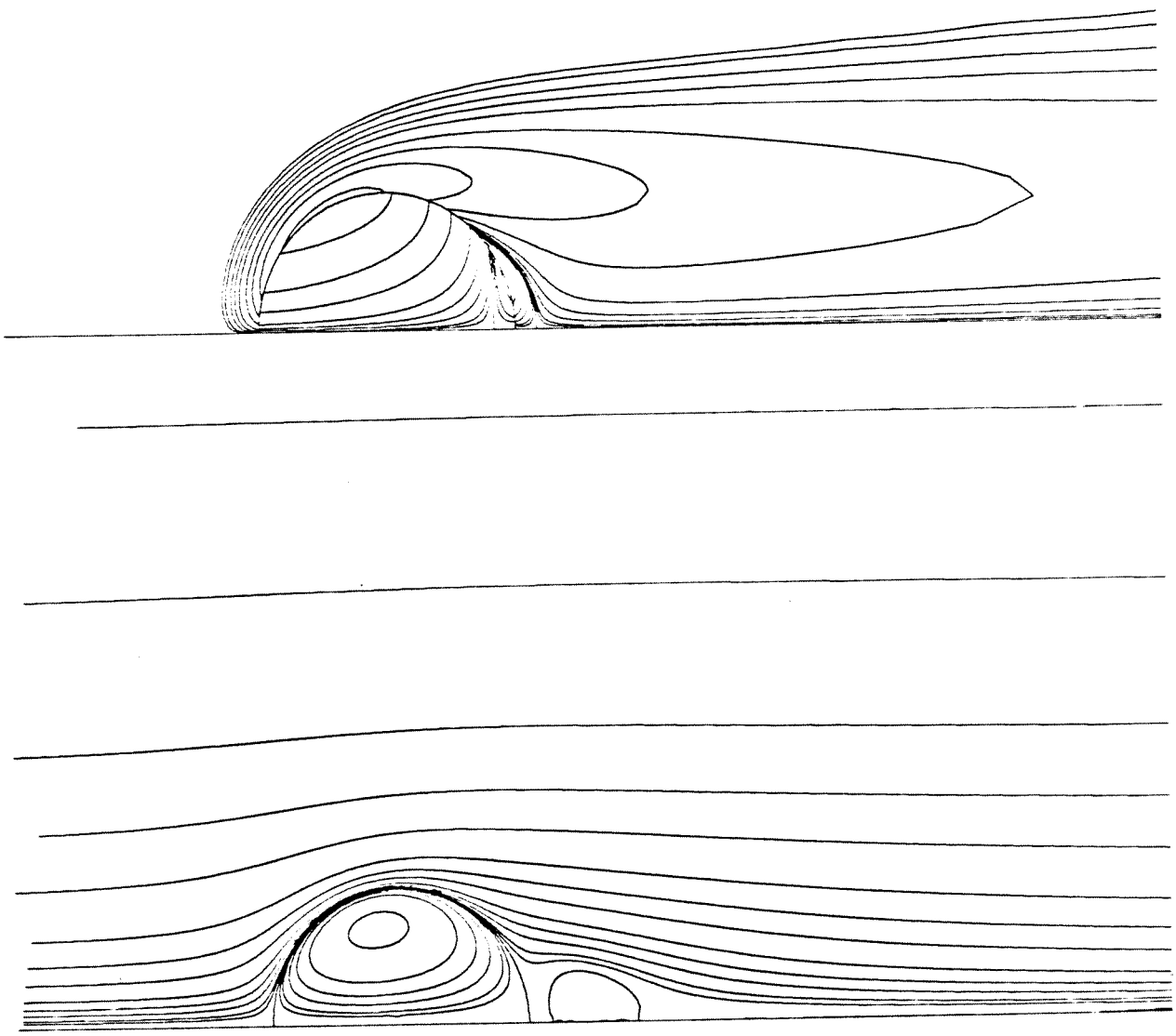

Re = 100 λ = 3

We = 1 ξ = 0.909

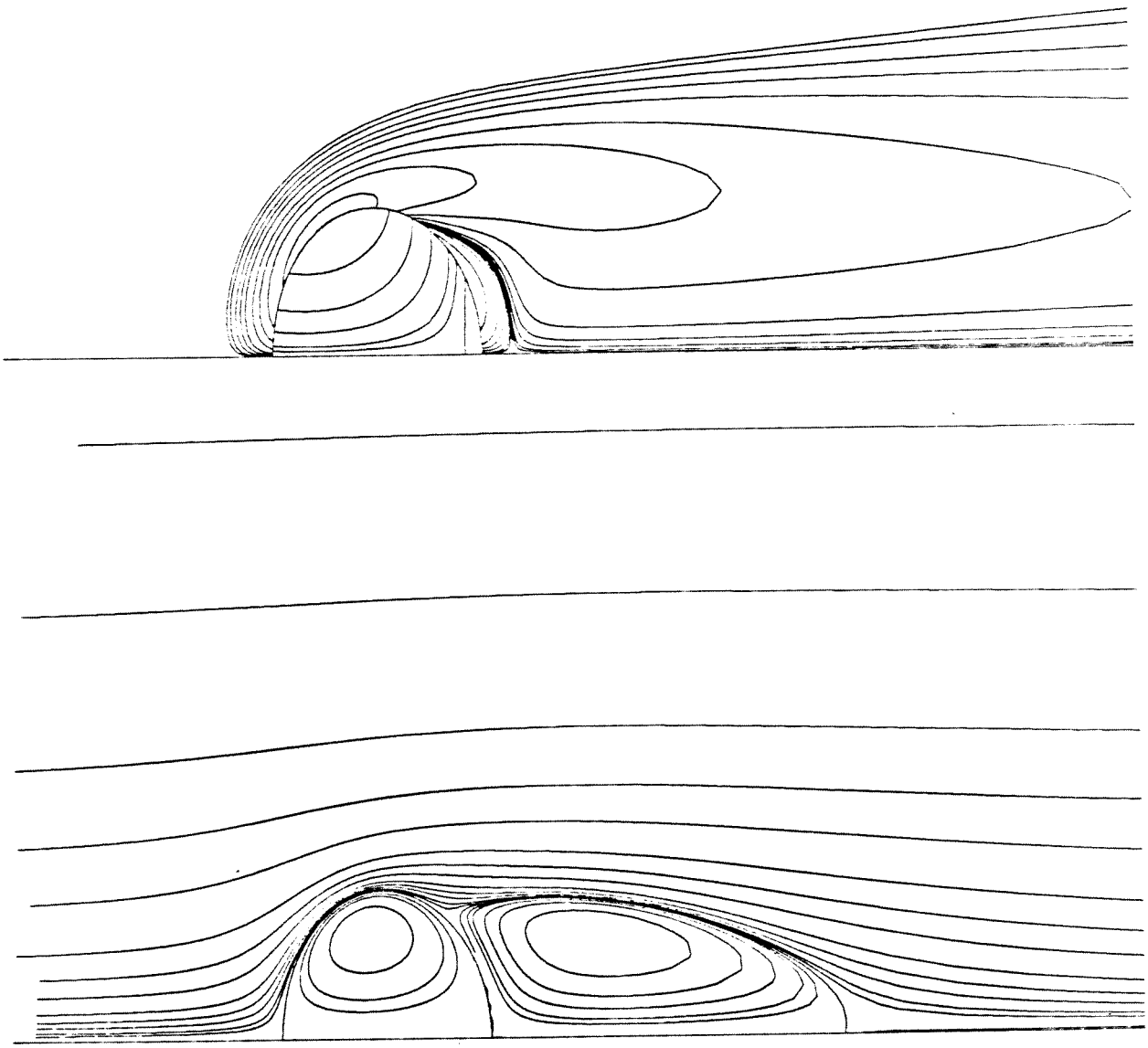

$Re = 100 \qquad \lambda = 50$

$We = 4 \qquad \zeta = 20$

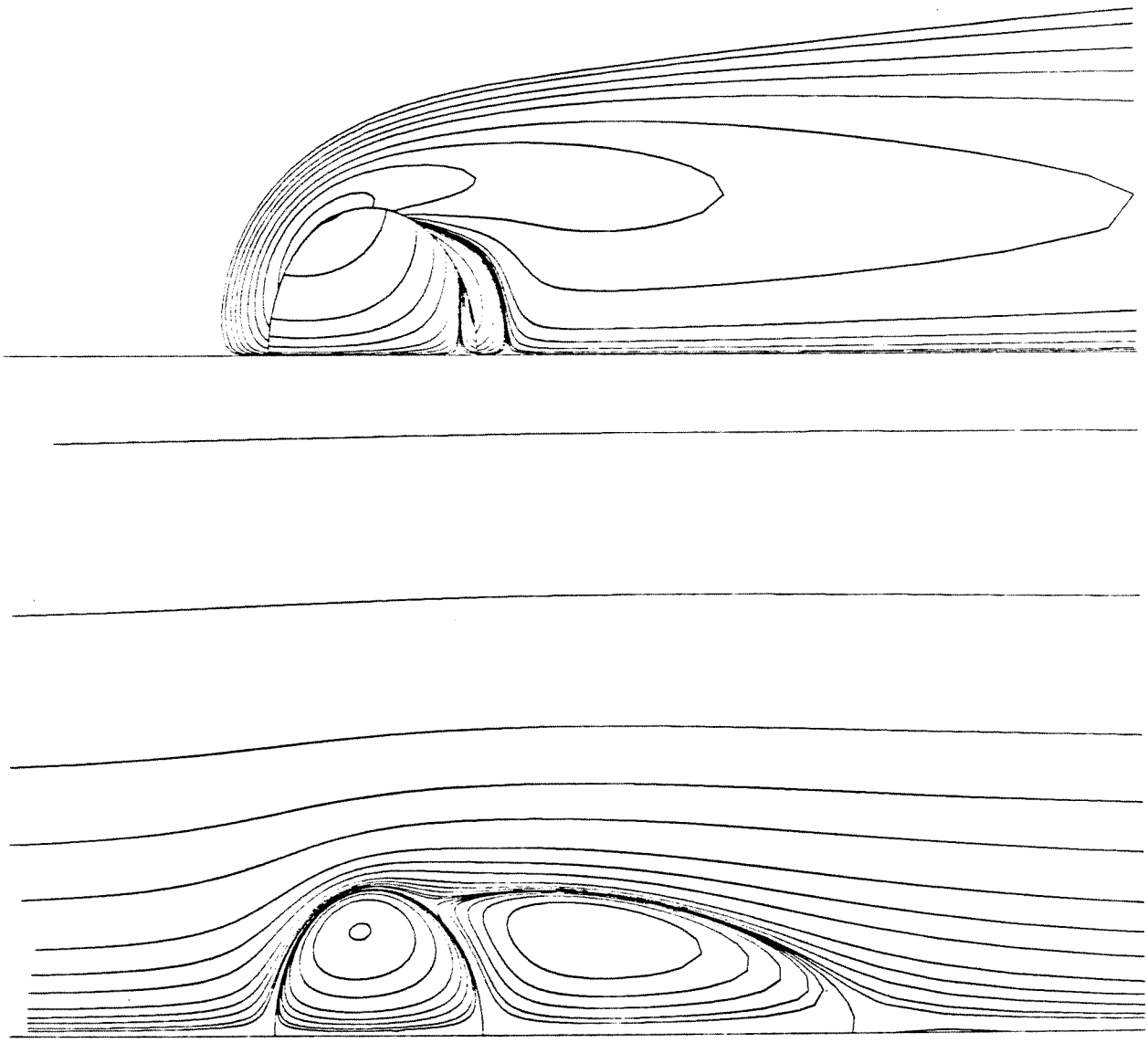

$Re = 100$ $\lambda = 100$

$We = 4$ $\zeta = 200$

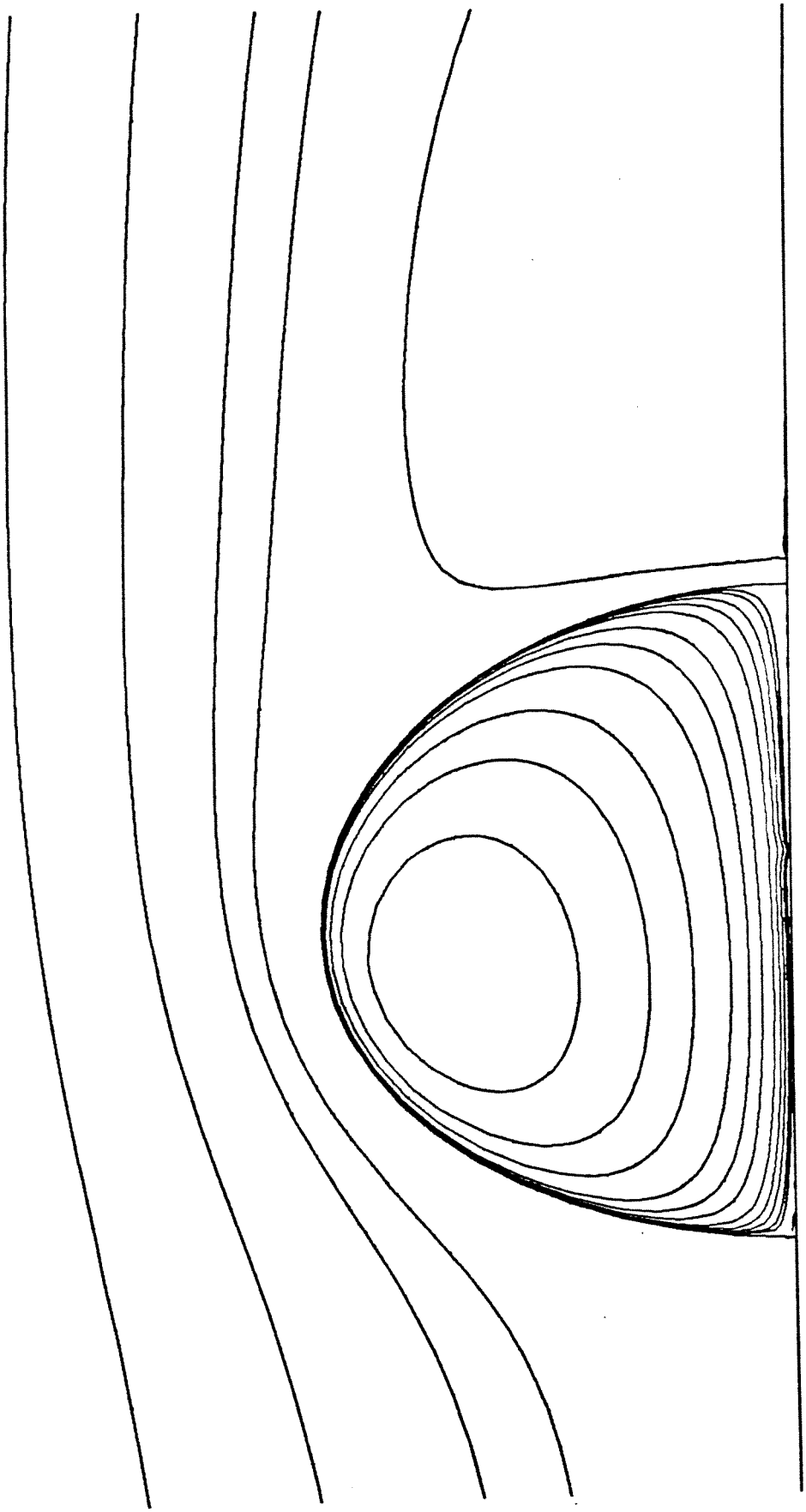
Re = 100 λ = 10
We = 4 ξ = 0.909

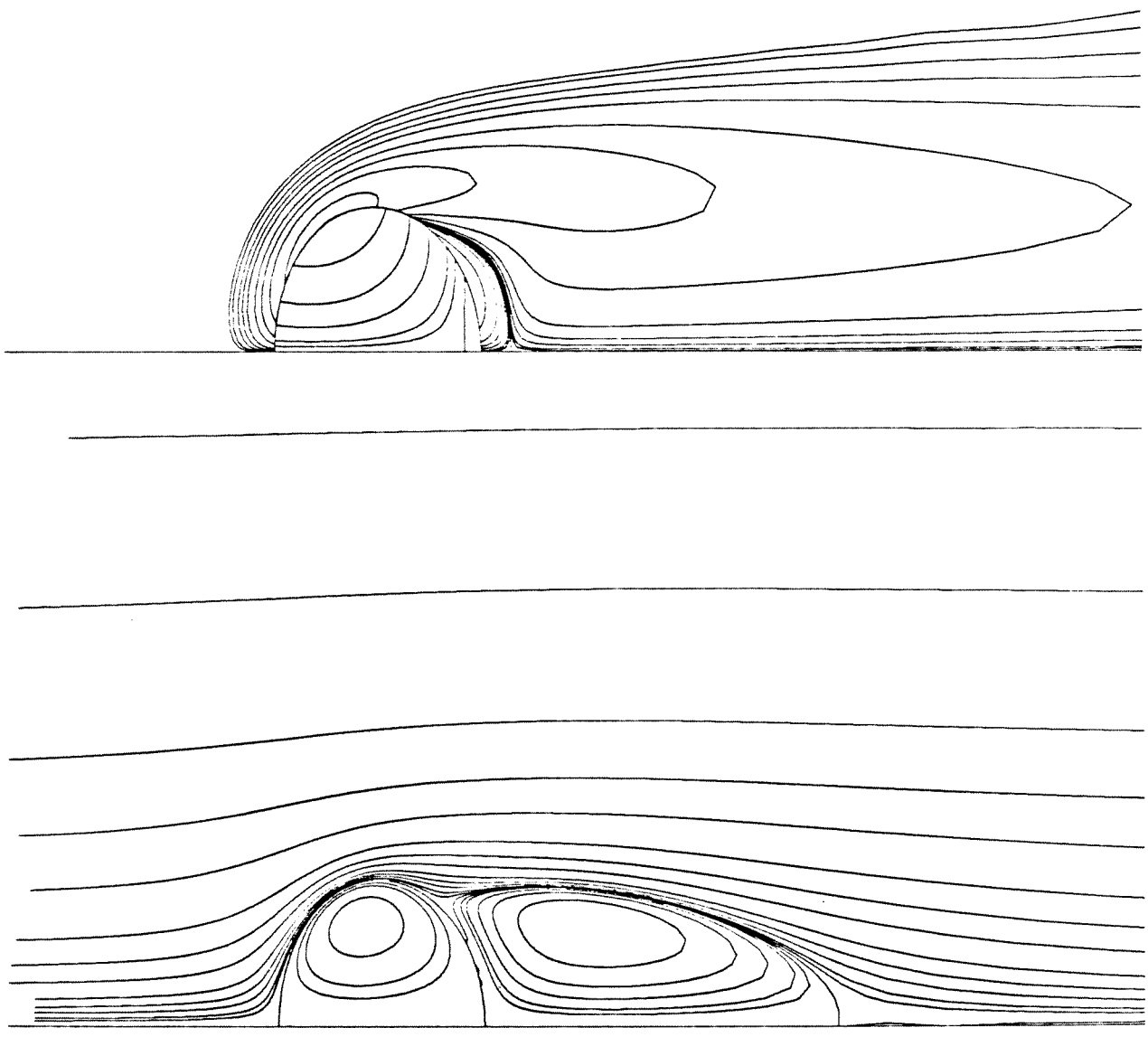

Re = 100 $\lambda = 50$

We = 4 $\zeta = 0.909$

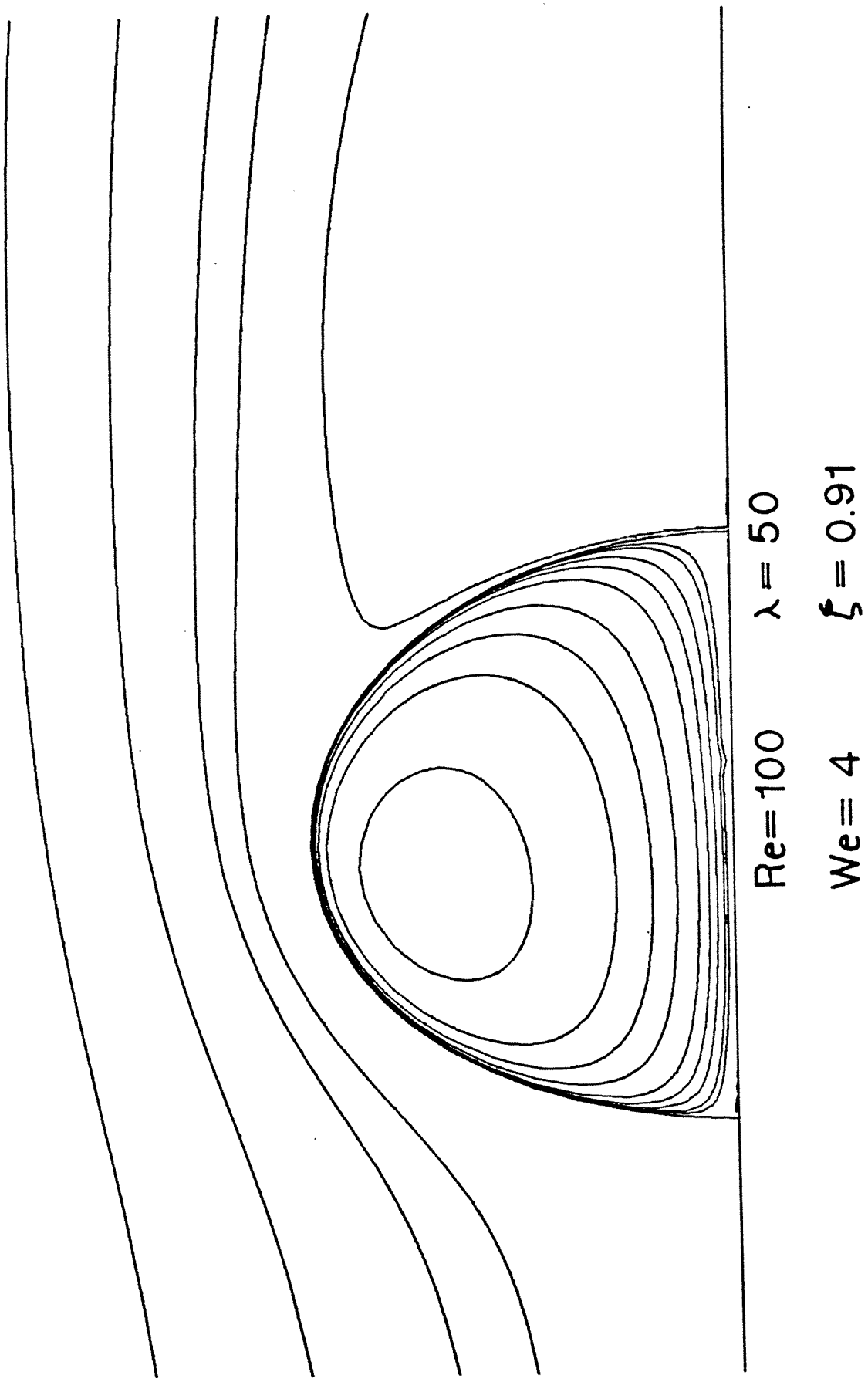
Re=100
λ = 50
We = 4
ξ = 0.91

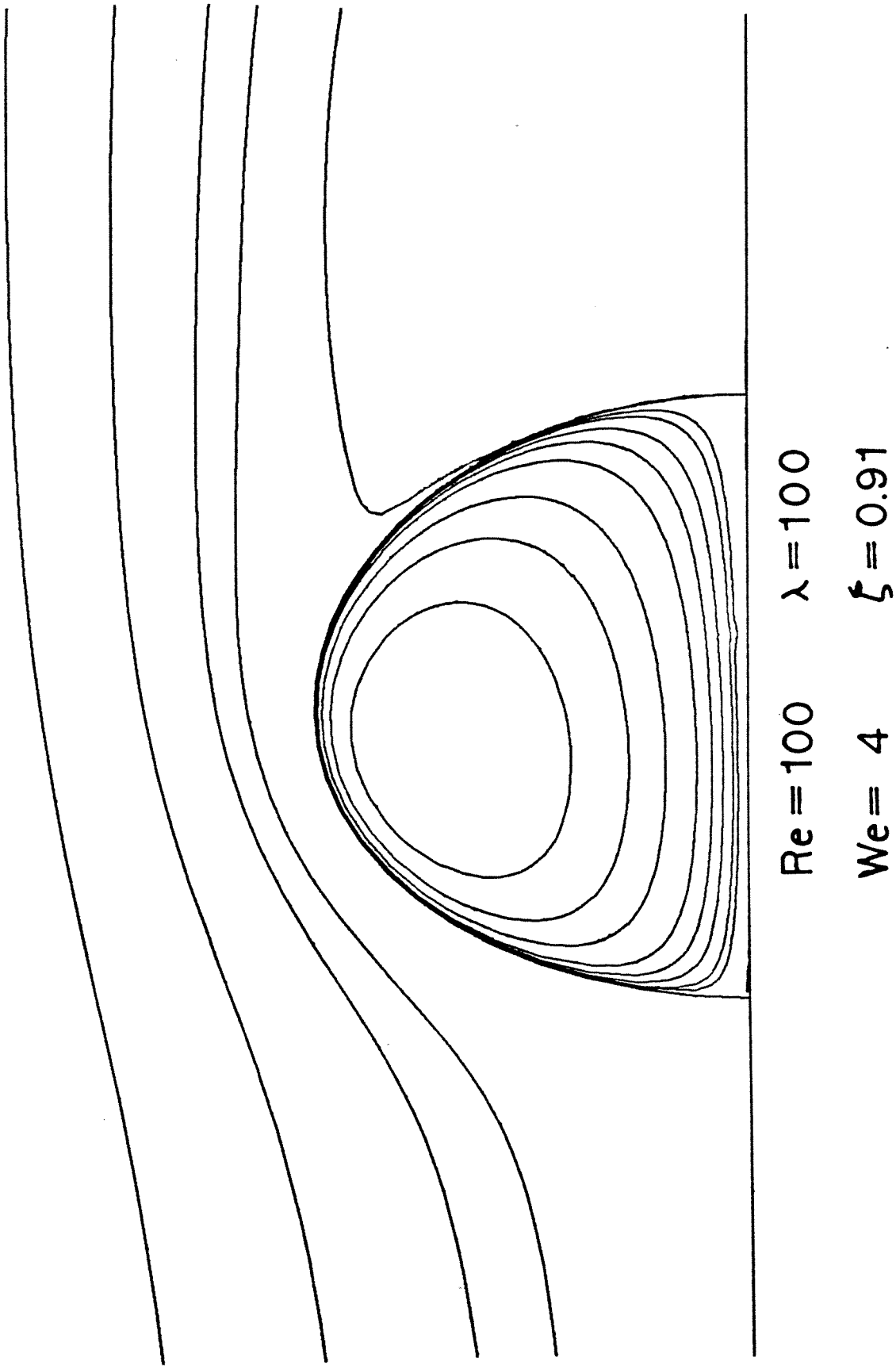
Re = 100
λ = 100
We = 4
ζ = 0.91

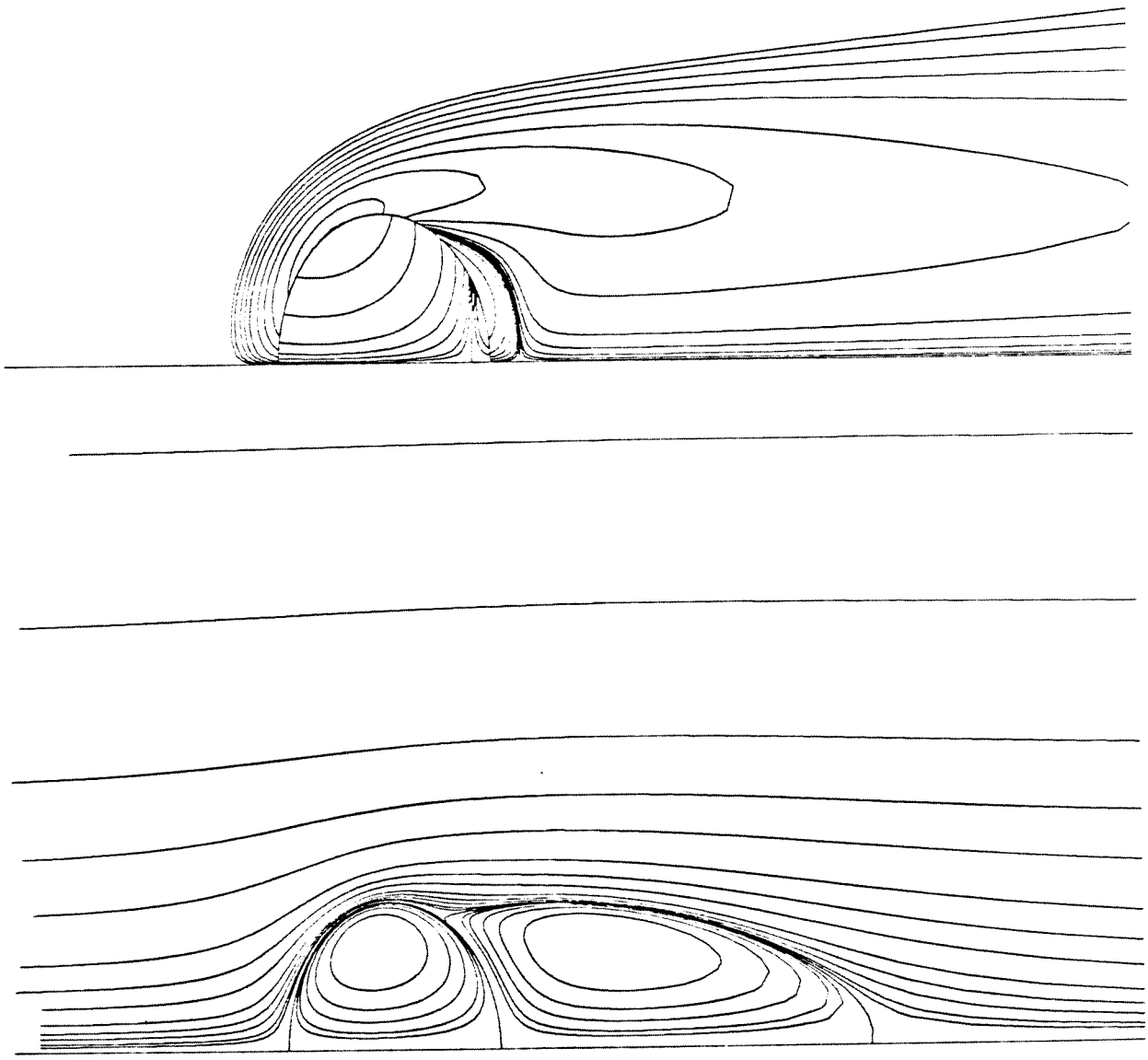

Re = 100 λ = 500

We = 4 ζ = 0.909

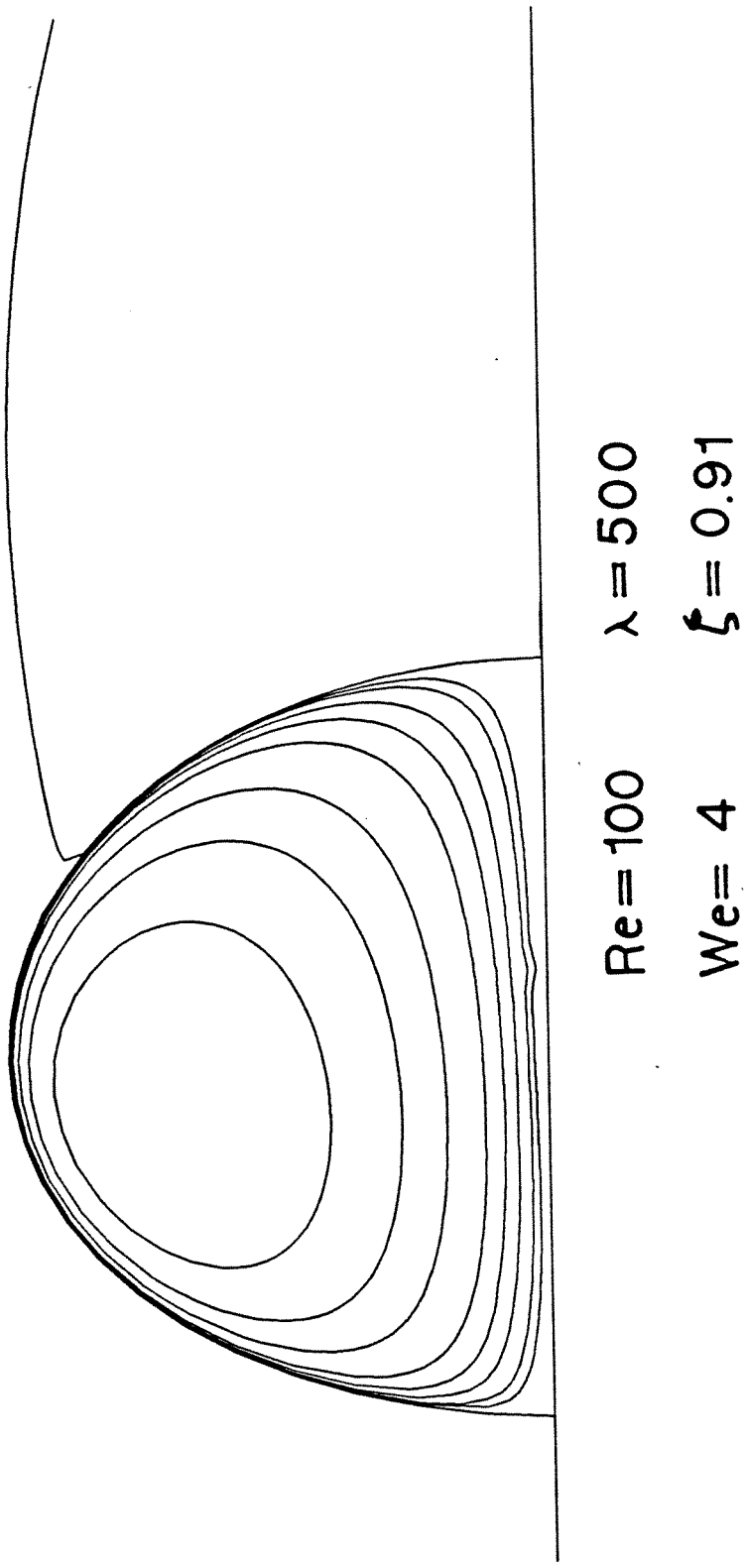
Re=100
We= 4
λ=500
ξ=0.91

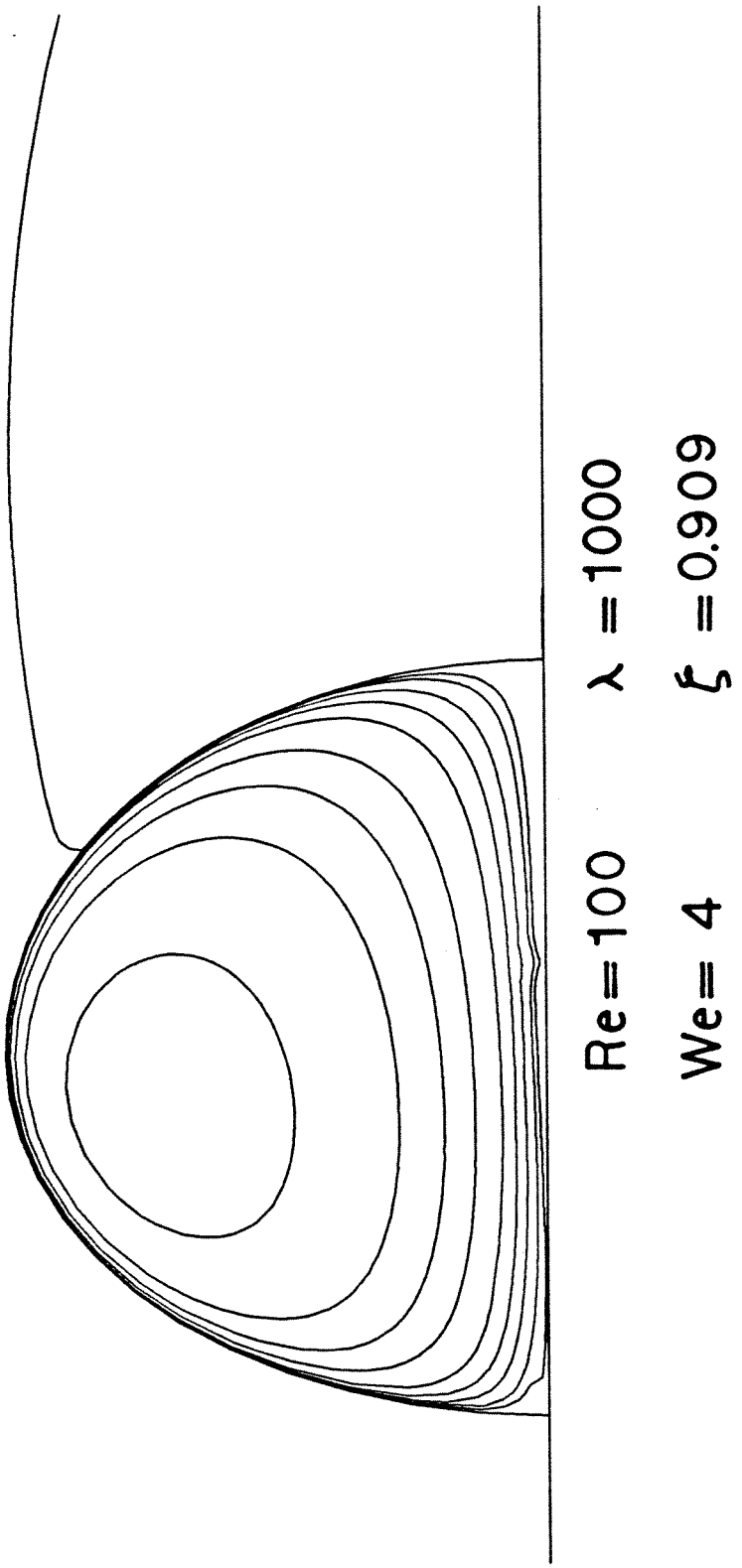
Re=100
We= 4
λ =1000
ξ =0.909

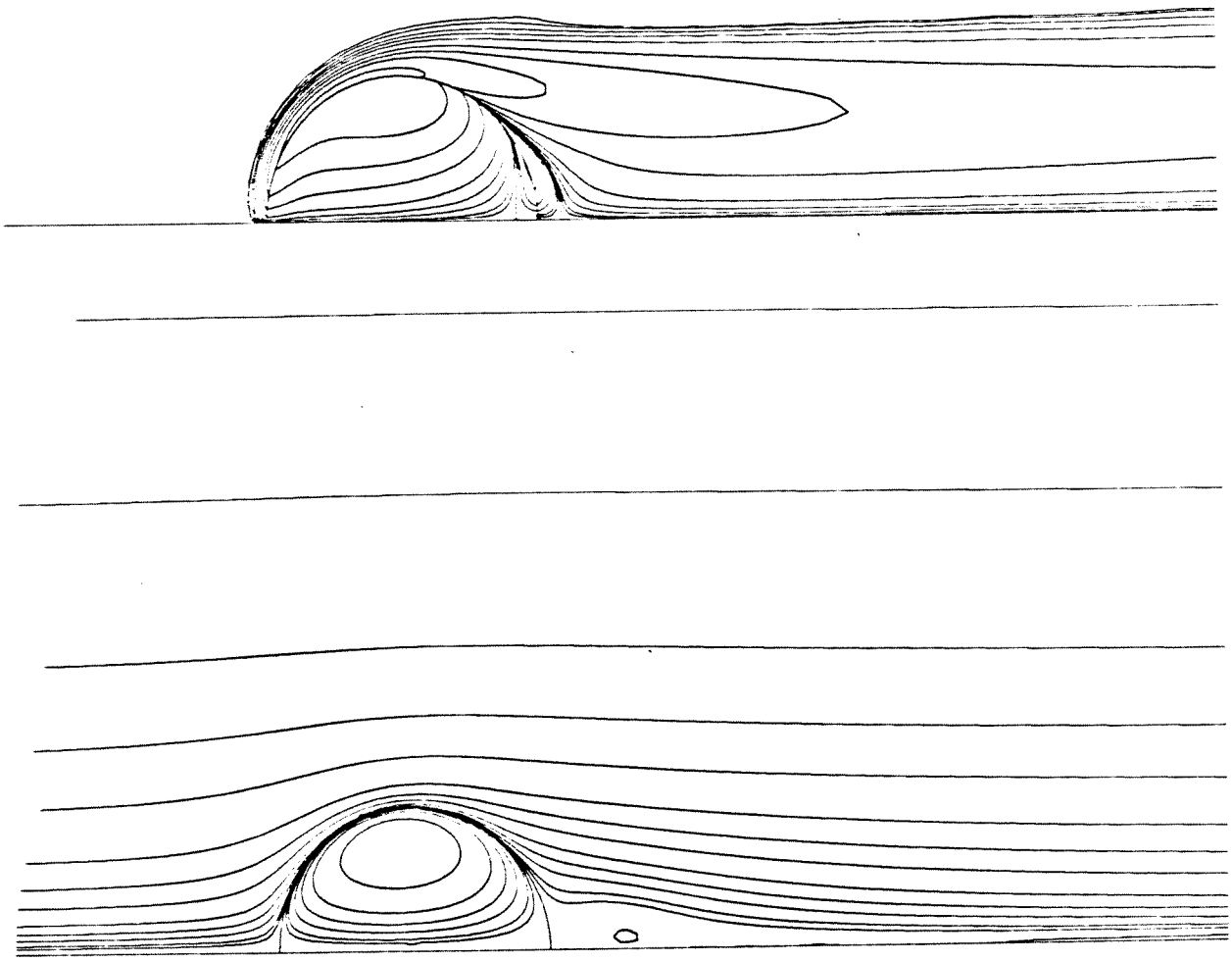

Re = 300 λ = 2.5

We = 1 ζ = 0.909

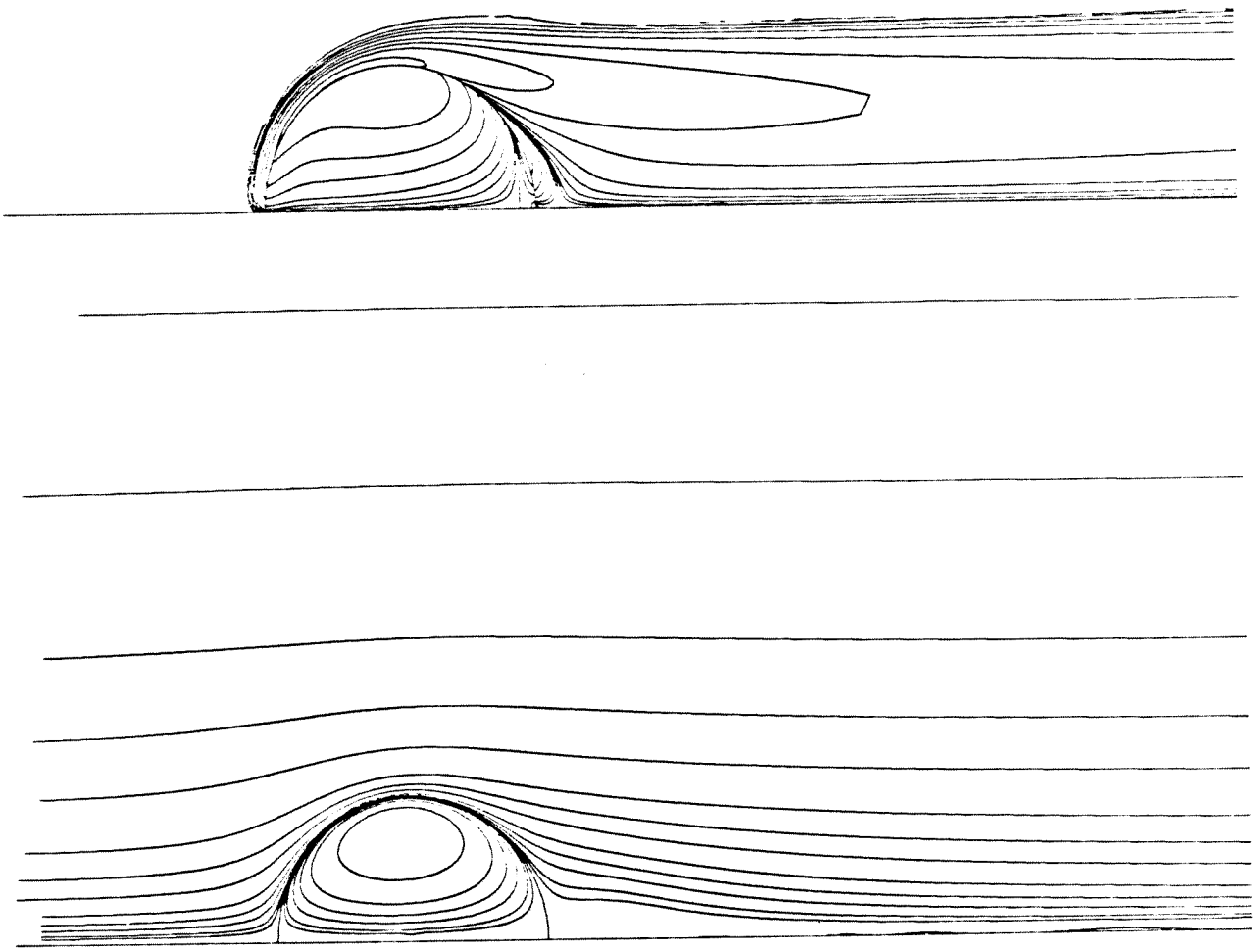

Re = 350 λ = 2.5

We = 1 ζ = 0.909

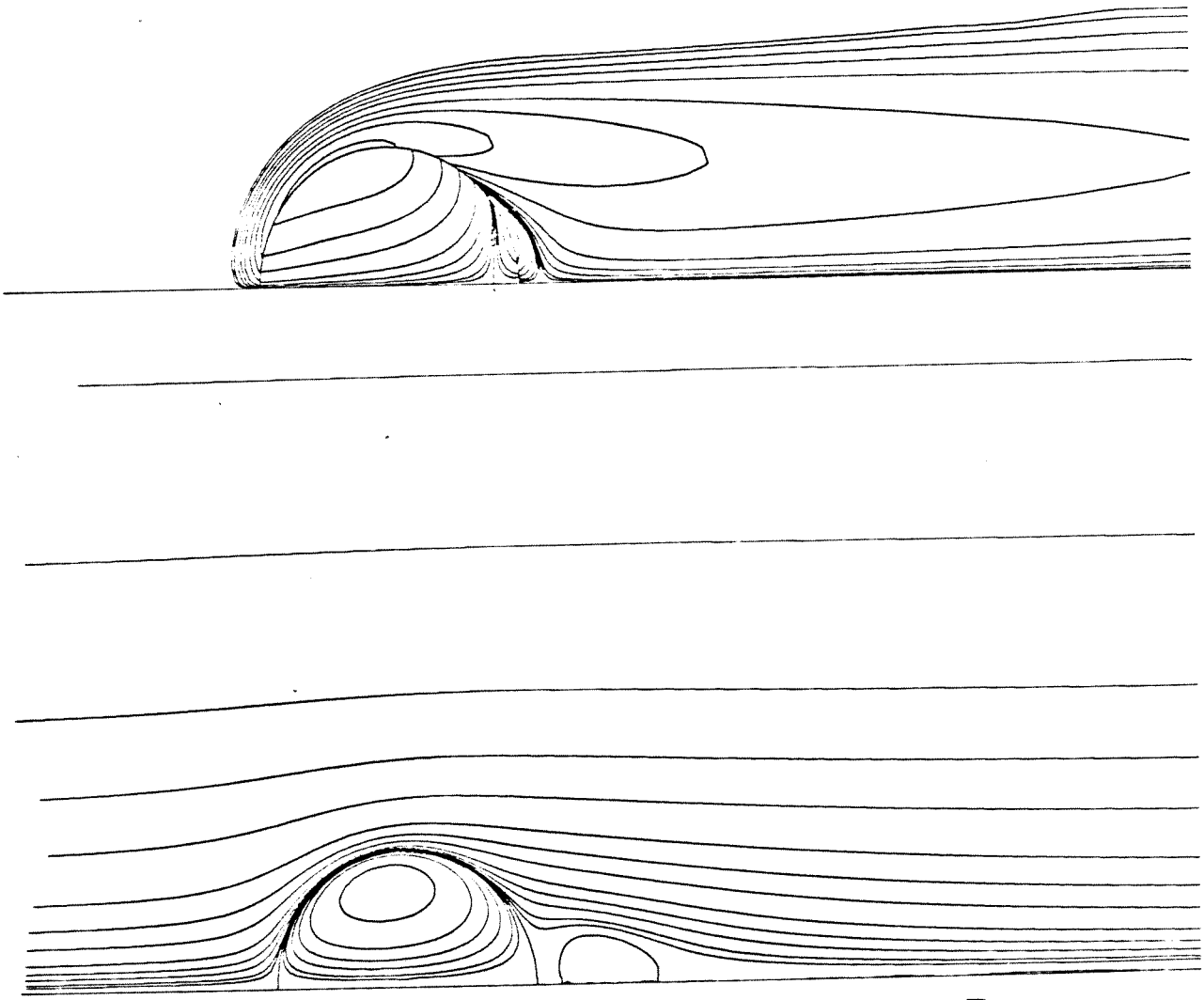

Re = 150 λ = 2.5

We = 1 ξ = 0.909

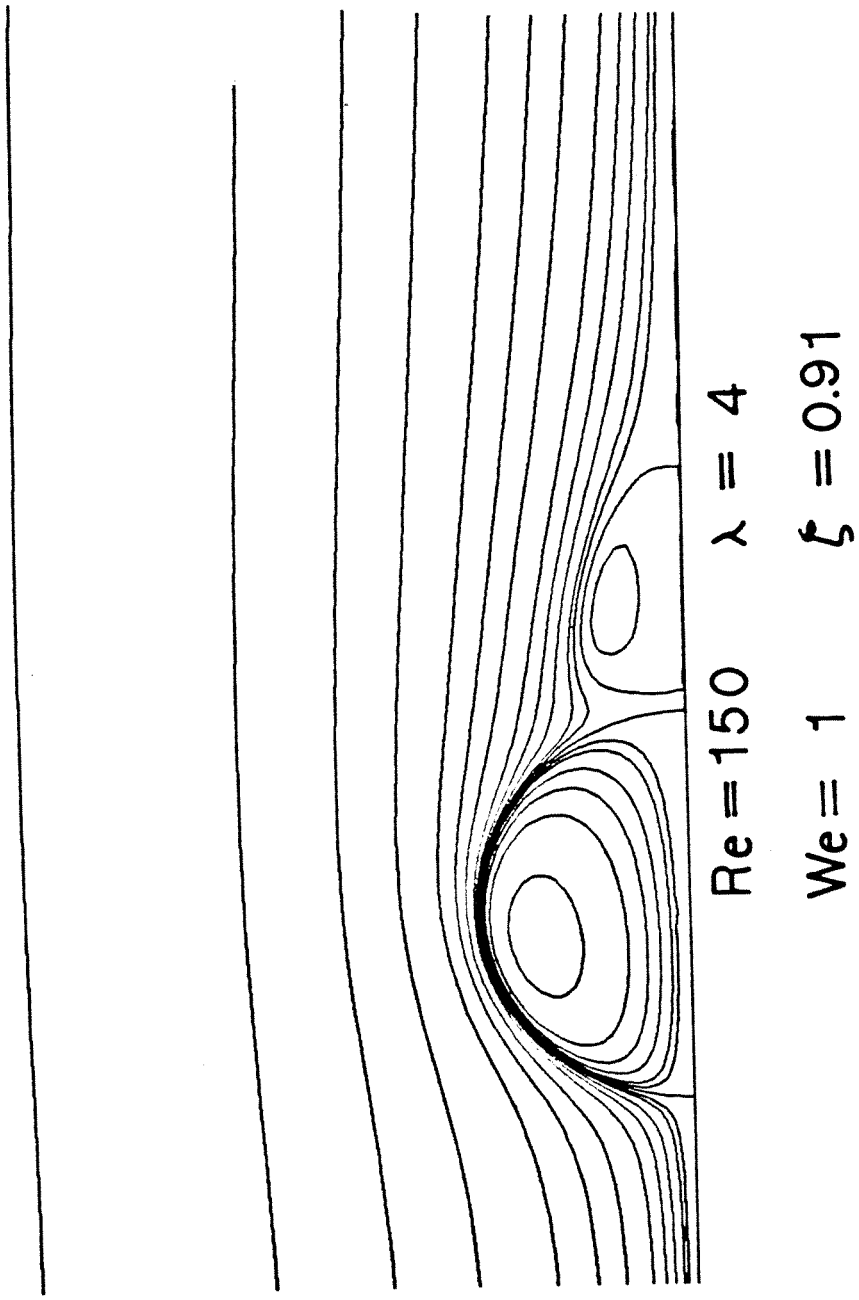
Re = 150 λ = 4
We = 1 ξ = 0.91

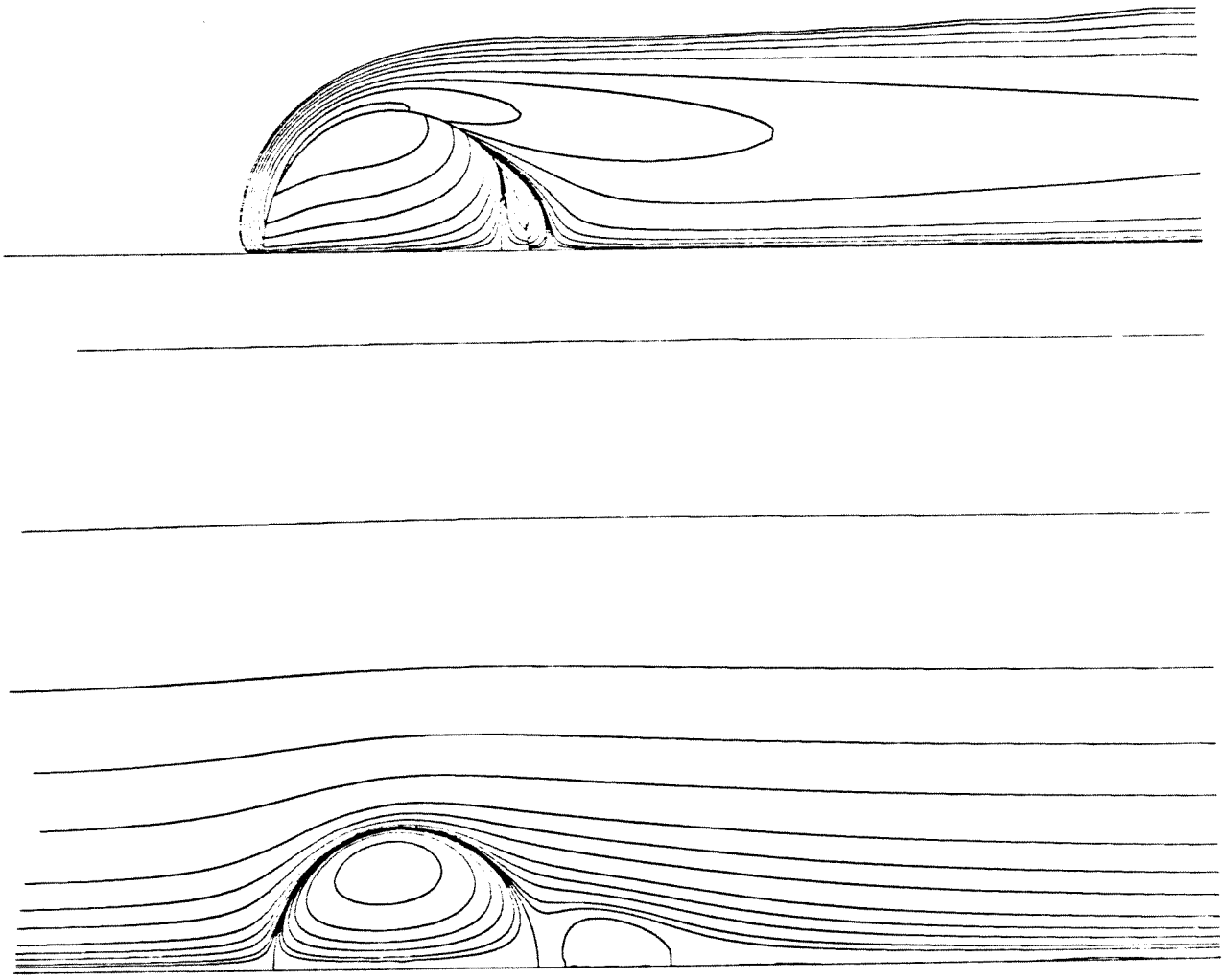

Re = 200 λ = 2.5

We = 1 ζ = 0.909

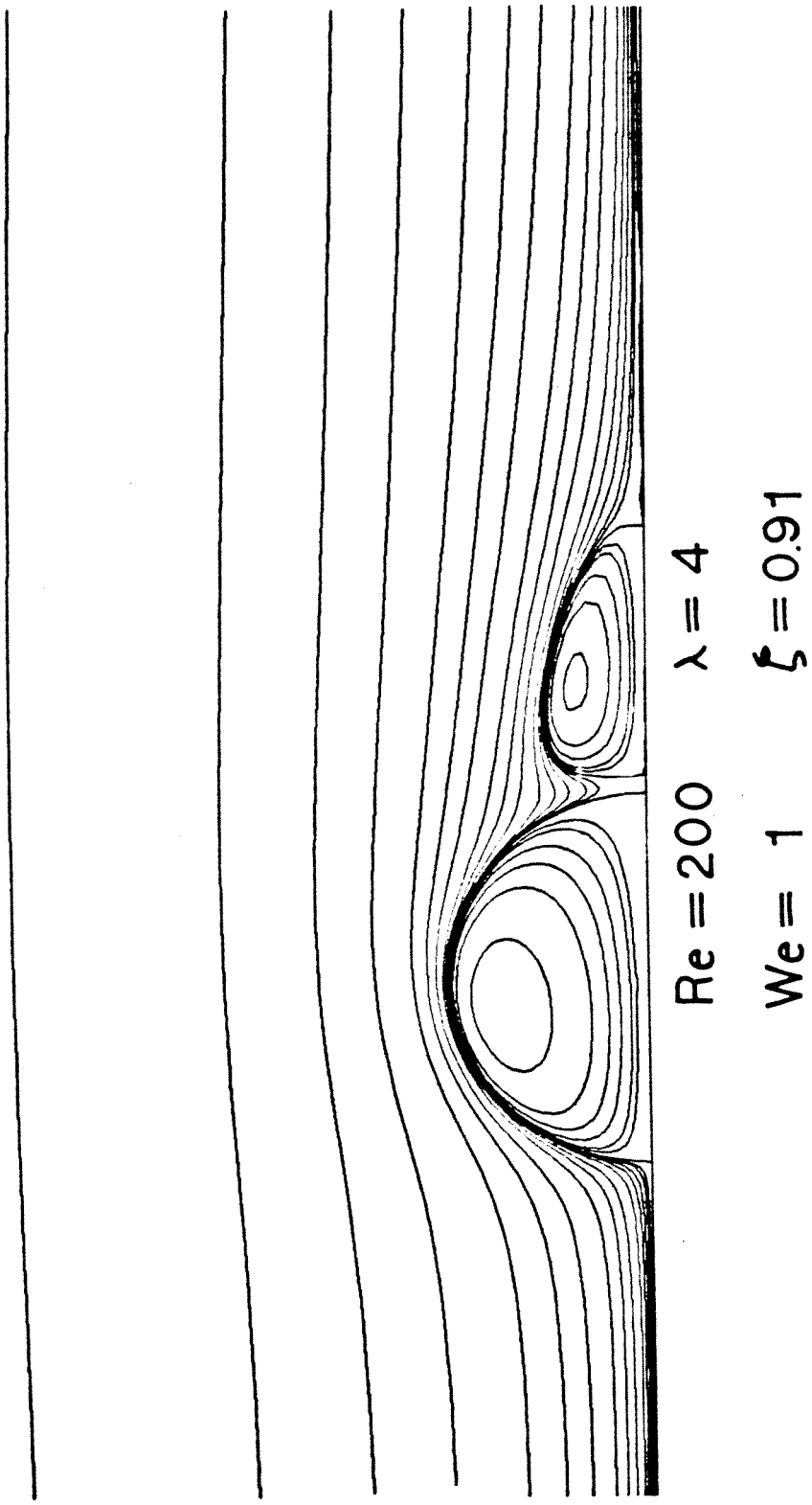
Re = 200 λ = 4
We = 1 ζ = 0.91

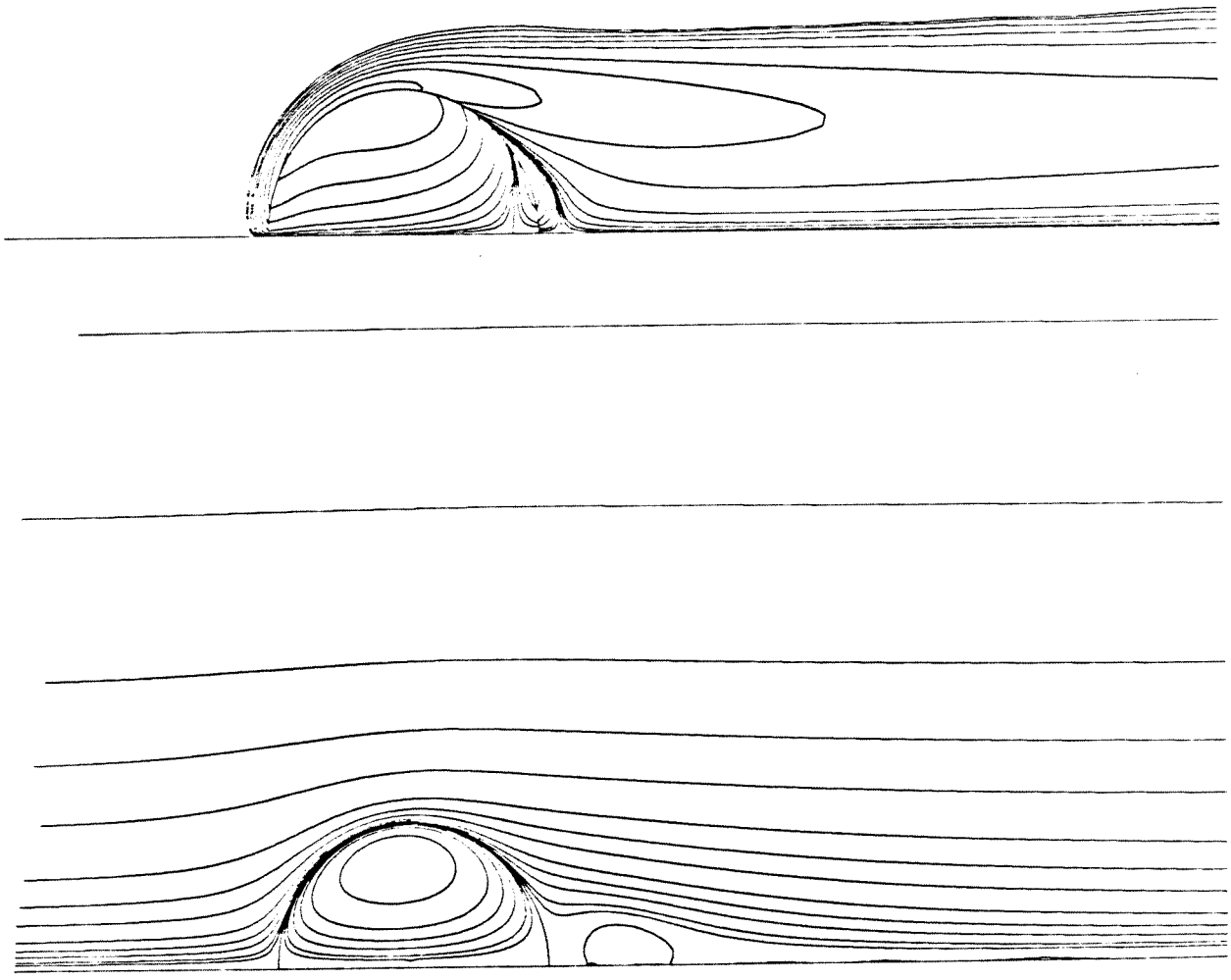

Re = 250 λ = 2.5

We = 1 ζ = 0.909

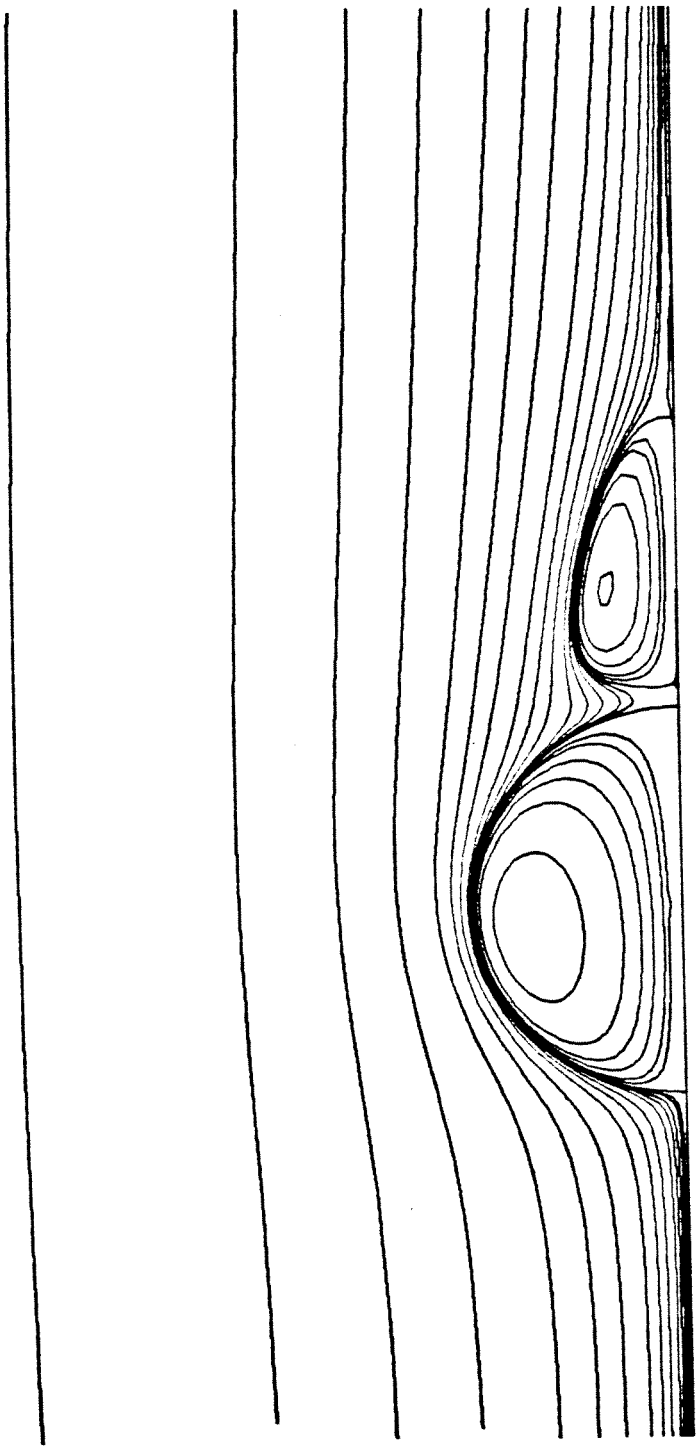
Re = 250 λ = 4
We = 1 ζ = 0.91

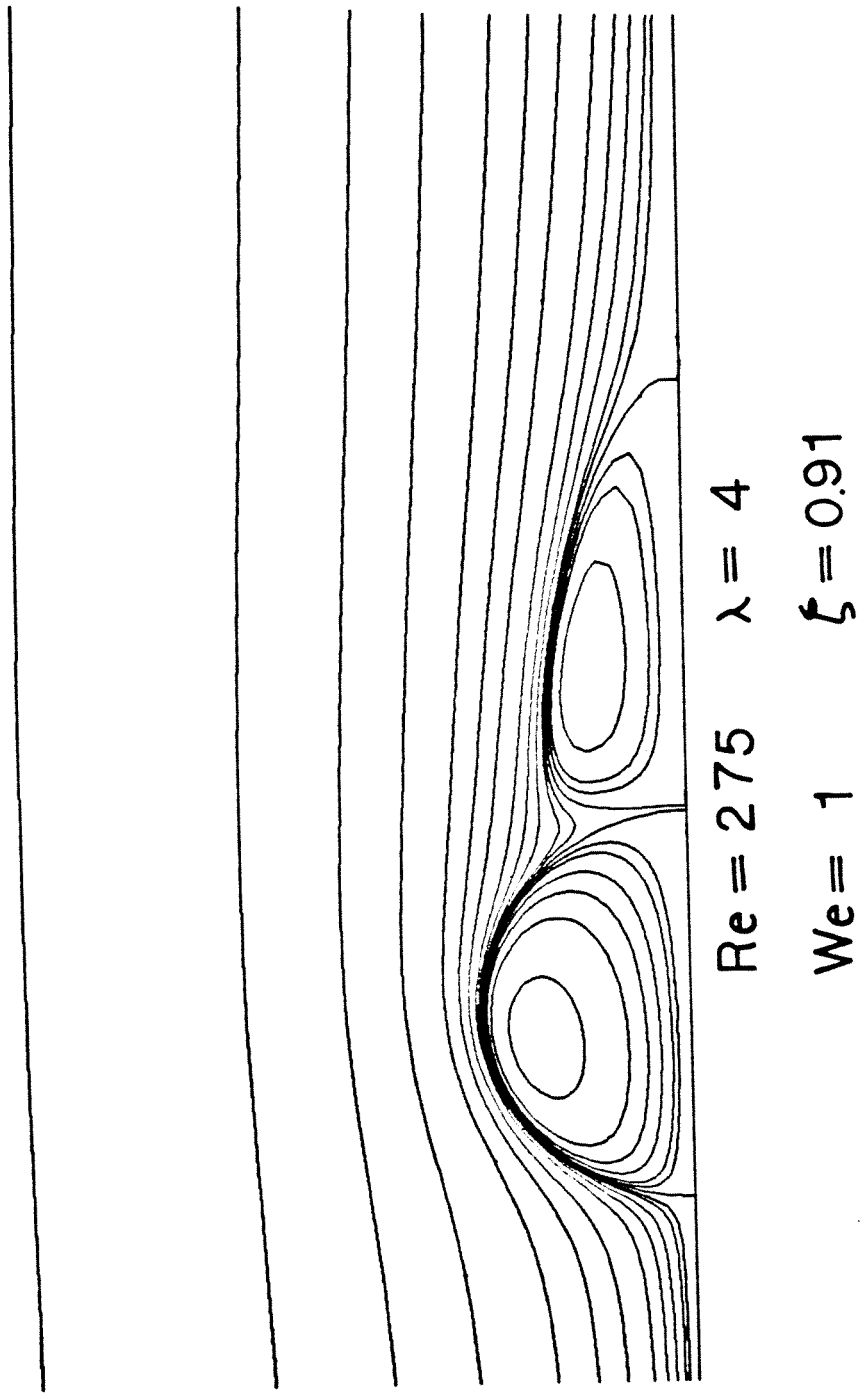
Re = 275 λ = 4
We = 1 ξ = 0.91

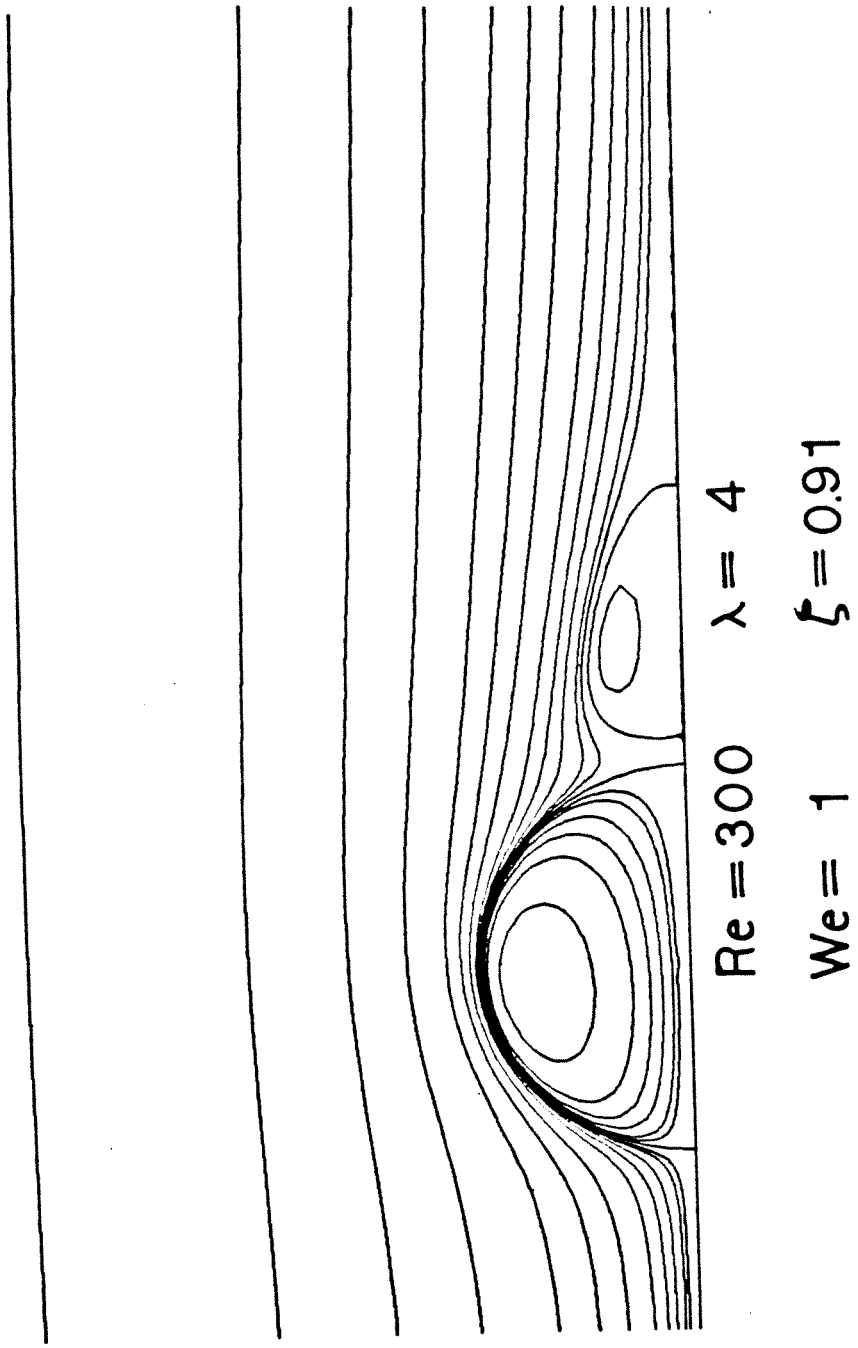
Re = 300
λ = 4
We = 1
ζ = 0.91

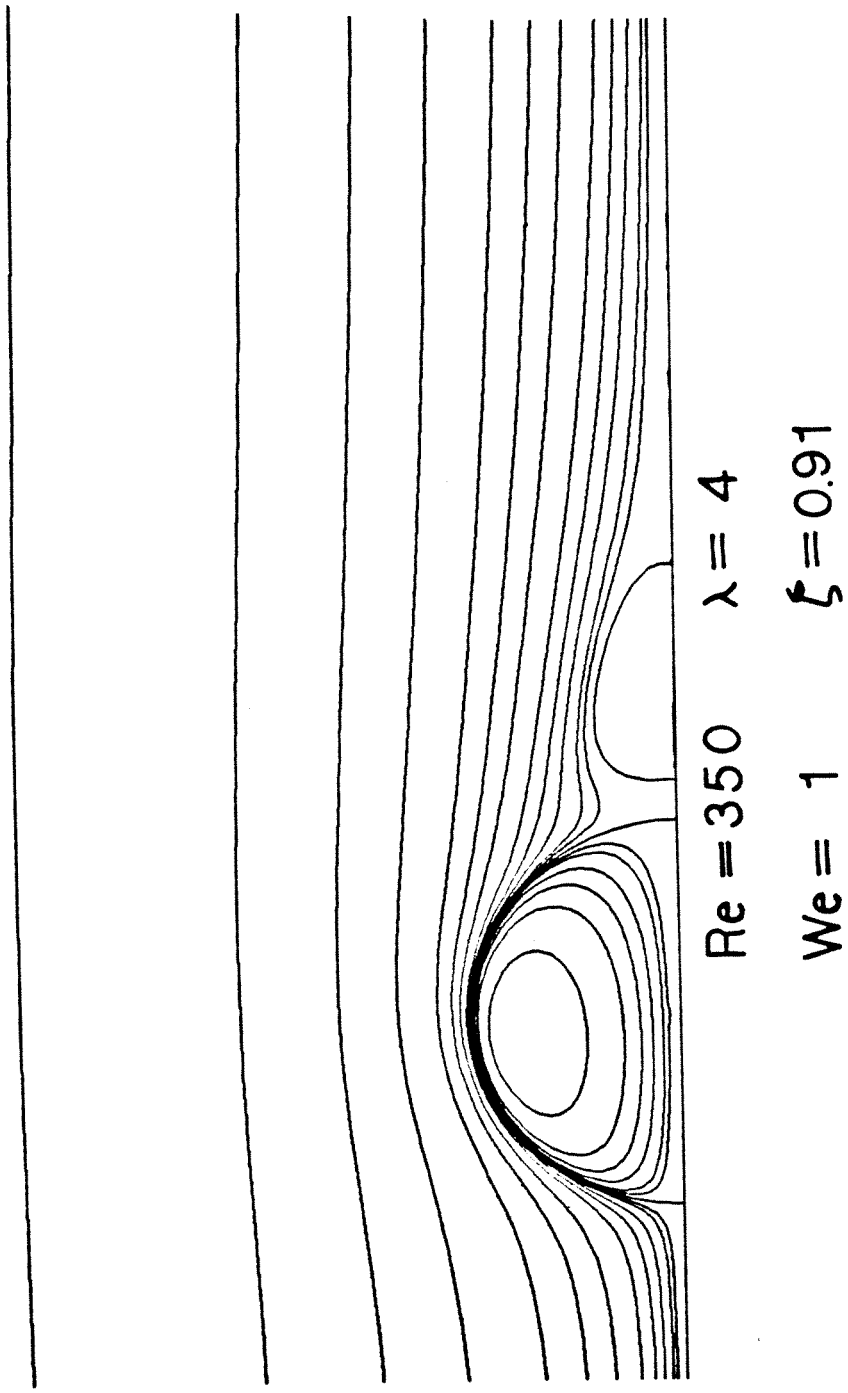
Re = 350 λ = 4
We = 1 ζ = 0.91

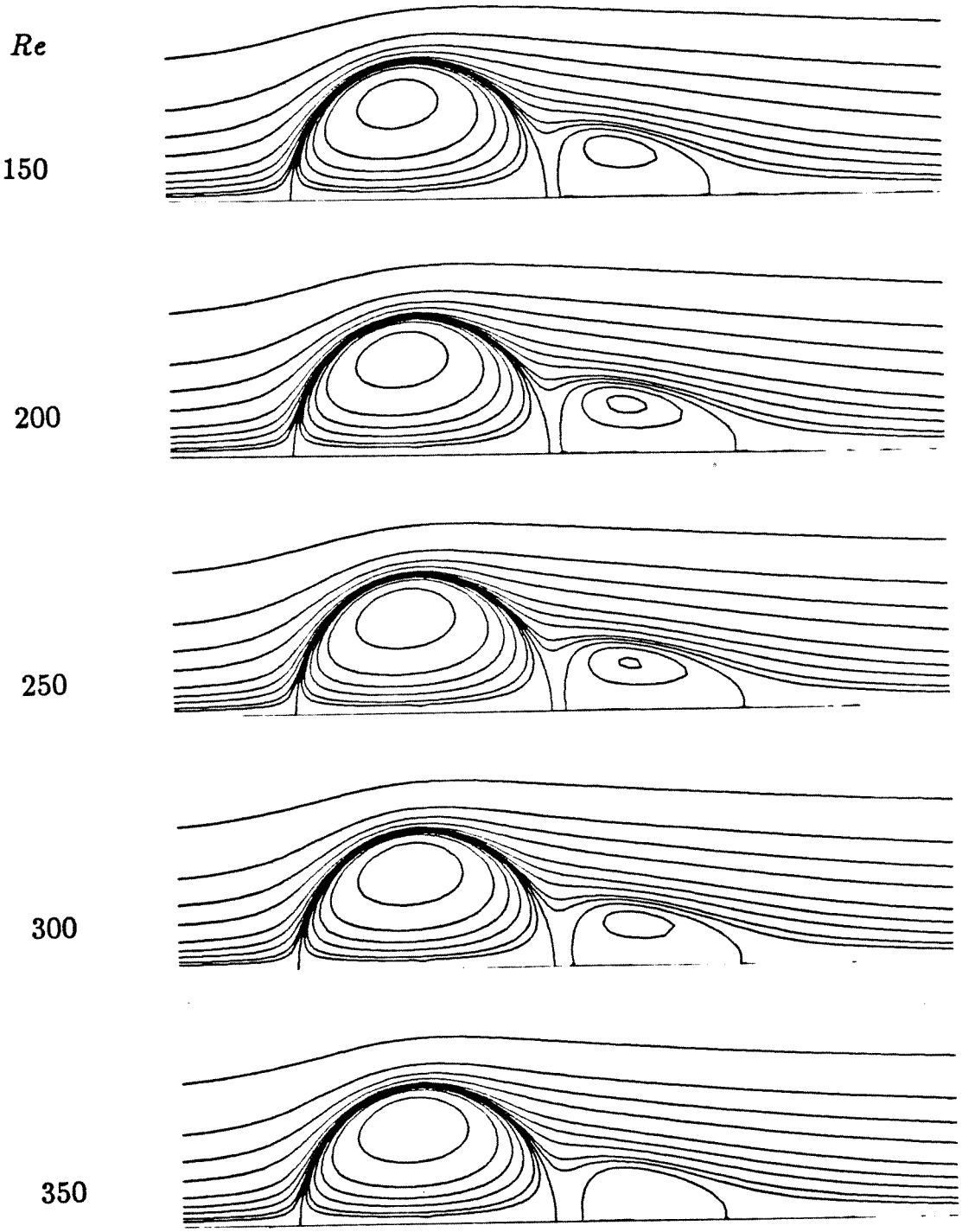

$We = 1$ $\varsigma = 0.91$ $\lambda = 3$

Chapter II

A Note on Boundary-Layer Separation From a Smooth Slip Surface

The text of Chapter II consists of an article which appears in *Physics of Fluids* **29** (1986).

A Note on Boundary-Layer Separation From a Smooth Slip Surface

by

D.S. Dandy and L.G. Leal

Department of Chemical Engineering
California Institute of Technology
Pasadena, California 91125

Abstract

Numerical results are presented for the streaming motion of an incompressible Newtonian fluid past axisymmetric ellipsoids of fixed shape, subject to the condition of zero tangential stress on the body surface. It is demonstrated that a substantial, closed-streamline wake appears behind the ellipsoid at moderate Reynolds numbers, $O(20-50)$, when the ellipsoid is sufficiently nonspherical, and that this wake initially increases in size with increase of Reynolds number, but then eventually decreases in size and disappears when the Reynolds number is sufficiently large, $O(200-250)$ in our cases. The existence of streaming flow past a smooth, slip surface without separation is consistent with predictions from laminar boundary layer theory. It is concluded that the recirculating wake that appears behind moderately deformed bubbles is strictly a finite Reynolds number phenomenon that cannot be predicted (or understood) via a boundary layer analysis.

I. Introduction

In the fluid mechanics literature, there are two quite distinct explanations for the existence of recirculating wakes behind nonstreamlined bodies at large Reynolds numbers, Re.

In the first explanation, the wake is viewed as being a consequence of vorticity accumulation at the rear of the body due to the asymmetry of vorticity transport, and its relative inefficiency in this region, at moderate to large Reynolds numbers. Boundary layer separation is then seen as a necessary consequence of the existence of the recirculating eddy. This view is intuitive if we study the time-dependent evolution of the wake structure when a nonstreamlined body, such as a sphere or circular cylinder, is impulsively started into motion from an initial state in which both the fluid and body are at rest[1].

In the second explanation, it is the breakdown and detachment of the boundary layer which is viewed as the primary event, and the presence of a recirculating wake is then accepted as being a consequence of this detachment. In this description, the presence of a no-slip condition at the boundary plays a critical role, providing a mechanism along with viscosity for decreasing the momentum of a fluid element near the boundary (relative to what it would have in the absence of viscosity) so that its tangential motion can be completely arrested (and thus the boundary layer become detached) when it encounters a region of increasing pressure. Although this second explanation for the existence of the recirculating wake is based upon boundary layer theory, and thus strictly applies only in the asymptotic limit of infinite Reynolds number, its relevance to real flows at *finite* Reynolds number would seem to be strongly supported by the fact that boundary layer theory yields predictions for separation[2], including the position of the separation point, which are in good qualitative agreement with experimental observation for solid bodies such as a sphere or circular cylinder, in spite of the fact that the observations are inevitably made at finite (and usually even quite moderate, $O(10-100)$), values of the Reynolds number.

This apparently straightforward connection between experimental observations at finite Re, and predictions from boundary layer theory ($Re \longrightarrow \infty$) appears somewhat less obvious, however, when we consider experimental and theoretical results for single gas bubbles rising through a quiescent fluid. Numerous experimental studies of this problem have shown that a stable recirculating wake exists, provided that Re is sufficiently large (but finite) and the surface tension γ is small enough to allow significant deformation[3–5]. However, we have already noted that the breakdown and detachment of a boundary layer is critically dependent upon the presence of a no-slip boundary at the body surface. Indeed, a theoretical boundary layer analysis of Moore[6–8] for motion of either a spherical or an oblate spheroidal bubble in the asymptotic limit $Re \longrightarrow \infty$, shows that there is no flow detachment in these cases except possibly at the rear stagnation point on the bubble surface. Further, Moore's analysis can be extended to a bubble of arbitrary but smooth shape with the same result. As a consequence, there has been some reluctance to accept the experimental observations for bubbles as evidence that separation can occur at a smooth slip boundary. Instead, it was suggested that the interface could have been contaminated with surfactant, so that at least a partial transition toward no-slip conditions was effected.

Recently, however, Ryskin & Leal[9] carried out a detailed numerical study of bubble motion at intermediate Reynolds numbers and Weber numbers, We. Their study included a determination of the bubble shape, using the full Navier-Stokes equations and the boundary condition of zero tangential stress that applies if the bubble surface is uncontaminated. Ryskin & Leal's[9] solutions again showed the existence of attached recirculating wakes for steady, axisymmetric bubbles when $Re \gtrsim 10$ and $2 \lesssim We \lesssim 20$. Furthermore, comparision of the numerical solution for $Re = 20$, $We = 15$ with a shadowgraph picture for $Re = 19.4$, $We = 15.3$ (see Ref. 5) showed nearly perfect quantitative agreement for the geometry of the bubble and the recirculating wake, as well as

excellent qualitative agreement between the calculated streamline pattern in the wake and the lines of constant refractive index visible in Hnat & Buckmaster's photograph[5].

Thus, it must now be accepted that both numerical and experimental studies show unequivocable evidence for the existence of recirculating wakes behind clean, uncontaminated bubbles at finite Re. In view of the fact that boundary layer theory predicts no separation for bubbles of any smooth shape (finite curvature), we can only conclude that the presence of a recirculating wake in the case of a bubble is a finite Reynolds number phenomenon for which boundary layer theory provides no insight. Furthermore, the mechanism for existence of the wake must be vorticity accumulation since spontaneous breakdown of a boundary layer, leading to detachment and thus a wake, cannot occur at a smooth, slip surface.

There is, of course, nothing paradoxical about this view – one would not generally expect an asymptotic theory for $Re \longrightarrow \infty$ to provide insight into flow behavior at moderate Reynolds numbers of $O(10-200)$. The lack of qualitative agreement between boundary layer predictions and actual flow behavior in the present context, however, is still somewhat of a surprise because of the apparently excellent agreement between boundary layer predictions and separation phenomena in similar flows past no-slip bodies at comparable Reynolds numbers.

In particular, it is evident that the existence of a recirculating wake for a bubble at finite Reynolds number has nothing to do with the physics of true boundary layer separation, but is instead a consequence of vorticity accumulation in the wake region.

Of course, it remains to be established that the flow past a bubble does become consistent with the boundary layer prediction of no separation when Re becomes sufficiently large. This was not possible in the work of Ryskin & Leal[9] because of the fact that the bubble shape, and thus the local curvature of the

bubble, continued to change up to the maximum Reynolds numbers that could be achieved. Therefore, the rate of vorticity production at the surface (due to curvature) increased right along with the ability of the flow to convect the vorticity away, with the result that no asymptotic behavior could be observed.

In the present paper, we explore further the structure of the recirculating wake behind axisymmetric bodies on which a zero tangential shear stress condition is imposed as a boundary condition. We consider solutions of the full Navier-Stokes equations as a function of Re for axisymmetric oblate ellipsoids of *fixed* shape. By doing this, the Reynolds number dependence of the vorticity transport mechanism is effectively decoupled from the dependence of the surface curvature and surface vorticity on the same parameter. In this case we show that the finite sized recirculating wake which exists behind a "slip" body of sufficient curvature at finite Re, will actually decrease in size and even disappear for larger values of Reynolds number when the boundary shape is fixed, thus giving evidence of approach to an asymptotic state that is consistent with boundary layer theory for $Re \longrightarrow \infty$. We choose oblate spheroids with a sufficient ratio of the major to minor axes to insure that a finite recirculating wake does appear, but not so large that some evidence of an approach to the $Re \longrightarrow \infty$ asymptote cannot be achieved in the range of Reynolds numbers (say, $Re \lesssim 300$) that is readily accessible to numerical computation. We demonstrate that a finite recirculating wake can appear behind a slip body of fixed shape at large, but finite Re, which has nothing to do with boundary layer separation in the usual sense. By doing this, we also lend further credence to the concept of vorticity accumulation as a mechanism for the existence of recirculating wakes at finite Re. We do not suggest that a real bubble will necessarily follow a similar trend in which the recirculating wake eventually diminshes in size and vanishes for sufficiently high Reynolds numbers. We believe that this would be the case if the bubble approached a fixed, asymptotic shape with finite curvature as $Re \longrightarrow \infty$, because the maximum vorticity at its surface would then approach a finite fixed value

in the same limit. However, we cannot rule out the possibility that the surface curvature of a bubble would continue to increase for arbitrarily large Re in such a way that sufficient boundary vorticity is generated to maintain a finite wake even in the limit $Re \longrightarrow \infty$.

II. Flow past a slip body at intermediate Reynolds number

We thus consider the streaming motion of a viscous incompressible, Newtonian fluid past an axisymmetric body whose shape is fixed, but on whose surface the condition of zero tangential shear stress is imposed. The fluid surrounding the body is characterized by the constant viscosity μ and density ρ. For our purposes the body must be smooth, but with enough curvature that a recirculating wake is achieved at moderate Re. For simplicity, an oblate ellipsoid has been chosen with major and minor axes $2b$ and $2a$, respectively (it has been observed both numerically[9] and experimentally[10] that a real gas bubble will be roughly ellipsoidal if $Re = O(10 - 100)$ and $Eo = O(1 - 10)$, where $Eo = \rho g b^2/\gamma$, γ being the surface tension). The geometry of the system is shown in Fig. 1. The dependence of the wake structure on Re will be examined for fixed axis ratio $\varsigma = b/a$.

To nondimensionalize the equations of motion, we use b as the characteristic length, U_∞ as the velocity scale, and $\frac{1}{2}\rho U_\infty^2$ as the appropriate pressure scale. The Reynolds number is then defined as $Re = 2\rho b U_\infty/\mu$. With the body shape specified, the method developed by Ryskin & Leal[11] was used to numerically generate an orthogonal boundary-fitted coordinate system (ξ, η). The reasons for using this numerically generated coordinate system will be discussed shortly. In this curvilinear coordinate system, the nondimensional equations of motion written in terms of the streamfunction ψ, and vorticity ω, are

$$\mathcal{L}^2(\omega\sigma) - \frac{1}{2}\frac{Re}{h_\xi h_\eta}\left[\frac{u_\xi}{h_\xi}\frac{\partial}{\partial\xi}\left(\frac{\omega}{\sigma}\right) + \frac{u_\eta}{h_\eta}\frac{\partial}{\partial\eta}\left(\frac{\omega}{\sigma}\right)\right] = 0 \tag{1}$$

and

$$\mathcal{L}^2\psi + \omega = 0, \tag{2}$$

where

$$\mathcal{L}^2 \equiv \frac{1}{h_\xi h_\eta}\left[\frac{\partial}{\partial\xi}\left(\frac{f}{\sigma}\frac{\partial}{\partial\xi}\right) + \frac{\partial}{\partial\eta}\left(\frac{1}{f\sigma}\frac{\partial}{\partial\eta}\right)\right]. \tag{3}$$

Here, the velocity components are

$$u_\xi = -\frac{1}{\sigma h_\eta}\frac{\partial \psi}{\partial \eta}$$
$$u_\eta = \frac{1}{\sigma h_\xi}\frac{\partial \psi}{\partial \xi} \tag{4}$$

while the scale factors of the coordinate system are

$$h_\xi = \left[\left(\frac{\partial z}{\partial \xi}\right)^2 + \left(\frac{\partial \sigma}{\partial \xi}\right)^2\right]^{\frac{1}{2}}$$
$$h_\eta = \left[\left(\frac{\partial z}{\partial \eta}\right)^2 + \left(\frac{\partial \sigma}{\partial \eta}\right)^2\right]^{\frac{1}{2}} \tag{5}$$

and the ratio of scale factors is denoted as

$$f = \frac{h_\eta}{h_\xi}. \tag{6}$$

There are two difficulties which arise in attempting to solve a flow problem such as this in an unbounded domain. The first is that it is not possible to numerically produce coordinate transformation functions $z(\xi,\eta)$ and $\sigma(\xi,\eta)$ which reach infinite values. The second is that at large distances from the body the velocity asymptotically approaches the streaming flow form $\psi \sim \frac{1}{2}\sigma^2$. To remove this singularity in the streamfunction we define a modified streamfunction by subtracting off a function which has the same asymptotic behavior at large distances and satisfies homogenous conditions at the other three boundaries. The modified streamfunction is $\psi^* = \psi - \frac{1}{2}\sigma^2(1-\xi^3)$. The subtracted term is the potential flow solution for a spherical bubble, but it has no simple physical meaning for an ellipse. From the Oseen solution[12] we know that ψ^* is bounded at infinity, and because this point is a singular point of the differential equation, boundedness is a sufficient condition for solution[13].

To reduce the infinite physical domain to a finite computational region we used the following procedure: a conformal mapping was used to transform the infinite (z,σ) domain to an auxiliary finite domain (z^*,σ^*), followed by a

numerically generated orthogonal mapping from the auxiliary domain to a unit square in the (ξ, η) domain. The conformal mapping we employed was $z + i\,\sigma = (z^* - i\,\sigma^*)^{-1}$; the point $z^* = \sigma^* = 0$ corresponds to infinity in the z, σ-plane. The alternative of course, is to simply truncate the (z, σ) domain at some distance from the body. However, Grosch & Orszag[14] compared solutions obtained using coordinate inversion to those obtained via domain truncation for a variety of unbounded domain problems, including Burger's equation, and concluded that mapping is often better. In particular, it will yield more accurate solutions than those obtained with truncation, provided that the solution being sought vanishes rapidly or approaches constant values at infinity. In addition, they found that if a mapping is used, an algebraic mapping of the infinite region onto a finite domain works better than a logarithmic map.

Once the physical domain has been mapped onto the (z^*, σ^*) auxiliary domain, the resulting body is prolate spheroidal, with the origin corresponding to infinity in the physical domain. It is unfortunately impossible to use a prolate spheroidal coordinate system due to the fact that the origin in our domain is a point, while it is a line segment lying on the z^*-axis in prolate spheroidal coordinates. Thus, as indicated earlier, we use a numerically generated, orthogonal and boundary-fitted coordinate grid. One advantage of this approach is that it is very easy to control the grid densities at different points in the domain through proper choice of the distortion function f. In general, there is also the advantage that one is not restricted to a body shape that corresponds to a coordinate line of some analytical coordinate system.

The problem of determining the correct numerical boundary condition for the streamfunction at infinity is usually a serious one. Physically, we know what its asymptotic form should be but experience (e.g., see Ref. 15) has shown that the numerical implementation of any condition on a truncated domain requires a lot of experimentation. However, the coordinate transformation is just a different analytical representation of the infinite domain, and in this case we

generally replace the condition at infinity by a boundedness condition on ψ^* at $\xi = 0$. Due to the differencing scheme we used, along with the use of the conformal mapping and a uniform (ξ, η) grid, the value of the coefficient multiplying $\psi^*(0, \eta)$ in the difference equations approximating Eq. (2) is on the order of the square of the mesh size, or 10^{-4}. For a spherical shape the coefficient is identically zero. Therefore, as long as $\psi^*(0, \eta)$ is finite, it does not contribute to the solution of $\psi^*(\xi, \eta)$. Computationally, $\psi^*(0, \eta)$ need only be an $O(1)$ constant, and for simplicity we chose zero. To verify that the value of $\psi^*(0, \eta)$ did not affect the solutions, we made two special runs for an elliptical shape ($\varsigma = 1.48$), one at $Re = 50$ and one at $Re = 200$, with the infinity boundary condition $\psi^*(0, \eta) = 5$. Although the value of $\psi^*(0, \eta)$ does not appreciably affect Eq. (2), we know that $\psi^*(0, \eta)$ does enter the finite difference representation of Eq. (1) through the velocity u_η, so it is important to make sure that the steady state values of $\psi^*(\xi, \eta)$ and $\omega(\xi, \eta)$ are independent of the choice of $\psi^*(0, \eta)$. For both cases ψ^* was unchanged (to within the order of the method) from the results obtained with the original boundary condition, and the most that ω varied was less than $\frac{1}{2}\%$, and this occurred in the region far downstream of the body. Also, as pointed out by Fornberg[15], any errors in the vorticity far downstream of the body decrease exponentially in the upwind direction. That is, an $O(1)$ error in the downstream vorticity boundary condition should not propagate upstream towards the body. Indeed, we found that in imposing the condition $\omega(0, \eta) = 0$, the values of vorticity in the region far downstream of the body were always less than 3% of the maximum surface vorticity.

To solve the equations of motion subject to the above boundary conditions, a ficticious time dependence was imbedded into the equations and the implicit alternating-direction method of Peacemann & Rachford[16] used. This method is stable, it converges rather quickly, and it works well when boundary conditions are not known explicitly. The partial derivatives in the equations were approxi-

mated by second order accurate, centered finite differences. Since the goal was to find steady state solutions to Eqs. (1) and (2), each time step was treated as an iteration and thus the two equations were separated and solved successively at each iteration. The grid size used was 61x61; the reason for this choice will be discussed in §4.

All calculations were done on a FPS-164 array processor with the code compiled at optimization level 2. Each solution took approximately 10-15 minutes CPU, depending on the Reynolds number.

III. Numerical results and discussion

The axis ratio ς was chosen so that the body would have enough curvature to produce a wake at least $O(a)$ in size, but not so much curvature that the upper bound on Re would be reached before conclusive evidence of existence or non-existence of a wake for $Re \longrightarrow \infty$ could be observed. By trial and error, it was found that the above requirements were met for ς in the range $1.55 \lesssim \varsigma \lesssim 1.75$. The flow results showed that for a fixed ς, a recirculating wake appeared at some critical Re ; as Re was increased the wake size increased until it reached a maximum. As the Reynolds number was further increased, the wake shrank until it eventually disappeared. Figure 2 shows the streamlines for the case $\varsigma = 1.65$. Of particular note is the actual disappearance of the wake occured at $Re \approx 240$, that is, at a Reynolds number high enough so that boundary layer theory might be expected to be applicable. We then see that recirculating wakes exist on bodies with slip boundary conditions at finite Re provided the boundary curvature is, at least locally, sufficiently high to produce enough vorticity, even though boundary layer theory predicts no separation. However, the numerical solutions become qualitatively consistent with boundary layer theory when Re is increased further. This trend was observed for all the values of ς chosen, except the first case $\varsigma = 1.84$ for which the numerical upper bound on Re was reached before the wake disappeared. Figure 3a shows the dimensionless wake length $\alpha = \ell/b$ as a function of Re for various values of ς, and Fig. 3b shows the dimensionless wake height $\beta = w/b$. Here, we have defined the wake length ℓ as the distance that the recirculating region extends behind the body. The length of the actual wake is infinite, but its width tends to zero as the Reynolds number goes to infinity Not surprisingly, the higher the curvature, the larger the size of the wake at any fixed Re.

In Fig. 4, the maximum surface vorticity ω_m is plotted as a function of Re for various values of ς ranging from 1.60 to 2.05; we did several runs at higher values of ς for the sole purpose of observing the point of initial separation.

The quantity ω_m at first increases with Re, but then approaches a constant asymptotic limit for $Re \gg 1$. What is important is that the square marker on each curve corresponds to the value of Re for which flow detachment first occurs. The corresponding value of ω_m is approximately 5.25, independent of the value of ς ; therefore, flow detachment occurs when the maximum surface vorticity reaches the critical value of $\omega_c \approx 5.25$. While this critical value is certainly valid only for the geometry used here, the important fact remains that flow separation occurs when the vorticity produced at the body surface reaches a critical value. At this point, vorticity is presumably generated at the body surface faster than it can be convected away, and the flow near the boundary detaches as a consequence of the accumulation of vorticity (i.e., the existence of a recirculating flow region) behind the body. However, since the geometry is fixed, ω_m becomes independent of Re for $Re \gg 1$, and the increased efficiency of vorticity convection eventually overcomes the tendency for vorticity to accumulate in the wake region and the wake disappears as $Re \longrightarrow \infty$.

The wake behind the body at finite Reynolds number is then viewed as the result of the inability of convection to transport vorticity away from the body. It is possible that this mechanism is also operative in recirculating wakes behind no-slip bodies at finite Re. In this case, the apparent correspondence between boundary layer theory ($Re \longrightarrow \infty$) and real flows at finite Re would have to be viewed essentially as an accident. We do not suggest that this is necessarily true. We do believe that one should exercise some caution in interpreting the existence of recirculating wakes at finite Reynolds number as a manifestation of separation as described by boundary layer theories for infinite Reynolds number.

IV. Numerical accuracy

The results and conclusions presented above rely on the accuracy of the numerical calculations. In the following section we examine the accuracy of our numerical scheme.

It is well known that central differencing may lead to unphysical oscillatory behavior in regions where convection strongly dominates diffusion[17]. Specifically, this problem arises in implicit methods when the Reynolds number is on the order of several hundred. Due to these numerical instabilities, we were not able to obtain solutions on any grid for flows where $Re > 340$. For the case $\varsigma = 1.84$ we actually calculated solutions for the range $10 \leq Re \leq 310$ on three different grid densities: 41x41, 61x61, and 81x81 nodes. With $Re < 240$ the values for C_D on the three grids agreed to within less than 2%. However, we were not able to obtain reliable solutions on the 41x41 grid for $Re > 250$ in spite of the fact that the machine would compute results all the way up to $Re = 340$. Specifically, we found that the drag coefficient C_D increased when Re went from 250 to 260 but then continued to decrease until the calculations failed at $Re = 310$. In addition, the wake size at $Re = 270$ was larger than the wake size at $Re = 260$, although the wake size had been decreasing up to that point and continued to decrease after it. The increase in the wake length at $Re = 270$ was on the order of the mesh size at that distance from the body. We feel that these errors are due to the inability of the 41x41 coordinate grid to accurately resolve the downstream end of the recirculation bubble. Support for this assertion comes from an examination of the streamfunction just below the critical Reynolds number, which shows that the end of the wake is severely distorted. In contrast, however, we found that the 61x61 grid and the 81x81 grid both gave consistent results until $Re \approx 310$: the drag coefficient differed between the two grids by less than 1%, and the wake size differed by the order of the mesh size (that is, roughly 5%). Thus, as a compromise between cost and accuracy we chose to use the 61x61 grid for the rest of the calculations.

TABLE I. Drag Coefficients Calculated by Moore[7,8] and Present Work.

ς	1	1.16	1.33	1.48	1.60	1.65
Re	300	150	180	180	200	240
Moore	0.140	0.355	0.327	0.356	0.343	0.293
Present Work	0.143	0.345	0.334	0.362	0.351	0.298

A number of other tests were done to determine the accuracy of the numerical results. First, we compared the drag coefficients we obtained from the present calculations with those of Moore[7,8] for a spherical shape and for ellipses with axis ratios $\varsigma = 1.16, 1.33, 1.48, 1.60,$ and 1.65. We used results for each shape at Reynolds numbers that were high enough for the wake to have disappeared. The drag coefficient, C_D was calculated from our solutions by integrating the stress over the surface of the body. For the sphere, at a Reynolds number of 300 Moore found $C_D = 0.140$, while we obtained a value of 0.143. The difference is 2.1%. Comparing the drag coefficients in the range $200 \leq Re \leq 300$ we found that the percent difference decreased as Re increased. The results for the range of axis ratios are summarized in Table I. The difference between the drag coefficients of Moore and those we calculate are all less than 5%. This agreement is good considering that the Reynolds numbers used are below values for which Moore's asymptotic theory strictly applies. We also obtained a solution for the spherical shape with $Re = 10^{-3}$; the resulting drag coefficient was 16370, compared to Stoke's result $C_D = 16/Re = 16000$. Once again the agreement is good because the discrepancy with Stoke's solution in ψ^* in the outer regions is $O(r)$, where $r = (z^2 + \sigma^2)^{\frac{1}{2}}$. To perform an internal self-consistency check on our drag coefficients, we compared the drag calculated via surface integrals of pressure and stress with the drag found by computing the total rate of viscous dissipation using the Bobyleff-Forsythe formula[18]. To find the rate of viscous dissipation, one must integrate the square of the vorticity over the entire solution domain. For all the axis ratios considered, if $Re \lesssim 90$ the two calculations differed by

less than 1%, and for $100 \lesssim Re \lesssim 250$ the difference was between 1 and 5%. The agreement between the two computations is good considering that when we integrate over the domain we amplify any errors that occur in the far-field vorticity.

TABLE II. Drag Coefficients Calculated From Ref. 10 and Present Work.

Re	20	40	73.6	120	150	180
Ref. 10	2.735	1.788	1.274	0.992	0.889	0.815
Present Work	2.738	1.781	1.266	0.984	0.880	0.822

TABLE III. Separation Angle Measured From Front Stagnation Point.

Re	40	73.6	120	150	180
Ref. 10	144.4	131.7	123.7	120.4	117.8
Present Work	144.	132.	124.	120.5	118.

TABLE IV. Dimensionless Wake Length.

Re	40	73.6	120	150	180
Ref. 10	0.32	0.71	1.1	1.3	1.4
Present Work	0.31	0.71	1.07	1.35	1.45

As a final check on the accuracy of the numerical scheme, and particularly as a check on the accuracy of our calculated wake lengths and widths, we used our method to examine streaming flow past a solid sphere, and then compared the results with those presented in Ref. 10, Chap. 5. This reference details the work done by many researchers on flow past solid spheres, with results presented in both graphical and correlation form. From our numerical solutions, we computed C_D, and measured separation angle and wake length, and compared these

with the results in Ref. 10 (Table 5.2, Eq. 5-10, and Fig. 5.7, respectively). Tables II, III, and IV show that in all cases the agreement is excellent. Figures 5a and 5b dramatically illustrate the agreement between our results for wake geometry and the experimental observations of Taneda[19]. We discontinued the runs above $Re = 200$ due to cost, but the wake continued to grow monotonically up to this point, reaching a length roughly twice the diameter of the sphere, so we are confident that the scheme accurately models the wake. Had the shrinking of the wake in the slip-surface case been an artifact of the numerics, we should have encountered the same qualitative behavior here.

V. Conclusions

In this study we have demonstrated that a recirculating wake can exist behind a smooth slip body of fixed shape at moderate Reynolds numbers, say $O(100)$, in direct disagreement with the predictions of boundary layer theory. Although the wake initially increases in size with increase in Re, the wake eventually begins to decrease in size with further increase in Re, until the wake finally disappears when the Reynolds number becomes large enough. Thus, when $Re = O(200 - 300)$, the results of our numerical calculations agree with the solutions from boundary layer theory: there is no wake behind the body. We conclude that the mechanism responsible for the presence of a recirculating wake behind a slip body at modest Re is not the same one present in boundary layer detachment, but rather is vorticity accumulation behind the body.

The closed streamline wakes behind slip bodies are qualitatively similar in structure to those observed behind *no*-slip bodies at modest Reynolds numbers. An obvious question then is, whether the recirculating wakes behind no-slip bodies at moderate Reynolds numbers are truly a consequence of boundary layer separation as we always assume, or actually reflect the vorticity accumulation mechanism that is observed for a bubble.

Acknowledgement

The authors wish to acknowledge the contribution of G. Ryskin in helping to formulate the ideas that are inherent in this work, and A. Acrivos with whom we discussed this work on several occasions.

This work was supported by a grant from the Fluid Mechanics Program at the National Science Foundation.

Appendix: Boundary layer theory for slip surfaces

In this section we will examine high Reynolds number streaming flow past both smooth slip surfaces and slip surfaces whose curvature is not necessarily small. The reason for looking at both of these cases is to determine criteria for the existence or non-existence of steady recirculating wakes behind bubbles. We will prove that for smooth surfaces, that is, surfaces where the curvature is everywhere finite, that in the asymptotic limit $Re \longrightarrow \infty$ boundary layer theory predicts no separation when a shear-free boundary condition is imposed at the surface. We will also show that when the curvature of the body is *not* finite, that boundary layer theory simply breaks down at the point of high curvature, and that separation is likely to occur at this point.

I. Arbitrary smooth surfaces

To attack this problem, the solution will be assumed to have the form of a singular perturbation expansion. We will examine which conditions are necessary for separation to occur, and then show that the conditions can never be met.

First, assume that there exists a body of revolution, as shown in Fig. A1. The contour of the body is specified by the radius $r(x)$, where x is the length measured along the body from the front stagnation point. Provided that $|r''(x)|^2 = O(1)$ (that is, the body is "smooth"), the boundary layer equations take the nondimensional form[20,21]:

$$u\frac{\partial u}{\partial x} + V\frac{\partial u}{\partial Y} = u_e\frac{du_e}{dx} + \frac{\partial^2 u}{\partial Y^2} \qquad (A1a)$$

$$\frac{\partial}{\partial x}(r\,u) + \frac{\partial}{\partial Y}(r\,V) = 0 \qquad (A1b)$$

where u and V are the velocities parallel and normal to the boundary, and $u_e(x)$ is the tangential component of the potential flow solution evaluated at the body surface. The boundary conditions for this problem are

$$u = 0 \qquad \text{at } x = 0 \qquad (A2a)$$

$$\tau_{yx} = 0, \quad V = 0 \qquad \text{at } Y = 0 \tag{A2b}$$

$$u \longrightarrow u_e \qquad \text{as } Y \longrightarrow \infty \tag{A2c}$$

It is well known that in the boundary layer on a pure-slip surface the velocity, to leading order, is the same order of magnitude as the free stream velocity; that is, the velocity changes by $O(Re^{-\frac{1}{2}})$ across the boundary layer[22]. Thus, in the boundary layer, the velocity is just the potential flow velocity plus a correction of $o(Re^{-\frac{1}{2}})$, denoted by $\tilde{u}$. Now assume that $\tilde{u}$ can be expressed as an asymptotic expansion of the form

$$\tilde{u}(x,Y) = \sum_{i=1}^{\infty} \phi_i(Re)\, u_i(x,Y) \tag{A3}$$

where the $\{\phi_i\}$ form an asymptotic sequence and the u_i are $O(1)$; one would expect from the above arguments that $\phi_1 = Re^{-\frac{1}{2}}$. If the potential flow solution is denoted by $U(x,y)$, then $u = U + \tilde{u}$, and from Eqs. (A1) the $O(Re^{-\frac{1}{2}})$ problem becomes

$$\frac{\partial}{\partial x}(u_e\, u_1) - Y q(x) \frac{\partial u_1}{\partial Y} = \frac{\partial^2 u_1}{\partial Y^2} \tag{A4}$$

where

$$q(x) = \frac{1}{r}\frac{d}{dx}(u_e\, r).$$

The boundary condtions corresponding to Eq. (A4) are

$$\frac{\partial u_1}{\partial Y} = f(x) \qquad \text{at } Y = 0 \tag{A5a}$$

$$u_1 \longrightarrow 0 \qquad \text{as } Y \longrightarrow \infty \tag{A5b}$$

$$u_1 = 0 \qquad \text{at } x = 0 \tag{A5c}$$

The function $f(x)$ is the non-vanishing tangential stress calculated from the potential flow solution, and is $O(1)$.

In order for the assumed form for Eq. (A3) to be correct, there must exist a solution of Eq. (A4) in $\Omega \stackrel{\text{def}}{=} [0,1] \times [0,\infty)$, the solution must be bounded everywhere in Ω, and also be unique.

a. existence

In the domain $\Omega_o \stackrel{\text{def}}{=} (0,1] \times [0,\infty)$, Eq. (A4) can be rewritten in the form

$$a(x)\frac{\partial^2 u}{\partial Y^2} + Y\,b(x)\frac{\partial u}{\partial Y} - c(x)\,u - \frac{\partial u}{\partial x} = 0 \qquad (A6)$$

where

$$a(x) = \frac{1}{u_e(x)}$$

$$b(x) = \frac{d}{dx}\ln(u_e r)$$

and

$$c(x) = \frac{d}{dx}\ln u_e.$$

It's obvious that Eq. (A6) is parabolic everywhere in Ω_o. For all physically realistic situations, the coefficients a, b, and c will be continuous functions of x in Ω_o. For example, for a sphere, $a(x) = \csc x$, $b(x) = 2\cot x$, and $c(x) = \cot x$. Further, the initial condition is simply $u_1(0,Y) = 0$, and since $u \longrightarrow 0$ as $Y \longrightarrow \infty$, we are guaranteed the existence of a solution in Ω [23].

b. boundedness

First multiply each term in Eq. (A4) by u_1 and integrate over the domain of Y:

$$\begin{aligned}\frac{u_e}{2}\int_0^\infty \frac{\partial u_1^2}{\partial x}\,dY + \frac{du_e}{dx}\int_0^\infty u_1^2\,dY \\ - \frac{1}{2}\frac{1}{r}\frac{\partial}{\partial x}(u_e r)\int_0^\infty Y\frac{\partial u_1^2}{\partial Y}\,dY = \int_0^\infty u_1\frac{\partial^2 u_1}{\partial Y^2}\,dY\end{aligned} \qquad (A7)$$

But,

$$\int_0^\infty Y\frac{\partial u_1^2}{\partial Y}\,dY = u_1^2 Y\Big|_0^\infty - \int_0^\infty u_1^2\,dY = -\int_0^\infty u_1^2\,dY \qquad (A8)$$

and,

$$\begin{aligned}\int_0^\infty u_1\frac{\partial^2 u_1}{\partial Y^2}\,dY &= u_1\frac{\partial u_1}{\partial Y}\Big|_0^\infty - \int_0^\infty \left(\frac{\partial u_1}{\partial Y}\right)^2 dY \\ &= u_1(x,0)\,f(x) - \int_0^\infty \left(\frac{\partial u_1}{\partial Y}\right)^2 dY\end{aligned} \qquad (A9)$$

If the relations in Eqs. (A8) and (A9) are substituted into Eq. (A7), one obtains

$$\begin{aligned} \frac{u_e}{2}\int_0^\infty \frac{\partial u_1^2}{\partial x}\,dY + \frac{du_e}{dx}\int_0^\infty u_1^2\,dY + \frac{1}{2}\frac{1}{r}\frac{\partial}{\partial x}(u_e r)\int_0^\infty u_1^2\,dY \\ = u_1(x,0)\,f(x) - \int_0^\infty \left(\frac{\partial u_1}{\partial Y}\right)^2 dY \end{aligned} \tag{A10}$$

Rearrangement of Eq. (A10) yields

$$\frac{d}{dx}\left[r\,u_e^3\int_0^\infty u_1^2\,dY\right] + 2ru_e^2\int_0^\infty \left(\frac{\partial u_1}{\partial Y}\right)^2 dY = r\,u_e^2\,g \tag{A11}$$

where $g(x) = u_1(x,0)\,f(x)$. Integration of Eq. (A11) in x from 0 to x gives

$$\begin{aligned} r\,u_e^3\int_0^\infty u_1^2(x,Y)\,dY + 2\int_0^x\int_0^\infty r(\lambda)\left[u_e(\lambda)\frac{\partial u_1}{\partial Y}(\lambda,Y)\right]^2 dY\,d\lambda \\ = \int_0^x r(\lambda)\,u_e^2(\lambda)\,g(\lambda)\,d\lambda \end{aligned} \tag{A12}$$

Now, because of the orientation of the coordinate system, $u_e(x) \geq 0$, and also $r(x) \geq 0$ due to the fact that r is a cylindrical coordinate. Thus, both integrals on the left hand side of Eq. (A12) are positive for any $x > 0$, and therefore must be bounded *if* the integral on the right hand side of Eq. (A12) is positive and bounded. Boundedness of the integrals on the left hand side necissitate the boundedness of $u_1(x,Y)$ and its derivative with respect to Y.

It now remains to be shown that

$$\int_0^x r(\lambda)\,u_e^2(\lambda)\,g(\lambda)\,d\lambda \; < M \tag{A13}$$

where M is a finite, positive quantity, $M \in \Re^1$. We know that $r(x)$ and $u_e^2(x)$ are both positive and bounded, so it is only necessary to show that $g(x) = u_1(x,0)\,f(x)$ is positive and bounded. From Eq. (A3), we have

$$u(x,0) = \hat{U}(x,0) + Re^{-\frac{1}{2}}u_1(x,0), \tag{A14}$$

where $\hat{U}(x,Y) \stackrel{\text{def}}{=} U(x,y)$, and also, because of the orientation of the coordinates $u(x,y)$, $\hat{U}(x,Y) \geq 0$. In addition, the velocity in the boundary layer will be

less than in the free stream, so $u(x,Y) \leq \hat{U}(x,Y)$. Thus, from Eq. (A14), $u_1(x,0) \leq 0$. The tangential stress residual $f(x)$ is known from the potential flow solution and is less than or equal to zero. Therefore, $g(x) \geq 0$ and as a result $M \geq 0$.

We also know that $\hat{U}(x,Y) = O(1)$, so $f(x) = \frac{\partial U}{\partial y}(x,0) = O(1)$. All that is left to proof then is that $u_1(x,0)$ is bounded; if this is so then M is bounded. The proof is formulated as follows: at each x, we assume that in the region $Y \in (0,\delta)$, $0 < \delta < \infty$ that u_1 is defined, and further that $u_1 \in \mathrm{C}^1[(0,\delta)]$. Because the residual of the shear stress is bounded at $y = 0$, we know that

$$\lim_{Y \to 0^+} \frac{\partial u_1}{\partial Y} = m \tag{A15}$$

where m is a known bounded function. Since $\frac{\partial u_1}{\partial Y}$ is bounded at $Y = 0$, it is not unreasonable that it also be continuous in the range $(0,\delta)$ — however small — then the mean value theorem can be applied:

$$\left|u_1(x,y_1) - u_1(x,y_2)\right| = \left|\frac{\partial u_1}{\partial Y}(x,\xi)\right| \left|y_1 - y_2\right| \tag{A16}$$

Further, the Lipschitz condition will also be satisfied:

$$\left|u_1(x,y_1) - u_1(x,y_2)\right| < K \left|y_1 - y_2\right| \tag{A17}$$

The conditions must hold for all $y_1,\ y_2 \in (0,\delta)$. Then, take the interval $(0,\delta)$ and the sequence $\{y_n\}$ such that $0 < y_j < \delta$, and construct the sequence $\{u_1(x,y_n)\}$. Because u_1 satisfies Eqs. (A16) and (A17), the sequence $\{u_1(x,y_n)\}$ is a Cauchy sequence which converges to a *finite* limit β as the sequence $\{y_n\}$ converges to zero. Therefore,

$$\lim_{Y \to 0^+} u_1(x,Y) \longrightarrow \beta \tag{A18}$$

We have thus proven that $u_1(x,Y)$ is bounded in the domain $0 \leq x \leq 1,\ 0 \leq Y < \infty$, and $u_1 \in \mathrm{C}^2\{\,[0,1] \times [0,\infty)\,\}$.

c. uniqueness

Assume that there are two distinct solutions $\hat{u}$ and $\bar{u}$ which satisfy Eq. (A4) plus the boundary conditions in Eqs. (A5). Since the equations are all linear, $w = \hat{u} - \bar{u}$ must also be a solution. The equations for $w(x, Y)$ are

$$\frac{\partial}{\partial x}(u_e\, w) \;-\; Y q(x) \frac{\partial w}{\partial Y} \;=\; \frac{\partial^2 w}{\partial Y^2}, \tag{A19}$$

along with the boundary conditions

$$\frac{\partial w}{\partial Y} \;=\; 0 \qquad\qquad \text{at } Y = 0 \tag{A20a}$$

$$w \longrightarrow 0 \qquad\qquad \text{as } Y \longrightarrow \infty \tag{A20b}$$

$$w \;=\; 0 \qquad\qquad \text{at } x = 0 \tag{A20c}$$

In a manner similar to the proof of boundedness above, multiply Eq. (A19) by w and integrate over the domain of Y:

$$\begin{aligned} \int_0^\infty u_e\, w \frac{\partial w}{\partial x}\, dY \;+\; \int_0^\infty w^2 \frac{du_e}{dx}\, dY \\ - \int_0^\infty Y\, q(x)\, w \frac{\partial w}{\partial Y}\, dY \;=\; \int_0^\infty w \frac{\partial^2 w}{\partial Y^2}\, dY \end{aligned} \tag{A21}$$

After some manipulation, one obtains

$$r u_e^3 \int_0^\infty w^2\, dY \;+\; 2 \int_0^x \int_0^\infty r \left(u_e \frac{\partial w}{\partial Y} \right)^2 dY\, d\lambda \;=\; 0 \tag{A22}$$

Since the integrands in Eq. (A22) are both positive semi-definite, the only way Eq. (A22) can be satisfied is if $w(x, Y) \equiv 0$, that is, $\hat{u} \equiv \bar{u}$, and the solution $u_1(x, Y)$ is therefore unique.

Although the body in question in three-dimensional, for which there will (or will not) be a separation line rather than a separation point, it is reasonable to assume that separation (if it occurs) will occur at the same x position all around the body. So it is obvious that a necessary condition for flow detachment to occur

is $u(x,0) = 0$ at some point $0 < x < 1$. It has been shown that the flow solution can be expressed as

$$u \;=\; U + \tilde{u} \;=\; U + Re^{-\frac{1}{2}}\, u_1 + \cdots \qquad (A23)$$

and so the condition that $u(x,0) = 0$ will only be satisfied if each term in Eq. (A23) vanishes individually. Thus, a necessary condition for separation is $U(x,0) \stackrel{\text{def}}{=} u_e(x) = 0$ for some $0 < x < 1$. For streaming flow past smooth bodies it is obvious that $u_e \neq 0$ for any $0 < x < 1$. Therefore, boundary layer theory predicts no flow detachment.

II. High curvature

We now consider the situation where an arbitrary axisymmetric body (see Fig. A2) with a surface whose local curvature may not be finite at some point. The geometry is described by an orthogonal curvilinear coordinate system having components (x_1, x_2, ϕ), such that $x_1 = 0$ is the body surface. In this coordinate system, the continuity equation is

$$\frac{\partial}{\partial x_1}(h_2 h_3 u_1) + \frac{\partial}{\partial x_2}(h_1 h_3 u_2) \;=\; 0 \qquad (A24)$$

where the h_i are the scale factors (h_3 is in the ϕ-direction). In the boundary layer, the velocity field can be written as

$$\mathbf{u} \;=\; \mathbf{U} + \tilde{\mathbf{u}} \qquad (A25)$$

where $\mathbf{u} = (u_1, u_2)^T$, $\mathbf{U} = (\bar{V}, \bar{U})^T$ is the potential flow solution, and $\tilde{\mathbf{u}} = (\tilde{u}_1, \tilde{u}_2)^T$ is the perturbation to the potential flow solution ($\|\tilde{\mathbf{u}}\| \ll \|\mathbf{U}\|$). So, for the perturbation velocity the continuity equation is

$$\frac{\partial}{\partial x_1}(h_2 h_3 \tilde{u}_1) + \frac{\partial}{\partial x_2}(h_1 h_3 \tilde{u}_2) \;=\; 0 \qquad (A26)$$

The equations of motion in the tangential and normal directions ("2" and "1", respectively) are

$$\begin{aligned}
&\frac{1}{h_2}\frac{\partial}{\partial x_2}(\bar{U}\tilde{u}_2) + \frac{\tilde{u}_1}{h_1}\frac{\partial \bar{U}}{\partial x_1} + \frac{\bar{V}}{h_1}\frac{\partial \tilde{u}_2}{\partial x_1} \\
&\quad + \frac{\bar{U}\tilde{u}_1}{h_1 h_2}\frac{\partial h_2}{\partial x_1} + \frac{\bar{V}\tilde{u}_2}{h_1 h_2}\frac{\partial h_2}{\partial x_1} - \frac{2\bar{V}\tilde{u}_1}{h_1 h_2}\frac{\partial h_1}{\partial x_2} \\
&\quad = -\frac{1}{h_2}\frac{\partial \tilde{p}}{\partial x_2} + \frac{1}{Re}\left\{ \frac{1}{h_1 h_3}\left[\frac{\partial}{\partial x_1}(\tilde{u}_2 h_2) - \frac{\partial}{\partial x_2}(\tilde{u}_1 h_1)\right]\frac{\partial}{\partial x_1}\left(\frac{h_3}{h_1 h_2}\right)\right. \\
&\quad + \frac{1}{h_1^2 h_2}\frac{\partial^2}{\partial x_1^2}(\tilde{u}_2 h_2) + \frac{1}{h_1 h_2^2 h_3}\frac{\partial^2}{\partial x_2^2}(\tilde{u}_2 h_1 h_3) \\
&\quad + \frac{1}{h_1^2 h_2}\frac{\partial}{\partial x_2}\left(\frac{h_1}{h_2 h_3}\right)\frac{\partial}{\partial x_2}(\tilde{u}_2 h_1 h_3) \\
&\quad \left. + \frac{1}{h_1^2 h_2}\frac{\partial}{\partial x_2}\left(\frac{\tilde{u}_1 h_1^2}{h_2 h_3}\right)\frac{\partial}{\partial x_1}\left(\frac{h_2 h_3}{h_1}\right) + \frac{\tilde{u}_1}{h_2^2 h_3}\frac{\partial^2}{\partial x_2 \partial x_1}\left(\frac{h_2 h_3}{h_1}\right)\right\}
\end{aligned} \tag{A27a}$$

$$\begin{aligned}
&\frac{1}{h_1}\frac{\partial}{\partial x_1}(\bar{V}\tilde{u}_1) + \frac{\tilde{u}_2}{h_2}\frac{\partial \bar{V}}{\partial x_2} + \frac{\bar{U}}{h_2}\frac{\partial \tilde{u}_1}{\partial x_2} \\
&\quad + \frac{\bar{U}\tilde{u}_1}{h_1 h_2}\frac{\partial h_1}{\partial x_2} + \frac{\bar{V}\tilde{u}_2}{h_1 h_2}\frac{\partial h_1}{\partial x_2} - \frac{2\bar{U}\tilde{u}_2}{h_1 h_2}\frac{\partial h_2}{\partial x_1} \\
&\quad = -\frac{1}{h_1}\frac{\partial \tilde{p}}{\partial x_1} + \frac{1}{Re}\left\{ -\frac{1}{h_2 h_3}\left[\frac{\partial}{\partial x_1}(\tilde{u}_2 h_2) - \frac{\partial}{\partial x_2}(\tilde{u}_1 h_1)\right]\frac{\partial}{\partial x_2}\left(\frac{h_3}{h_1 h_2}\right)\right. \\
&\quad + \frac{1}{h_1 h_2^2}\frac{\partial^2}{\partial x_2^2}(\tilde{u}_1 h_1) + \frac{1}{h_1^2 h_2 h_3}\frac{\partial^2}{\partial x_1^2}(\tilde{u}_1 h_2 h_3) \\
&\quad + \frac{1}{h_1 h_2^2}\frac{\partial}{\partial x_1}\left(\frac{h_2}{h_1 h_3}\right)\frac{\partial}{\partial x_1}(\tilde{u}_1 h_2 h_3) \\
&\quad \left. + \frac{1}{h_1 h_2^2}\frac{\partial}{\partial x_1}\left(\frac{\tilde{u}_2 h_2^2}{h_1 h_3}\right)\frac{\partial}{\partial x_2}\left(\frac{h_1 h_3}{h_2}\right) + \frac{\tilde{u}_2}{h_1^2 h_3}\frac{\partial^2}{\partial x_2 \partial x_1}\left(\frac{h_1 h_3}{h_2}\right)\right\}
\end{aligned} \tag{A27b}$$

where $\tilde{p}$ is the actual pressure in the boundary layer minus the potential flow pressure field.

Now, we must rescale the equations so that all of the derivatives become $O(1)$. In addition to the usual boundary layer rescaling, we must also take into account the possibility that the curvature may be large at some point on the

surface. The curvature in the tangential (or, "2") direction is

$$\kappa_2 \;=\; \frac{1}{h_1 h_2}\frac{\partial h_2}{\partial x_1} \qquad (A28)$$

Regardless of how high the curvature in the streamwise direction is, we can expect that h_1, h_3, and all their derivatives will be $O(1)$. To rescale the variables, let $x_1 = Y\,Re^{\alpha}$, $\tilde{u}_1 = v\,Re^{\beta}$, $\tilde{u}_2 = u\,Re^{\gamma}$, $\frac{1}{h_2}\frac{\partial h_2}{\partial x_1} = \kappa_2\,Re^{\lambda}$, $x_2 = x$, and $\bar{U} = U$. One would expect that α, β, $\gamma < 0$ and $\lambda \geq 0$ (for $\lambda = 0$ the Eqs. (A27) should just be the usual boundary layer equations). Further, because $\bar{V} = 0$ at $x_1 = 0$ and assumes its potential flow value at the outer edge of the boundary layer, $\frac{\partial \bar{V}}{\partial x_1} = O(1)$. This implies that $\bar{V} = O(Re^{\alpha})$, and so we define $\bar{V} = V\,Re^{\alpha}$.

The continuity equation, Eq. (A24), can be now written as

$$Re^{\beta+\lambda}\,h_3 v\kappa_2 \;+\; Re^{\beta-\alpha}\frac{\partial}{\partial Y}(h_3\,v) \;+\; Re^{\gamma}\frac{1}{h_2}\frac{\partial}{\partial x}(h_1 h_3 u) \;=\; 0 \qquad (A29)$$

The tangential stress balance is

$$\frac{h_2}{h_1}\frac{\partial}{\partial x_1}\Big(\frac{U}{h_2}\Big) + \frac{h_2}{h_1}\frac{\partial}{\partial x_1}\Big(\frac{\tilde{u}_2}{h_2}\Big) \;=\; 0 \qquad (A30)$$

From the potential flow solution, we know that the first term in Eq. (A30) is $O(1)$. Thus,

$$\frac{h_2}{h_1}\frac{\partial}{\partial x_1}\Big(\frac{U}{h_2}\Big) \;+\; Re^{\gamma-\alpha}\,\frac{1}{h_1}\frac{\partial u}{\partial Y} \;-\; Re^{\gamma+\lambda}\,\frac{u\kappa_2}{h_1} \;=\; 0. \qquad (A31)$$

The tangential component of the Navier-Stokes equations is

$$\begin{aligned}
&\underline{Re^{\gamma}\frac{1}{h_2}\frac{\partial}{\partial x}(U\,u)} + Re^{\beta}\frac{v}{h_1}\frac{\partial U}{\partial Y} + \underline{Re^{\gamma}\frac{V}{h_1}\frac{\partial u}{\partial Y}} + Re^{\beta+\lambda}\frac{U\,v}{h_1}\kappa_2 \\
&\quad + Re^{\alpha+\gamma+\lambda}\frac{V\,u}{h_1}\kappa_2 - Re^{\alpha+\beta}\frac{2V\,v}{h_1 h_2}\frac{\partial h_1}{\partial x_1} \\
&\quad = \; -\frac{1}{h_2}\frac{\partial \tilde{p}}{\partial x} + \frac{1}{h_1 h_3}\Bigg\{ Re^{\gamma-\alpha-1}\frac{\partial u}{\partial Y}\frac{\partial}{\partial x_1}\Big(\frac{h_3}{h_1}\Big) \\
&\quad - Re^{\gamma-\alpha+\lambda-1}\frac{h_3}{h_1}\frac{\partial u}{\partial Y}\kappa_2 + Re^{\gamma+\lambda-1}\,u\frac{\partial}{\partial x_1}\Big(\frac{h_3}{h_1}\Big)\kappa_2 - Re^{\gamma+2\lambda-1}\frac{u\,h_3}{h_1}\kappa_2^2 \\
&\quad - Re^{\beta-1}\frac{1}{h_2}\frac{\partial}{\partial x}(v\,h_1)\frac{\partial}{\partial x_1}\Big(\frac{h_3}{h_1}\Big) + Re^{\beta+\lambda-1}\frac{h_3}{h_1 h_2}\frac{\partial}{\partial x}(v\,h_1)\kappa_2\Bigg\}
\end{aligned}$$

$$
\begin{aligned}
&+ Re^{\gamma-1}\frac{u}{h_1^2 h_2}\frac{\partial^2 h_2}{\partial x_1^2} + Re^{\gamma-\alpha+\lambda-1}\frac{2}{h_1^2}\frac{\partial u}{\partial Y}\kappa_2 \\
&+ \underline{Re^{\gamma-2\alpha-1}\frac{1}{h_1^2}\frac{\partial^2 u}{\partial Y^2}} + \frac{Re^{\gamma-1}}{h_1 h_2^2 h_3}\frac{\partial^2}{\partial x^2}(u\, h_1 h_3) \\
&+ \frac{Re^{\gamma-1}}{h_1^2 h_2}\frac{\partial}{\partial x}\Big(\frac{h_1}{h_2 h_3}\Big)\frac{\partial}{\partial x}(u\, h_1 h_3) + \frac{Re^{\beta+\lambda-1}}{h_1^2}\frac{\partial}{\partial x}\Big(\frac{v\, h_1^2}{h_2 h_3}\Big)\kappa_2 \\
&+ \frac{Re^{\beta-1}}{h_1^2}\frac{\partial}{\partial x}\Big(\frac{v\, h_1^2}{h_2 h_3}\Big)\frac{\partial}{\partial x_1}\Big(\frac{h_3}{h_1}\Big) + \cdots \text{(H.O.T.)}. \qquad (32a)
\end{aligned}
$$

The normal component is

$$
\begin{aligned}
&\underline{Re^{\beta}\frac{1}{h_1}\frac{\partial}{\partial Y}(V\, v)} + Re^{\beta}\frac{U}{h_2}\frac{\partial v}{\partial x} + Re^{\alpha+\gamma}\frac{u}{h_2}\frac{\partial V}{\partial x} - \underline{Re^{\gamma+\lambda}\frac{U\, u}{h_1}\kappa_2} \\
&\quad + Re^{\alpha+\beta}\frac{V\, u}{h_1 h_2}\frac{\partial h_1}{\partial x} + Re^{\beta}\frac{U\, v}{h_1 h_2}\frac{\partial h_1}{\partial x} \\
&\quad = \underline{-\frac{Re^{-\alpha}}{h_1}\frac{\partial \tilde{p}}{\partial Y}} - \frac{1}{h_2 h_3}\Big\{ Re^{\gamma-\alpha-1}\frac{\partial u}{\partial Y}\frac{\partial}{\partial x}\Big(\frac{h_3}{h_1}\Big) \\
&\quad - Re^{\gamma-\alpha-1}\frac{h_3}{h_1 h_2}\frac{\partial u}{\partial Y}\frac{\partial h_2}{\partial x} + Re^{\gamma+\lambda-1}\, u\frac{\partial}{\partial x}\Big(\frac{h_3}{h_1}\Big)\kappa_2 \\
&\quad - Re^{\gamma+\lambda-1}\frac{u\, h_3}{h_1 h_2^2}\frac{\partial h_2}{\partial x}\kappa_2 - Re^{\beta-1}\frac{\partial}{\partial x}(v\, h_1)\frac{\partial}{\partial x}\Big(\frac{h_3}{h_1 h_2}\Big)\Big\} \\
&\quad + \frac{1}{h_1^2 h_3}\Big\{ 2Re^{\beta+\lambda-1}\kappa_2\frac{\partial}{\partial Y}(v\, h_3) + Re^{\beta-1}\frac{v\, h_3}{h_2}\frac{\partial^2 h_2}{\partial x_1^2} \\
&\quad + Re^{\beta-2\alpha-1}\frac{\partial^2}{\partial Y^2}(v\, h_3)\Big\} + Re^{\beta+2\alpha-1}\frac{v}{h_1^2}\kappa_2^2 + \frac{Re^{\beta-1}}{h_1 h_2^2}\frac{\partial^2}{\partial x^2}(v\, h_1) \\
&\quad + Re^{\beta+\lambda-1}\frac{h_3}{h_1}v\kappa_2\frac{\partial}{\partial x_1}\Big(\frac{1}{h_1 h_3}\Big) + Re^{\beta-\alpha+\lambda-1}\frac{\kappa_2}{h_1^2 h_3}\frac{\partial}{\partial Y}(v\, h_3) \\
&\quad + \frac{Re^{\beta-\alpha-1}}{h_1}\frac{\partial}{\partial x_1}\Big(\frac{1}{h_1 h_3}\Big)\frac{\partial}{\partial Y}(v\, h_3) + \cdots \text{(H.O.T.)}. \qquad (32b)
\end{aligned}
$$

The underlined terms are the ones that are present in the boundary layer equations when the curvature is finite ($\lambda \approx 0$), and it is obvious that when $\lambda = 0$ matching yields $\alpha = \gamma = -\frac{1}{2}$, $\beta = 1$. The resulting equations are the boundary layer equations:

$$
\frac{\partial}{\partial x}(U\, u) + V\frac{\partial u}{\partial Y} = \frac{\partial^2 u}{\partial Y^2} \qquad (A33a)
$$

$$
\frac{\partial \tilde{p}}{\partial Y} = O(Re^{-1}) \qquad (A33b)
$$

Here, however, we assume that $\lambda > 0$ to account for possible high curvature. As with normal boundary layer analysis, the terms in Eqs. (A32) must be examined with the intent of balancing the largest viscous and convective terms, but also balancing the largest of the terms involving the curvature. From the continuity equation, Eq. (A29), it can be seen that

$$\beta + \lambda = \beta - \alpha = \gamma \qquad (A34)$$

thus making all three terms the same order of magnitude. Similarly for the tangential stress condition, Eq. (A31), to insure that the last two terms balance the $O(1)$ first term,

$$\gamma - \alpha = \gamma + \lambda = 0 \qquad (A35)$$

The tangential component of the governing equations, Eq. (A32a), reveals that the largest convective terms are Re^{γ}, $Re^{\beta+\lambda}$, and $Re^{\alpha+\gamma+\lambda}$ $(= Re^{\beta+\lambda}$, from Eq. (A34) above), and the largest viscous terms are $Re^{\gamma-2\alpha-1}$ and $Re^{\gamma-\alpha+\lambda-1}$ $(= Re^{\lambda-1}$, from Eq. (A35) above). The various balances $\gamma = \beta+\lambda = \gamma-2\alpha-1 = \lambda - 1$ arising in the tangential component of the equations of motion can be satisfied if

$$\alpha = \gamma = -\frac{1}{2} \qquad \lambda = +\frac{1}{2} \qquad \beta = -1 \qquad (A36)$$

Using these exponents, the continuity equation becomes

$$h_3 v \kappa_2 + \frac{\partial}{\partial Y}(v\, h_3) + \frac{1}{h_2}\frac{\partial}{\partial x}(u\, h_1 h_3) = 0, \qquad (A37a)$$

the x-component of the Navier-Stokes equations (Eq. (A32a)) reduces to

$$\begin{aligned} \frac{\partial}{\partial x}(U\,u) + \frac{h_2}{h_1} V \frac{\partial u}{\partial Y} + \kappa_2 \frac{h_2}{h_1}(Uv + Vu) \\ = -\frac{\partial \tilde{p}}{\partial x} + \frac{\kappa_2 h_2}{h_1^2}\frac{\partial u}{\partial Y} - \frac{u\, h_2}{h_1^2}\kappa_2^2 + \frac{h_2}{h_1^2}\frac{\partial^2 u}{\partial Y^2} + O(Re^{-\frac{1}{2}}), \end{aligned} \qquad (A37b)$$

the Y-component (Eq. (A32b)) is

$$2Uu\kappa_2 = \frac{\partial \tilde{p}}{\partial Y} + O(Re^{-1}), \qquad (A37c)$$

and the shear stress condition is

$$\frac{\partial u}{\partial Y} - u\kappa_2 = -h_2 \frac{\partial}{\partial x_1}\left(\frac{U}{h_2}\right)\bigg|_{x_1=0} = f(x). \qquad (A37d)$$

Thus, when the curvature becomes important the pressure is *not* approximately constant across the boundary layer, as is true in Eq. (A33b), but instead is directly proportional to the curvature. In fact, Eq. (A37c) shows that the change in pressure across the boundary layer (that is, in the Y-direction) is equal to the centrifugal force due to the movement of fluid around the point of highest curvature. This result is physically realistic, and it points to a probable breakdown of the boundary layer at the point of high curvature.

References

[1] G. K. Batchelor, *An Introduction to Fluid Dynamics*, §4.12 (Cambridge University Press, Cambridge, 1967).

[2] S. Tomotika, Air Ministry Aeronautical Research Committee Reports and Memoranda No. 1678 (Printed and Published by His Majesty's Stationery Office, London, 1935).

[3] F. N. Peebles and H. J. Garber, Chem. Eng. Prog. **49**, 88 (1953).

[4] D. Bhaga and M. E. Weber, J. Fluid Mech. **105**, 61 (1981).

[5] J. G. Hnat and J. D. Buckmaster, Phys. Fluids **19**, 182 (1976).

[6] D. W. Moore, J. Fluid Mech. **6**, 113 (1959).

[7] D. W. Moore, J. Fluid Mech. **16**, 161 (1963).

[8] D. W. Moore, J. Fluid Mech. **23**, 749 (1965).

[9] G. Ryskin and L. G. Leal, J. Fluid Mech. **148**, 19 (1984).

[10] R. Clift, J. R. Grace, and M. E. Weber, *Bubbles, Drops, and Particles* (Academic Press, New York, 1978), p.181.

[11] G. Ryskin and L. G. Leal, J. Comput. Phys. **50**, 71 (1983).

[12] I. Proudman and J. R. A. Pearson, J. Fluid Mech. **2**, 237 (1957).

[13] P. M. Morse and H. Feshbach, *Methods of Theoretical Physics* (McGraw-Hill, New York, 1953).

[14] C. E. Grosch and S. A. Orszag, J. Comput. Phys. **25**, 273 (1977).

[15] B. Fornberg, J. Fluid Mech. **98**, 819 (1980).

[16] D. W. Peacemann and H. H. Rachford, J. Soc. Indust. Appl. Math. **3**, 28 (1955).

[17] P. J. Roache, *Computational Fluid Dynamics*, Hermosa Albuquerque, 1972.

[18] J. Serrin, Handbuch der Physik **8**, 125 (1959).

[19] S. Taneda, J. Phys. Soc. Jpn. **11**, 1104 (1956).

[20] H. Schlichting, *Boundary-Layer Theory* (McGraw-Hill, New York, 1955).

[21] E. Boltze, Grenzschichten an Rotationskörpern. Diss. Göttingen (1908).

[22] V.G. Levich, *Physiochemical Hydrodynamics*, Prentice-Hall, Englewood Clif NJ, 1962.

[23] A. Friedman, *Partial Differential Equations of Parabolic Type* (Prentice-Hall, Englewood Cliffs, NJ, 1964).

Figure captions

Figure 1. Sketch of the coordinate system for the exterior of an axisymmetric bubble with an attached wake region; the flow is from left to right.

Figure 2. Streamlines at various Reynolds numbers for the case $\varsigma = 1.65$.

Figure 3. (a) Dimensionless wake length $\alpha = \ell/b$ as a function of Reynolds number, and (b) dimensionless wake width $\beta = w/b$: $\varsigma = 1.60$, $\square$; 1.65, $\triangle$; 1.84, $\times$.

Figure 4. Maximum surface vorticity as a function of Reynolds number for various ς.

Figure 5. Streaming flow past solid sphere. Streamlines computed by authors and photographs of Taneda[19], for (a) $Re = 73.6$, and (b) $Re = 118$. (Photographs reproduced with permission.)

Figure A1. Schematic of the coordinate system for an arbitrary, smooth body of revolution.

Figure A2. Schematic of the coordinate system for a body of revolution whose surface curvature is not finite at a point.

$$\varsigma = \frac{b}{a} \text{ (fixed)} \qquad \alpha = \frac{\ell}{b} \qquad \beta = \frac{w}{b}$$

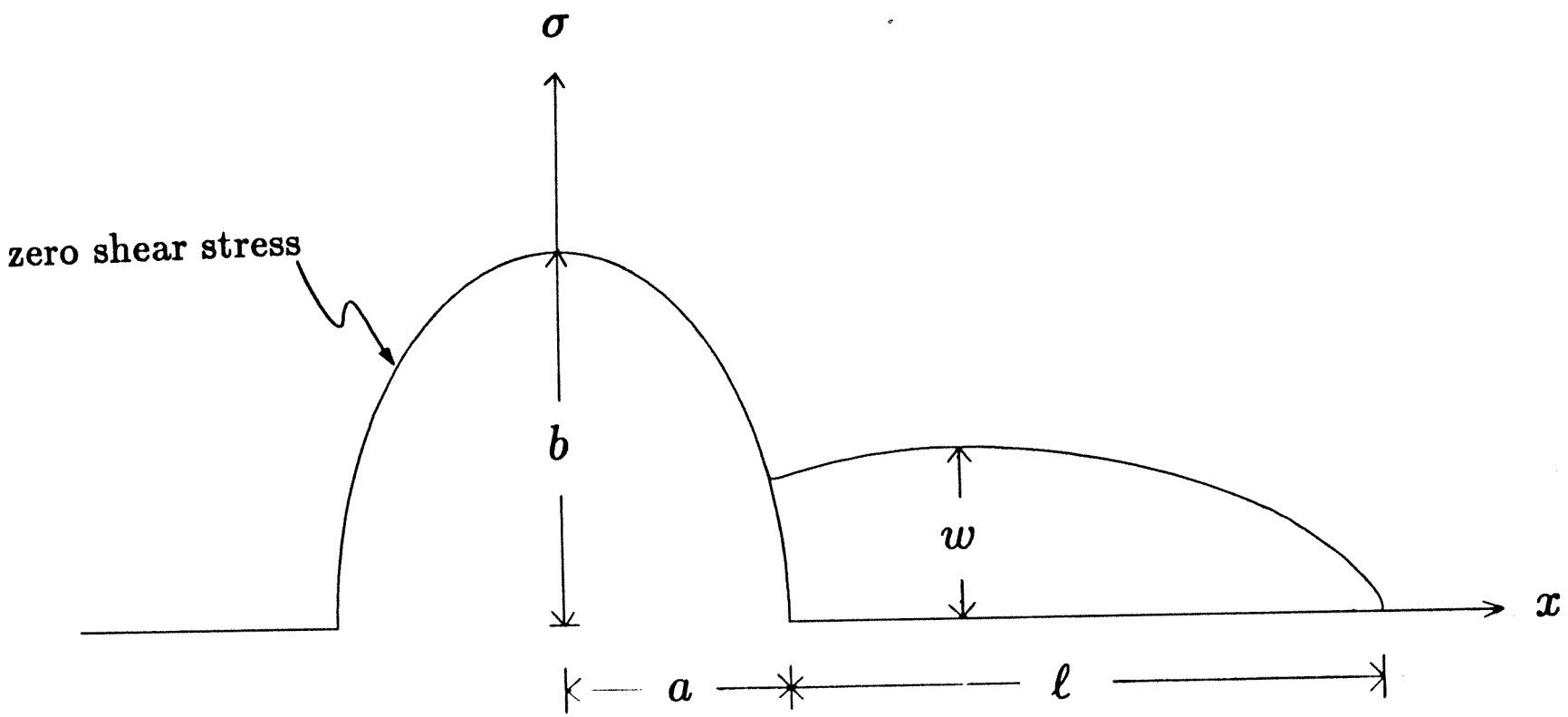

Figure 1.

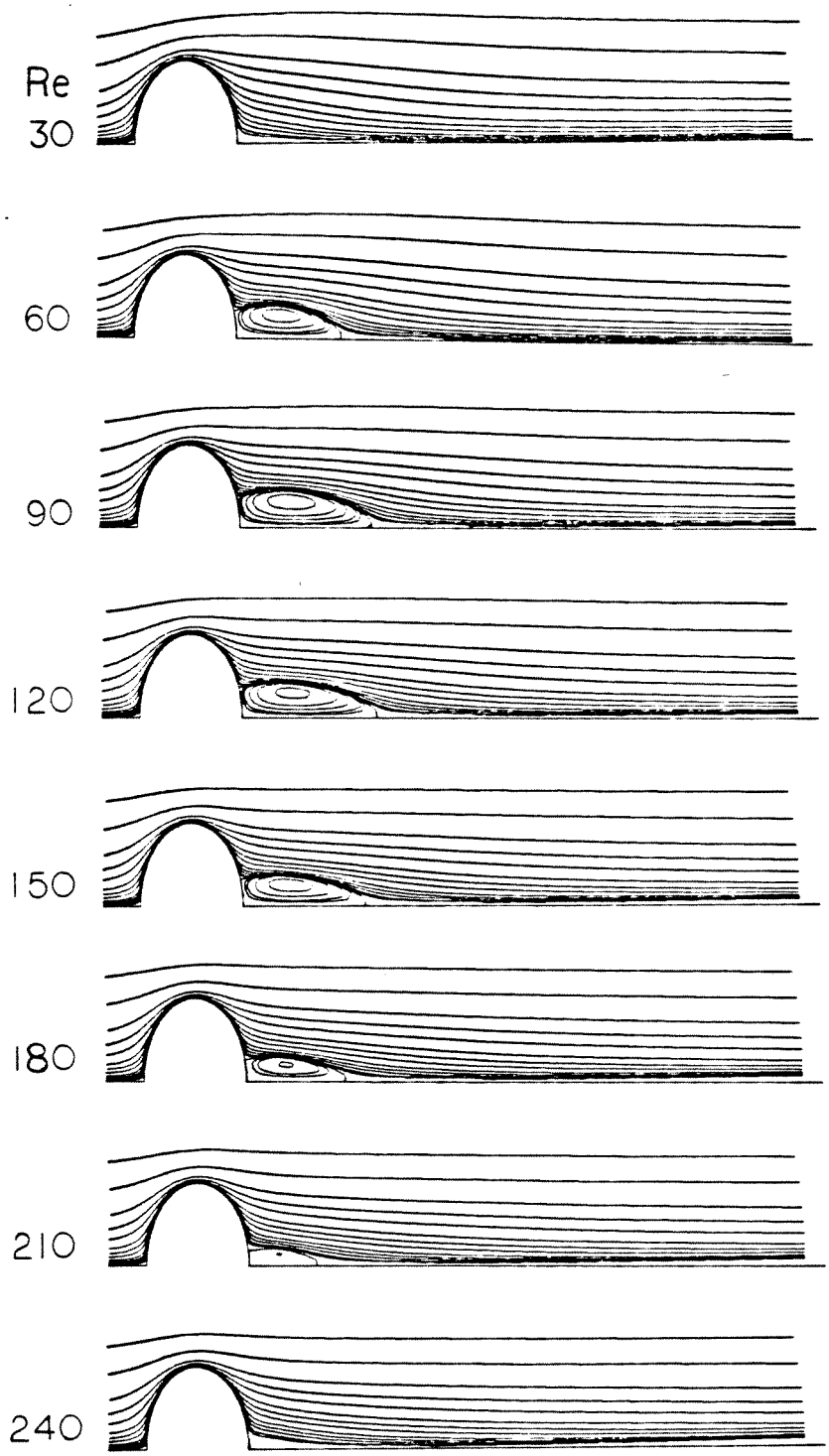

Figure 2.

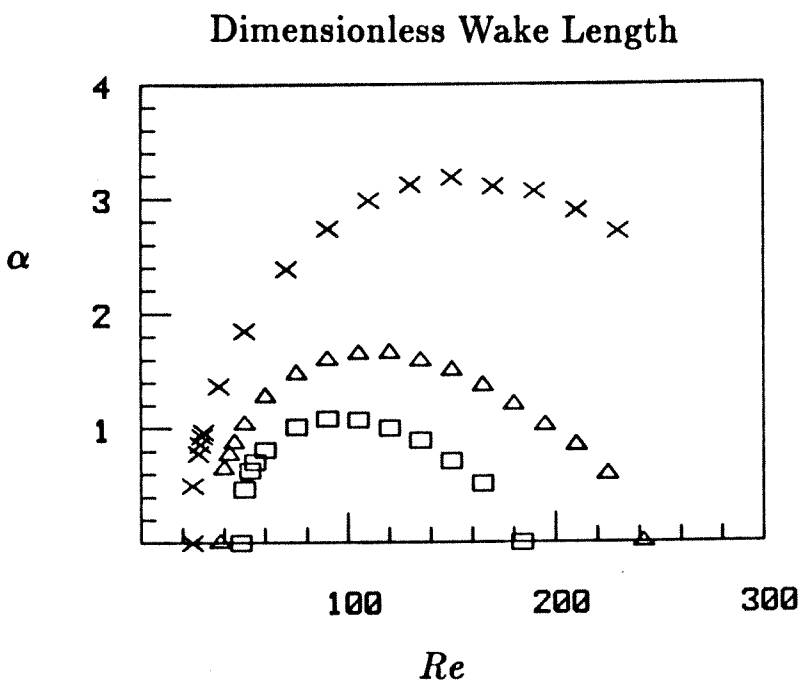

(a)

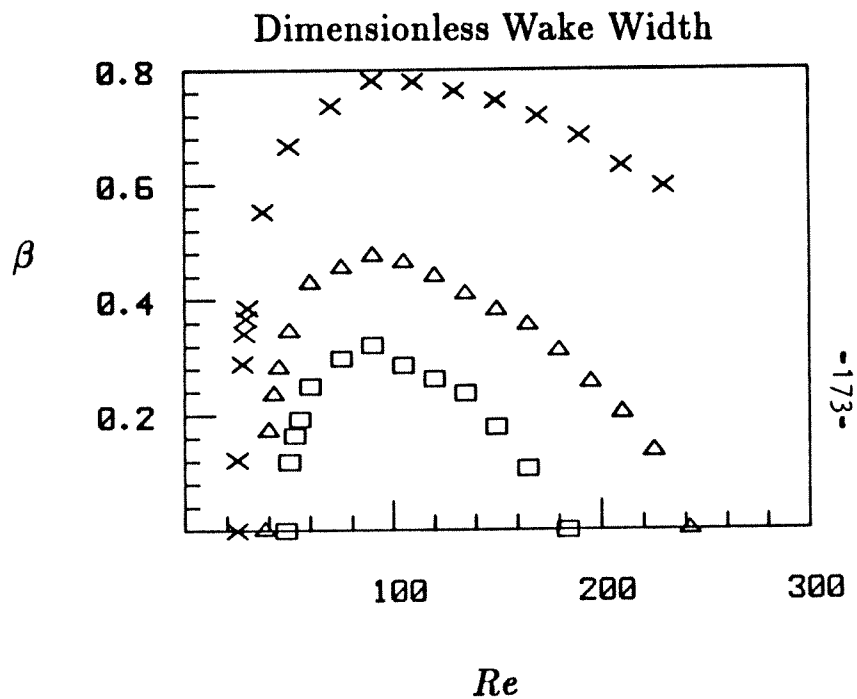

(b)

Figure 3.

$$\varsigma = \begin{cases} 1.60 - \square \\ 1.65 - \triangle \\ 1.84 - \times \end{cases}$$

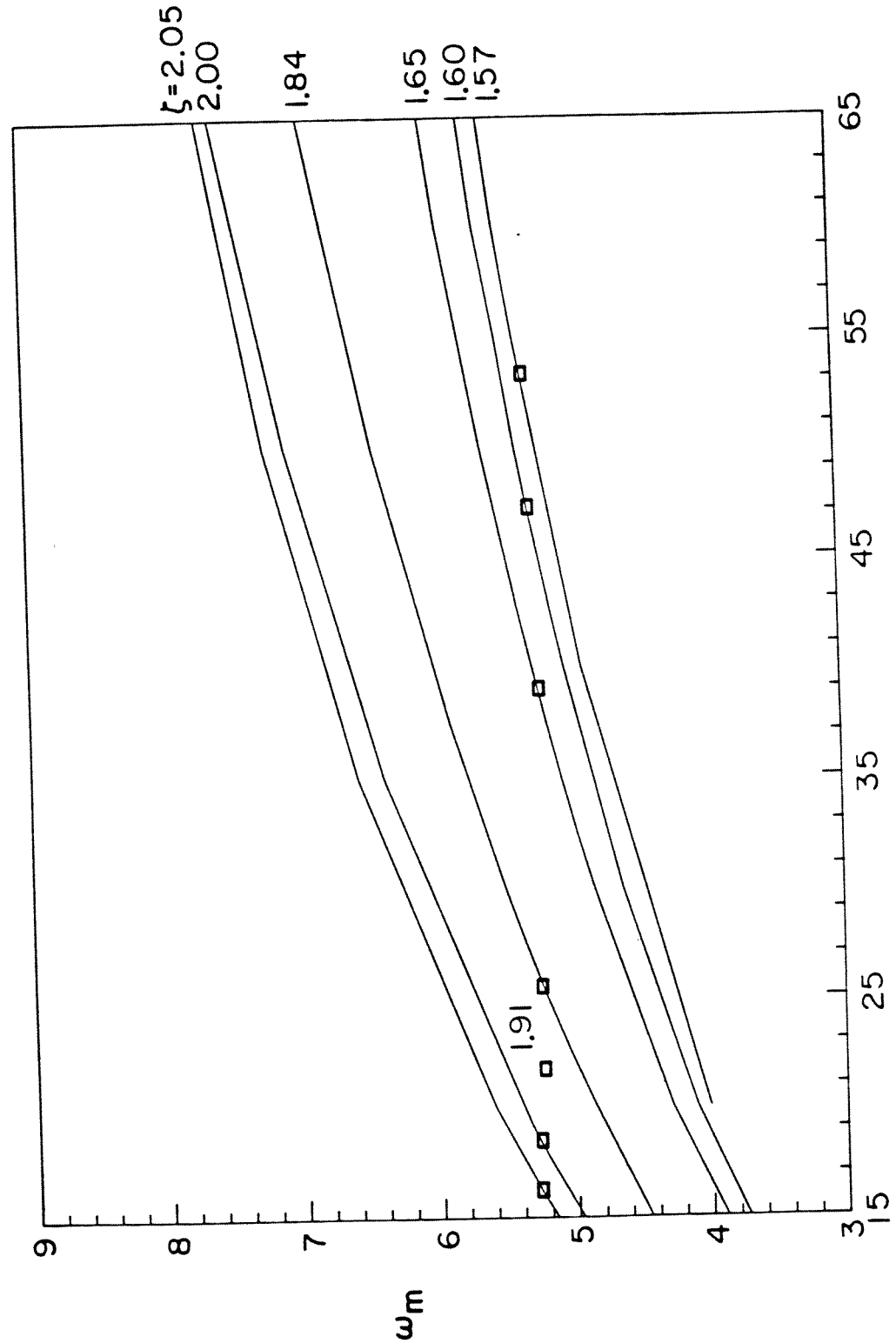

Figure 4.

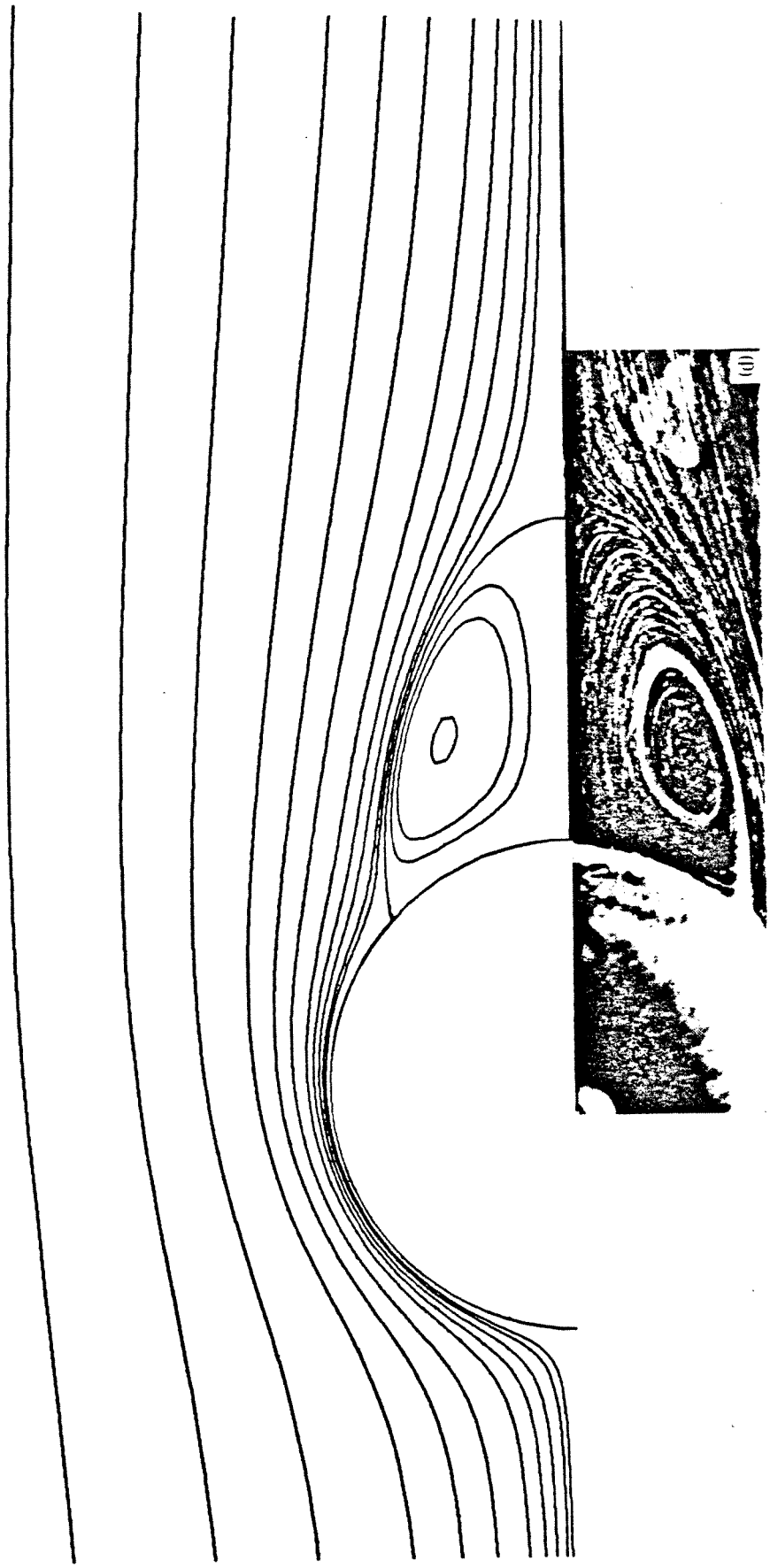

Re = 73.6

Figure 5a.

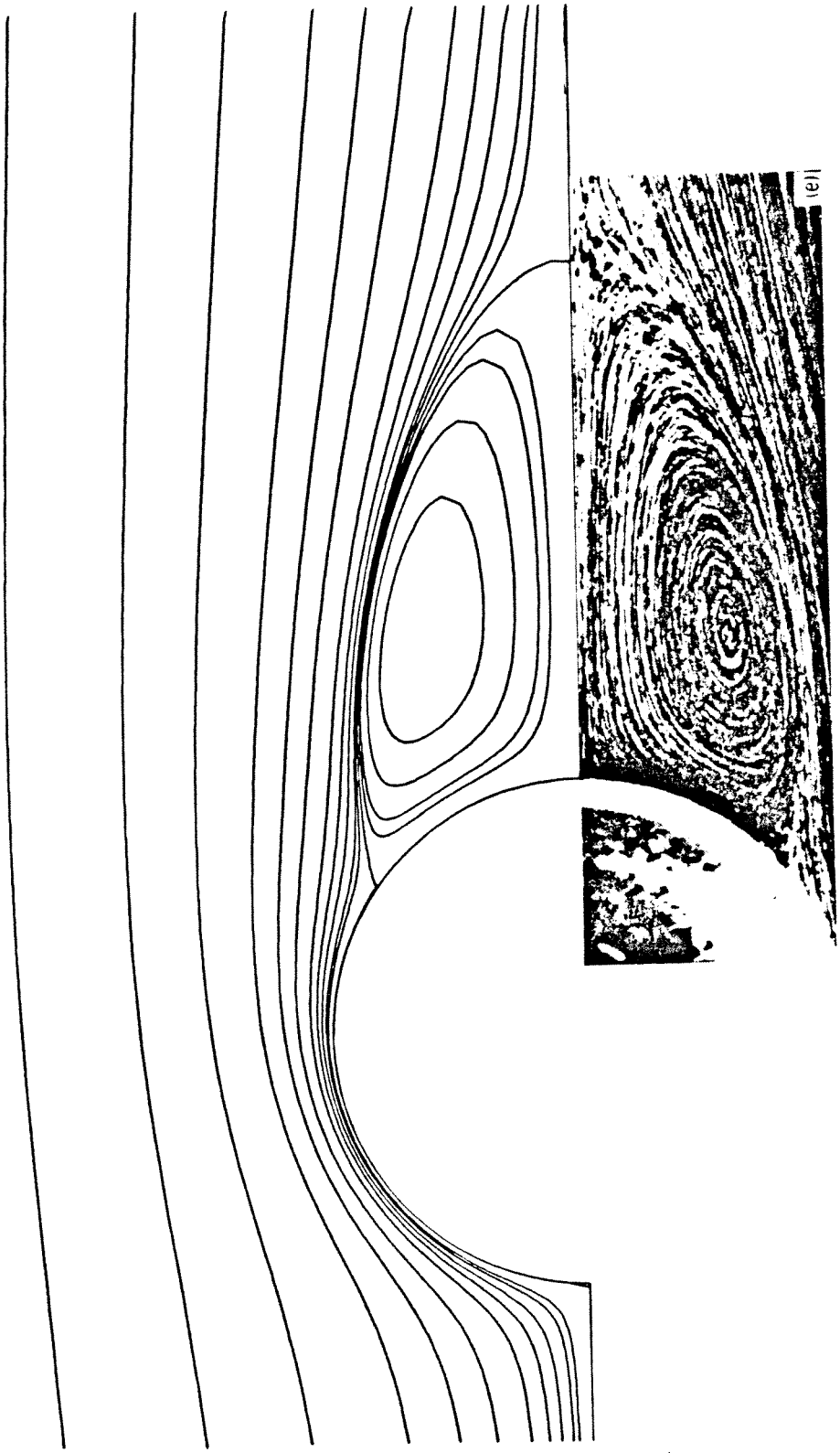

Re = 118

Figure 5b.

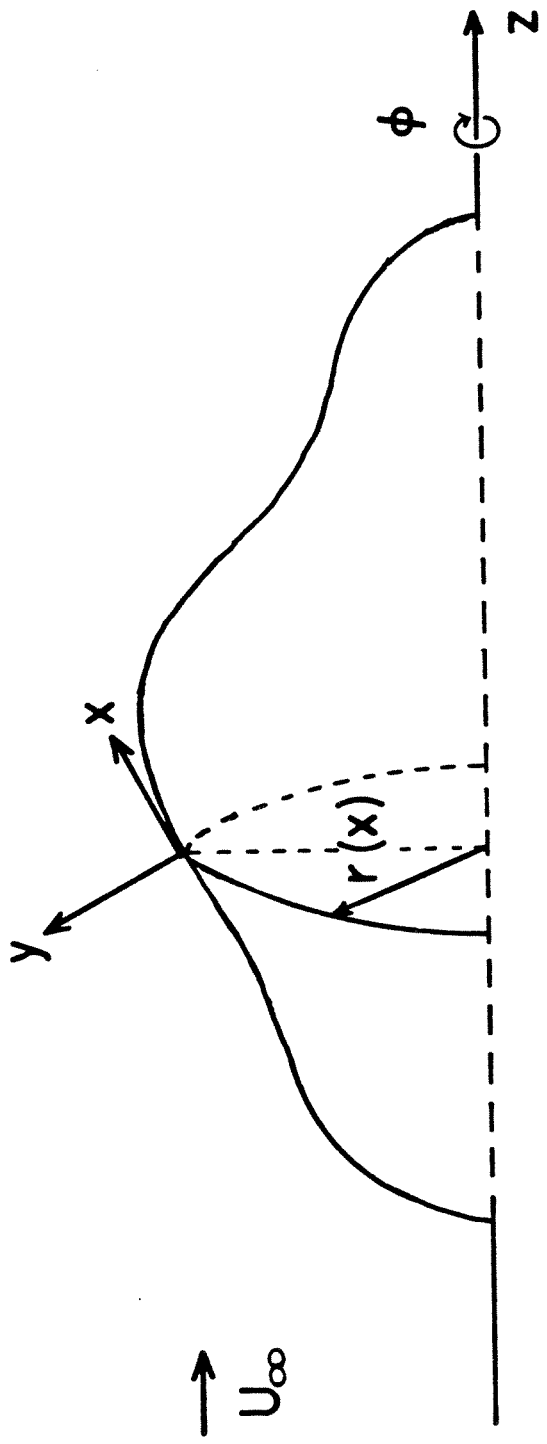

Figure A1.

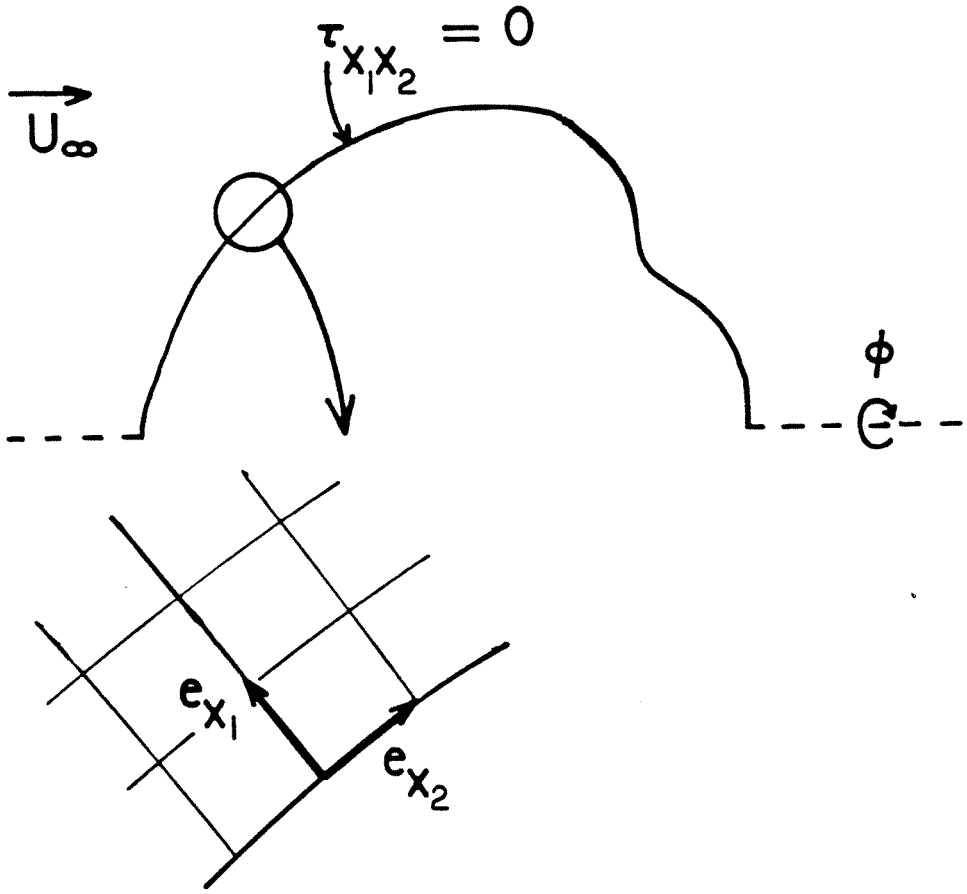

Figure A2.

Chapter III

Development of a Newton's method scheme for intermediate Reynolds number free-surface flow problems

I. Introduction

The theoretical study of the buoyancy-driven motion of a deformable bubble provides physical insight into the nature of transport processes near a free-surface, particularly at intermediate Reynolds numbers, where observed phenomena cannot be explained by any existing asymptotic theories. For example, both the shape and the flowfield can dramatically affect quantities such as heat or mass flux (Sundarajan and Ayyaswamy 1984).

There are some quite interesting and innovative numerical techniques which employ the boundary integral method for studying highly deformed, time dependent interfaces (Geller *et al* 1986; Appendix II, in this thesis; Miksis *et al* 1981). Unfortunately, this method is restricted to creeping or potential flow.

To date, much of the numerical work done in the more general area of intermediate Reynolds number free-surface flows has centered around the use of finite element techniques. Finite elements gained an early foothold in the intermediate Reynolds number category because of the difficulties encountered in finding suitable coordinate geometries for use with finite difference techniques. Early attempts at using finite differences were restricted to problems with domain boundaries coinciding with analytical coordinate lines, or else resorted to describing the boundaries and accompanying boundary conditions by interpolation between nodal points on the pre-assigned finite difference grid. However, finite difference techniques are slowly growing in popularity due to the advent of boundary-fitted grid generation techniques (Thompson *et al* 1985). Two examples of the use of finite differences for the motion of bubbles at intermediate Reynolds numbers are Ryskin and Leal (1984) and Christov and Volkov (1985). Although these two groups worked on the same problem, the first used an orthogonal boundary-fitted grid and the second a non-orthogonal grid. These works, together with Dandy and Leal (1987), represent *all* of the finite difference contributions to the intermediate Reynolds number free-surface flow area so far as we are aware. The general numerical technique used in all three of

these studies was successive approximations with the calculation of the interface shape decoupled from the flow variables.

Because of the quadratic nonlinearities present in the Navier-Stokes equations, successive approximation methods can be very slow to converge (that is, many iterations are needed) particularly when extreme under-relaxation is required. An alternative to successive approximations is to simultaneously iterate on all of the unknown variables (flowfield and shape). Equally important, we are trying to solve a set of coupled, nonlinear partial differential equations and boundary conditions, for which no theory exists on solution existence, uniqueness or boundedness. Consequently, it is of extreme interest to know the dependence of the solution on the dimensionless parameters of the problem—Reynolds number and Weber number—and Newton's method, which achieves quadratic convergence, provides us with powerful techniques for computer-aided study of this dependence, along with the ability to examine multiplicity (Brown *et al* 1980).

In this chapter, we will describe the use of Newton's method to solve the Navier-Stokes equations and boundary conditions for the shape and flowfield for a buoyant deformable bubble, using a solution of Laplaces equation to describe an orthogonal boundary-fitted coordinate grid, and finite difference approximations for all equations and boundary conditions. To implement Newton's method for this problem, it is necessary to include as unknowns not only the shape and flow variables, but also the mapping variables. We demonstrate that Newton's method is indeed a viable means of solving problems of this type.

II. Formulation

In this section we will discuss the formulation of the problem and the method of solution. We consider a gas bubble (void) that is assumed to undergo a steady rectilinear motion, due to the action of gravity, through an outer quiescient liquid. The continuous phase is characterized by a constant viscosity μ and density ρ. The interface is assumed to be completely described by a single constant parameter, the surface tension γ. As shown in Fig. 1, the geometry of the system is represented by cylindrical coordinates (z, σ, ϕ). We assume that the motion of the drop is rectilinear and thus that the shape and flowfield are both axisymmetric; therefore, all quantities are independent of ϕ. It is also assumed that both the dispersed and continuous phases are incompressible, and the volume of the bubble is therefore constant.

The position of the interface is represented by $r = g(\theta)$ in the spherical coordinate variables (r, θ, ϕ). The reason for representing the surface position in spherical variables rather than the cylindrical coordinate geometry mentioned above is that the cylindrical representation becomes double-valued in cases when a dimple forms at the rear of the bubble. We define a function R such that $R = r - g(\theta) = 0$. Then, the unit normal at the interface is

$$\begin{aligned} \mathbf{n} &= \frac{\nabla R}{\|\nabla R\|} \\ &= \left(g\,\mathbf{e}_r - g'\,\mathbf{e}_\theta\right) / K, \end{aligned} \tag{1}$$

where $g' = dg/d\theta$ and

$$K = \left[g^2 + (g')^2\right]^{1/2}.$$

Similarly, the unit tangent vector at the surface is

$$\mathbf{t} = \left(g'\,\mathbf{e}_r + g\,\mathbf{e}_\theta\right). \tag{2}$$

Because we are describing our system geometry in cylindrical coordinates it is necessary to transform the components of $\mathbf{n}$ and $\mathbf{t}$ from the local spherical to

cylindrical system. Since

$$\mathbf{e}_r = \mathbf{e}_\sigma \sin\theta + \mathbf{e}_z \cos\theta$$
$$\mathbf{e}_\theta = \mathbf{e}_\sigma \cos\theta - \mathbf{e}_z \sin\theta,$$

then

$$\begin{aligned} \mathbf{n} &= \frac{1}{K}\Big[\big(g\sin\theta - g'\cos\theta\big)\mathbf{e}_\sigma + \big(g\cos\theta + g'\sin\theta\big)\mathbf{e}_z\Big] \\ \mathbf{t} &= \frac{1}{K}\Big[\big(g'\sin\theta + g\cos\theta\big)\mathbf{e}_\sigma + \big(g'\cos\theta - g\sin\theta\big)\mathbf{e}_z\Big] \end{aligned} \tag{3}$$

Application of Newton's method to the solution of a system of algebraic equations is straightforward: the vector set of equations is symbolically represented by $\mathbf{G}(\mathbf{x};\ Re,\ We) = 0$, where $\mathbf{x}$ is the vector of unknowns. If we start with a "reasonable" initial guess $\mathbf{x}^{(\circ)}$, then at the $(n+1)$-st iteration, or Newton step, the approximation to the solution is

$$\mathbf{x}^{(n+1)} = \mathbf{x}^{(n)} - \big(\mathbf{A}^{(n)}\big)^{-1}\mathbf{G}^{(n)},$$

where $\mathbf{A}$ is the Jacobian matrix defined by $\mathbf{A} = \partial\mathbf{G}/\partial\mathbf{x}$. The difficulty comes in computing the elements of $\mathbf{A}$.

Although the goal of this work is to develop a scheme which will simultaneously solve for all unknowns in the system, we will present the formulation in three parts: the mapping equations, the flow equations and the complete problem. This fragmentation provides us with a means of checking the reliability of the components of the overall scheme.

a. The mapping equations

As was pointed out in Chapter I, axisymmetry enables us to simplify the mapping problem from construction of a three dimensional grid to a two dimensional grid. For reasons also mentioned in Chapter I, we perform an inverse conformal mapping to map the infinite flow domain to a finite auxilliary domain. We then solve the Laplace equations to obtain a discrete set $z^*(\xi,\eta)$ and $\sigma^*(\xi,\eta)$.

Inclusion of *all* equations and unknowns in a Newton's scheme requires use of the weak constraint method (Ryskin and Leal 1983); in particular, the explicit description of the interface position with a function $g(\theta)$ requires that the distortion function $f(\xi,\eta)$ be implicitly specified. Through the shape function g we are specifying the boundary correspondence, and therefore if $f(1,\eta)$ is also specified, the mapping problem will be over-determined. Thus, so long as we do not specify $f(1,\eta)$, we are free to determine $f(\xi,\eta)$ for $\xi < 1$ (that is, in the interior of the domain) with a variety of methods (Ryskin and Leal 1983; Chikhiwala and Yortsos 1985). The "formula" used to obtain f in the interior must be linear in the curvilinear coordinates (ξ,η) so that orthogonality is preserved. In the present work, to calculate f in the interior, we have chosen a simple interpolation formula, which will be presented below.

For the duration of this chapter, a shorthand notation will be used: partial derivatives of the dependent variables with respect to ξ will be denoted by the subscript x, and partial derivatives of the same variables with respect to η will be denoted by the subscript y. These subscripts are used to distinguish derivatives from components: $u_y = \partial u/\partial\eta$ whereas u_η is the component of velocity in the η direction.

In this shorthand notation, the equations describing the mapping are

$$f^2 z^*_{xx} + z^*_{yy} + f f_x z^*_x - f_y z^*_y/f = 0 \tag{4a}$$

and

$$f^2 \sigma^*_{xx} + \sigma^*_{yy} + f f_x \sigma^*_x - f_y \sigma^*_y/f = 0, \tag{4b}$$

where

$$\begin{aligned} f(\xi,\eta) = {} & \xi f(1,\eta) + (1-\eta) f(\xi,0) + \eta f(\xi,1) \\ & - \xi(1-\eta) f(1,0) - \xi\eta f(1,1). \end{aligned} \tag{4c}$$

Remember that the distortion function at the interface $\xi = 1$ is also unknown, and if we are to use a Newton's method to solve the mapping equations we must include $f(1,\eta)$ in the set of unknowns. For the required set of extra equations,

we use the definition of the distortion function:

$$\alpha(\eta) - \left[z_y^{*2} + \sigma_y^{*2}\right]^{1/2}\left[z_x^{*2} + \sigma_x^{*2}\right]^{-1/2}\Big|_{\xi=1} = 0. \qquad (4d)$$

We will use the notation $\alpha(\eta) \equiv f(1,\eta)$ throughout the rest of the chapter. The mapping functions must satisfy the following boundary conditions:

$$z^* = \sigma^* = 0 \qquad \text{at } (\xi,\eta) = (0,0) \qquad (5a)$$

$$\sigma^* = z_y^* = 0 \qquad \text{at } \eta = 0,1 \quad 0 < \xi < 1 \qquad (5b)$$

and

$$z^* = \cos\theta\,/\,g \qquad \sigma^* = \sin\theta\,/\,g \qquad \text{at } \xi = 1 \quad 0 \le \eta \le 1 \qquad (5c).$$

Because of the form of the boundary condition (5b) we have the freedom to specify the distortion function at the two boundaries $\eta = 0, 1$. This enables us to maintain some control over the grid spacing in the domain interior. Symbolically, we represent the choices of these distortion functions as $f(\xi,0) = a(\xi)$ and $f(\xi,1) = b(\xi)$, but in practice we chose $a(\xi) = b(\xi) = \pi\,\xi$. Using these values, the formula for the distortion function and it derivatives are

$$f(\xi,\eta) = \xi\alpha(\eta) + (1-\eta)a(\xi) + \eta b(\xi) - \xi(1-\eta)\alpha(0) - \xi\eta\alpha(1), \qquad (6a)$$

$$f_x(\xi,\eta) = \alpha(\eta) + (1-\eta)a_x(\xi) + \eta b_x(\xi) - (1-\eta)\alpha(0) - \eta\alpha(1), \qquad (6b)$$

and

$$f_y(\xi,\eta) = \xi\alpha_y(\eta) - a(\xi) + b(\xi) + \xi\alpha(0) - \xi\alpha(1). \qquad (6c)$$

It should be noted that in order to actually solve the Eqs. (4) subject to the the boudary conditions (5), another set of equations must be included if $g(\theta)$ is unknown. If, however, g is specified, Eqs. (4) and (5) constitute a well-posed problem.

To generate the set of algebraic equations that will be solved using Newton's method, we must discretize the differential equations and boundary conditions.

The derivatives are approximated using centered, second-order finite differences and, if we use a square computational grid with an equal number of nodes in both the ξ and η directions, we arrive at the functions

$$
\begin{aligned}
H_{ij} &= f_{ij}\left(f_{ij}+\epsilon(f_x)_{ij}\right)z^*_{i+1j} - 2\left(1+f_{ij}^2\right)z^*_{ij} + f_{ij}\left(f_{ij}-\epsilon(f_x)_{ij}\right)z^*_{i-1j} \\
&\quad + \left(1-\epsilon(f_y)_{ij}/f_{ij}\right)z^*_{ij+1} + \left(1+\epsilon(f_y)_{ij}/f_{ij}\right)z^*_{ij-1} = 0 \\
L_{ij} &= f_{ij}\left(f_{ij}+\epsilon(f_x)_{ij}\right)\sigma^*_{i+1j} - 2\left(1+f_{ij}^2\right)\sigma^*_{ij} + f_{ij}\left(f_{ij}-\epsilon(f_x)_{ij}\right)\sigma^*_{i-1j} \\
&\quad + \left(1-\epsilon(f_y)_{ij}/f_{ij}\right)\sigma^*_{ij+1} + \left(1+\epsilon(f_y)_{ij}/f_{ij}\right)\sigma^*_{ij-1} = 0, \\
P_{ij} &= \alpha_j - \Big[\left(\cos\theta_{j+1}/g_{j+1} - \cos\theta_{j-1}/g_{j-1}\right)^2 \\
&\quad + \left(\sin\theta_{j+1}/g_{j+1} - \sin\theta_{j-1}/g_{j-1}\right)^2\Big]^{1/2} \\
&\quad \times \Big[\left(3\cos\theta_j/g_j - 4z^*_{N-1j} + z^*_{N-2j}\right)^2 \\
&\quad + \left(3\sin\theta_j/g_j - 4\sigma^*_{N-1j} + \sigma^*_{N-2j}\right)^2\Big]^{-1/2} \\
&= 0,
\end{aligned}
\tag{7}
$$

$1 \le i,j \le N$, where $\epsilon = h/2$, and h is the mesh size; $h = 1/(N-1)$, where N is the number of mesh points in either the ξ or η directions. Assuming that $a(\xi) = b(\xi) = \pi\xi$,

$$f_{ij} = \xi_i\alpha_j + \pi\xi - \xi_i(1-\eta_j)\alpha_1 - \xi_i\eta_j\alpha_N, \tag{8a}$$

$$\left(f_x\right)_{ij} = \alpha_j + \pi - (1-\eta_j)\alpha_1 - \eta_j\alpha_N, \tag{8b}$$

$$\left(f_y\right)_{ij} = \xi_i\frac{\alpha_{j+1}-\alpha_{j-1}}{2h} + \xi_i(\alpha_1 - \alpha_N) \tag{8c}$$

The elements of the Jacobian matrix can then be computed by taking the Frechet derivatives of the algebraic equations (7). The details of this are shown in the appendix.

As an example of the size of the Jacobian matrix generated in this mapping problem, consider a square computational grid with 61 grid points on a side. In this case, for the mapping problem, the Jacobian is of order 7021. To make the numerical computations as efficient as possible, the band structure of the

Jacobian should be tight, and to achieve this tightness, care must be taken in the ordering of the equations. If we take the straightforward approach and order the equations in the order that they appear, that is, first the equations for z^*, then the equations for σ^* and finally the equations for α, we obtain a matrix with the non-zero structure shown in Fig. 2. The bandwidth is over 3500, and the level of fill would be enormous. If, however, we are more careful about the ordering, we can reduce the bandwidth to 118. Consider the representation of the computational grid shown in Fig. 3: because of the boundary conditions at the perimeter, we only have to solve the interior $(N-2)^2$ equations. To order the equations, we start at $i, j = 2$. The equations for z^* are numbered at this i for $j = 2, \cdots, N-1$, followed by the equations for σ^*. This sequence is then carried out at $i = 3, \cdots, N-1$ so that we end up $(N-2)^2$ equations, with alternating blocks of $N-2$ z^* and σ^* equations. Last we write the $N-2$ equations for α. Actually, z^*_{i1}, z^*_{iN}, α_1 and α_N are also unknown, but we can use Eq. (5b) and symmetry to write these variables in terms of the other unknowns. With the equations ordered in this manner, the band structure of the Jacobian takes the form shown in Fig. 4; the block-column of "N"-shaped structures in the matrix arise from the dependence of the equations on the distortion function α.

To check the formulation of the mapping equations we ran several tests: first, we considered the situation where the boundary shape (i.e., $g(\theta)$) is known. Then there are 7021 equations and unknowns. In the second test, we assumed that $g(\theta)$ was *not* known, but was required to satisfy an equation which specified the curvature at $\xi = 1$ (that is, $\nabla \cdot \mathbf{n}$ is known at each point on the surface; the set of equations is denoted by C_j, $2 \leq j \leq N-1$. This will be discussed in more detail in subsection (c)). The curvatures were chosen so that the final surface shape was the same as the one specified in the first test. In the second test, there are 7080 equations and unknowns. The band structure of this Jacobian is shown in Fig. 5. Results of these two tests were compared against each other, and with grids generated using the ADI scheme of Peacemann and Rachford

(1955). Several examples of these grids are shown in Figs. 6. The grids are everywhere orthogonal to within less than one percent and the results obtained using Newton's method agree with the ADI results to within 0.0001 percent. The difference between the Newton results and the ADI results is that it took 2 Newton steps to achieve convergence, and 1500-3000 ADI steps to achieve the same convergence.

As an aside, we also used Newton's method to experiment on the strong constraint method, in which $f(\xi,\eta)$ is explicitly specified everywhere in the domain. At $\xi = 1$, the boundary conditions on the unknowns are $\sigma^* =$ specified, and $z_x^* =$ specified. With the Neumann condition on z^* at $\xi = 1$, we have no control of the resulting boundary shape (unless we know *a priori* the correspondence between derivative and function), but the strong constraint method does nonetheless have its strengths (Ryskin and Leal 1984). We found that the strong constraint scheme would frequently converge in just 1 Newton step.

b. The flow equations

Due to the axisymmetry of the problem, it is convenient to cast the flow equations in terms of the streamfunction and vorticity rather than the primitive variables $\mathbf{u}$, p. The process for arriving at the final equations is carried out in detail elsewhere (Chapter II), but we will briefly review the steps here. First the steady Navier-Stokes and continuity equations are non-dimensionalized using a characteristic length a (the radius of an undeformed bubble of volume $\frac{4}{3}\pi a^3$), a characteric velocity U_∞ (the uniform streaming velocity at infinity) and a pressure scale $\frac{1}{2}\rho U_\infty^2$. The resulting equations contain the Reynolds number Re, which is defined as $Re = 2\rho a U_\infty/\mu$. The curl of the dimensionless Navier-Stokes equations is taken and we obtain an equation in terms of the vorticity $\omega \mathbf{e}_\phi$ and velocity $\mathbf{u}$. We then define the components of the velocities in the general (ξ,η) coordinate system using the streamfunction ψ:

$$u_\xi = -\frac{1}{\sigma h_\eta}\frac{\partial \psi}{\partial \eta}$$

$$u_\eta = \frac{1}{\sigma h_\xi}\frac{\partial \psi}{\partial \xi},$$

and substitute into the velocity-vorticity formulation to obtain

$$\mathcal{L}^2(\omega\sigma) - \frac{1}{2}\frac{Re}{h_\xi h_\eta}\left[\frac{u_\xi}{h_\xi}\frac{\partial}{\partial \xi}\left(\frac{\omega}{\sigma}\right) + \frac{u_\eta}{h_\eta}\frac{\partial}{\partial \eta}\left(\frac{\omega}{\sigma}\right)\right] = 0 \tag{9a}$$

$$\mathcal{L}^2\psi + \omega = 0, \tag{9b}$$

where

$$\mathcal{L}^2 \equiv \frac{1}{h_\xi h_\eta}\left[\frac{\partial}{\partial \xi}\left(\frac{f}{\sigma}\frac{\partial}{\partial \xi}\right) + \frac{\partial}{\partial \eta}\left(\frac{1}{f\sigma}\frac{\partial}{\partial \eta}\right)\right].$$

The scale factors of the coordinate system are

$$h_\xi = \left[\left(\frac{\partial z}{\partial \xi}\right)^2 + \left(\frac{\partial \sigma}{\partial \xi}\right)^2\right]^{1/2}$$

$$h_\eta = \left[\left(\frac{\partial z}{\partial \eta}\right)^2 + \left(\frac{\partial \sigma}{\partial \eta}\right)^2\right]^{1/2}$$

and the distortion function is

$$f = \frac{h_\eta}{h_\xi}.$$

When the operators in Eqs. (9) are expanded, we obtain the following:

$$\begin{aligned} f^2\omega_{xx} + \omega_{yy} + f\big(f_x + \frac{f}{\sigma}\sigma_x - \frac{Re}{2}h_\eta u_\xi\big)\omega_x \\ + \big(\frac{1}{\sigma}\sigma_y - \frac{1}{f}f_y - \frac{Re}{2}h_\eta u_\eta\big)\omega_y + \Big[\frac{Re}{2\sigma}h_\eta\big(f u_\xi \sigma_x + u_\eta \sigma_y\big) \\ - \frac{1}{\sigma^2}\big(f^2\sigma_x^2 + \sigma_y^2\big)\Big]\omega = 0, \end{aligned} \tag{10a}$$

and

$$\begin{aligned} f^2\psi^*_{xx} + \psi^*_{yy} + f\big(f_x - \frac{f}{\sigma}\sigma_x\big)\psi^*_x \\ - \big(\frac{1}{f}f_y + \frac{1}{\sigma}\sigma_y\big)\psi^*_y - 3f\xi\sigma\big(\frac{3}{2}f\xi\sigma_x + \frac{1}{2}\xi\sigma f_x + f\sigma\big) \\ + h_\eta^2\sigma\omega = 0. \end{aligned} \tag{10b}$$

Since ψ asymptotically approaches infinite values as $\sigma \longrightarrow \infty$, we have defined a modified streamfunction $\psi^* = \psi - \frac{1}{2}\sigma^2(1-\xi^3)$ which is bounded at infinity. With this modified streamfunction, we can write the velocity components as

$$h_\eta u_\xi = -\frac{1}{\sigma}\psi^*_y - (1-\xi^3)\sigma_y$$

and

$$h_\eta u_\eta = f\Big[\frac{1}{\sigma}\psi^*_x + (1-\xi^3)\sigma_x - \frac{3}{2}\sigma\xi^2\Big].$$

The boundary conditions for the flow equations require a detailed explanation, and this will be presented in a later section.

Note that the unknowns appearing in Eqs. (10) are ψ^*, ω, z and σ; but from the previous section, the coordinate unknowns are z^* and σ^*. Thus, everywhere that z, σ, and their derivatives appear in the governing equations and boundary conditions for the flow, the definitions appearing in Chapter I must be used to write all of these variables in terms of the auxilliary mapping variables z^* and σ^*. Also, note that the distortion function appearing in Eqs. (10) is the same as presented in (a) in Eqs. (6).

When we write the flow equations in finite difference form, the resulting algebraic equations are:

$$\begin{aligned} F_{ij} &= \big(f_{ij}^2 + \epsilon q_{1_{ij}}\big)\omega_{i+1j} + \big(q_{3_{ij}}h^2 - 2f_{ij}^2 - 2\big)\omega_{ij} \\ &\quad + \big(f_{ij}^2 - \epsilon q_{1_{ij}}\big)\omega_{i-1j} + \big(1+\epsilon q_{2_{ij}}\big)\omega_{ij+1} + \big(1-\epsilon q_{2_{ij}}\big)\omega_{ij-1} \qquad (11a) \\ &= 0 \end{aligned}$$

and

$$\begin{aligned} G_{ij} &= \big(f_{ij}^2 + w_{1_{ij}}\big)\psi^*_{i+1j} - 2\big(1+f_{ij}^2\big)\psi^*_{ij} + \big(f_{ij}^2 - \epsilon w_{1_{ij}}\big)\psi^*_{i-1j} \\ &\quad + \big(1+\epsilon w_{2_{ij}}\big)\psi^*_{ij+1} + \big(1-\epsilon w_{2_{ij}}\big)\psi^*_{ij-1} + h^2 w_{4_{ij}} \qquad (11b) \\ &= 0, \end{aligned}$$

where the coefficients are given by

$$q_{1_{ij}} = f_{ij}(f_x)_{ij} + \frac{f_{ij}^2}{\sigma_{ij}}(\sigma_x)_{ij} - \frac{Re}{2} f_{ij}(h_\eta u_\xi)_{ij}$$

$$q_{2_{ij}} = \frac{1}{\sigma_{ij}}(\sigma_y)_{ij} - \frac{1}{f_{ij}}(f_y)_{ij} - \frac{Re}{2}(h_\eta u_\eta)_{ij}$$

$$q_{3_{ij}} = \frac{Re}{2\sigma_{ij}}\Big[f_{ij}(h_\eta u_\xi)_{ij}(\sigma_x)_{ij} + (h_\eta u_\eta)_{ij}(\sigma_y)_{ij}\Big] - \frac{1}{\sigma_{ij}^2}\Big[f_{ij}^2(\sigma_x^2)_{ij} + (\sigma_y^2)_{ij}\Big]$$

and

$$w_{1_{ij}} = f_{ij}(f_x)_{ij} - \frac{f_{ij}^2}{\sigma_{ij}}(\sigma_x)_{ij}$$

$$w_{2_{ij}} = -\frac{1}{f_{ij}}(f_y)_{ij} - \frac{1}{\sigma_{ij}}(\sigma_y)_{ij}$$

$$w_{4_{ij}} = -3f_{ij}\xi_i\sigma_{ij}\Big(\frac{3}{2}f_{ij}\xi_i(\sigma_x)_{ij} + \frac{1}{2}\xi_i\sigma_{ij}(f_x)_{ij} + f_{ij}\sigma_{ij}\Big) + h_{\eta_{ij}}^2\sigma_{ij}\omega_{ij}.$$

The expressions for σ_x and σ_y are shown in the Appendix.

To check the formulation of the flow problem, we ran tests at several values of Re and compared them with results obtained using ADI. The tests were carried out by assuming that the shape was fixed, leaving as unknowns $\psi^*(\xi,\eta)$ and $\omega(\xi,\eta)$, $0 < \xi,\eta < 1$. The vorticity at the surface $\omega(1,\eta)$, $0 < \eta < 1$ is also unknown, and we included the tangential stress balance as the additional set of equations. For this problem, there are 7021 equations and unknowns—the structure of the Jacobian is shown in Fig. 7. We found that the Newton results and the ADI results agreed to within 0.00001 per cent. Several example solutions are shown in Figs. 8.

c. The full problem

Integration of the mapping problem and the flow problem obviously increases the complexity of the equations due to the coupling between the flow equations and the mapping variables z^* and σ^*. Additionally, we now relax the restriction on the fixed boundary shape, thereby further increasing the number of unknowns. The inclusion of the unknown $g(\theta)$'s requires the addition of another set of equations, and here we add the normal stress balance.

The set of boundary conditions take the form: along the axes of symmetry,

$$\omega,\ \psi^*,\ z_y^*,\ \sigma^* = 0 \qquad \text{at } \eta = 0,\ 1 \tag{12a}$$

and at infinity,

$$\psi^*,\ \omega,\ z^*,\ \sigma^* = 0 \qquad \text{at } \xi = 0. \tag{12b}$$

At the surface of the drop,

$$\psi^* = 0 \tag{12c}$$

because of zero normal velocity. The two remaining boundary conditions are the two components of the stress balance at the surface:

$$\mathbf{n} \cdot (\mathbf{T} - \hat{\mathbf{T}}) = \frac{4}{We}(\nabla \cdot \mathbf{n})\ \mathbf{n}, \tag{12d}$$

where the Weber number We is $We = 2\rho a U_\infty^2/\gamma$. In terms of the shape function $g(\theta)$, the curvature is

$$\nabla \cdot \mathbf{n} = \frac{2}{K} - \frac{g'}{gK}\cot\theta - \frac{1}{g}\Big[\frac{g''}{K} - \frac{(g')^2}{K^3}(g + g'')\Big], \tag{13}$$

where K is defined at the top of this section. Now, because the shape function is in spherical coordinates and the geometry of the system is in cylindrical coordinates, and also because the computational domain is in the arbitrary curvilinear coordinates (ξ, η), we must transform Eq. (12d) from spherical to cylindrical to curvilinear. To perform these operations, we take the cylindrical representation of $\mathbf{n}$ and $\mathbf{t}$ and operate on the stress tensor $\mathbf{T}$ in Eq. (12d). Upon doing so we obtain the two equations referred to as the normal and tangential stress balances:

$$\begin{aligned} M = {} & \frac{1}{K^2}\Big[\big(g\sin\theta - g'\cos\theta\big)^2\tau_{\sigma\sigma} \\ & + 2\big(g\sin\theta - g'\cos\theta\big)\big(g\cos\theta + g'\sin\theta\big)\tau_{\sigma z} \\ & + \big(g\cos\theta + g'\sin\theta\big)^2\tau_{zz}\Big] - p - \frac{4}{We}\Big\{\frac{2}{K} - \frac{g'}{gK}\cot\theta \\ & - \frac{1}{g}\Big[\frac{g''}{K} - \frac{(g')^2}{K^3}(g + g'')\Big]\Big\} \\ = {} & 0 \end{aligned} \tag{14}$$

and

$$\begin{aligned} N &= \left(g\sin\theta - g'\cos\theta\right)\left(g\cos\theta + g'\sin\theta\right)\left(\tau_{\sigma\sigma} - \tau_{zz}\right) \\ &\quad + \left[\left(g\cos\theta + g'\sin\theta\right)^2 - \left(g\sin\theta - g'\cos\theta\right)^2\right]\tau_{\sigma z} \\ &= 0. \end{aligned} \tag{15}$$

An expression for the pressure p in Eq. (14) is found by taking the η-component of the Navier-Stokes equations and integrating at $\xi = 1$:

$$p = \frac{3}{4}C_D z - u_\eta^2 - \frac{4}{Re}\int \frac{\alpha}{\sigma}\frac{\partial}{\partial\xi}(\omega\sigma)\,d\eta + \lambda,$$

where λ is the unknown constant of integration, and

$$C_D = 2\int_0^1 \sigma\sigma_y\left[u_\eta^2 + \frac{4}{Re}\left(\int^\eta \frac{\alpha}{\sigma}\frac{\partial}{\partial\xi}(\omega\sigma)\,d\hat{\eta} - \frac{2}{\sigma h_\eta}\frac{\partial}{\partial\eta}(u_\eta\sigma)\right)\right]d\eta.$$

Eqs. (14) and (15) contain components of the rate of strain tensor in cylindrical coordinates. It is necessary to represent these tensor components in terms of the curvilinear coordinate variables. We know that

$$\begin{aligned} \tau_{\sigma\sigma} &= \frac{8}{Re}\frac{\partial u_\sigma}{\partial\sigma} \\ &= -\frac{8}{Re}\left\{\frac{\sigma_x}{h_\xi^2}\left[\frac{z_x}{h_\xi}u_{\eta_x} + \frac{u_\eta}{h_\xi}\left(z_{xx} - \frac{z_x}{h_\xi^2}\left(z_x z_{xx} + \sigma_x\sigma_{xx}\right)\right) - \frac{z_y}{h_\eta}u_{\xi_x}\right]\right. \\ &\quad \left. + \frac{\sigma_y}{h_\eta^2}\left[\frac{z_x}{h_\xi}u_{\eta_y} + \frac{u_\eta}{h_\xi}\left(z_{xy} - \frac{z_x}{h_\xi^2}\left(z_x z_{xy} + \sigma_x\sigma_{xy}\right)\right)\right]\right\} \end{aligned} \tag{16}$$

$$\begin{aligned} \tau_{zz} &= \frac{8}{Re}\frac{\partial u_z}{\partial z} \\ &= \frac{8}{Re}\left\{\frac{z_x}{h_\xi^2}\left[\frac{\sigma_x}{h_\xi}u_{\eta_x} + \frac{u_\eta}{h_\xi}\left(\sigma_{xx} - \frac{\sigma_x}{h_\xi^2}\left(z_x z_{xx} + \sigma_x\sigma_{xx}\right)\right) - \frac{\sigma_y}{h_\eta}u_{\xi_x}\right]\right. \\ &\quad \left. + \frac{z_y}{h_\eta^2}\left[\frac{\sigma_x}{h_\xi}u_{\eta_y} + \frac{u_\eta}{h_\xi}\left(\sigma_{xy} - \frac{\sigma_x}{h_\xi^2}\left(z_x z_{xy} + \sigma_x\sigma_{xy}\right)\right)\right]\right\} \end{aligned} \tag{17}$$

$$
\begin{aligned}
\tau_{\sigma z} &= \frac{4}{Re}\Big(\frac{\partial u_\sigma}{\partial z} + \frac{\partial u_z}{\partial \sigma}\Big) \\
&= \frac{4}{Re}\Big\{-\frac{z_x}{h_\xi^2}\Big[\frac{z_x}{h_\xi}u_{\eta_x} + \frac{u_\eta}{h_\xi}\big(z_{xx} - \frac{z_x}{h_\xi^2}(z_x z_{xx} + \sigma_x \sigma_{xx})\big) - \frac{z_y}{h_\eta}u_{\xi_x}\Big] \\
&\quad - \frac{z_y}{h_\eta^2}\Big[\frac{z_x}{h_\xi}u_{\eta_y} + \frac{u_\eta}{h_\xi}\big(z_{xy} - \frac{z_x}{h_\xi^2}(z_x z_{xy} + \sigma_x \sigma_{xy})\big)\Big] \\
&\quad + \frac{\sigma_x}{h_\xi^2}\Big[\frac{\sigma_x}{h_\xi}u_{\eta_x} + \frac{u_\eta}{h_\xi}\big(\sigma_{xx} - \frac{\sigma_x}{h_\xi^2}(z_x z_{xx} + \sigma_x \sigma_{xx})\big) - \frac{\sigma_y}{h_\eta}u_{\xi_x}\Big] \\
&\quad + \frac{\sigma_y}{h_\eta^2}\Big[\frac{\sigma_x}{h_\xi}u_{\eta_y} + \frac{u_\eta}{h_\xi}\big(\sigma_{xy} - \frac{\sigma_x}{h_\xi^2}(z_x z_{xy} + \sigma_x \sigma_{xy})\big)\Big]\Big\}.
\end{aligned}
\tag{18}
$$

At $\xi = 1$ the derivatives of u_η and u_ξ are

$$
\begin{aligned}
u_{\eta_x} &= \frac{1}{\sigma h_\xi}\psi^*_{xx} - \frac{\psi^*_x}{\sigma h_\xi}\Big[\frac{\sigma_x}{\sigma} + \frac{1}{h_\xi^2}\big(z_x z_{xx} + \sigma_x \sigma_{xx}\big)\Big] \\
&\quad - \frac{3}{h_\xi}\big(\frac{3}{2}\sigma_x + \sigma\big) + \frac{3}{2}\frac{\sigma}{h_\xi^3}\big(z_x z_{xx} + \sigma_x \sigma_{xx}\big),
\end{aligned}
\tag{19}
$$

$$
\begin{aligned}
u_{\eta_y} &= -\frac{1}{\sigma h_\eta}\psi^*_{xy} - \frac{\sigma_y}{h_\xi}\big(\frac{3}{2} + \frac{1}{\sigma^2}\psi^*_x\big) \\
&\quad + \frac{1}{h_\xi^3}\big(z_x z_{xy} + \sigma_x \sigma_{xy}\big)\big(\frac{3}{2}\sigma - \frac{1}{\sigma}\psi^*_x\big)
\end{aligned}
\tag{20}
$$

and

$$
u_{\xi_x} = -\frac{1}{\sigma h_\eta}\psi^*_{xy} + 3\frac{\sigma_y}{h_\eta}. \tag{21}
$$

So, for the full problem, we have the following unknowns: there are $(N-2)^2$ interior unknowns for ψ^*_{ij}, ω_{ij}, z^*_{ij} and σ^*_{ij}, for a total of $4(N-2)^2$ interior unknowns; at the interface $\xi = 1$, there are $(N-2)$ unknowns for ω_{Nj}, g_j and α_j, and λ, for a total of $3(N-2)+1$ unknowns. Thus, there are a grand total of $4(N-2)^2 + 3(N-2) + 1$ unknowns; for our 61×61 mesh, we then have 14102 unknowns. Eqs. (7), (11), (14), and (15) provide us with a total of $4(N-2)^2 + 3(N-2)$ (14101, for the 61^2 grid) equations, which leaves us with one more unknown than equation. This extra unknown is λ, the constant of integration in the pressure. Adding an extra constraint to the system will determine a unique λ, and so we require that the volume of the bubble remain

constant. The final equation can be written as

$$V = 2 - \int_0^{\pi} g^3(\theta) \sin\theta \, d\theta = 0. \tag{22}$$

To reduce Eqs. (11), (14) and (15) from differential equations to algebraic equations, it is a simple matter of using centered, second-order finite differences, just as was done to obtain Eq. (7). It is also necessary to eliminate the integrals appearing in Eq. (22) and the expression for the pressure and replace them with algebraic expressions. To approximate the integrals, we used Simpson's rule for Eq. (22) and the drag coefficient C_D, and a trapezoidal rule for the integral appearing in the pressure. The reason for using the two different integration schemes is that although Simpson's rule has higher accuracy than the trapezoidal rule, it requires that the number of points in the integration be odd—which is true when we integrate over the surface from 0 to π since there are 61 points—but when we integrate over only part of the surface (from 0 to η_j) the number of points alternates between odd and even as j increases. The algebraic equation resulting from Eq. (22) is

$$V = 2 - \frac{\Delta\theta}{3}\Big[4 \sum_{\substack{j=2 \\ \text{even}}}^{N-1} g_j^3 \sin\theta_j + 2 \sum_{\substack{j=3 \\ \text{odd}}}^{N-2} g_j^3 \sin\theta_j \Big] = 0.$$

To achieve a tight band structure in the Jacobian matrix, we again order the equations and unknowns in alternating groups of $(N-2)$, starting at $i, j = 2$: for each i, in order of appearance, we write $(N-2)$ equations for ψ^*, ω, z^* and σ^*. After all of the governing Eqs. (7a,b) and (11) have been written, we include the boundary conditions in the following order: normal stress balance (14), tangential stress balance (15), the definition of α (7c) and finally the volume constraint (22). The band structure arising from this ordering is shown in Fig. 9. There is a high degree of density in the normal stress balance due to the integral terms. In this matrix of order 14102 we have a bandwidth of 708.

III. Details of the numerical scheme

Solution of the linear systems generated in previous sections (a), (b) and (c) requires the use of a sparse matrix package, one which efficiently orders and stores the elements of the Jacobian and also provides a fast, accurate solution. We have experimented with four such sparse matrix library packages: SPARSPAK (George *et al* 1980), SMPAK (Yale), ILUPACK (Simon 1984) and Harwell MA32 (AERE Harwell 1985). Both SPARSPAK and SMPAK proved unusable because neither makes any provision for pivoting, which is crucial in our problems. They also assume that the matrix is symmetric and positive definite, and this acts to reduce the efficiency of storage and elimination. ILUPACK was designed to efficiently solve large sparse unsymmetric linear systems by conjugate gradient-type iterative methods; additionally, ILUPACK uses incomplete LU factorization extensions to SPARSPAK. There are seven possible conjugate gradient methods for the user to choose from. They are

1 The ORTHOMIN(K) method of Vinsome (1976); K is an integer denoting the dimension of the subspace used for approximation.

2 The minimum residual method (Elman 1982) is a simple descent method.

3 The generalized conjugate residual method GCR(K) is a restarted version of Orthomin.

4 The generalized minimum residual method GMRES(K) uses orthogonality of the basis vectors to construct a solution which minimizes the residual norm over the subspace (Saad and Schultz 1983).

5 USYMLQ (Saunders, Simon and Yip 1984) uses a subspace for computing approximate solution vectors which is built by using multiplications of the matrix and its transpose in turn. This method minimizes the Euclidean norm of the error over the subspace.

6 USYMQR is like USYMLQ except that it minimizes the residual norm over the subspace, rather than the Euclidean norm.

7 LSPR uses conjugate gradients applied to the normal equations (Paige and

Saunders 1982).

We found that GMRES(K) out-performed all of the other six methods in tests run on the mapping problem and the flow problem. In actuality, only two of the other methods would even work on our test problems (ORTHOMIN(K) and GCR(K)); the other methods either "blew up" or converged to incorrect finite solutions. For both the mapping and the flow tests, the order of the system of equations was 7021; one Newton step, using GMRES(K) as the solver, took 2-2.5 CPU seconds on a CRAY XM-P/24. (The CRAY used was located at Boeing Computer Services). This time includes evaluation of the matrix elements and right hand side, and all calls to ILUPACK. One disadvantage of ILUPACK is that it is an in-core matrix solver. Although the package efficiently orders and stores the elements of the sparse matrix, the workspace required by ILUPACK is nonetheless quite high—almost 2 million words for each problem. This is half of the core memory of the XM-P/24, and to use more than half is very expensive (since it would effectively be taking memory away from the second processor). Clearly this memory limitation has serious consequences for the full problem, where the order of the system is over 14000.

The package with which we have had the most success is MA32 from Harwell. MA32 solves large sparse systems by the frontal method, optionally using disk storage for the matrix factors; it is a direct solver employing partial pivoting. Aside from the obvious strength of being able to solve *very* large problems in a specified and relatively small amount of core storage, MA32 was written so that equations can be input by the user in one of two ways: (i) by elements, as is natural in finite element calculations or (ii) by a row at a time, as is natural when using finite differencing. During elimination, the number of variables needed in core (or, in the "front") at any time is essentially dependent on the bandwidth of the matrix, provided that the matrix has some regular pattern structure. MA32 accepts input by equation, and will commence elimination on a variable when that variable is fully summed, that is, the variable is available

for use as a pivot in Gaussian elimination when it has appeared for the last time and does not occur in future equations.

We have found that for the mapping, flow, and full problems the minimum front size allowable is 157×196, 118×156 and 313×469, respectively. For these front sizes, the disk spaces needed to store the UQ decompositions (in double precision words) are 637 440, 503 806 and 3 068 928. The amount of real work space needed by MA32 varies from 250 000 to 500 000, depending on the front size and output buffer. All of the tests with MA32 have been performed on a CRAY XM-P/48 located at the San Diego Supercomputer Center. Execution times for these cases are approximately 2, 3, and 16.5 CPU seconds, respectively, per Newton step. Unfortunately, SDSC does not possess a SSD (Solid state Storage Device), so the temporary files are created on the local disks. Access to SSD for temporary storage would increase the I/O speed by a factor of 100-1000. The run time for the full problem seems unusually high, but at present we have not been able to detect any irregularities in the operation of the matrix library. Because of the seemingly excessive time required for the full problem, we have incorporated a chord method into the Fortran code. Preliminary tests with the Newton-chord method indicate that a chord step usually requires only 2 seconds of CPU.

The convergence criteria that we have been using for these runs is very simple; we require that the magnitudes of the elements of the residual vector G (that is, the vector of equations) satisfy the following:

$$\max_i G_i \leq \beta_\infty$$

$$\frac{1}{M}\Big[\sum_{i=1}^{M} G_i^2\Big]^{1/2} \leq \beta_2.$$

We have found that reasonable values for these tolerances are $\beta_\infty = 10^{-8}$ and $\beta_2 = 10^{-10}$.

One disadvantage to MA32—compared to the other sparse matrix libraries tested—is the necessity to give MA32 the locations of the non-zero elements

twice, once for the package to determine when each variable is fully summed and again for MA32 to perform the eliminations. Additionally, this process must be repeated twice for each Newton step. In other words, in libraries like SPARSPAK and ILUPAK, the user must give the package the non-zero indices only when the structure of the matrix changes, and for problems such as ours, this means we only have to give the structure once, at the beginning of the run. However, MA32 loses the index information between each solution, so that the index information must be given to MA32 twice for each Newton step. Aside from the increased computational cost, this behavior almost doubles the amount of Fortran source code, appreciably increasing the compilation time. Except for this inconvenience, MA32 has proved to be a versatile sparse matrix package.

IV. Continuation

Continuation can play a vital role in the development of a Newton's method scheme, particularly when the solution behavior changes dramatically with small changes in one or more of the parameters. Schreiber and Keller (1983), in a study of driven cavity flows, present what they call "Euler-Newton" continuation (based on procedures developed by Keller (1977)). In this method, the Jacobian of the converged solution at a particular value of a parameter—for example, the Reynolds number— is used to obtain an initial guess to the solution at a slightly different value of this parameter.

If we denote $\mathbf{G}$ as our vector set of the equations and $\mathbf{x}$ the vector set of unknowns, then the Jacobian can be symbolically represented by

$$\mathbf{A} = \frac{\partial \mathbf{G}}{\partial \mathbf{x}}.$$

Then, if we wish to perform continuation in Reynolds number we take the derivative of $\mathbf{G}$ with respect to Re:

$$\frac{\partial \mathbf{G}}{\partial Re} = \frac{\partial \mathbf{G}}{\partial \mathbf{x}} \frac{\partial \mathbf{x}}{\partial Re} = \mathbf{A} \frac{\partial \mathbf{x}}{\partial Re}. \tag{23}$$

We obtain a similar expression for the We:

$$\frac{\partial \mathbf{G}}{\partial We} = \frac{\partial \mathbf{G}}{\partial \mathbf{x}} \frac{\partial \mathbf{x}}{\partial We} = \mathbf{A} \frac{\partial \mathbf{x}}{\partial We}. \tag{24}$$

Thus, with the Jacobian $\mathbf{A}$ obtained from the converged solution, we can calculate $\partial \mathbf{x}/\partial Re$ or $\partial \mathbf{x}/\partial We$ by solving either of the linear systems (23) or (24). An initial guess is found by taking an Euler step:

$$\mathbf{x}^{(\circ)}(Re,\ We + \Delta We) = \mathbf{x}(Re,\ We) + \Delta We \frac{\partial \mathbf{x}}{\partial We}(Re,\ We) \tag{25}$$

or

$$\mathbf{x}^{(\circ)}(Re + \Delta Re,\ We) = \mathbf{x}(Re,\ We) + \Delta Re \frac{\partial \mathbf{x}}{\partial Re}(Re,\ We), \tag{26}$$

where $\mathbf{x}(Re,\ We)$ is the converged solution at the current Reynolds number and Weber number. Obviously, this continuation algorithm will only succeed if the matrix $\mathbf{A}$ is regular; it breaks down at a branch point. This is a serious restriction if we wish to do continuation at limit points.

To circumvent this difficulty, we turn to arc length continuation. This type of continuation is described in a variety of texts, but the source of most of our information on this area is Kubíček and Marek (1983). We want to generate a complete dependence $\mathbf{x}(Re)$ or $\mathbf{x}(We)$ which forms a continuous smooth curve in $(M+1)$-dimensional space ($x_1,\ x_2,\ \ldots,\ x_M,\ Re$ or We). This continuation method get its name because we will use the arc length s of the solution curve as a parameter of the method. Rather than differentiate the residual vector $\mathbf{G}$ with respect to Re or We—as we did above for Euler-Newton continuation—we differentiate with respect to the length of arc s:

$$\frac{dG_i}{ds} = \frac{\partial G_i}{\partial Re}\frac{dRe}{ds} + \sum_{j=1}^{M}\frac{\partial G_i}{\partial x_j}\frac{dx_j}{ds} = 0, \tag{27}$$

if we are performing continuation in Re, and

$$\frac{dG_i}{ds} = \frac{\partial G_i}{\partial We}\frac{dWe}{ds} + \sum_{j=1}^{M}\frac{\partial G_i}{\partial x_j}\frac{dx_j}{ds} = 0, \tag{28}$$

if we are considering We. With the addition of arc length s into the set of equations, we need one more constraint on the system. This extra condition specifies the normalized length of the curve in solution space. Thus, we require

$$\left(\frac{dx_1}{ds}\right)^2 + \left(\frac{dx_2}{ds}\right)^2 + \cdots + \left(\frac{dx_M}{ds}\right)^2 + \left(\frac{dRe}{ds}\right)^2 = 1, \tag{29}$$

if we are again considering continuation in Re, for example. Now, Eq. (27) forms a set of M linear algebraic equations in the $(M+1)$ unknowns dx_i/ds, $i = 1,\ldots,M+1$, where $x_{M+1} \equiv Re$. The number of unknowns in Eq. (27) can be reduced by one if we define a new set of unknowns κ_i such that

$$\frac{dx_i}{ds} = \kappa_i\frac{dx_k}{ds}, \qquad i = 1,2,\ldots,k-1,k+1,\ldots,M+1, \tag{30}$$

for some $\partial x_k/\partial s \neq 0$, $1 \leq k \leq M+1$. Equation (27) then reduces to a system of M equations and M unknowns, which can be solved for the κ_i's. The coefficient matrix of this linear system is

$$\hat{\mathbf{A}} = \begin{pmatrix} \partial G_1/\partial x_1 & \dots & \partial G_1/\partial x_{k-1} & \partial G_1/\partial x_{k+1} & \dots & \partial G_1/\partial x_{M+1} \\ \partial G_2/\partial x_1 & \dots & \partial G_2/\partial x_{k-1} & \partial G_2/\partial x_{k+1} & \dots & \partial G_2/\partial x_{M+1} \\ \vdots & \ddots & \vdots & \vdots & \ddots & \vdots \\ \partial G_M/\partial x_1 & \dots & \partial G_M/\partial x_{k-1} & \partial G_M/\partial x_{k+1} & \dots & \partial G_M/\partial x_{M+1} \end{pmatrix}.$$

This matrix is, in general, nonsingular at limit points, making arc length continuation a valuable means of branching around limit points. With the values of κ_i, we can then compute dx_k/ds by using Eq. (29). These equations comprise a set of $(M+1)$ coupled differential equations which can be solved by a variety of methods.

We have tested the Euler-Newton continuation on the flow problem and the full problem and found that it works reasonably well in the regions of parameter space considered (low Re and We). Specifically, with the initial guess generated using continuation, we were always able to obtain a solution at the new parameter value with Newton's method. However, in all cases done, we were also always able to obtain a solution—usually in the same number of steps—at the new parameter value using the solution at the old parameter value as the initial guess. Basically, we find (so far) that the initial guess is not as important as is usually claimed for this method. This will undoubtedly change as a branch point is approached. We have not yet tested the arc length continuation, but as it is much more versatile than the Euler-Newton continuation, it will be incorporated into the code in the future.

V. Discussion

Although we have done extensive tests and run numerous cases of the mapping and flow problems, some of which are mentioned in Section II, for the full problem we have thus far obtained results at only a limited number of values of Reynolds number and Weber number, specifically for the (Re, We) pairs (0.5, 0.5), (2, 0.5) and (2, 2). The flowfields for these cases are shown in Fig. 10. Deformation of the bubble is slight at the low values of We presented here, but the bubble does show the characteristic flattening at the rear for $We = 2$. Ryskin and Leal (1984) used a different numerical technique (ADI) to calculate shapes and flowfields for this problem, that is, for the steady rectilinear motion of a deformable bubble. In Table I we present a comparison of drag coefficients between the results of the present work, the earlier numerical work of Ryskin and Leal, and the low Re, We asymptotic analysis of Taylor and Acrivos (1964). The important conclusion of this comparison is that the numerical results of the present work (obtained using Newton's method) and the results of Ryskin and Leal (obtained with ADI) are in agreement to within at least three decimal places. For the case (Re, We) = (0.5, 0.5), we used the following initial condition:

$$z^*_{ij} = \xi_i \cos(\pi\eta_j) \qquad \sigma^*_{ij} = \xi_i \sin(\pi\eta_j) \qquad 1 \le i,j \le N$$

$$\psi^*_{ij} = \omega_{ij} = 0 \qquad 1 \le i,j \le N$$

$$g_j = 1 \qquad 1 \le j \le N$$

$$\alpha_j = \pi \qquad 1 \le j \le N$$

and

$$\lambda = 1.$$

Convergence was reached in 2 Newton steps. As an initial guess for (Re, We) = (2, 0.5) we tried two different things: the solution for (0.5, 0.5), and continuation in Re from this solution. Both of these initial guesses converged to the solution

in 2 Newton steps. Finally, for $(Re,\ We) = (2,\ 2)$ we used the same approach for the initial guess: the solution for (2, 0.5), and continuation in We from this solution. The initial guess from continuation converged in 2 Newton steps, but the initial guess from the previous solution took 3. (For practical purposes it required two steps, because the error was just above the tolerance after two steps.)

Acknowledgements

Computations using the library package ILUPACK were carried out on Boeing Computer Services' CRAY X-MP/24, and the authors wish to acknowledge the expert help and time spent by Boeing employee Horst Simon.

Computations using the Harwell library were carried out on the CRAY X-MP/48 at San Diego Supercomputer Center. We would like to thank Bob Leary for his help in getting started with MA32.

The authors would especially like to thank Prof. Bob Brown, without whose knowledge of Newton's method we would not have succeeded in this project.

This work was supported by grants from the Fluid Mechanics Program and the Office of Advanced Scientific Computing at the National Science Foundation.

Appendix

For a system of equations as complicated as the one we are trying to solve, it is not possible to display all of the expressions generated after taking the Frechet derivatives of the algebraic equations. However, because of the use of the general curvilinear coordinate system, the problem under consideration is sufficiently general that presenting some of these derivatives may be useful. Before proceeding, we must note two things: (1) although z and σ appear in the governing equations for the flow, and the normal and tangential stress balances, the unknown mapping functions are really z^* and σ^*; and (2) The Frechet derivatives of the aforementioned flow equations and stress boundary conditions with respect to z^* and σ^* are too complicated to display. These derivatives are just combinations of derivatives of z, σ, z_x, σ_x, z_y, σ_y, ..., so we will present only *these* Frechet derivatives.

a. The coordinate inversion

The coordinate inversion used in the derivation of the equations takes the form

$$z + i\sigma = \frac{1}{z^* - i\sigma^*}, \tag{A1}$$

so that the mapping variables are related by

$$\begin{aligned} z &= \frac{z^*}{z^{*2} + \sigma^{*2}} \\ \sigma &= \frac{\sigma^*}{z^{*2} + \sigma^{*2}}. \end{aligned} \tag{A2}$$

Then the derivatives of z and σ are

$$\sigma_x = \left(1 - \frac{2\sigma^{*2}}{X}\right)\frac{\sigma_x^*}{X} - \frac{2\sigma^* z^* z_x^*}{X^2} \tag{A3}$$

$$z_x = \left(1 - \frac{2z^{*2}}{X}\right)\frac{z_x^*}{X} - \frac{2\sigma^* z^* \sigma_x^*}{X^2} \tag{A4}$$

$$\sigma_y = \left(1 - \frac{2\sigma^{*2}}{X}\right)\frac{\sigma_y^*}{X} - \frac{2\sigma^* z^* \sigma_y^*}{X^2} \tag{A5}$$

$$z_y = \Big(1 - \frac{2z^{*2}}{X}\Big)\frac{z_y^*}{X} - \frac{2\sigma^* z^* \sigma_y^*}{X^2} \tag{A6}$$

$$\begin{aligned}\sigma_{xx} = {} & \frac{(z^{*2} - \sigma^{*2})\sigma_{xx}^*}{X^2} - \frac{2\sigma^* z^* z_{xx}^*}{X^2} + 2\sigma^*\Big(\frac{4\sigma^{*2}}{X} - 3\Big)\frac{(\sigma_x^*)^2}{X^2} \\ & + 2\sigma^*\Big(\frac{4z^{*2}}{X} - 1\Big)\frac{(z_x^*)^2}{X^2} + 4z^*\Big(\frac{4\sigma^{*2}}{X} - 1\Big)\frac{z_x^*\sigma_x^*}{X^2}\end{aligned} \tag{A7}$$

$$\begin{aligned}z_{xx} = {} & \frac{(\sigma^{*2} - z^{*2})z_{xx}^*}{X^2} - \frac{2\sigma^* z^* \sigma_{xx}^*}{X^2} + 2z^*\Big(\frac{4z^{*2}}{X} - 3\Big)\frac{(z_x^*)^2}{X^2} \\ & + 2z^*\Big(\frac{4\sigma^{*2}}{X} - 1\Big)\frac{(\sigma_x^*)^2}{X^2} + 4\sigma^*\Big(\frac{4z^{*2}}{X} - 1\Big)\frac{z_x^*\sigma_x^*}{X^2}\end{aligned} \tag{A8}$$

$$\begin{aligned}\sigma_{yy} = {} & \frac{(z^{*2} - \sigma^{*2})\sigma_{yy}^*}{X^2} - \frac{2\sigma^* z^* z_{yy}^*}{X^2} + 2\sigma^*\Big(\frac{4\sigma^{*2}}{X} - 3\Big)\frac{(\sigma_y^*)^2}{X^2} \\ & + 2\sigma^*\Big(\frac{4z^{*2}}{X} - 1\Big)\frac{(z_y^*)^2}{X^2} + 4z^*\Big(\frac{4\sigma^{*2}}{X} - 1\Big)\frac{z_y^*\sigma_y^*}{X^2}\end{aligned} \tag{A9}$$

$$\begin{aligned}z_{yy} = {} & \frac{(\sigma^{*2} - z^{*2})z_{yy}^*}{X^2} - \frac{2\sigma^* z^* \sigma_{yy}^*}{X^2} + 2z^*\Big(\frac{4z^{*2}}{X} - 3\Big)\frac{(z_y^*)^2}{X^2} \\ & + 2z^*\Big(\frac{4\sigma^{*2}}{X} - 1\Big)\frac{(\sigma_y^*)^2}{X^2} + 4\sigma^*\Big(\frac{4z^{*2}}{X} - 1\Big)\frac{z_y^*\sigma_y^*}{X^2}\end{aligned} \tag{A10}$$

$$\begin{aligned}\sigma_{xy} = {} & \frac{(z^{*2} - \sigma^{*2})\sigma_{xy}^*}{X^2} - \frac{2z^*\sigma^* z_{xy}^*}{X^2} + 2\sigma^*\Big(\frac{4\sigma^{*2}}{X} - 3\Big)\frac{\sigma_x^*\sigma_y^*}{X^2} \\ & + 2\sigma^*\Big(\frac{4z^{*2}}{X} - 1\Big)\frac{z_x^* z_y^*}{X^2} + \frac{2z^*}{X^2}\Big(\frac{4\sigma^{*2}}{X} - 1\Big)\big(\sigma_x^* z_y^* + \sigma_y^* z_x^*\big)\end{aligned} \tag{A11}$$

$$\begin{aligned}\sigma_{xy} = {} & \frac{(\sigma^{*2} - z^{*2})z_{xy}^*}{X^2} - \frac{2z^*\sigma^*\sigma_{xy}^*}{X^2} + 2z^*\Big(\frac{4z^{*2}}{X} - 3\Big)\frac{z_x^* z_y^*}{X^2} \\ & + 2z^*\Big(\frac{4\sigma^{*2}}{X} - 1\Big)\frac{\sigma_x^*\sigma_y^*}{X^2} + \frac{2\sigma^*}{X^2}\Big(\frac{4z^{*2}}{X} - 1\Big)\big(\sigma_x^* z_y^* + \sigma_y^* z_x^*\big)\end{aligned} \tag{A12}$$

We have used the shorthand notation $X \equiv z^{*2} + \sigma^{*2}$.

b. The vorticity equation F

$$\frac{\partial F_{ij}}{\partial \psi_{i+1j}^*} = \frac{1}{4} h\, Re \frac{f}{\sigma}\Big(\frac{\omega}{\sigma}\sigma_y - \omega_y\Big)\Big|_{ij} \tag{A13}$$

(The right hand side in Eq. (A13), and in all of the following equations, is evaluated at the (i,j) point.)

$$\frac{\partial F_{ij}}{\partial \psi^*_{i-1j}} = -\frac{\partial F_{ij}}{\partial \psi^*_{i+1j}} \tag{A14}$$

$$\frac{\partial F_{ij}}{\partial \psi^*_{ij+1}} = -\frac{1}{4} h\, Re \frac{f}{\sigma}\left(\frac{\omega}{\sigma}\sigma_x - \omega_x\right) \tag{A15}$$

$$\frac{\partial F_{ij}}{\partial \psi^*_{ij-1}} = -\frac{\partial F_{ij}}{\partial \psi^*_{ij+1}} \tag{A16}$$

$$\frac{\partial F_{ij}}{\partial \omega_{ij}} = -2\left(1 + f^2\right) + q_{3_{ij}} \tag{A17}$$

$$\frac{\partial F_{ij}}{\partial \omega_{i+1j}} = f^2 + \epsilon\, q_{1_{ij}} \tag{A18}$$

$$\frac{\partial F_{ij}}{\partial \omega_{i-1j}} = f^2 - \epsilon\, q_{1_{ij}} \tag{A19}$$

$$\frac{\partial F_{ij}}{\partial \omega_{ij+1}} = 1 + \epsilon\, q_{2_{ij}} \tag{A20}$$

$$\frac{\partial F_{ij}}{\partial \omega_{ij-1}} = 1 - \epsilon\, q_{2_{ij}} \tag{A21}$$

c. The streamfunction equation G

$$\frac{\partial G_{ij}}{\partial \psi^*_{ij}} = -2\left(1 + f^2\right) \tag{A22}$$

$$\frac{\partial G_{ij}}{\partial \psi^*_{i+1j}} = f^2 + \epsilon\, w_{1_{ij}} \tag{A23}$$

$$\frac{\partial G_{ij}}{\partial \psi^*_{i-1j}} = f^2 - \epsilon\, w_{1_{ij}} \tag{A24}$$

$$\frac{\partial G_{ij}}{\partial \psi^*_{ij+1}} = 1 + \epsilon\, w_{2_{ij}} \tag{A25}$$

$$\frac{\partial G_{ij}}{\partial \psi^*_{ij-1}} = 1 - \epsilon\, w_{2_{ij}} \tag{A26}$$

$$\frac{\partial G_{ij}}{\partial \omega_{ij}} = h_\eta^2 \sigma \tag{A27}$$

d. The mapping equations H and L

$$\frac{\partial H_{ij}}{\partial z^*_{ij}} = \frac{\partial L_{ij}}{\partial \sigma^*_{ij}} = -2\left(1 + f^2\right) \tag{A28}$$

$$\frac{\partial H_{ij}}{\partial z^*_{i+1j}} = \frac{\partial L_{ij}}{\partial \sigma^*_{i+1j}} = f\left(f + \epsilon f_x\right) \tag{A29}$$

$$\frac{\partial H_{ij}}{\partial z^*_{i-1j}} = \frac{\partial L_{ij}}{\partial \sigma^*_{i-1j}} = f\left(f - \epsilon f_x\right) \tag{A30}$$

$$\frac{\partial H_{ij}}{\partial z^*_{ij+1}} = \frac{\partial L_{ij}}{\partial \sigma^*_{ij+1}} = 1 - \epsilon f_x / f \tag{A31}$$

$$\frac{\partial H_{ij}}{\partial z^*_{ij-1}} = \frac{\partial L_{ij}}{\partial \sigma^*_{ij-1}} = 1 + \epsilon f_x / f \tag{A32}$$

e. Other Frechet deriatives appearing in the governing equations

The only mapping variables appearing explicitly in the governing equations are σ, σ_x, σ_y and h_η^2.

$$\frac{\partial \sigma}{\partial z^*_{ij}} = -2\sigma z \tag{A33}$$

$$\frac{\partial \sigma}{\partial \sigma^*_{ij}} = z^2 - \sigma^2 \tag{A34}$$

$$\frac{\partial \sigma_x}{\partial z^*_{ij}} = -\frac{2}{X^2}\sigma^* z^*_x + \frac{2}{X^3}\left[z^* \sigma^*_x (3\sigma^{*2} - z^{*2}) + 4\sigma^* z^{*2} z^*_x\right] \tag{A35}$$

$$\frac{\partial \sigma_x}{\partial z^*_{i+1j}} = -\frac{z\sigma}{h} \tag{A36}$$

$$\frac{\partial \sigma_x}{\partial z^*_{i-1j}} = \frac{z\sigma}{h} \tag{A37}$$

$$\frac{\partial \sigma_x}{\partial \sigma^*_{ij}} = -\frac{2}{X^2}\left(2\sigma^*\sigma^*_x + z^* z^*_x\right) + \frac{2}{X^3}\left[\sigma^*\sigma^*_x\left(3\sigma^{*2} - z^{*2}\right) + 4\sigma^{*2} z^* z^*_x\right] \tag{A38}$$

$$\frac{\partial \sigma_x}{\partial \sigma^*_{i+1j}} = \frac{z^2 - \sigma^2}{2h} \tag{A39}$$

$$\frac{\partial \sigma_x}{\partial \sigma^*_{i-1j}} = \frac{\sigma^2 - z^2}{2h} \tag{A40}$$

$$\frac{\partial \sigma_y}{\partial z^*_{ij}} = -\frac{2}{X^2}\sigma^* z^*_y + \frac{2}{X^3}\left[z^*\sigma^*_y(3\sigma^{*2} - z^{*2}) + 4\sigma^* z^{*2} z^*_y\right] \tag{A41}$$

$$\frac{\partial \sigma_y}{\partial z^*_{ij+1}} = -\frac{z\sigma}{h} \tag{A42}$$

$$\frac{\partial \sigma_y}{\partial z^*_{ij-1}} = \frac{z\sigma}{h} \tag{A43}$$

$$\frac{\partial \sigma_y}{\partial \sigma^*_{ij}} = -\frac{2}{X^2}(2\sigma^*\sigma^*_y + z^* z^*_y) + \frac{2}{X^3}\left[\sigma^*\sigma^*_y(3\sigma^{*2} - z^{*2}) + 4\sigma^{*2} z^* z^*_y\right] \tag{A44}$$

$$\frac{\partial \sigma_y}{\partial \sigma^*_{ij+1}} = \frac{z^2 - \sigma^2}{2h} \tag{A45}$$

$$\frac{\partial \sigma_y}{\partial \sigma^*_{ij-1}} = \frac{\sigma^2 - z^2}{2h} \tag{A46}$$

$$\frac{\partial h^2_\eta}{\partial z^*_{ij}} = -4z h^2_\eta \tag{A47}$$

$$\frac{\partial h^2_\eta}{\partial z^*_{ij+1}} = \frac{z^*_y}{hX^2} \tag{A48}$$

$$\frac{\partial h^2_\eta}{\partial z^*_{ij-1}} = -\frac{z^*_y}{hX^2} \tag{A49}$$

$$\frac{\partial h^2_\eta}{\partial \sigma^*_{ij}} = -4\sigma h^2_\eta \tag{A50}$$

$$\frac{\partial h^2_\eta}{\partial \sigma^*_{ij+1}} = \frac{\sigma^*_y}{hX^2} \tag{A51}$$

$$\frac{\partial h^2_\eta}{\partial \sigma^*_{ij-1}} = -\frac{\sigma^*_y}{hX^2} \tag{A52}$$

f. The distortion function f

Each N-shaped block structure generated by differentiating F_{ij}, G_{ij}, H_{ij} and L_{ij} is composed of a tridiagonal portion, plus the first two and last two

columns. The first and last two columns arise because of the presence of α_1 and α_N in *every* one of the $4(N-2)^2$ governing equations. Although α_1 and α_N are technically unknown, we can eliminate them by using the fact that $d\alpha/d\eta = 0$ at $\eta = 0, 1$. Thus,

$$\alpha_1 = \frac{1}{3}(4\alpha_2 - \alpha_3)$$

and

$$\alpha_N = \frac{1}{3}(4\alpha_{N-1} - \alpha_{N-2}),$$

and now α_2, α_3, α_{N-2} and α_{N-1} appear in every one of the governing equations. The components of the Jacobian arising from differentiation with respect to α can then be computed by taking the derivatives of f, f_x and f_y with respect to α_2, α_3, α_{j-1}, α_j, α_{j+1}, α_{N-2} and α_{N-1}, $2 \leq j \leq N-1$.

The normal and tangential stress boundary conditions present the largest amount of work in terms of evaluating the Frechet derivatives. All possible derivatives of z, σ and ψ^* appear in these two equations, and it must be remembered that all of these derivatives with respect to ξ are approximated by one-sided differences, not centered differences. The multitude of terms arising from taking all of the Frechet derivatives are not presented here, but they are available upon request.

Re, We	C_D		
	Present Work	Ryskin and Leal	Taylor and Acrivos
0.5, 0	33.6	33.6	33.7
0.5, 0.5	34.7	34.7	35.1
2, 0.5	9.62	9.62	-
2, 2	10.6	10.6	-

Table I. Comparison of the present results for the drag coefficient C_D with the results of Ryskin and Leal (1984) and with the low *Re,We* asymptotic results of Taylor and Acrivos (1964).

References

Brown, R.A., Scriven, L.E. and Silliman, W.J. 1980 *New Approaches in Nonlinear Dynamics*, SIAM, Philadelphia.

Chikhiwala, E.D. and Yortsos, Y.C. 1985 *J. Comput. Phys.* **57**, 391-402.

Christov, C.I. and Volkov, P.K. 1985 *J. Fluid Mech.* **158**, 341-364.

Dandy, D.S. and Leal, L.G. 1987 *J. Fluid Mech.*, submitted.

Elman, H.C. 1982 Research Report No. 229, Yale University, Dept. of Computer Sci.

Geller, A.S., Lee, S.H. and Leal, L.G. 1986 *J. Fluid Mech.* **169**, 27-69.

George, A., Liu, J. and Ng, E. 1980 *User Guide for SPARSPAK: Waterloo Sparse Linear Equations Package*, University of Waterloo, Waterloo, Ontario, Canada.

Keller, H.B. 1977 *Applications if Bifurcation Theory*, Academic Press, New York.

Kubíček, M. and Marek, M. 1983 *Computational Methods in Bifurcation Theory and Dissipative Structures*, Springer-Verlag, New York.

Miksis, M., Vanden-Broeck, J.-M., and Keller, J.B. 1981 *J. Fluid Mech.* **108**, 89-100.

Paige, C.C. and Saunders, M.A. 1982 *ACM TOMS* **8**, 43-71.

Peacemann, D.W. and Rachford, H.H. 1955 *J. Soc. Indust. Appl. Math.* **3**, 28.

Ryskin, G. and Leal, L.G. 1983 *J. Comput. Phys.* **50**, 71-100.

Ryskin, G. and Leal L.G. 1984 *J. Fluid Mech.* **148**, 1-17.

Ryskin, G. and Leal, L.G. 1984 *J. Fluid Mech.* **148**, 19-35.

Saad, Y. and Schultz, M.H. 1983 Research Report No. 254, Yale University, Dept. of Computer Sci.

Saunders, M.A., Simon, H.D. and Yip, E.L. 1984 Report ETA-TR-18, Boeing Computer Services.

Schreiber, R. and Keller, H.B. 1983 *J. Comput. Phys.* **49**, 310-333.

Simon, H.D. 1985 *User Guide for ILUPACK: Incomplete LU Factorization and Iterative Methods. Extensions to SPARSPAK.*, Boeing Computer Services, Tukwila, WA.

Sundarajan, T. and Ayyaswamy, P.S. 1984 *J. Fluid Mech.* **149**, 33-58.

Taylor, T.D. and Acrivos, A. 1964 *J. Fluid Mech.* **18**, 466-476.

Thompson, J.F., Warsi, Z.U.A., and Mastin, C.W. 1985 *Numerical Grid Generation: Foundations and Applications.* Elsevier.

Vinsome, P.K.W. 1976 SPE Proceedings of the Fourth Symposium on Reservoir Simulation, 149-159.

Figure captions

Figure 1: Schematic sketch of the problem.

Figure 2: Band structure of the mapping Jacobian arising from non-optimal ordering.

Figure 3: Representation of the $(\xi,\ \eta)$ finite difference grid.

Figure 4: Band structure of the mapping Jacobian arising from optimal ordering.

Figure 5: Band structure of the mapping Jacobian arising from optimal ordering when the shape is also considered unknown.

Figure 6: Weak constraint maps generated using Newton's method: (a) a finite auxiliary grid and (b) an actual grid.

Figure 7: Band structure of the flow Jacobian arising from optimal ordering of the equations.

Figure 8: Flowfields for fixed spheroidal shapes. (a) sphere with $Re = 20$, $C_D = 1.404$ and (b) Ellipse with $Re = 90$, $C_D = 0.862$.

Figure 9: Band structure of the Jacobian of the full problem.

Figure 10: Flowfields and shapes of the full problem for the following $(Re,\ We)$ pairs: (a) (0.5, 0.5), (b) (2, 0.5) and (c) (2, 2).

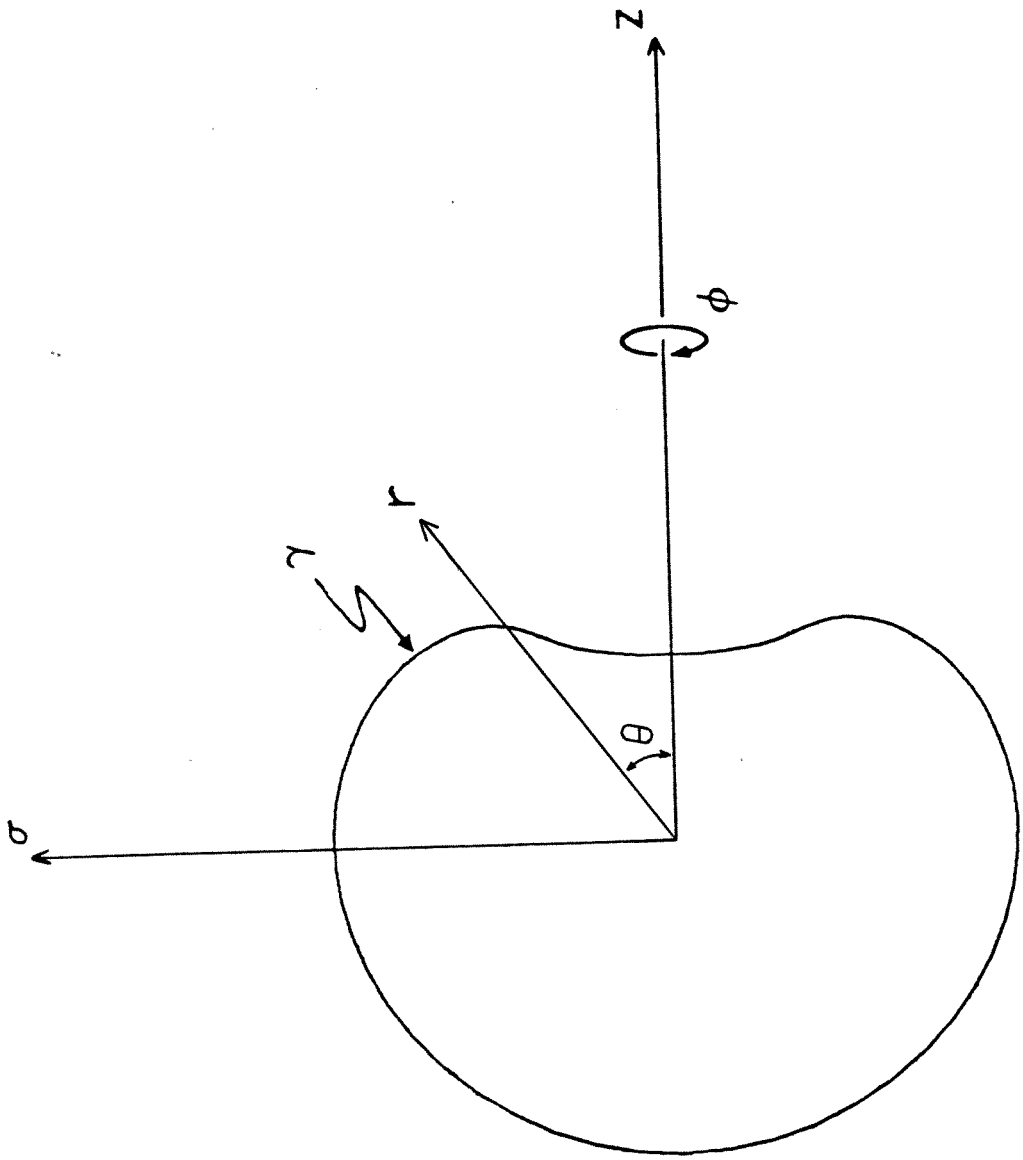

Figure 1

ρ μ

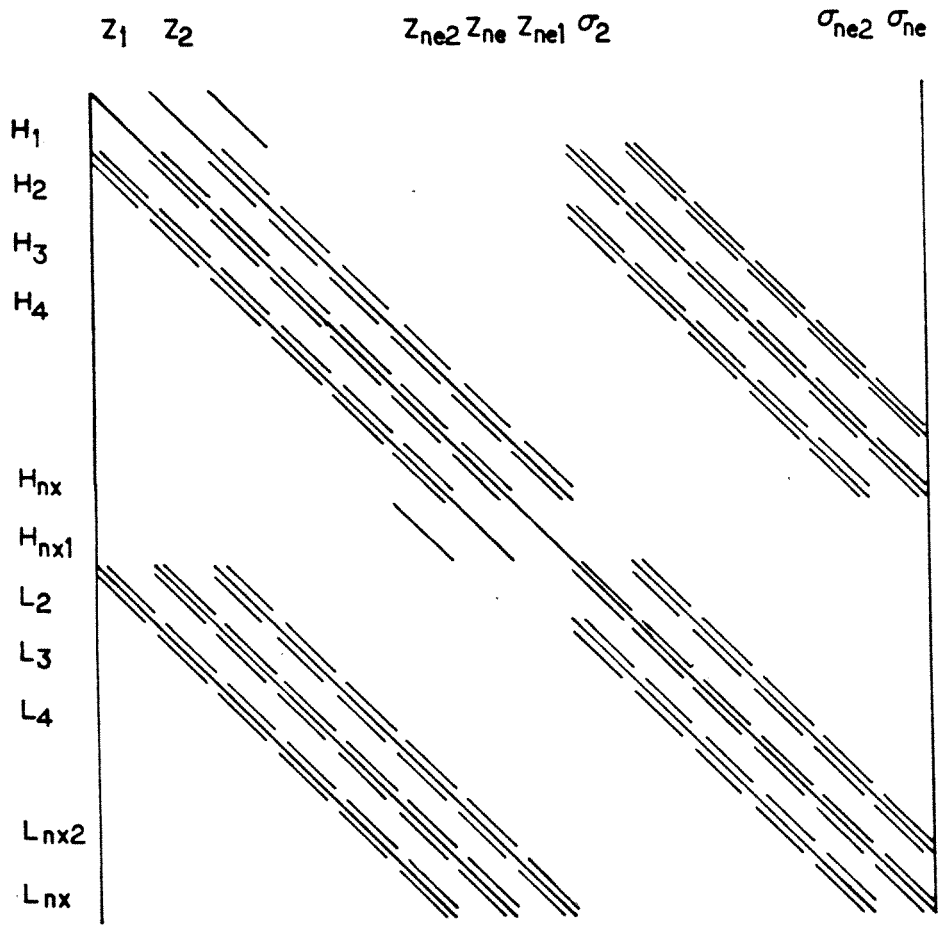
Z_1 Z_2
Z_{ne2} Z_{ne} Z_{ne1} σ_2
σ_{ne2} σ_{ne}
H_1
H_2
H_3
H_4
H_{nx}
H_{nx1}
L_2
L_3
L_4
L_{nx2}
L_{nx}

Figure 2

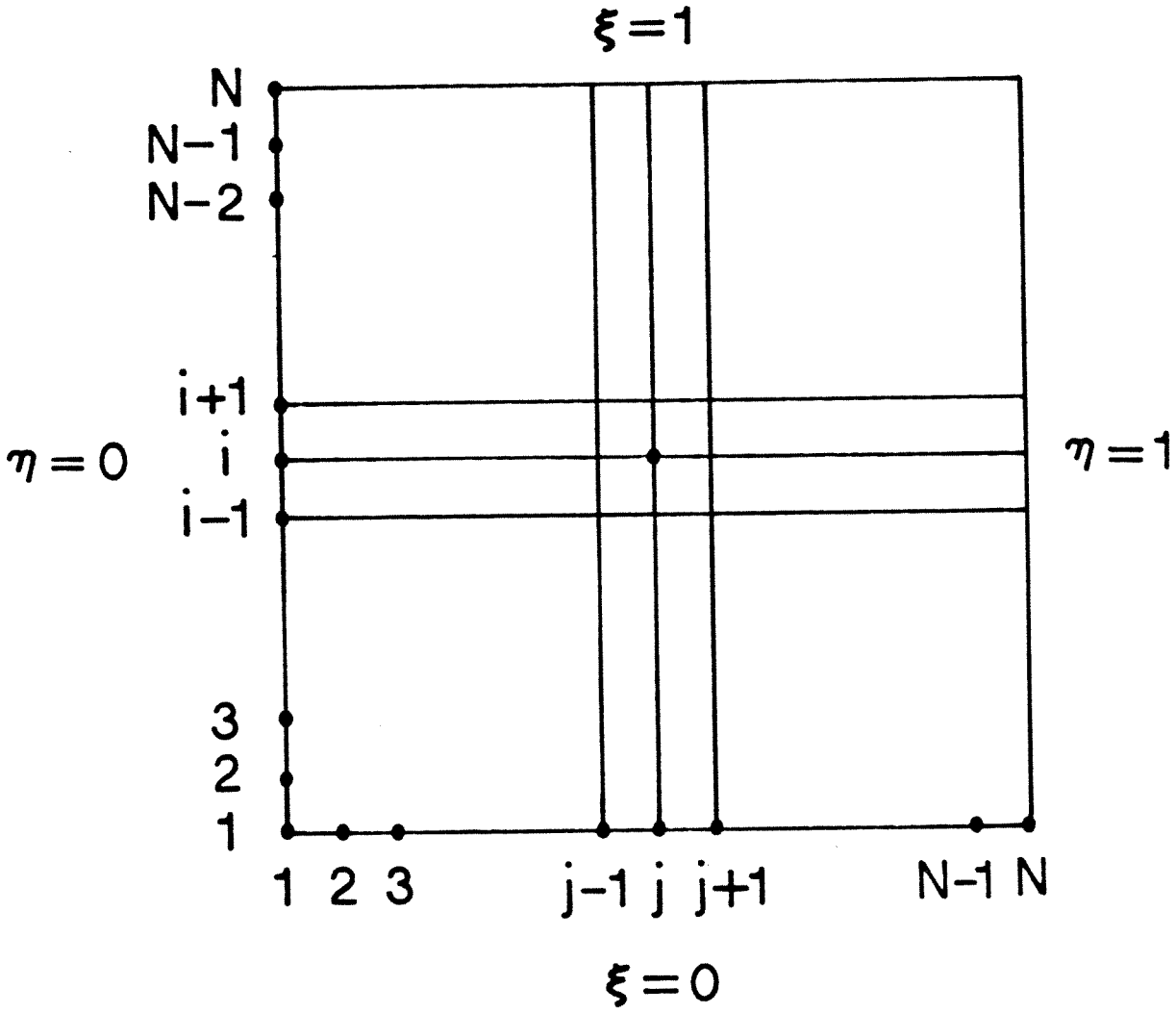

Figure 3

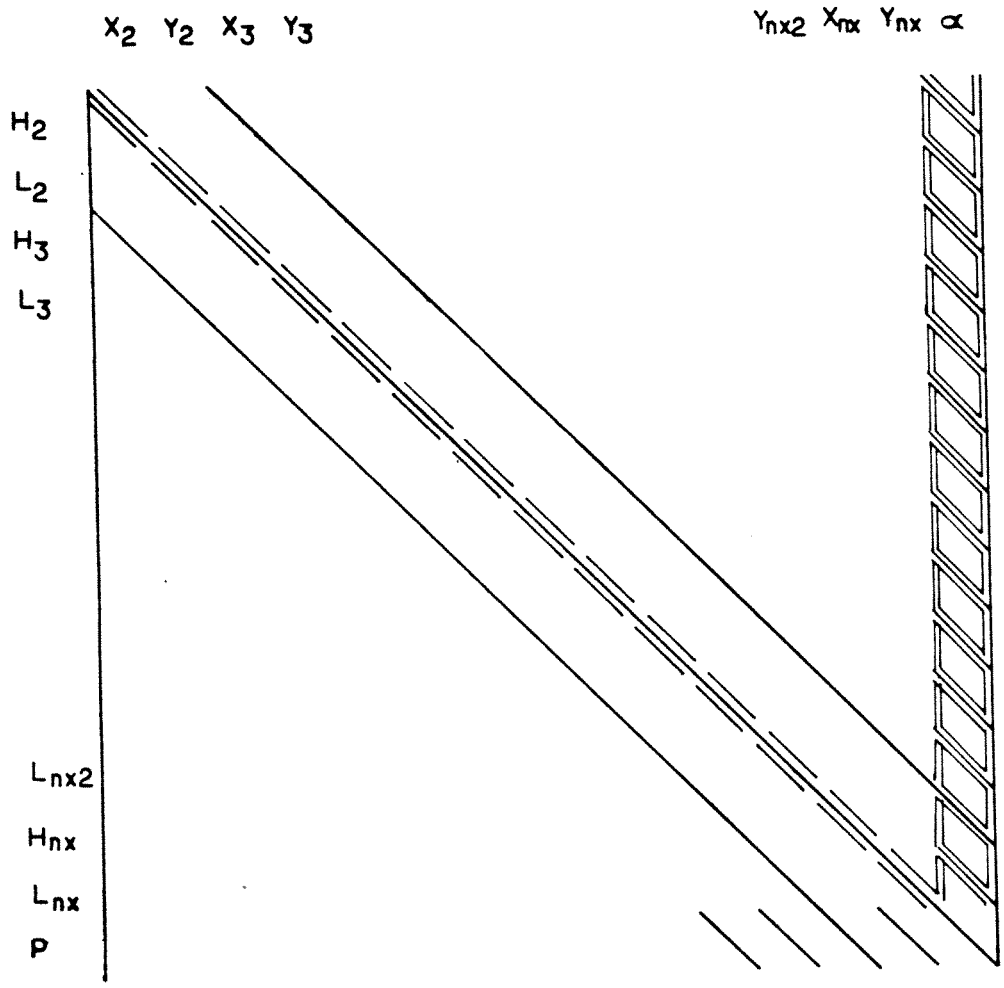

Figure 4

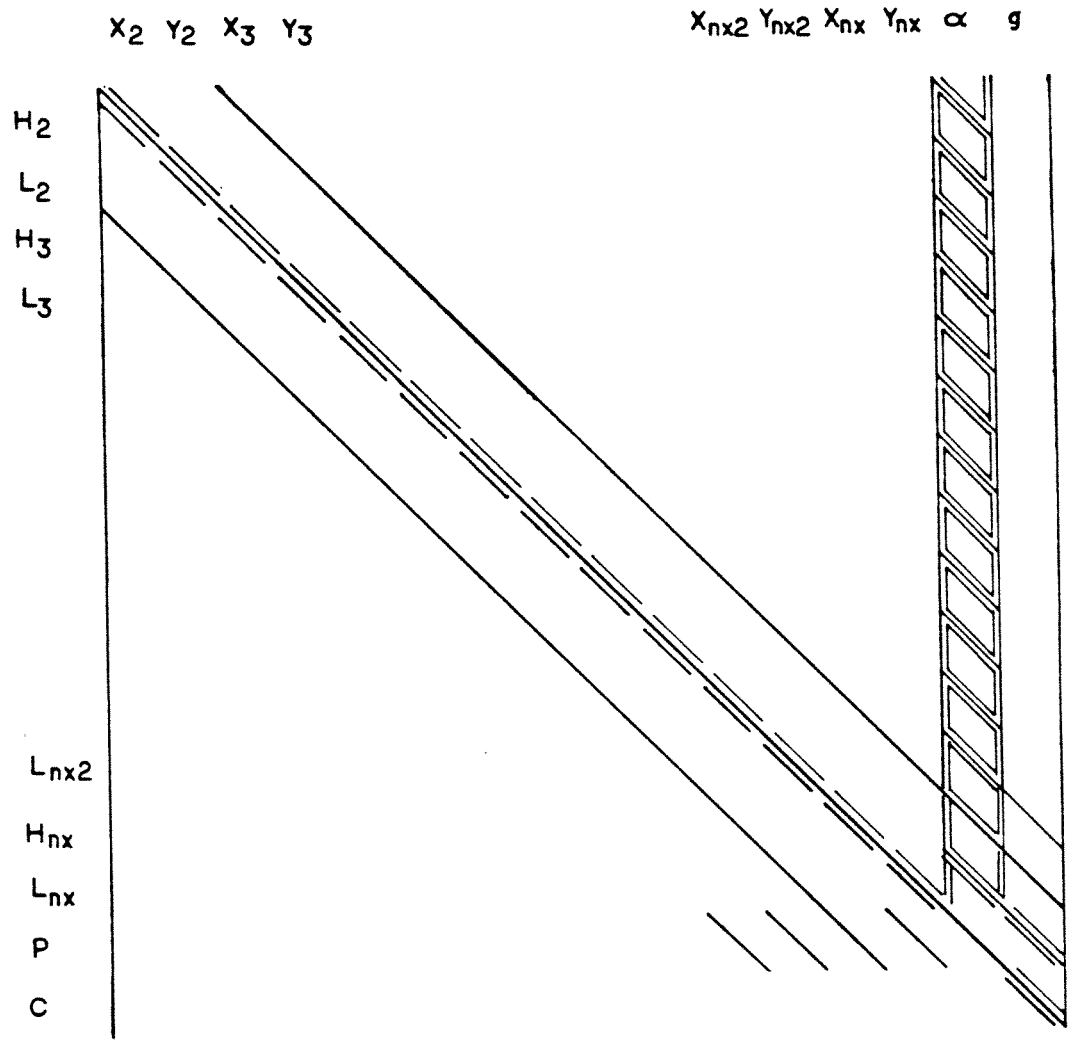

Figure 5

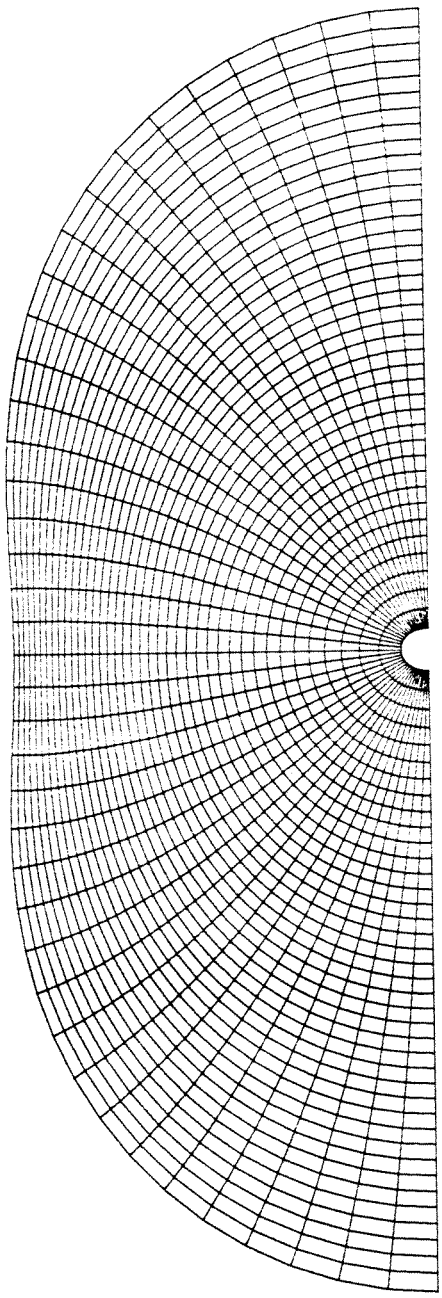

Figure 6a

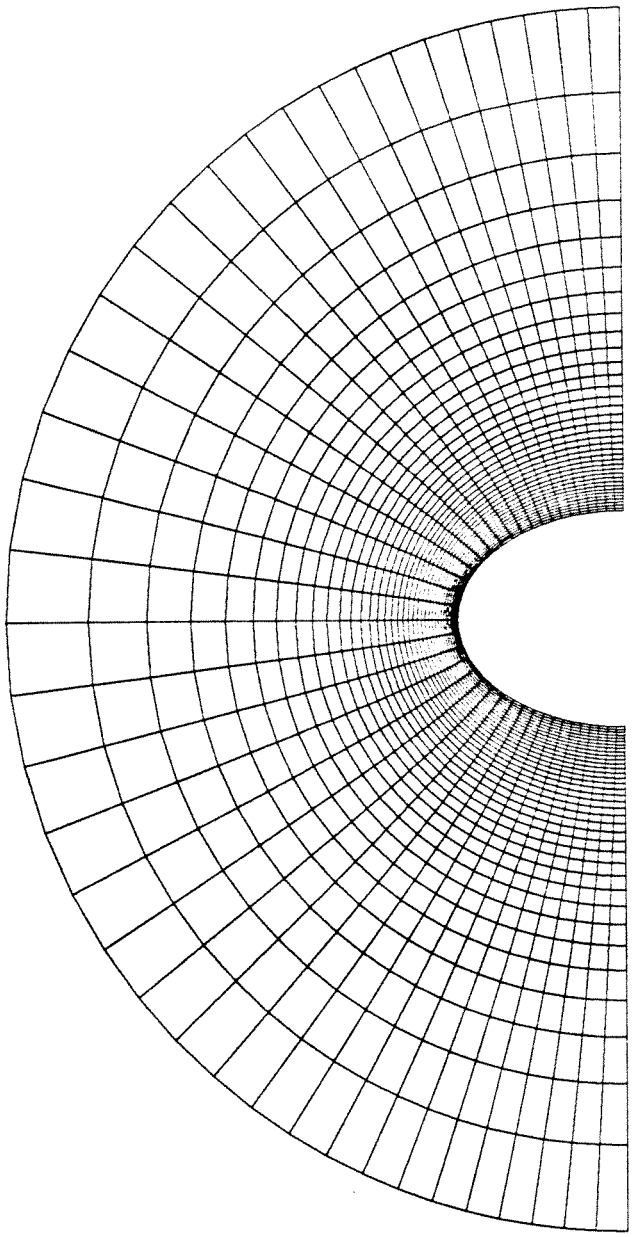

Figure 6b

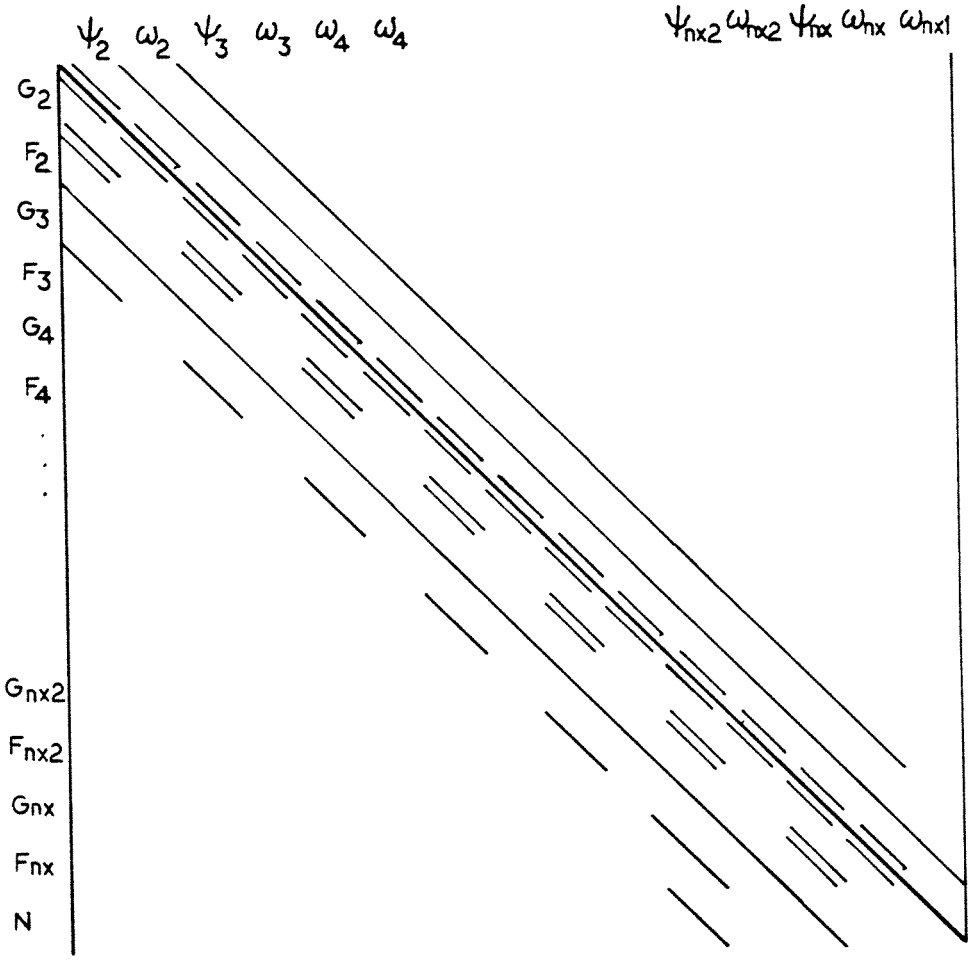
ψ_2 ω_2 ψ_3 ω_3 ω_4 ω_4
ψ_{nx2} ω_{nx2} ψ_{nx} ω_{nx} ω_{nx1}
G_2
F_2
G_3
F_3
G_4
F_4
G_{nx2}
F_{nx2}
G_{nx}
F_{nx}
N

Figure 7

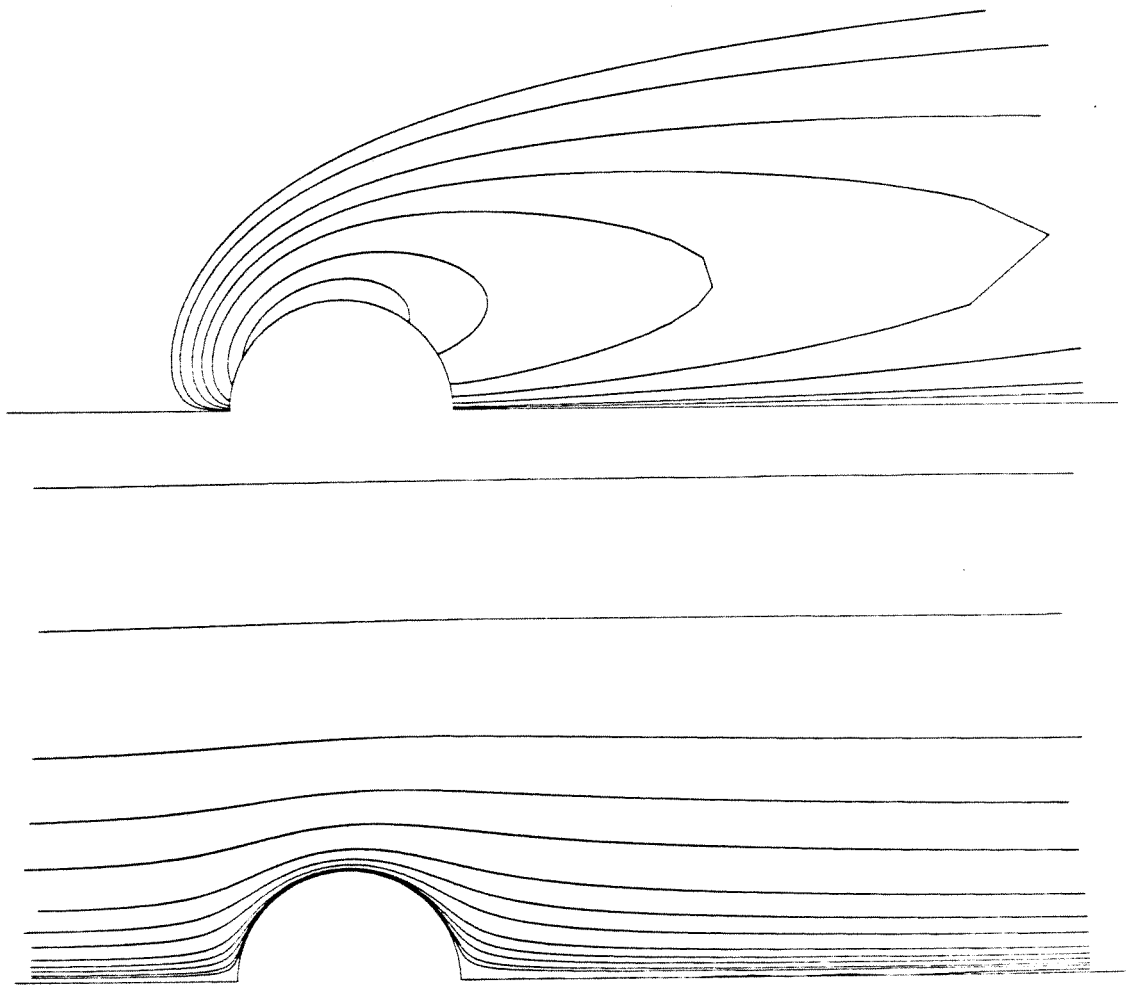

Re = 20

Figure 8a

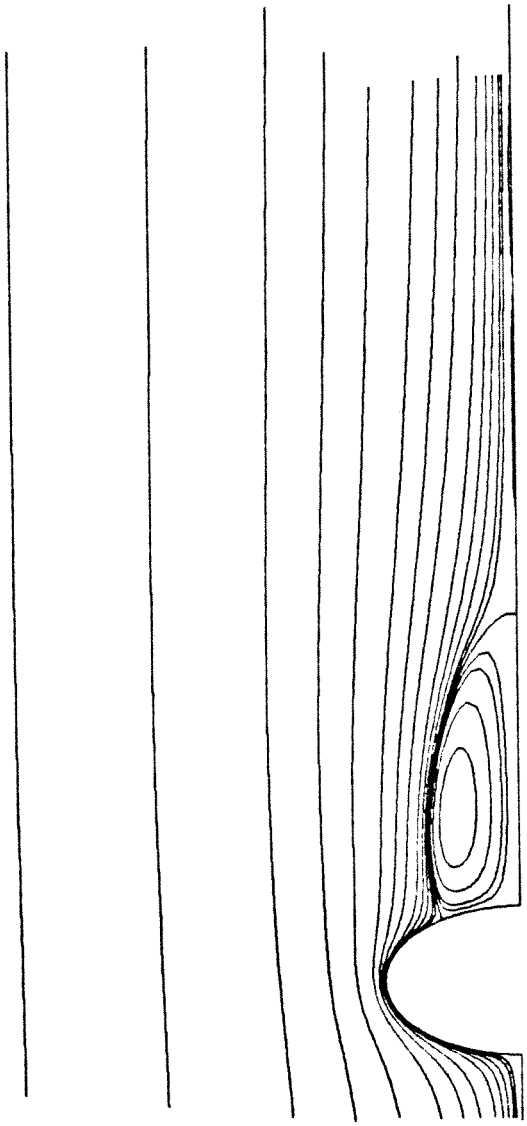

Re = 90

Figure 8b

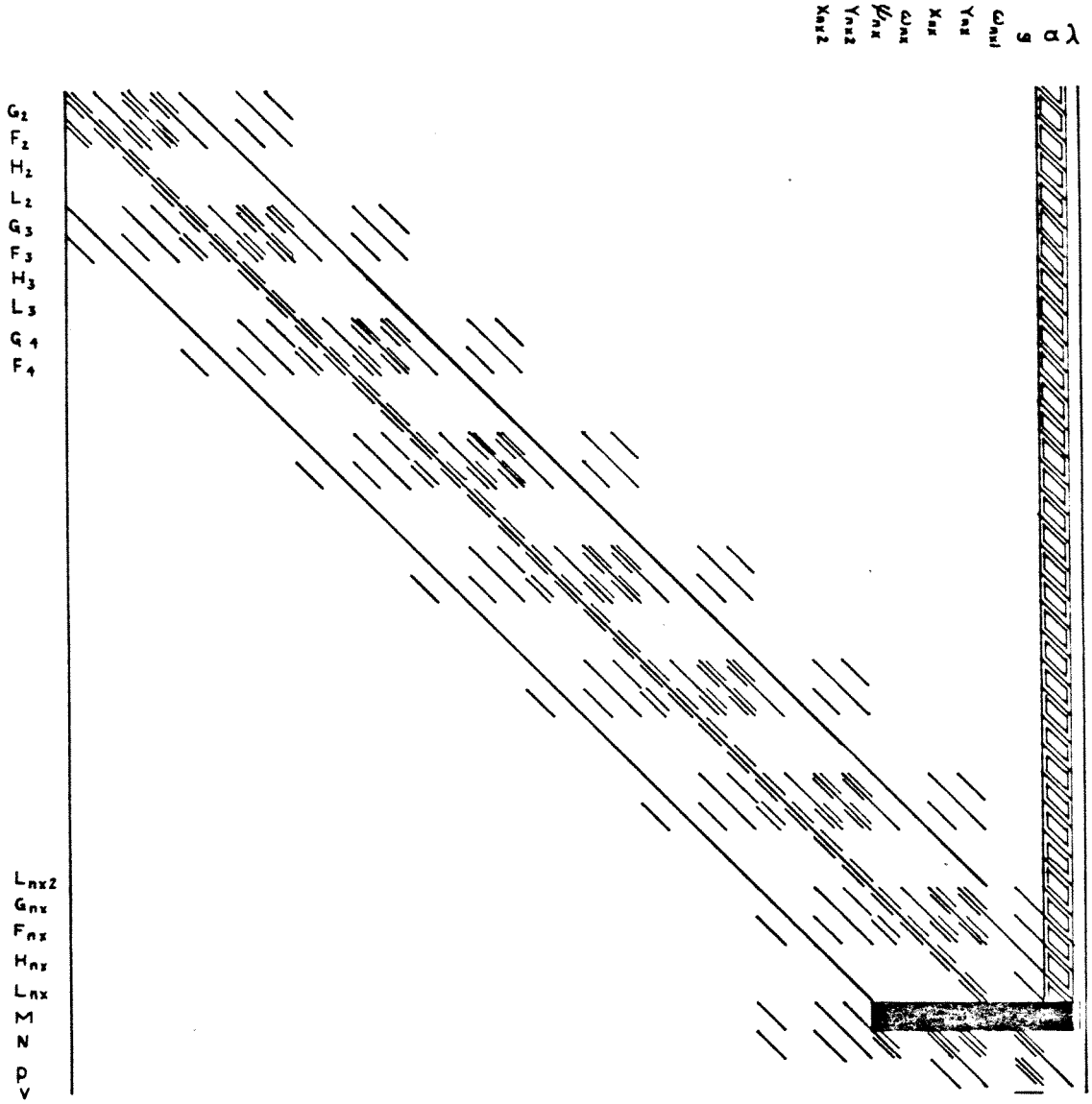
G_2
F_2
H_2
L_2
G_3
F_3
H_3
L_3
G_4
F_4
L_{nx2}
G_{nx}
F_{nx}
H_{nx}
L_{nx}
M
N
p
v
X_{nx2}
Y_{nx2}
β_{nx}
α_{nx}
X_{nx}
Y_{nx}
α_{nxl}
g
α
λ

Figure 9

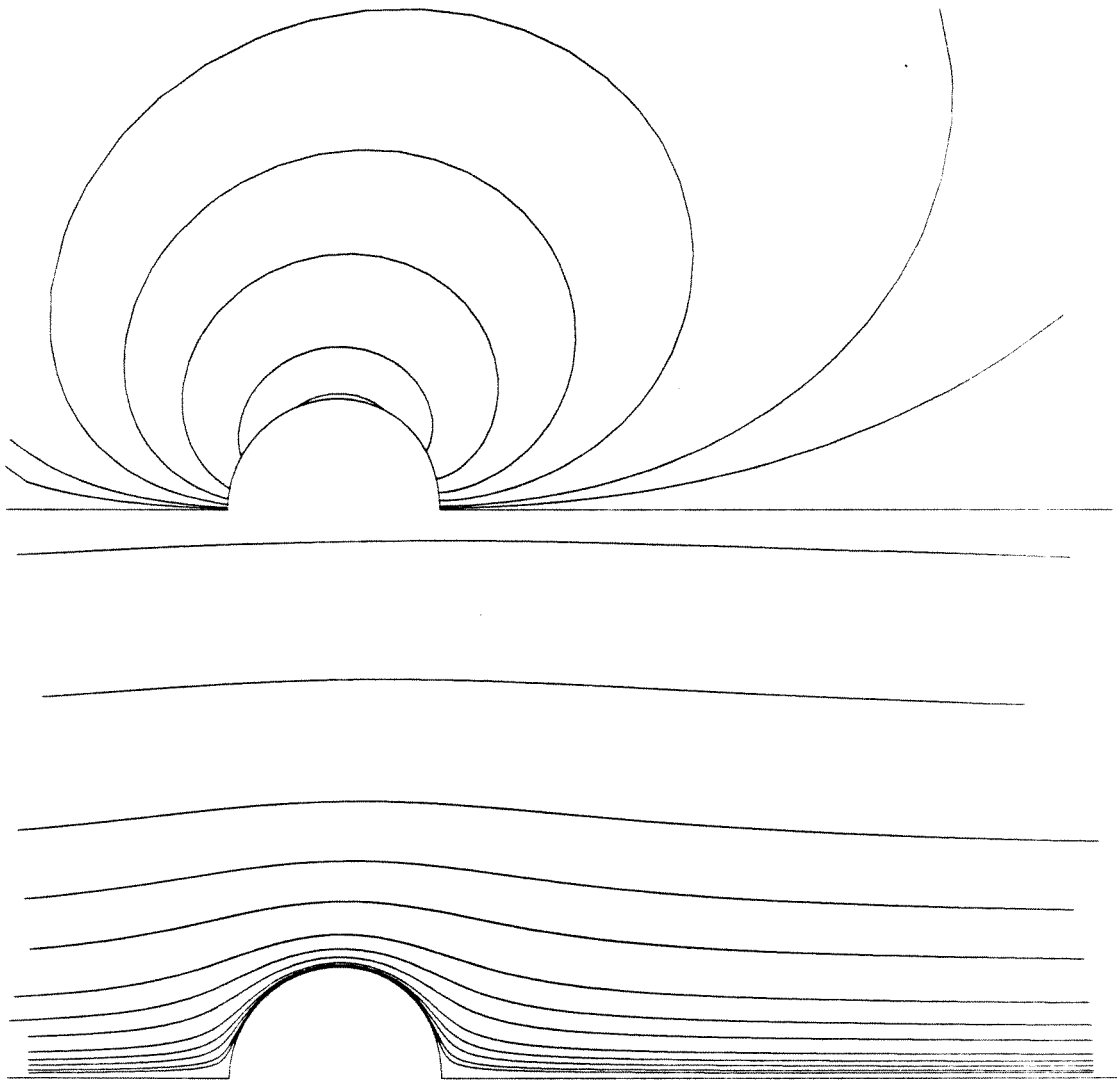

Re = 0.5

We = 0.5

Figure 10a

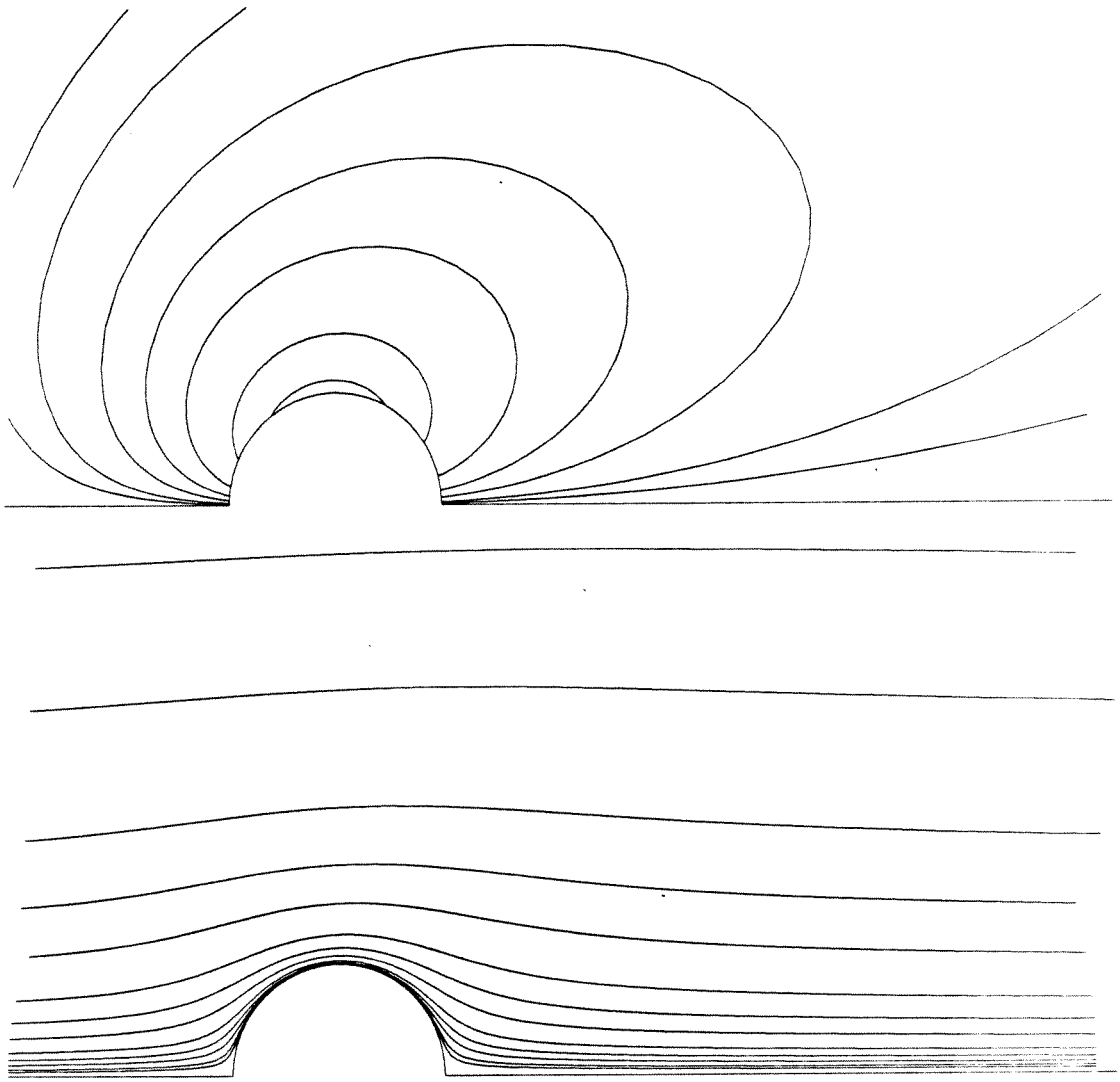

Re = 2

We = 0.5

Figure 10b

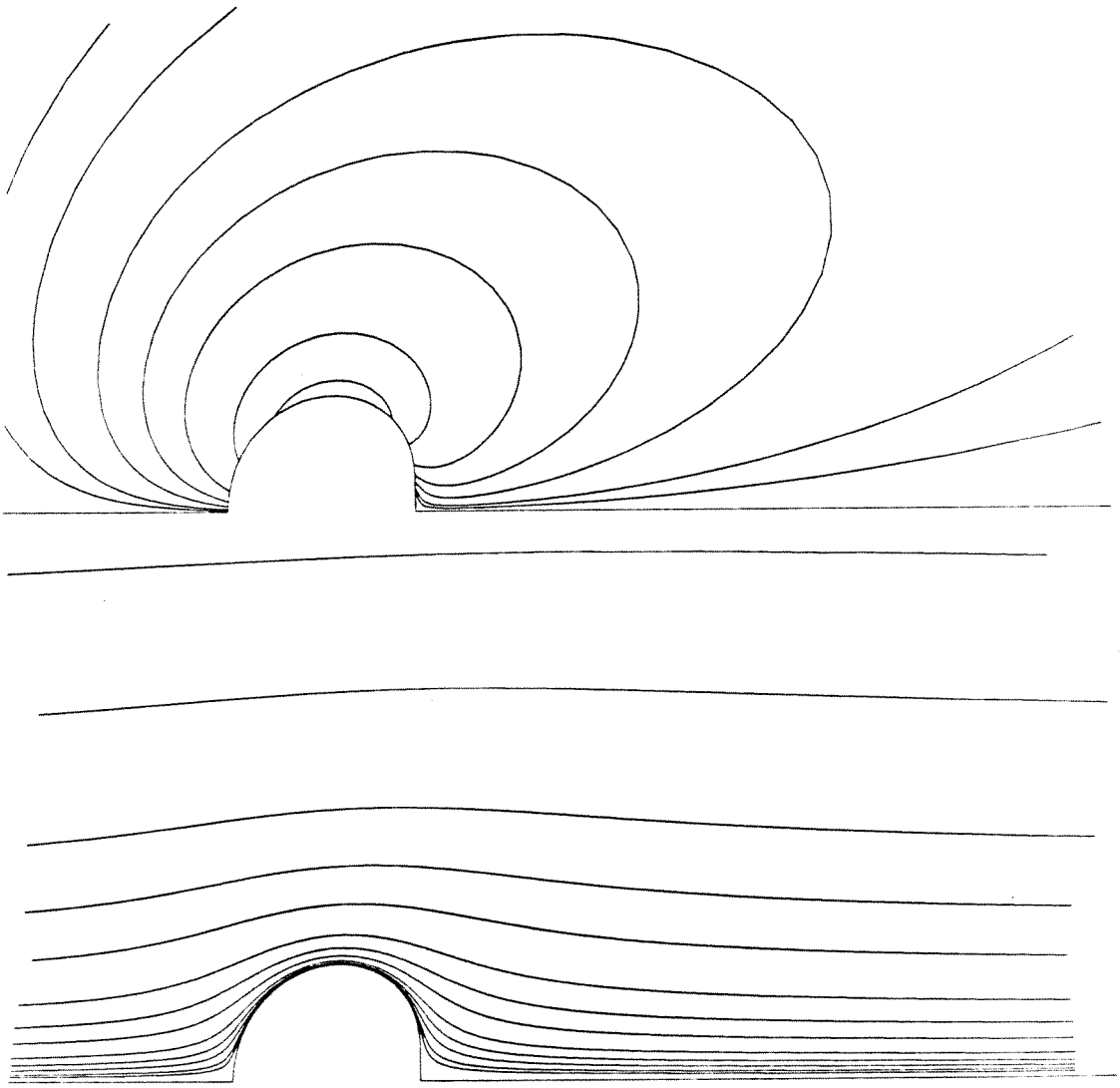

Re = 2

We = 2

Figure 10c

Appendix I

A Note on Distortion Functions for the Strong Constraint Method of Numerically Generating Orthogonal Coordinate Grids

The text of the Appendix I consists of an article which has been accepted for publication in the *Journal of Computational Physics*

A Note on Distortion Functions for the Strong Constraint Method of Numerically Generating Orthogonal Coordinate Grids

by

D.S. Dandy, E.P. Ascoli, and L.G. Leal

Department of Chemical Engineering
California Institute of Technology
Pasadena, California 91125

Abstract

In the strong constraint method of Ryskin and Leal, a boundary-fitted orthogonal coordinate grid is constructed by solution of the covariant Laplace equation on a unit square. The ratio of the diagonal elements of the metric tensor is specified as input to the method, thereby providing control over spacing of the resultant coordinate grid. In this note a proof is presented for the existence for orthogonal mappings generated by the strong constraint method.

I. Introduction

The emergence of large scale computing facilities in the last two decades has made it possible to solve problems that had previously been considered as intractable. In particular, the complicated partial differential equations which arise in areas such as fluid dynamics, optics, structural analysis, and quantum chemistry can now be solved efficiently using either finite difference or finite element techniques. An important advance in the application of finite difference techniques has been the development of methods to construct boundary-fitted curvilinear coordinates so that solutions can be obtained on domains of quite general shape without loss of any accuracy in the application of boundary conditions. An extensive survey of research in grid generation was done in an early paper by Thompson *et al* [1], and more recently by Eiseman [2]. In the most comprehensive work on grid generation to date, Thompson *et al* [3] compiled a list of virtually every known method of grid generation. There is a broad spectrum of coordinate grid types that can be created, either analytically or numerically; these grids can be orthogonal, nonorthogonal, conformal, or non-conformal.

The most common approach to numerically construct curvilinear coordinate grids is to solve an elliptic partial differential system, usually subject to Dirichlet conditions at the four boundaries. The solution of the two equations is a set of points $x(\xi,\eta)$, $y(\xi,\eta)$ which represent a discrete mapping between the physical (x,y) space and the curvilinear (computational) (ξ,η) space. For example, the points $x(\xi,\eta_\circ)$ and $y(\xi,\eta_\circ)$ correspond to a coordinate line of constant $\eta = \eta_\circ$ in (x,y) space. Of the elliptic PDE techniques, one that has proven to be extremely powerful in the study of free surface flow problems in fluid dynamics is a method due to Ryskin & Leal [4] (henceforth referred to as R&L). This method was developed for the construction of boundary-fitted orthogonal curvilinear coordinate systems in 2D, with the mapping defined by the covariant Laplace equation, and constraints imposed on the components of the metric tensor to insure orthogonality and to control grid spacing. Its power for the solution of

free surface flow problems is primarily due to the the method of implementation that R&L refer to as the strong constraint method. The underpinnings of the theory behind this method are also presented in some detail in Thompson *et al* [3], although the work of R&L is not mentioned.

The strong constraint method is a one-step method of mapping a discrete set of points evenly distributed inside a unit square in a (ξ, η) curvilinear coordinate domain onto a discrete set of points in (x, y). The two coordinate grids are related via the metric tensor, and to insure orthogonality of the generated grid the off-diagonal components of the metric tensor are required to be zero. The diagonal components of the metric tensor – referred to as the scale factors by R&L – are defined by

$$\begin{aligned} h_\xi &= \left[\left(\frac{\partial x}{\partial \xi} \right)^2 + \left(\frac{\partial y}{\partial \xi} \right)^2 \right]^{\frac{1}{2}} \\ h_\eta &= \left[\left(\frac{\partial x}{\partial \eta} \right)^2 + \left(\frac{\partial y}{\partial \eta} \right)^2 \right]^{\frac{1}{2}} \end{aligned} \tag{1a}$$

The ratio $h_\eta(\xi, \eta)/h_\xi(\xi, \eta)$ is called the distortion function and is denoted by $f(\xi, \eta)$. In the strong constraint method of R&L the distortion function is allowed to vary with position in the domain, and, in fact is specified on the (ξ, η) domain $[0, 1] \times [0, 1)$ as input to the method. In contrast, the ratio of the diagonal components would be unity for a comformal mapping.

The system to be solved for the mapping functions $x(\xi, \eta)$ and $y(\xi, \eta)$ on a unit square in (ξ, η) is

$$\begin{aligned} \frac{\partial}{\partial \xi}\left(f \, \frac{\partial x}{\partial \xi} \right) + \frac{\partial}{\partial \eta}\left(\frac{1}{f} \, \frac{\partial x}{\partial \eta} \right) &= 0 \\ \frac{\partial}{\partial \xi}\left(f \, \frac{\partial y}{\partial \xi} \right) + \frac{\partial}{\partial \eta}\left(\frac{1}{f} \, \frac{\partial y}{\partial \eta} \right) &= 0. \end{aligned} \tag{1b}$$

Particular to free surface problems in conjunction with the strong constraint method is the boundary condition on the above mapping system which is applied at the free surface ($\xi = 1$): here h_ξ is specified. This boundary condition is of

neither Neumann or Dirichlet type and it, in part, reflects the functional coupling of x and y along the free boundary.

Roughly speaking, a particular value of the distortion function $f(\xi_\circ, \eta_\circ)$ corresponds to the ratio of the sides of an infinitesimal rectangle in the (x, y) plane which is the image of an infinitesimal square in the (ξ, η) plane about the point $(\xi_\circ, \eta_\circ)$. Thus, f is a measure of the stretching of the coordinate grid from a conformal mapping to an orthogonal one. However, since an arbitrary stretching of an orthogonal grid can produce a highly skewed, non-orthogonal grid, it is not obvious that an orthogonal mapping should exist for all choices of $f(\xi, \eta)$. The lack of criteria for choosing an f that will insure the existence of an orthogonal map is the most important limitation of the strong constraint method of orthogonal mapping. In the present note, we show that for a restricted class of distortion functions, the strong constraint method can be looked upon as a two-step process for which the first step is stretching of the (ξ, η) coordinate lines to an intermediate set of coordinates, and the second step a conformal map of the intermediate coordinates to (x, y). As might be anticipated, a group of distortion functions which allow this interpretation are those which stretch ξ along itself independent of η, and η along itself independent of ξ, and so, in a manner analogous to classical separation of variables, a product form for f, that is, $f(\xi, \eta) = \Phi(\xi)\,\Theta(\eta)$, suggests itself. The following analysis shows that if f *is* of a product form, then the mapping equations, Eq. (1b), with their associated boundary conditions comprise a well-posed problem and that the existence of an othogonal coordinate grid is guaranteed (subject, of course, to discretization error in the numerical implementation). Necessary restrictions on Φ and Θ will be discussed.

II. Formulation

The strong constraint method splits a free boundary problem via Picard type iterations into two distinct sequences of components: (a) dynamic flow problems, and (b) coordinate grid generation problems. In terms of finite differencing, at each iteration a coordinate grid is generated for which the free surface corresponds to a coordinate line. In turn, the dynamic component provides updated information concerning the shape of the free boundary.

For illustrative purposes, consider the problem of flow past a deformable drop or bubble described by R&L. In terms of the natural cartesian variables (x, y) the external flow domain is of infinite extent. In R&L, as well as in this paper, a preliminary conformal transformation is performed (see Fig. 1). The fluid interface Γ in (x, y) space is transformed to Γ^* in (x^*, y^*), so that infinity in (x, y) is transformed to the origin in (x^*, y^*), and this simple transformation replaces the unbounded coordinates (x, y), eliminating the need for truncation of the domain. The bounded domain (x^*, y^*) is then mapped via the grid generation method of R&L onto a unit square in which (ξ, η) are the working variables. Computation of the dynamic portion of the problem takes place in this unit square. The coordinate line $\xi = 1$ corresponds to the free surface Γ^*, while $\xi = 0$ corresponds to the origin in the (x^*, y^*) space. The coordinate η is of "angular" type (ξ is of radial type) and is required to satisfy periodic constraints, so that $(\xi, 0)$ and $(\xi, 1)$ correspond to the same point in (x^*, y^*). Relative to the system (x^*, y^*) the coordinate grid generation problem may be mathematically formulated as follows: the covariant Laplace equations for the mapping functions $x^*(\xi, \eta)$ and $y^*(\xi, \eta)$ are

$$\begin{aligned} \frac{\partial}{\partial \xi}\left(f \frac{\partial x^*}{\partial \xi}\right) + \frac{\partial}{\partial \eta}\left(\frac{1}{f} \frac{\partial x^*}{\partial \eta}\right) &= 0 \\ \frac{\partial}{\partial \xi}\left(f \frac{\partial y^*}{\partial \xi}\right) + \frac{\partial}{\partial \eta}\left(\frac{1}{f} \frac{\partial y^*}{\partial \eta}\right) &= 0. \end{aligned} \tag{2}$$

Due to the connection between the system of Laplace equations and the Cauchy-Riemann equations in conformal mapping, it is evident that one can write an

analogous set of equations:

$$f\,\frac{\partial x^*}{\partial \xi} \;=\; \frac{\partial y^*}{\partial \eta} \qquad\qquad \frac{\partial x^*}{\partial \eta} \;=\; -\,f\,\frac{\partial y^*}{\partial \xi}.$$

As mentioned before, the distortion function f is specified as input in the strong constraint method, along with the scale factor $h^*_\xi(1,\eta)$ for $\eta \in [0,1)$. Here,

$$\begin{aligned} h^*_\xi &\stackrel{\text{def}}{=} \left[\left(\frac{\partial x^*}{\partial \xi}\right)^2 + \left(\frac{\partial y^*}{\partial \xi}\right)^2\right]^{\frac{1}{2}} \\ h^*_\eta &\stackrel{\text{def}}{=} \left[\left(\frac{\partial x^*}{\partial \eta}\right)^2 + \left(\frac{\partial y^*}{\partial \eta}\right)^2\right]^{\frac{1}{2}} \end{aligned} \tag{3a}$$

The curve defining the free surface is

$$\Gamma^* \;=\; \{x^*(1,\eta),\; y^*(1,\eta) \;:\; \eta \in [0,1)\;\}. \tag{3b}$$

Due to periodicity,

$$(x^*(\xi,1), y^*(\xi,1)) \;=\; (x^*(\xi,0), y^*(\xi,0)) \qquad\qquad \xi \in [0,1], \tag{3c}$$

and the origin is defined by

$$(x^*(0,\eta), y^*(0,\eta)) \;=\; (0,0) \qquad\qquad \eta \in [0,1). \tag{3d}$$

Finally, we require that

$$y^*(1,0) = 0. \tag{3e}$$

Conditions (3d) and (3e) are imposed to make the mapping concrete, such that Eq. (3d) fixes a particular translation of the coordinates, and Eq. (3e) fixes the "starting point" of the angular type coordinate η.

To reiterate, in this framework, the information provided by the dynamic problem at the most recent step is a new set of values for $h^*_\xi(1,\eta)$. The variable f, referred to as the distortion functon in R&L is to be specified in advance by the implementer, and is incorporated into the method to provide control over grid spacing. Little guidance toward the choice of f is available. Further, R&L do not discuss the question of the existence of solutions to Eq. (2) relative to the choice of f. This note demonstrates the existence of solutions to Eq. (2) for a restricted class of f's, specifically the case when f is of special separable (that is, product) form in the variables ξ and η.

III. The proof

It must be shown that there exists a path between the unit square in the (ξ, η) domain and the desired domain $\mathcal{D}$ in the (x^*, y^*) plane. This will be accomplished by breaking the path up into three steps (see Fig. 2), with the first step being a change of variables $r = f_1(\xi)$ and $\theta = f_2(\eta)$, from a unit square in the (ξ, η) computational domain to a rectangle in a circular cylindrical-type (r, θ) coordinate domain (maintaining the radial sense of ξ and the angular sense of η). The functions $f_1(\xi)$ and $f_2(\eta)$ are assumed to be one-to-one and smooth †, and are normalized and shifted for convenience so that $f_1(0) = 0$, $f_1(1) = 1$, $f_2(0) = 0$, and $f_2(1) = 2\pi$. Beyond these elementary restrictions f_1 and f_2 are arbitrary. The function f_1 represents a stretching or shrinking of the coordinate ξ, independent of η, and likewise, f_2 causes a stretching or shrinking of η independent of ξ. The functions f_1 and f_2 will be used to construct the distortion funtion f. In this context then, freedom in choosing f_1 and f_2 corresponds to control over grid spacing. As mentioned above, the coordinate variables r and θ are circular cylindrical-type, and so the rectangle in (r, θ) can be transformed to a unit disk in (u, v) space using the relations $u = r\cos\theta$ and $v = r\sin\theta$. The motivation for carrying out these two coordinate transformations (from (ξ, η) to (r, θ) to (u,v)) arises from complex variable theory, where the Riemann Mapping theorem guarantees the existence of a conformal map connecting a *given*, non-trivial two-dimensional domain to a unit disk. We have an analogous situation here except that for the strong constraint method the actual domain $\mathcal{D}$ in (x^*, y^*) is *not* known, since the boundary Γ^* of $\mathcal{D}$ is itself unknown. What is known instead is $h^*_\xi(1, \eta)$.

Consider a particular choice for f, namely

$$f(\xi, \eta) = \frac{f_1(\xi)\, f_2'(\eta)}{f_1'(\xi)}, \tag{4}$$

† In theory, f_1 and f_2 should be C^∞ but in numerical implementation this restriction may be relaxed.

For this choice of distortion function, Eq. (2) on the unit disk reduces to

$$\begin{aligned} \frac{\partial^2 x^*}{\partial u^2} + \frac{\partial^2 x^*}{\partial v^2} &= 0 \\ \frac{\partial^2 y^*}{\partial u^2} + \frac{\partial^2 y^*}{\partial v^2} &= 0. \end{aligned} \tag{5}$$

This choice of distortion function $f(\xi,\eta)$ is a product of the functions $f_1(\xi)/f_1'(\xi)$ and $f_2'(\eta)$, and the form may appear confusing at first glance due to the term f_1 in the numerator. However, this term is present because it is the necessary "length" factor required when dealing with angular and radial type coordinate systems.

The form of Eq. (5) suggests that we seek an analytic function F of the form $F(w) \equiv F(u+\imath v) = x^* + \imath y^*$ on the closed unit disk $u^2+v^2 \leq 1$. This function maps the unit disk onto the domain $\mathcal{D}$. Direct manipulation shows that specification of $h_\xi^*(1,\eta)$ is equivalent to specifying $|F'|$, the norm of the derivative of the analytic function, on the boundary of the disk. As a result of the Cauchy-Riemann equations

$$\frac{\partial x^*}{\partial u} = \frac{\partial y^*}{\partial v} \qquad\qquad \frac{\partial x^*}{\partial v} = -\frac{\partial y^*}{\partial u},$$

Eq. (5) is identically satisfied.

Further, Eqs. (3a)-(3d) reduce to the very simple constraints

$$F(0) = 0 \tag{6a}$$

and

$$\arg\{F(1)\} = 0. \tag{6b}$$

The analytic function $F(w)$ is required to be invertible, so in addition to the above two constraints we impose $|F'| \neq 0$ on the closed disk.

As mentioned earlier, if Γ^* (or equivalently, the value of F on the boundary of the disk) is known, then the Riemann mapping theorem guarantees the existence of the conformal mapping $F(w)$, and therefore the existence of an orthogonal mapping between (ξ,η) and (x,y). Here instead we have $|F'|$ specified

on the boundary, and it is necessary to prove the existence of $F(w)$. This is carried out as follows: first, define the function

$$G(u+\imath v) \;=\; \log(F') \;=\; \ln|F'| \;+\; \imath \arg\{F'\},$$

where the $k=0$ branch of the log has been selected. The function F is assumed analytic on the disk, implying that F', and therefore $G^{\dagger}$, is also analytic on the disk. As a result, specification of $|F'|$ on the boundary (of the disk) is equivalent to specification of $\Re\{G\}$ on the boundary. Poisson's formula immediately gives $\Re\{G\}$ in the interior of the disk ($r<1$):

$$\Re\{G(re^{\imath\theta})\} \;=\; \frac{1}{2\pi}\int_0^{2\pi} \frac{1-r^2}{1-2r\cos(\theta-\alpha)+r^2}\,\Re\{G(e^{\imath\alpha})\}\,d\alpha. \tag{7}$$

Then, $\Im\{G\} = \arg\{F'\}$ is determined in the disk via the Cauchy-Riemann equations for G

$$\frac{\partial\Im\{G\}}{\partial v} \;=\; \frac{\partial\Re\{G\}}{\partial u} \qquad\qquad \frac{\partial\Im\{G\}}{\partial u} \;=\; -\frac{\partial\Re\{G\}}{\partial v} \tag{8}$$

and subsequent direct integration, and further, $\arg\{F'\} \;=\; s(u,v)+c_1 \;=\; S(u+\imath v)+c_1$, where c_1 is a real constant resulting from the integration. The total derivative $F'(w)$ is then recovered as $F' \;=\; |F'|\,\exp[\imath S + c_1]$. Analyticity of F' implies the existence of a Taylor series representation in the disk

$$F'(w) \;=\; e^{\imath c_1}\,(a_0 + a_1 w + \cdots) \tag{9}$$

where $w = u+\imath v$. A subsequent complex integration of $F'(w)$ yields $F(w)$ to within a second complex constant, c_2:

$$F(w) \;=\; c_2 + e^{\imath c_1}\,(a_0 w + \frac{1}{2}a_1 w + \cdots)w \tag{10}$$

Application of condition (6a) yields $c_2 = 0$, and the real constant c_1 represents the rotational orientation of the mapping and is fixed by condition (6b). Therefore, the mapping $F(w)$ does exist subject to the constraints mentioned above.

---

† since $|F'| \neq 0$ on the disk, G is well defined

Thus, by a route involving two coordinate transformations and one conformal map, we have shown that an orthogonal mapping between (ξ, η) and (x, y) *does* exist, and that it is determined by specification of $h^*_\xi(1, \eta)$ along with a special product form for the distortion function f.

IV. Conclusions

The purpose of the strong constraint method is to generate an orthogonal coordinate system by imposing suitable boundary conditions on the computational (ξ, η) domain, in conjunction with specification of the distortion function $f(\xi, \eta)$. The boundary conditions reflect the periodicity of the angular coordinate direction and the fact that the image of a boundary line in the (ξ, η) space is the origin in the (x^*, y^*) coordinate plane. In addition, along the coordinate line $\xi = 1$ (corresponding to the free surface in physical space) the distortion function h^*_ξ is specified.

One very important consideration is the relationship between the choice of f and the existence of an orthogonal mapping. It is intuitive that an arbitrary stretching of a conformal map will yield a non-orthogonal mesh, or mapping, and further that a solution to Eq. (2) may not even exist for certain choices of f. In this note we have shown that if f is of a special product form, represented by Eq. (4), and if h^*_ξ is specified at one boundary, then an orthogonal mapping *does* exist between (ξ, η) and (x, y).

Acknowledgements

This work was partially supported by a grant from the National Science Foundation. The authors also wish to thank the Chevron Oil Field Research Company for partial support of this research.

Appendix: Details of the proof

The main text of Chapter III provides little detail regarding the necessary coordinate transformations, how the form for the distortion function f arises, and the connection between $h^*_\xi(1,\eta)$ on the computational domain and $|F'|$ on the boundary of the unit disk; in this section we will derive the equations in the previous section.

I. the coordinate transformations

To demonstrate that a path exists between (x^*, y^*) and (ξ, η) it is more convenient to proceed in the reverse order to the one presented above. That is, we will follow the path from (x^*, y^*) to (ξ, η) rather than from (ξ, η) to (x^*, y^*). The Laplace equations (the mapping equations) in terms of the cartesian-like variables (u, v) are

$$\begin{aligned} \frac{\partial^2 x^*}{\partial u^2} + \frac{\partial^2 x^*}{\partial v^2} &= 0 \\ \frac{\partial^2 y^*}{\partial u^2} + \frac{\partial^2 y^*}{\partial v^2} &= 0. \end{aligned} \tag{A1}$$

By using the relations $u = r\cos\theta$ and $v = r\sin\theta$, these equations can be written in the (r, θ) domain as

$$\begin{aligned} \frac{1}{r}\frac{\partial}{\partial r}\left(r\frac{\partial x^*}{\partial r}\right) + \frac{1}{r^2}\frac{\partial^2 x^*}{\partial \theta^2} &= 0 \\ \frac{1}{r}\frac{\partial}{\partial r}\left(r\frac{\partial y^*}{\partial r}\right) + \frac{1}{r^2}\frac{\partial^2 y^*}{\partial \theta^2} &= 0, \end{aligned} \tag{A2}$$

where the scale factors for this coordinate system are

$$\begin{aligned} h_r &= \left[\left(\frac{\partial x^*}{\partial r}\right)^2 + \left(\frac{\partial y^*}{\partial r}\right)^2\right]^{\frac{1}{2}} = 1 \\ h_\theta &= \left[\left(\frac{\partial x^*}{\partial \theta}\right)^2 + \left(\frac{\partial y^*}{\partial \theta}\right)^2\right]^{\frac{1}{2}} = r. \end{aligned} \tag{A3}$$

Application of the chain rule, along with the relationship $F(u + \imath v) = x^* + \imath y^*$

to the derivatives in Eq. (A2) yields

$$\begin{aligned}
\frac{\partial x^*}{\partial r} &= \cos\theta \frac{\partial \Re\{F\}}{\partial u} + \sin\theta \frac{\partial \Re\{F\}}{\partial v} \\
\frac{\partial y^*}{\partial r} &= \cos\theta \frac{\partial \Im\{F\}}{\partial u} + \sin\theta \frac{\partial \Im\{F\}}{\partial v} \\
\frac{\partial x^*}{\partial \theta} &= -r\sin\theta \frac{\partial \Re\{F\}}{\partial u} + r\cos\theta \frac{\partial \Re\{F\}}{\partial v} \\
\frac{\partial y^*}{\partial \theta} &= -r\sin\theta \frac{\partial \Im\{F\}}{\partial u} + r\cos\theta \frac{\partial \Im\{F\}}{\partial v}.
\end{aligned} \tag{A4}$$

These relations, together with the Cauchy-Riemann equations

$$\frac{\partial \Im\{F\}}{\partial v} = \frac{\partial \Re\{F\}}{\partial u} \qquad \frac{\partial \Im\{F\}}{\partial u} = -\frac{\partial \Re\{F\}}{\partial v}, \tag{A5}$$

show that the coordinate mapping defined by Eq. (A2) is orthogonal.

Now, we transform coordinates from the circular cylindrical-type (r, θ) domain to the (ξ, η) domain via the relations $r = f_1(\xi)$ and $\theta = f_2(\eta)$. Noting that

$$\begin{aligned}
\frac{\partial}{\partial \xi} &= \frac{\partial r}{\partial \xi}\frac{\partial}{\partial r} = f_1' \frac{\partial}{\partial r} \\
\frac{\partial}{\partial \eta} &= \frac{\partial \theta}{\partial \eta}\frac{\partial}{\partial \theta} = f_2' \frac{\partial}{\partial \theta},
\end{aligned} \tag{A6}$$

then Eq. (A3) can be written as

$$\begin{aligned}
\frac{1}{f_1 f_1'}\frac{\partial}{\partial \xi}\left(\frac{f_1}{f_1'}\frac{\partial x^*}{\partial \xi}\right) + \frac{1}{f_1^2 f_2'}\frac{\partial}{\partial \eta}\left(\frac{1}{f_2'}\frac{\partial x^*}{\partial \eta}\right) &= 0 \\
\frac{1}{f_1 f_1'}\frac{\partial}{\partial \xi}\left(\frac{f_1}{f_1'}\frac{\partial y^*}{\partial \xi}\right) + \frac{1}{f_1^2 f_2'}\frac{\partial}{\partial \eta}\left(\frac{1}{f_2'}\frac{\partial y^*}{\partial \eta}\right) &= 0.
\end{aligned} \tag{A7}$$

Multiplying Eqs. (A7) by $f_1 f_1' f_2'$ we obtain

$$\begin{aligned}
\frac{\partial}{\partial \xi}\left(\frac{f_1 f_2'}{f_1'}\frac{\partial x^*}{\partial \xi}\right) + \frac{\partial}{\partial \eta}\left(\frac{f_1'}{f_1 f_2'}\frac{\partial x^*}{\partial \eta}\right) &= 0 \\
\frac{\partial}{\partial \xi}\left(\frac{f_1 f_2'}{f_1'}\frac{\partial y^*}{\partial \xi}\right) + \frac{\partial}{\partial \eta}\left(\frac{f_1'}{f_1 f_2'}\frac{\partial y^*}{\partial \eta}\right) &= 0.
\end{aligned} \tag{A8}$$

Thus, if we denote the function $f_1 f_2' / f_1'$ as the distortion function $f(\xi, \eta)$, Eqs. (A8) reduce to the mapping equations of R&L shown in Eqs. (2) of the

previous section, and this f is of separable (product) form. It is now clear that the particular choice of the form of f in Eq. (4) of the previous section arose from requiring that Eqs. (A8) simplify to the R&L's mapping equations when going from the (r,θ) domain to the (ξ,η) domain.

Finally, we must show that the coordinate mapping functions $x^*(\xi,\eta)$ and $y^*(\xi,\eta)$ resulting from the solution of Eqs. (A8) form an orthogonal coordinate grid, and that the Cauchy Riemann-like equations for this system are the same as the ones found by R&L. First, define the vector $\mathbf{R} = x^*\mathbf{e}_{x^*} + y^*\mathbf{e}_{y^*}$. Then,

$$\mathbf{e}_r = \frac{\partial\mathbf{R}/\partial r}{|\partial\mathbf{R}/\partial r|} = \frac{\frac{\partial x^*}{\partial r}\mathbf{e}_{x^*} + \frac{\partial y^*}{\partial r}\mathbf{e}_{y^*}}{(\frac{\partial x^*}{\partial r})^2 + (\frac{\partial y^*}{\partial r})^2}, \qquad (A9)$$

and thus

$$\mathbf{e}_\xi = \frac{\partial\mathbf{R}/\partial\xi}{|\partial\mathbf{R}/\partial\xi|} = \frac{f_1'\frac{\partial\mathbf{R}}{\partial r}}{\left|f_1'\frac{\partial\mathbf{R}}{\partial r}\right|} = \mathbf{e}_r. \qquad (A10)$$

Similarly, we find that $\mathbf{e}_\eta = \mathbf{e}_\theta$. Since the (r,θ) coordinate system is orthogonal it is clear that the (ξ,η) coordinate system is also orthogonal, with $\mathbf{e}_\xi \cdot \mathbf{e}_\eta \equiv \mathbf{e}_r \cdot \mathbf{e}_\theta = 0$.

To prove that the solutions of Eqs. (A8) form an orthogonal mapping, we must show that

$$\frac{\partial x^*}{\partial\xi}\frac{\partial x^*}{\partial\eta} + \frac{\partial y^*}{\partial\xi}\frac{\partial y^*}{\partial\eta} = 0. \qquad (A11)$$

Equation (A11) corresponds to the off-diagonal component of the metric tensor relating (x^*,y^*) and (ξ,η), and we denote the components of this matrix by g_{ij}.

Substitution of the relations in Eqs. (A6), (A4), and (A5) into Eq. (A11) yields

$$\begin{aligned} g_{ij} &= f_1' f_2' \Big(\frac{\partial x^*}{\partial r}\frac{\partial x^*}{\partial \theta} + \frac{\partial y^*}{\partial r}\frac{\partial y^*}{\partial \theta} \Big) \\ &= f_1' f_2' \Bigg[\Big(\cos\theta \frac{\partial \Re\{F\}}{\partial u} + \sin\theta \frac{\partial \Re\{F\}}{\partial v} \Big) \\ &\qquad \times \Big(-r\sin\theta \frac{\partial \Re\{F\}}{\partial u} + r\cos\theta \frac{\partial \Re\{F\}}{\partial v} \Big) \\ &\quad + \Big(-\cos\theta \frac{\partial \Re\{F\}}{\partial v} + \sin\theta \frac{\partial \Re\{F\}}{\partial u} \Big) \\ &\qquad \times \Big(r\sin\theta \frac{\partial \Re\{F\}}{\partial v} + r\cos\theta \frac{\partial \Re\{F\}}{\partial u} \Big) \Bigg] \\ &= 0. \end{aligned} \tag{A12}$$

In the (r, θ) coordinate domain the Cauchy Riemann-like equations are

$$\frac{\partial x^*}{\partial r} = \frac{1}{r}\frac{\partial y^*}{\partial \theta} \qquad \frac{1}{r}\frac{\partial x^*}{\partial \theta} = -\frac{\partial y^*}{\partial r}, \tag{A13}$$

so that substitution of the relations in Eq. (A6) into Eq. (A13) gives us

$$\frac{1}{f_1'}\frac{\partial x^*}{\partial \xi} = \frac{1}{f_1 f_2'}\frac{\partial y^*}{\partial \eta} \qquad \frac{1}{f_1 f_2'}\frac{\partial x^*}{\partial \eta} = -\frac{1}{f_1'}\frac{\partial y^*}{\partial \xi}. \tag{A14}$$

When both equations in Eq. (A14) are multiplied by $f_1 f_2'$ we obtain the relations found by R&L, again provided that the distortion function f is of the form given in Eq. (4) of §III of this chapter.

II. The boundary condition at $\xi = 1$

As described in §II of this chapter, the boundary condition applied at the free surface is the specification of the scale factor, $h_\xi^*(1, \eta)$. The scale factor is defined by

$$h_\xi^* \stackrel{\text{def}}{=} \left[\left(\frac{\partial x^*}{\partial \xi} \right)^2 + \left(\frac{\partial y^*}{\partial \xi} \right)^2 \right]^{\frac{1}{2}}, \tag{A15}$$

and use of the relations in Eq. (A6) yields

$$h_\xi^* = f_1' \left[\left(\frac{\partial x^*}{\partial r} \right)^2 + \left(\frac{\partial y^*}{\partial r} \right)^2 \right]^{\frac{1}{2}}. \tag{A16}$$

Finally, employing Eqs. (A4) and (A5) we can write Eq. (A16) as

$$
\begin{aligned}
h^*_\xi = \; & f_1' \Bigg[\left(\cos\theta \frac{\partial \Re\{F\}}{\partial u} + \sin\theta \frac{\partial \Re\{F\}}{\partial v} \right)^2 \\
& + \left(\cos\theta \frac{\partial \Im\{F\}}{\partial u} + \sin\theta \frac{\partial \Im\{F\}}{\partial v} \right)^2 \Bigg]^{\frac{1}{2}} \\
= \; & f_1' \Bigg[\left(\cos\theta \frac{\partial \Re\{F\}}{\partial u} - \sin\theta \frac{\partial \Im\{F\}}{\partial u} \right)^2 \\
& + \left(\cos\theta \frac{\partial \Im\{F\}}{\partial u} + \sin\theta \frac{\partial \Re\{F\}}{\partial u} \right)^2 \Bigg]^{\frac{1}{2}} \\
= \; & f_1' \left[\left(\frac{\partial \Re\{F\}}{\partial u} \right)^2 + \left(\frac{\partial \Im\{F\}}{\partial u} \right)^2 \right]^{\frac{1}{2}} \\
\equiv \; & f_1' \left| F'(u + \imath v) \right|.
\end{aligned}
\tag{A17}
$$

It is obvious, then, that specification of $h^*_\xi(1, \eta)$ is equivalent to specification of $|F'(w)|$ on the boundary of the unit disk in the (u, v) domain.

References

1. J.F. Thompson, F.C. Thames, and C.W. Mastin, "Automatic numerical generation of body-fitted curvilinear coordinate system for field containing any number of arbitrary two-dimensional bodies", *J. Comp. Phys.* **15**, 299-319 (1974).

2. P.R. Eiseman, "Grid generation for fluid mechanics computations", *Ann. Rev. Fluid Mech.* **17**, 487-522 (1985).

3. J.F. Thompson, Z.U.A. Warsi, and C.W. Mastin, *Numerical Grid Generation*, Elsevier Science Publishing Co., New York (1985).

4. G. Ryskin and L.G. Leal, "Orthogonal mapping", *J. Comp. Phys.* **50**, 71-100 (1983).

Figure captions

Figure 1: Conformal mapping between the infinite physical domain and the finite auxiliary domain.

Figure 2: Schematic representation of the transformation path between the finite auxiliary domain and a unit square in the computational domain.

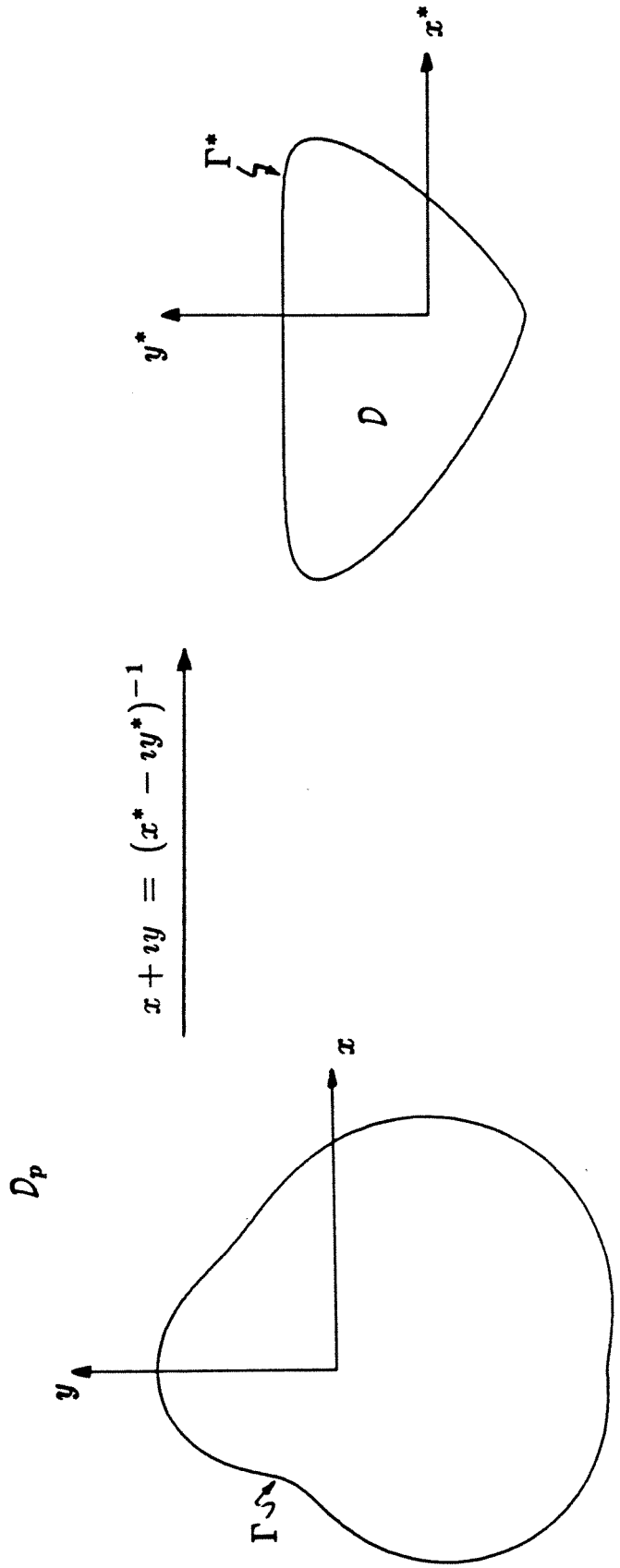

Figure 1.

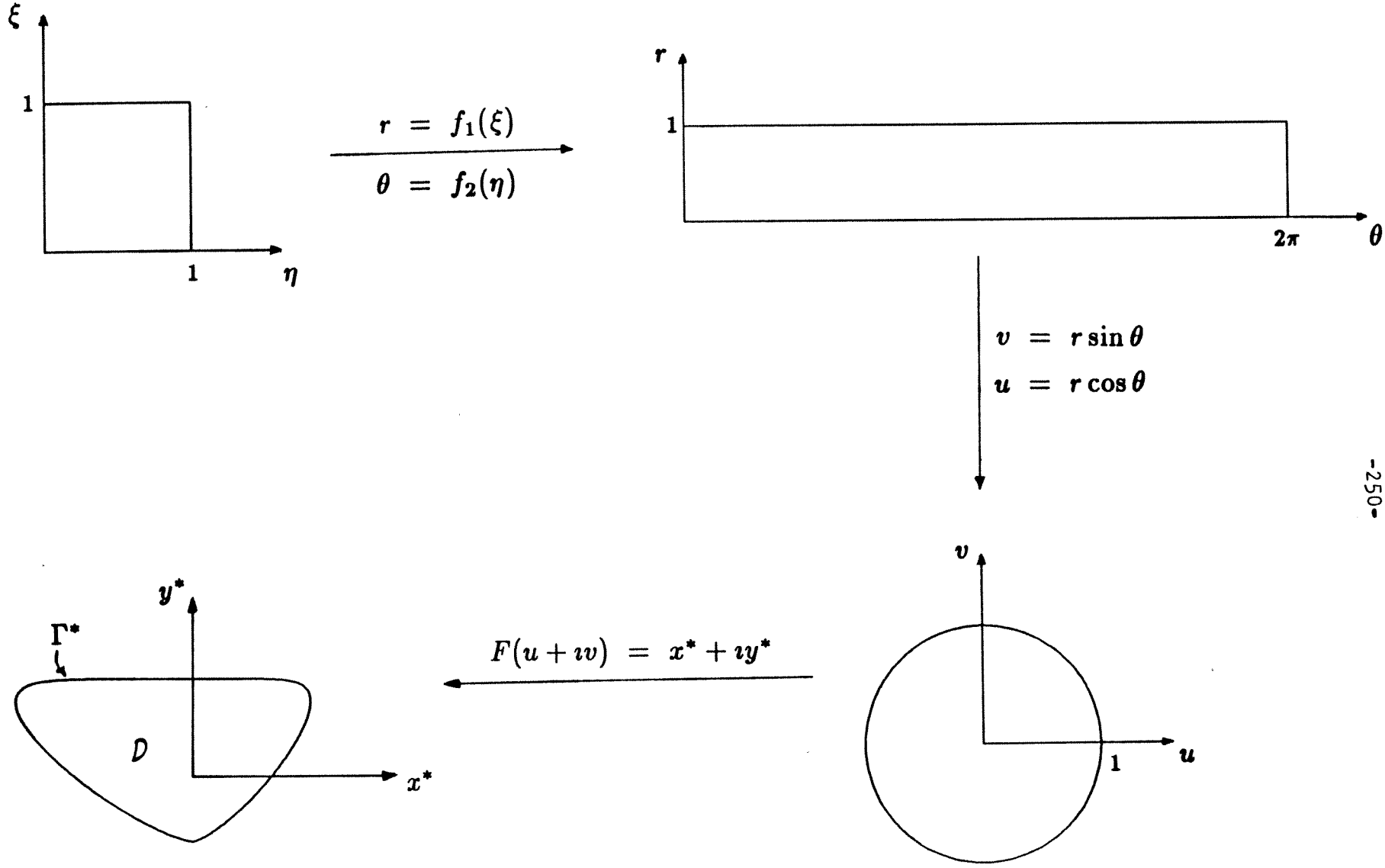

Figure 2.

Appendix II

The growth of creeping plumes

This is a collaborative effort with
Edward Ascoli, California Institute of Technology.

I. Introduction

In this chapter we present an efficient numerical scheme for studying the creeping motion of bubbles and drops in the presence of, or attached to a rigid plane boundary. Specifically, we will focus on the growth of a creeping plume. This scheme is based on the now-familar boundary integral technique first exploited in the study of low Reynolds number flows by Youngren and Acrivos (1976) when they considered streaming flow past an arbitrary body of revolution. In their work, Youngren and Acrivos took advantage of an integral reformulation of the Stokes' system derived by Odqvist (1930): the problem is reduced to calculation of unknown normal tractions at the surface of the body. Their computations were further simplified by the axisymmetry of the geometry, which lowers the domain of integration from two dimensions to one. The approach taken by Youngren and Acrivos was ideally suited to the infinite flow domain, because the boundary integral method—as indicated by its name—reduces a problem over the full domain (usually a subset of $\Re^3$) to integration over *all* of the boundaries of the domain (a subset of $\Re^2$), and in the infinite domain problem considered by Youngren and Acrivos this means integration over the body surface. In concept, there are no restrictions on the number of surfaces comprising the boundaries of a domain, but since the number of boundaries is equal to the number of surface integrals, in numerical practice the number of surfaces (i.e., integrals) matters greatly, since the transition from a continuous integral equation to a discrete sum is a tradeoff between desired accuracy and actual computational tractability. Specifically, as far as computations are concerned, the boundary element method requires the solution of a linear system having a dense coefficient matrix; the order of the matrix is $4N$, where N is the total number of sub-elements into which all of the surfaces have been divided. Clearly, the cost in computational speed and storage requirements must dictate the level of accuracy, in terms of discretization, which can be achieved.

Recently, researchers have turned their attention to applying the boundary

integral method to bodies in the presence of boundaries. The reason for the work is twofold: first, the influence of walls or deformable interfaces on the rise or settling of particles is of industrial importance, and also is a more realistic situation than an "infinite" domain free of boundaries. Second, the situation lends itself to more complicated flowfields and behavior due to the interaction between the wall and the body, and thus can be considered inherently interesting. Several examples of this phenomenon are the sedimentation of solid particles towards a rigid boundary or through an interface between two immiscible liquids, and the coalescence problem, in which a drop of one liquid moves under the action of buoyancy through a second liquid towards an interface separating the continuous fluid from the drop fluid. Lee and Leal (1982) considered the case of a solid sphere moving with constant velocity in a direction normal to a rigid interface. Berdan (1982) and Geller *et al* (1986) extended this earlier work to study the motion of a solid sphere moving in a direction normal to a deformable liquid-liquid interface. The latter study focused on large deformations of the interface, in particular, the formation of relatively long tails of fluid "pulled" along with the sphere as it passed through the plane of the undeformed interface. As with the work of Youngren and Acrivos, Berdan, Geller *et al* and Chi and Leal (1987) also used the fundamental singular solution (or Green's function) put forth by Odqvist (c.f. Ladyzhenskaya 1963). The numerical implementation of the boundary integral technique involved numerical integration not only over the surface of the solid sphere, but also over the interface, theoretically extending out to infinity.

There is a large class of problems, however, which involves the motion of a body (or bodies) in the presence of a plane wall: the growth of an attached drop due to the flow of fluid through an orifice (that is, a plume); the growth of an attached vapor bubble due to boiling; the motion of a deformable drop or bubble due to the action of gravity; the stretching and eventual breakage of a pendant drop; and the well-known coating flow problem. All of these problems are strong

candidates for solution via the boundary integral (i.e., BI) method because a knowledge of the full velocity and stress fields is of secondary importance relative to the shape and velocity of free surface. Of course, the BI method is limited to situations where the Reynolds number is, in theory, zero or infinite, whereas several of the examples above involve flows where Re can be large but finite, especially boiling and coating flows, and the technique is obviously not valid in conjunction with these problems. This is not to say that all boiling and coating problems are characterized by high Reynolds number, and the strengths of the BI method—relatively low computational memory requirements and suitability for use with complicated geometries—make it a potentially powerful tool to study these problems.

To demonstrate the effectiveness of the method, we will consider as an illustrative example the pendant drop problem. The static pendant drop problem has received considerable attention due to its use as a means of computing interfacial tension (e.g., Pierson and Whitaker 1976). The static problem provides a check on the long time behavior of the boundary integral scheme because it can be compared with the static analysis of Brown *et al* (1980). In the static analysis, the position of the contact line is assumed known and the angle is allowed to vary. More on this will be said in the discussion. The dynamic pendant drop (or, plume) is of considerable interest in oceanography (Olson and Singer 1985), and considerable experimental work has been done in this area (Rouse *et al* 1952; Richards 1963). Creeping plumes are divided into two classes: diapiric plumes, for which the viscosities of the plume fluid and surrounding fluid are approximately equal, and cavity plumes, for which the viscosity ratio of the plume is much less than the ambient fluid viscosity. Diapiric plumes are characterized by thick tails, while cavity plumes have thin, thread-like tails. In the experimental work of Olson and Singer, laboratory plumes were generated by injecting a glucose solution through a very small orifice into another glucose solution of different density. Almost all of the previous theoretical work on creeping

plumes has been concerned with steady motion; similarity solutions have been obtained for steady-state plumes when heat transfer is neglected (Brand and Lahey 1967; Roberts 1977) and also when heat transfer is considered (Spaulding and Cruddace 1961).

The time-dependent growth and formation of plumes has not received as much attention. There have been two-dimensional plume experiments (Foster 1971; Boss and Sacks 1985) and Morris (1985) obtained an approximate asymptotic solution for the growth of a two-dimensional plume. Additionally all of this previous work on plume growth has focused on diapirs. Here, we will obtain solutions for plumes at a variety of viscosity ratios and show that when the viscosity ratio is $O(1)$ we do indeed see diapirs, and when the viscosity ratio is less than 1 cavity plumes are observed.

The approach taken to solve this plume problem differs from previous boundary integral work mentioned above in the choice of the Green's function. We will demonstrate that a particular choice of the Green's function eliminates surface integrals involving the wall, thereby allowing greater nodal density at the surface of the plume. That is, since the wall is not included in the integral equations it is not necessary to truncate the domain due to computational considerations. Further, from the standpoint of computational cost there is a limit on the total number of sub-elements into which the boundaries can be divided. Removal of one of the boundaries (the wall) allows the use of more sub-elements on the surface of the plume, increasing the accuracy of the method. Although the problem under consideration is axisymmetric, this approach is fully applicable to and is extremely well-suited for three dimensional problems; in three dimensions, distributing elements on the surface of the body does not prove intractable in terms of computational ability since it is not necessary to discretize the wall.

To model the injection of the buoyant plume fluid, we use a solution in Happel and Brenner (1983 pp. 153-154) for steady flow through a circular orifice.

For constant head (pressure drop across the orifice) there is an exact solution in oblate spheroidal coordinates. The disturbance velocity and stress induced by this flow will be seen to depend on a dimensionless volumetric flow rate M, and the expressions for velocity and stress can be found in the Appendix.

The qualitative features of the solutions to the creeping plume problem will be seen to depend on several dimensionless quantities: the viscosity ratio λ; the capillary number Ca, which reflects the relative magnitude of viscous and surface tension forces; and the gravity number Cg, which is the ratio of body force to surface tension force. For the results obtained here, the mass flow rate M was chosen sufficiently small that it had no effect on the motion of the plume, yet large enough to supply necessary mass flow.

In §II the governing equations and boundary conditions are presented, and the integral equations are derived. A brief summary of the mechanics behind implementation follow. A discussion of the results obtained is given in §III.

II. Formulation

a. Equations and boundary conditions

We consider a drop which is attached to a plane wall, as shown in Fig. 1. The drop fluid will be denoted as fluid 1 and the outer phase as fluid 2. It is convenient to describe the geometry in terms of the cylindrical coordinates (ρ, θ, z) (since the problem under consideration is axisymmetric, the coordinates will usually be referred to as (ρ, z)), with $z = 0$ corresponding to the wall. Both the drop and the surrounding liquid are assumed to be Newtonian and incompressible, so that the inner fluid is characterized by constant viscosity μ_1 and density ϱ_1, and the outer fluid by μ_2 and ϱ_2. The analysis relies on the assumption that movement of the plume is slow enough so that the effects of inertia are negligibile both inside and outside the drop. This statement can be expresssed mathematically as

$$\frac{U\,a}{\nu_2} \ll 1.$$

The characteristic velocity U is the terminal velocity of a spherical drop having the initial volume as the plume and a is the radius of this sphere. The governing equations, the Stokes equations, have been derived in dimensionless form elsewhere (Lee and Leal 1982) and are restated below:

$$\begin{aligned} 0 &= -\nabla p^{(1)} + \lambda \nabla^2 \mathbf{u}^{(1)} \\ 0 &= \nabla \cdot \mathbf{u}^{(1)} \end{aligned} \tag{1}$$

for the inner fluid, and in the outer:

$$\begin{aligned} 0 &= -\nabla p^{(2)} + \nabla^2 \mathbf{u}^{(2)} \\ 0 &= \nabla \cdot \mathbf{u}^{(2)}, \end{aligned} \tag{2}$$

where $\lambda = \mu_1/\mu_2$ and arises due to nondimensionalization of the pressure. The boundary conditions are

$$\mathbf{u}^{(2)} \longrightarrow 0 \qquad \text{as } \|\mathbf{x}\| \longrightarrow \infty \tag{3}$$

in the upper half-space, and at the interface $\mathbf{x} \in S_I$:

$$\mathbf{u}^{(1)} = \mathbf{u}^{(2)}. \tag{4}$$

The stress jump at the interface S_I is

$$\left(\lambda \mathbf{n} \cdot \mathbf{T}_I^{(1)} - \mathbf{n} \cdot \mathbf{T}_I^{(2)}\right) = -\mathbf{n}\left(\frac{1}{Ca} \nabla \cdot \mathbf{n} + \frac{1}{Cg} z\right), \tag{5}$$

and the kinematic condition is

$$\frac{DF}{dt} = \frac{\partial F}{\partial t} + \mathbf{u} \cdot \nabla F = 0. \tag{6}$$

The stress tensor $\mathbf{T}^{(i)}$ in Eq. (5) does not contain the hydrostatic contribution, and so the body force term appears explicitly as the second term on the right hand side of the stress balance. However, in Eqs. (1) and (2) the body force is incorporated into the pressure.

The function F appearing in the kinematic equation, Eq. (6), is the parametrical representation of the position of the surface $F\big(\rho(s), z(s); t\big) = 0$ at any time t in terms of the arc-length s. By convention, arc-length is measured from the contact point between the interface and the wall. (In actuality, there is a contact line between the plume and the wall, but in the axisymmetric computation the line reduces to a point.) The normal to the surface is outward-pointing from fluid 1, and is defined in terms of F as

$$\mathbf{n} = \frac{\nabla F}{\|\nabla F\|}.$$

Using an arclength parametrization of the interface position has many advantages over using a representation which relies on describing the position in terms of a function of one of the independent coordinate variables (Simmons 1985). The coordinate representation is only valid when the functional representation of the interface position is single valued. For cartesian and cylindrical type representations, the onset of double valued behavior is manifested by very large (or infinite) values of the derivative of the coordinate functional. For example,

Geller *et al* (1986) analyze the creeping motion of a solid sphere normal to a deformable, initially flat interface. To represent the interface, three different "shape functions" were required, resulting from the use of three matched coordinate systems: two cylindrical and one spherical. Obviously, an arclength parametrization suffers from none of these difficulties.

In terms of the parametrization, the components of the unit normal to the surface are

$$\begin{aligned} n_\rho &= \frac{\dot{z}}{\left(\dot{\rho}^2 + \dot{z}^2\right)^{1/2}} \\ n_z &= -\frac{\dot{\rho}}{\left(\dot{\rho}^2 + \dot{z}^2\right)^{1/2}}, \end{aligned} \tag{7}$$

and the curvature is

$$\nabla \cdot \mathbf{n} = \frac{\dot{z}}{\rho\left(\dot{\rho}^2 + \dot{z}^2\right)^{1/2}} + \frac{\dot{\rho}\ddot{z} - \ddot{\rho}\dot{z}}{\left(\dot{\rho}^2 + \dot{z}^2\right)^{3/2}}. \tag{8}$$

The dot refers to differentiation with respect to the parameter s.

There are three dimensionless parameters resulting from nondimensionalization of the equations and boundary conditions. They are the viscosity ratio, $\lambda = \mu_1/\mu_2$; the capillary number $Ca = \mu_2 U/\gamma$; and the gravity number $Cg = \mu_2 U/a^2 g(\varrho_2 - \varrho_1)$. Additionally, a fourth parameter M arises, which is the volumetric flow rate through the orifice.

b. The boundary integral method

The crux of the boundary integral technique is the transformation of a linear partial differential system into an integral system. The technique used to accomplish this parallels the standard conversion of linear ordinary differential equations into integral equations via Green's functions and the adjoint operator (Coddington and Levinson 1955). In a manner analogous to the earlier work of Lee and Leal (1982) we can obtain an integral expression for an unknown velocity $\mathbf{u}$ at any arbitrary point $\mathbf{x} \in \Omega$ (Ω is the domain under consideration):

$$-\left(\mathbf{u}(\mathbf{x})\right)_j = \int_{\partial\Omega} \left(\mathbf{n} \cdot \mathbf{T}(\xi) \cdot \mathbf{v}^j(\mathbf{x}, \xi) - \mathbf{n} \cdot \Sigma^j(\mathbf{x}, \xi) \cdot \mathbf{u}(\xi)\right) dS_\xi \tag{9}$$

where $\mathbf{T}$ is the unknown stress, $\mathbf{v}^j$ and $\boldsymbol{\Sigma}^j$ are Green's functions for velocity and stress, respectively and dS_ξ denotes integration over $\partial\Omega$ with respect to the variable vector ξ. In Eq. (9), the velocity v_i^j is the ith velocity component at the point ξ due to a unit force in the j direction applied at the point $\mathbf{x}$. Eq. 9 will be evaluated at inner and outer surfaces of the drop and together with the boundary conditions (4) and (5) comprise a set of integral equations for the unknown boundary velocity and stress.

Past work (Youngren and Acrivos 1975, 1976; Rallison and Acrivos 1978; Lee and Leal 1982; Geller *et al* 1986; Chi and Leal 1987) has employed Green's functions for $\mathbf{v}^j$ and $\boldsymbol{\Sigma}^j$ put forth by Ladyzhenskaya, but here we use a Green's function presented by Blake (1971), whose solution stemmed from the earlier work of Oseen (1927):

$$\begin{aligned} v_i^j &= -\frac{1}{8\pi}\left\{\frac{\delta_{ij}}{r} + \frac{r_i r_j}{r^3} - \frac{\delta_{ij}}{R} - \frac{R_i R_j}{R^3}\right. \\ &\qquad \left. + 2x_3\Delta_j \frac{\partial}{\partial R_j}\left[\frac{x_3 R_i}{R^3} - \frac{\delta_{i3}}{R} - \frac{R_i R_3}{R^3}\right]\right\} \\ &= -\frac{1}{8\pi}\left\{\frac{\delta_{ij}}{r} + \frac{r_i r_j}{r^3} - \frac{\delta_{ij}}{R} - \frac{R_i R_j}{R^3}\right. \\ &\qquad + 2x_3\Delta_j\left[x_3\left(\frac{\delta_{ij}}{R^3} - \frac{3R_iR_j}{R^5}\right) + \frac{\delta_{i3}}{R^3}R_j\right. \\ &\qquad \left.\left. - \frac{1}{R^3}\left(\delta_{ij}R_3 + R_i\delta_{3j}\right) + \frac{3R_iR_jR_3}{R^5}\right]\right\}, \end{aligned} \tag{10}$$

with pressure

$$p^j = \frac{1}{4\pi}\left[\frac{r_j}{r^3} - \frac{R_j}{R^3} - 2x_3\Delta_j\left(\frac{\delta_{3j}}{R^3} - \frac{3R_jR_3}{R^5}\right)\right], \tag{11}$$

where $\mathbf{r} = (\xi_1 - x_1,\ \xi_2 - x_2,\ \xi_3 - x_3)^T$, $\mathbf{R} = (\xi_1 - x_1,\ \xi_2 - x_2,\ \xi_3 + x_3)^T$, $r = \left[(\xi_1 - x_1)^2 + (\xi_2 - x_2)^2 + (\xi_3 - x_3)^2\right]^{1/2}$, $R = \left[(\xi_1 - x_1)^2 + (\xi_2 - x_2)^2 + (\xi_3 + x_3)^2\right]^{1/2}$, and $R_3 = \xi_3 + x_3$. The quantity Δ_j has value $+1$ for $j = 1,\ 2$ and -1 for $j = 3$. Using Eqs. (10) and (11), the fundamental stress can be evaluated:

$$\begin{aligned} \Sigma_{ik}^j &= \frac{3}{4\pi}\left\{\frac{r_i r_j r_k}{r^5} - \frac{R_i R_j R_k}{R^5} - 2x_3\Delta_j\left[-\frac{x_3}{R^5}\delta_{ik}R_j\right.\right. \\ &\qquad \left.\left. + \frac{\xi_3}{R^5}\left(R_i\delta_{jk} + \delta_{ij}R_k\right) + \frac{R_i\delta_{3j}R_k}{R^5} - \frac{5R_iR_jR_k\xi_3}{R^7}\right]\right\}. \end{aligned} \tag{12}$$

The advantage of using this particular choice for the Green's function is that there is no contribution when Eq. (9) is applied at the wall. Quite simply, this Green's function solution to Stokes equations also satisfies the no-slip condition at the wall.

The details of applying Eqs. (9), (4) and (5) at the interface are presented in Lee and Leal (1982). Here we will present only the results. Because of the superposed orifice flow, it is convenient to work with a disturbance velocity in fluid 1. Hence, we we define a velocity $\mathbf{u}_D = \mathbf{u}^{(1)} - \mathbf{u}^*$, where $\mathbf{u}^*$ is the velocity due to the orifice, such that $\mathbf{u}_D = 0$ for $\mathbf{x} \in P^*$ (see Fig. 1). Similar disturbance quantities are defined for the pressure and stress. At the interface S_I we obtain the two vector equations

$$\begin{aligned} \frac{1}{2}\big(\mathbf{u}_I(\mathbf{x}_s)\big)_j = & -\int_{S_I} \boldsymbol{\Sigma}^j(\mathbf{x}_s,\xi)\cdot\mathbf{u}_I(\xi)\cdot\mathbf{n}\,dS_\xi \\ & -\int_{S_I} \mathbf{v}^j(\mathbf{x}_s,\xi)\cdot\mathbf{f}^{(2)}(\xi)\,dS_\xi \qquad\qquad \mathbf{x}_s \in S_I, \end{aligned} \tag{13}$$

and

$$\begin{aligned} \frac{1}{2}\big(\mathbf{u}_I(\mathbf{x}_s)\big)_j = & \frac{\lambda-1}{\lambda+1}\int_{S_I} \boldsymbol{\Sigma}^j(\mathbf{x}_s,\xi)\cdot\mathbf{u}_I(\xi)\cdot\mathbf{n}\,dS_\xi \\ & -\frac{\lambda}{\lambda+1}\int_{S_I} \boldsymbol{\Sigma}^j(\mathbf{x}_s,\xi)\cdot\mathbf{u}^*(\xi)\cdot\mathbf{n}\,dS_\xi \\ & +\frac{1}{\lambda+1}\int_{S_I} \mathbf{v}^j(\mathbf{x}_s,\xi)\cdot\Big(\hat{\mathbf{f}}(\xi) - \lambda\mathbf{f}^*(\xi)\Big)\,dS_\xi \\ & +\frac{1}{2}\frac{\lambda}{\lambda+1}\mathbf{u}^*(\mathbf{x}_s) \qquad\qquad \mathbf{x}_s \in S_I, \end{aligned} \tag{14}$$

and two vector unknowns $\mathbf{u}_I$ and $\mathbf{f}^{(2)}$ at any point $\mathbf{x}_s \in S_I$. Here we have defined

$$\begin{aligned} \hat{\mathbf{f}} &\stackrel{\text{def}}{=} \mathbf{n}\Big(-\frac{1}{Ca}\nabla\cdot\mathbf{n} + \frac{1}{Cg}z\Big) \\ \mathbf{f}^* &\stackrel{\text{def}}{=} \mathbf{n}\cdot\mathbf{T}^* \\ \mathbf{f}^{(2)} &\stackrel{\text{def}}{=} \mathbf{n}\cdot\mathbf{T}^{(2)}, \end{aligned} \tag{15}$$

The quantity $\hat{\mathbf{f}}$ is known at each time step since the interface position is known and the curvature can be calculated using Eq. (8).

Since this problem is axisymmetric, the work required to solve Eqs. (13) and (14) can be greatly reduced if the terms are first integrated analytically in the azimuthal direction, leaving line integrals to be solved numerically. The azimuthal integration is performed by expanding all of the terms in $\mathbf{n} \cdot \boldsymbol{\Sigma}^j \cdot \mathbf{u}$ and $\mathbf{v}^j \cdot \mathbf{f}$ into Cartesian components, and integrating the trigonemetric functions from zero to 2π. After integration, at each of the N nodes there are four scalar unknowns u_ρ, u_z, f_ρ, and f_z, for a total of $4N$ unknowns and $4N$ accompanying equations. Here, u_ρ and u_z are the scalar components of the unknown velocity $\mathbf{u}_I$, while f_ρ and f_z are the components of the unknown normal traction $\mathbf{f}^{(2)}$. The resulting equations take the form

$$\begin{aligned}\begin{pmatrix} u_\rho(\mathbf{x}_s) \\ u_z(\mathbf{x}_s) \end{pmatrix} &= -2 \int_{s_o}^{s_f} \mathbf{P}(\mathbf{x}_s, \xi) \cdot \begin{pmatrix} u_\rho \\ u_z \end{pmatrix} d\hat{s} \\ &\quad - 2 \int_{s_o}^{s_f} \mathbf{Q}(\mathbf{x}_s, \xi) \cdot \begin{pmatrix} f_\rho \\ f_z \end{pmatrix} d\hat{s} \qquad \mathbf{x}_s \in S_I,\end{aligned} \tag{16}$$

and

$$\begin{aligned}\begin{pmatrix} u_\rho(\mathbf{x}_s) \\ u_z(\mathbf{x}_s) \end{pmatrix} &= 2\frac{\lambda - 1}{\lambda + 1} \int_{s_o}^{s_f} \mathbf{P}(\mathbf{x}_s, \xi) \cdot \begin{pmatrix} u_\rho \\ u_z \end{pmatrix} d\hat{s} \\ &\quad - 2\frac{\lambda}{\lambda + 1} \int_{s_o}^{s_f} \mathbf{P}(\mathbf{x}_s, \xi) \cdot \begin{pmatrix} f_\rho^* \\ f_z^* \end{pmatrix} d\hat{s} \\ &\quad + \frac{2}{\lambda + 1} \int_{s_o}^{s_f} \mathbf{Q}(\mathbf{x}_s, \xi) \cdot \begin{pmatrix} \hat{f}_\rho - \lambda f_\rho^* \\ \hat{f}_z - \lambda f_z^* \end{pmatrix} d\hat{s} \\ &\quad + \frac{\lambda}{\lambda + 1} \mathbf{u}^*(\mathbf{x}_s) \qquad \mathbf{x}_s \in S_I,\end{aligned} \tag{17}$$

where

$$d\hat{s} = ds\, \rho \left(\dot{\rho}^2 + \dot{z}^2\right)^{1/2}.$$

The components of the matrices $\mathbf{P}$ and $\mathbf{Q}$ are listed in the Appendix.

The derivatives of the shape parametrization F from which the surface normal and curvature are constructed were computed using a cubic spline polynomial. A spline function was fit through the N points defining the position of the surface, and the derivates $\dot{\rho}$, $\ddot{\rho}$, $\dot{z}$, and $\ddot{z}$ evaluated analytically at the nodes. The distribution of node points along the surface tends to convect in

the course of moving the surface at each time step, and so it was necessary to use the spline function to periodically redistribute the points. Further, since the length of the arc of the interface increases as the drop deforms, it is important to add node points to preserve accuracy. This was accomplished by calculating the arc length between nodes at each time step, and inserting a new point when the length was greater than some predefined tolerance.

Starting with a given initial shape at time $t = 0$, the quantities $\mathbf{f}^*$, $\mathbf{u}^*$, and $\hat{\mathbf{f}}$ known, Eqs. (13) and (14) can be solved numerically for $\mathbf{u}_I$ and $\mathbf{f}^{(2)}$ at each node $\mathbf{x}_i$, $i = 1, 2, \ldots N$ on the interface. The shape of the interface is then modified by moving each node on the interface with the normal component of its local velocity, that is, for each node i

$$\begin{aligned} \rho(s_i,\, t+\Delta t) &= \rho(s_i,\, t) + n_\rho(s_i,\, t)\Big[u_\rho(s_i,\, t)\, n_\rho(s_i,\, t) \\ &\qquad + u_z(s_i,\, t)\, n_z(s_i,\, t)\Big]\Delta t \\ z(s_i,\, t+\Delta t) &= z(s_i,\, t) + n_z(s_i,\, t)\Big[u_\rho(s_i,\, t)\, n_\rho(s_i,\, t) \\ &\qquad + u_z(s_i,\, t)\, n_z(s_i,\, t)\Big]\Delta t, \end{aligned} \tag{18}$$

where n_ρ and n_z are the components of $\mathbf{n}$.

The method used to solve these integral equations is a simple collocation method. The collocation technique converts the integral equations into a system of coupled linear algebraic equations (Lee and Leal 1982; Geller *et al* 1986). The arc denoting the surface of the interface is divided up into N elements, or segments, with the surface nodes lying at the center of each element. It is assumed that the elements are sufficiently small that the values of $\mathbf{u}$ and stress $\mathbf{f}^{(2)}$ in an element can be reasonably approximated by their respective values at the center of the element. In this manner, from Eq. (16) the velocity of the ith

element is approximated by

$$\begin{pmatrix} u_\rho(\mathbf{x}_i) \\ u_z(\mathbf{x}_i) \end{pmatrix} \simeq -2\sum_{j=1}^{N}\left\{\left[\int_{s_j} \mathbf{P}(\mathbf{x}_i,\xi)\,d\hat{s}\right]\cdot\begin{pmatrix} u_\rho \\ u_z \end{pmatrix}\right\} - 2\sum_{j=1}^{N}\left\{\left[\int_{s_j} \mathbf{Q}(\mathbf{x}_i,\xi)\,d\hat{s}\right]\cdot\begin{pmatrix} f_\rho \\ f_z \end{pmatrix}\right\} \tag{19}$$

The matrices $\mathbf{P}$ and $\mathbf{Q}$ are integrated numerically in each segment using Gaussian steps. However, the integrals in Eq. (17) containing $\mathbf{u}^*$, $\mathbf{f}^*$, and $\hat{\mathbf{f}}$ are not evaluated in quite the same manner: since the source velocity and stress are known everywhere in the domain, and since $\hat{\mathbf{f}}$ can be calculated anywhere on the interface through use of the cubic spline, it is more accurate to evaluate the entire integral, rather than assume that the quantities are constant in an element. A complication arises when $\xi \longrightarrow \mathbf{x}$, because $r \longrightarrow 0$ and the integrands become singular, and thus cannot be evaluated numerically. Instead, a very small region of size ϵ is "cut out" on both sides of the singular point, and the integration over this small region is carried out analytically, using an expansion in ϵ. The expression resulting from this integration is presented in the Appendix.

As mentioned above, the output of the collocation approximation is a set of $4N$ linear equations, which in principle could be solved for velocity and stress using a variety of methods. Instead of doing this directly, we instead make use of the fact that Eq. (17) has only one vector unknown, namely the velocity $\mathbf{u}_I$. It proves to be significantly faster to solve the $2N$ linear equations arising from Eq. (17), and use the solution $\mathbf{u}_I$ to find the stress by solving another $2N$ equations arising from Eq. (16). Gaussian elimination with partial pivoting was used to solve the two systems of equations.

III. Discussion

In the terminology that will follow, a pendant drop denotes an attached drop of constant volume, that is, $M = 0$, while a plume denotes an attached drop for which $M > 0$, so that volume increases with time at a fixed rate. As far as the qualitative features of the results are concerned, there is little difference between dynamic pendant drops and plumes. The reason for this is twofold: first, the starting volumes of both dynamic pendant drops and plumes were always chosen so buoyancy forces would be larger than surface tension forces, in other words, to insure that the attached buoyant drops would rise for all $t > 0$. Second, M was chosen small enough, usually $O(10^{-2})$, that the motion of the fluid through the orifice would not visibly affect the bulk motion of the plume. The range of M's for the plume calculations was chosen by trial and error. The initial shapes for plumes and pendant drops were always chosen to be normal distributions, that is, Gaussian in shape. We chose this particular shape because it is a common initial pendant shape in static experiments (Pierson and Whitaker 1976). Fig. 2 shows a typical solution for a pendant drop, along with the corresponding inner and outer flowfields. The length of each arrow is proportional to the magnitude of the velocity field at that point. This result corresponds to the parameters $M = 0$, $(Ca,\ Cg,\ \lambda) = (10,\ 0.075,\ 0.1)$ and dimensionless time $t = 1.32$. Because of continuity, a recirculating vortex forms around the outside of the drop. In Fig. 3 we present results at successive times for the case (5, 0.02, 1) and $M = 0.01$. With $Ca > 1$ the plume is able to develop regions of relatively high curvature. When Fig. 3 is contrasted with the left photograph of a laboratory plume in Fig. 4 (Fig. 3 of Olson and Singer 1985) we see striking similarities. The tail of the plume is broad, and it thickens as it gets closer to the head. The head is a spherical cap, terminating in essentially a singular curvature point. We had to halt computations at this time step because the interface had crossed itself at the end point of the head (a possibility when using arc length parametrization).

Figure 5 shows the case (0.5, 0.05, 0.5), again with $M = 0.01$. The head formed rapidly, and after travelling one of its lengths, the tail has suddenly thinned to one third its original width. Once the tail thins, the translation of the head proceeds with the tail gradually thinning, and waves beginning to appear. Figure 6 demonstrates the other extreme in viscosity ratio. This result corresponds to (5, 0.02, 20), $M = 0.025$. The capilliary number is sufficiently large that a head has not yet formed, and the high viscosity of the inner fluid causes it to rise as a thick finger. In these pendant drop problems, we have found that the physical parameters affect the solution behavior in the following manner: Ca, in conjunction with λ affects whether or not a head will form, and how deformed the head can be if it does form. The viscosity ratio λ affects the thickness of the tail. For $\lambda < 1$ the tail is thread-like and wavy, and as λ increases, the tail gets thicker. For small λ the fluid "drains" up the tail faster than the head translates, and the head will continue to grow at the expense of the tail. The density number Cg affects the time scale over which things occur. The smaller Cg, the smaller the time step needed in the numerical scheme. Cg also affects whether a steady solution exists.

There is further numerical work to be done on the plume problem; although calculations were done for relatively large Capilliary number, is will be more realistic for comparison purposes to perform calculations for the limiting case of infinite Capilliary number. The role of λ is also not fully understood. Calculations at a wider range of the viscosity ratio will be enlightening. Last, it is of interest (Olson and Singer 1985) to know the ascent rate of a plume as a function of the dimensionless parameters. Until now, models have been based on treating the diapir as a cylinder, which is not totally unreasonable when $\lambda \gg 1$, and cavity plumes are assumed to approach power law ascent rates for large times. In particular, Olson and Singer find that the ascent velocity of a cavity plume increases with time as $t^{2/5}$. These models are empirical in nature and strongly linked to experimental observation.

As a check on the boundary integral method, a value of Cg was chosen so that a steady pendant shape should exist. The contact point was fixed and the contact angle allowed to vary with the local velocity. The solution obtained by taking a very large number of time steps was compared with the steady analysis of Brown *et al* (1980). Brown *et al* used Newton's method to solve the dimensionless Young-Laplace equation, containing the dimensionless parameter $B \equiv Ca/Cg$, for steady shapes of sessile and pendant drops. For the test, we used a constant dimensionless volume of 0.9 and a Bond number $B = 2.8$. The initial shape for each method was a normal distribution of volume 0.9. After 2 Newton steps and 5000 boundary integral steps, the two solutions are superimposed in Fig. 7; they are indistinguishable.

A final point should be made regarding the attached drop calculations. For all of the calculation done with attached drops, the contact point was assumed to be fixed, with the angle determined by the local velocity. We also did several tests where the contact angle was fixed, and the point was allow to move with a slip velocity proportional to the local velocity. The two different methods of treating the contact point yielded visually identical results due to the microscopic velocity near the wall. This "boundary condition" will be investigated further in subsequent work.

As another test of the numerical scheme we took the limiting case of a sedimenting solid sphere, in order to compare normalized drag with an exact expression derived by Brenner (1961). This was achieved by letting $\lambda \longrightarrow \infty$ and formulating the boundary conditions so that the point $s = 0$ corresponded to $\rho = 0$ at the bottom of the sphere, instead of the attached point as it did for the plume problem. The test has no direct bearing on the accuracy of the plume calculations since the solid sphere is not attached, and a limiting case of the viscosity ratio is used, but it does give an indication of the overall performance of the method when the Green's functions in Eqs. (10)-(12) are used. This case

is simpler to solve than the more general λ cases: Eq. (16) reduces to

$$\begin{pmatrix} 0 \\ -1 \end{pmatrix} = - \int_{s_o}^{s_f} \mathbf{Q}(\mathbf{x}_s, \xi) \cdot \begin{pmatrix} f_\rho \\ f_z \end{pmatrix} d\hat{s} \qquad \mathbf{x}_s \in S_I.$$

Solving this system of equations yields point values for the ρ and z components of the stress, which can be summed to obtain the drag. This calculated drag is divided by the Stokes drag and the resulting quantity is denoted by β. We computed β at a variety of gaps (that is, the distance between the bottom of the sphere and the wall), ranging from $100 \geq z_{gap} \geq 0.05$ for four different sphere surface discretizations: 10, 20, 30 and 40 surface elements. Brenner's analytical result is shown in the first column of Table I and the numerical calculations are displayed in the remaining columns. The agreement between our results and those of Brenner a quite good, and accuracy of the boundary intergral method increases as the number of surface elements increases.

Appendix

a. The single and double layers

In section 2 it was shown that after integrating analytically in the axial direction, the integrands reduce to the form

$$\begin{pmatrix} P_{11} & P_{12} \\ P_{21} & P_{22} \end{pmatrix} \begin{pmatrix} u_\rho \\ u_z \end{pmatrix} \tag{A1}$$

and

$$\begin{pmatrix} Q_{11} & Q_{12} \\ Q_{21} & Q_{22} \end{pmatrix} \begin{pmatrix} f_\rho \\ f_z \end{pmatrix}, \tag{A2}$$

where $\mathbf{P}$ and $\mathbf{Q}$ arise from the double and single layers, respectively. The components of these two matrices are the result of operating the cartesian components of the fundamental solutions on the components of the unknown velocity and stress. The elements of the matrices are:

$$\begin{aligned} P_{11} = {} & \rho\rho_\circ^2 n_\rho (C_5^{03} - \hat{C}_5^{03}) + \rho_\circ \big[\rho n_z (r_3 C_5^{02} - R_3 \hat{C}_5^{02}) \\ & + n_\rho (2\rho^2 + \rho_\circ^2)(C_5^{02} - \hat{C}_5^{02})\big] + \rho n_\rho (2\rho_\circ^2 + \rho^2)(C_5^{01} - \hat{C}_5^{01}) \\ & + n_z (\rho^2 + \rho_\circ^2)(r_3 C_5^{01} - R_3 \hat{C}_5^{01}) + \rho\rho_\circ \big[\rho n_\rho (C_5^{00} - \hat{C}_5^{00}) \\ & + n_z (r_3 C_5^{00} - R_3 \hat{C}_5^{00})\big] - 2x_3 \big\{-x_3 n_\rho (\rho \hat{C}_5^{01} + \rho_\circ \hat{C}_5^{00} \\ & + z\big\{2\rho_\circ n_\rho \hat{C}_5^{02} + (2\rho n_\rho + n_z R_3)\hat{C}_5^{01}\big\}\big] + 10x_3 z \big[\rho\rho_\circ^2 n_\rho \hat{C}_7^{03} \\ & + \rho_\circ \big\{\rho n_z R_3 + n_\rho (2\rho^2 + \rho_\circ^2)\big\}\hat{C}_7^{02} + \big\{\rho n_\rho (2\rho_\circ^2 + \rho^2) \\ & + n_z R_3 (\rho^2 + \rho_\circ^2)\big\}\hat{C}_7^{01} + \rho\rho_\circ (\rho n_\rho + n_z R_3)\hat{C}_7^{00}\big] \end{aligned} \tag{A3}$$

$$\begin{aligned} P_{12} = {} & \rho\rho_\circ n_\rho (r_3 C_5^{02} - R_3 \hat{C}_5^{02}) + \rho n_z (r_3^2 C_5^{01} - R_3^2 \hat{C}_5^{01}) \\ & + n_\rho (\rho^2 + \rho_\circ^2)(r_3 C_5^{01} - R_3 \hat{C}_5^{01}) + \rho_\circ \big\{\rho n_\rho (r_3 C_5^{00} - R_3 \hat{C}_5^{00}) \\ & + n_z (r_3^2 C_5^{00} - R_3^2 \hat{C}_5^{00})\big\} - 2x_3 \big[-x_3 n_z (\rho \hat{C}_5^{01} + \rho_\circ \hat{C}_5^{00}) \\ & + z n_\rho R_3 \hat{C}_5^{01}\big] + 10x_3 z R_3 \big[\rho\rho_\circ n_\rho \hat{C}_7^{02} \\ & + \big\{\rho n_z R_3 + (\rho^2 + \rho_\circ^2) n_\rho\big\}\hat{C}_7^{01} + \rho_\circ (\rho n_\rho + n_z R_3)\hat{C}_7^{00}\big] \end{aligned} \tag{A4}$$

$$
\begin{aligned}
P_{21} = {} & \rho_\circ^2 n_\rho (r_3 C_5^{02} - R_3 \hat{C}_5^{02}) + 2\rho\rho_\circ n_\rho (r_3 C_5^{01} - R_3 \hat{C}_5^{01}) \\
& + \rho_\circ n_z (r_3^2 C_5^{01} - R_3^2 \hat{C}_5^{01}) + \rho^2 n_\rho (r_3 C_5^{00} - R_3 \hat{C}_5^{00}) \\
& + \rho n_z (r_3^2 C_5^{00} - R_3^2 \hat{C}_5^{00}) + 2x_3 \big[-x_3 n_\rho R_3 \hat{C}_5^{00} \\
& + z n_z (\rho_\circ \hat{C}_5^{01} + \rho \hat{C}_5^{00}) + \rho_\circ^2 n_\rho \hat{C}_5^{02} \\
& + \rho_\circ (2\rho n_\rho + n_z R_3) \hat{C}_5^{01} \rho (\rho n_\rho + n z R_3) \hat{C}_5^{00} \big] \\
& - 10 x_3 z R_3 \big[\rho_\circ^2 n_\rho \hat{C}_7^{02} + \rho_\circ (2\rho n_\rho + n_z R_3) \hat{C}_7^{01} \\
& + \rho (\rho n_\rho + n_z R_3) \hat{C}_7^{00} \big]
\end{aligned}
\tag{A5}
$$

$$
\begin{aligned}
P_{22} = {} & \rho_\circ n_\rho (r_3^2 C_5^{01} - R_3^2 \hat{C}_5^{01}) + \rho n_\rho (r_3^2 C_5^{00} - R_3^2 \hat{C}_5^{00}) \\
& + n_z (r_3^3 C_5^{00} - R_3^3 \hat{C}_5^{00} + 2x_3 \big[-x_3 R_3 n_z \hat{C}_5^{00} \\
& + z \big\{ \rho_\circ n_\rho \hat{C}_5^{01} + (\rho n_\rho + 2 n_z R_3) \hat{C}_5^{00} \big\} \big] \\
& + 2x_3 R_3 \big[\rho_\circ n_\rho \hat{C}_5^{01} + (\rho n_\rho + n_z R_3) \hat{C}_5^{00} \big] \\
& - 10 x_3 z R_3^2 \big[\rho_\circ n_\rho \hat{C}_7^{01} + (\rho n_\rho + n_z R_3) \hat{C}_7^{00} \big]
\end{aligned}
\tag{A6}
$$

$$
\begin{aligned}
Q_{11} = {} & C_1^{01} - \hat{C}_1^{01} + \rho\rho_\circ (C_3^{02} - \hat{C}_3^{02}) + (\rho^2 + \rho_\circ^2)(C_3^{01} - \hat{C}_3^{01}) \\
& + \rho\rho_\circ (C_3^{00} - \hat{C}_3^{00}) - 2x_3 z \big[\hat{C}_3^{01} \\
& - 3 \big\{ (\rho^2 + \rho_\circ^2) \hat{C}_5^{01} + \rho\rho_\circ (\hat{C}_5^{02} + \hat{C}_5^{00}) \big\} \big]
\end{aligned}
\tag{A7}
$$

$$
\begin{aligned}
Q_{12} = {} & \rho (r_3 C_3^{01} - R_3 \hat{C}_3^{01}) + \rho_\circ (r_3 C_3^{00} - R_3 \hat{C}_3^{00}) \\
& + 2x_3 \big[\rho \hat{C}_3^{01} + \rho_\circ \hat{C}_3^{00} + 3 z R_3 (\rho \hat{C}_5^{01} + \rho_\circ \hat{C}_5^{00}) \big]
\end{aligned}
\tag{A8}
$$

$$
\begin{aligned}
Q_{21} = {} & \rho_\circ (r_3 C_3^{01} - R_3 \hat{C}_3^{01}) + \rho (r_3 C_3^{00} - R_3 \hat{C}_3^{00}) \\
& + 2x_3 \big[\rho_\circ \hat{C}_3^{01} + \rho \hat{C}_3^{00} - 3 z R_3 (\rho_\circ \hat{C}_5^{01} + \rho \hat{C}_5^{00}) \big]
\end{aligned}
\tag{A9}
$$

$$
\begin{aligned}
Q_{22} = {} & C_1^{00} - \hat{C}_1^{00} + r_3^2 C_3^{00} - R_3^2 \hat{C}_3^{00} \\
& + 2x_3 z (\hat{C}_3^{00} - 3 R_3^2 \hat{C}_5^{00}).
\end{aligned}
\tag{A10}
$$

The symbols C_p^{nm} and $\hat{C}_p^{nm}$ represent various elliptic integral functions, and these will be listed in the next section. The point $(\rho,\ z)$ corresponds to the location of integration, and $(\rho_\circ,\ x_3)$ is the singular point. Also, $r_3 = z - x_3$ and $R_3 = z + x_3$.

b. The elliptic integrals

The elliptic integral arise from analytic integration of the trigonemetric functions appearing in the surface integrals. All of the elliptic integrals shown in the previous section are of the form

$$C_p^{nm} \equiv \frac{2}{\gamma^{p/2}} \int_0^\pi \frac{\sin^n 2x \cos^m 2x}{\left[1 - k^2 \sin^2 x\right]^{p/2}} dx \qquad (A11)$$

and

$$\hat{C}_p^{nm} \equiv \frac{2}{\gamma_R^{p/2}} \int_0^\pi \frac{\sin^n 2x \cos^m 2x}{\left[1 - k_R^2 \sin^2 x\right]^{p/2}} dx, \qquad (A12)$$

where

$$\gamma = \left(\rho + \rho_\circ\right)^2 + r_3^2$$
$$k^2 = \frac{4\rho\rho_\circ}{\gamma}$$

and

$$\gamma_R = \left(\rho + \rho_\circ\right)^2 + R_3^2$$
$$k_R^2 = \frac{4\rho\rho_\circ}{\gamma_R}.$$

Using standard integral tables, all integrals of the form shown in Eq. (A11) or (A12) can be reduced to the two functions

$$K(k) = 2\int_0^\pi \frac{dx}{\left[1 - k^2 \sin^2 x\right]^{1/2}}$$
$$E(k) = 2\int_0^\pi \frac{dx}{\left[1 - k^2 \sin^2 x\right]^{3/2}}.$$

The elliptic integrals appearing in Eqs. (A3)-(A10) are listed below:

$$C_1^{00} = \frac{4}{\gamma^{1/2}} K \qquad (A13)$$

$$C_1^{01} = C_1^{00} - \frac{8}{k^2\gamma^{1/2}}(K - E) \qquad (A14)$$

$$C_3^{00} = \frac{4}{\hat{k}^2\gamma^{3/2}} E \qquad (A15)$$

$$C_3^{01} = \frac{4}{k^2\gamma^{3/2}}\left[2K - \frac{1+\hat{k}^2}{\hat{k}^2} E\right] \qquad (A16)$$

$$C_3^{20} = \frac{16}{k^4\gamma^{3/2}}\left[(1+\hat{k}^2)K - 2E\right] \tag{A17}$$

$$C_3^{03} = C_3^{01} - C_3^{20} + \frac{32}{3k^6\gamma^{3/2}}\left[(k^2-8)E + (8-5k^2)K\right] \tag{A18}$$

$$C_5^{00} = \frac{4}{3\hat{k}^2\gamma^{5/2}}\left[\frac{2(1+\hat{k}^2)}{\hat{k}^2}E - K\right] \tag{A18}$$

$$C_5^{01} = \frac{4}{3k^2\hat{k}^2\gamma^{5/2}}\left[(1+\hat{k}^2)K - \frac{2}{\hat{k}^2}(\hat{k}^2+k^4)E\right] \tag{A19}$$

$$C_5^{20} = \frac{16}{3k^4\gamma^{5/2}}\left[\frac{1+\hat{k}^2}{\hat{k}^2}E - 2K\right] \tag{A20}$$

$$C_5^{03} = C_5^{01} - C_5^{20} + \frac{32}{3k^6\gamma^{5/2}}\left[\frac{1+7\hat{k}^2}{\hat{k}^2}E - (8-3k^2)K\right] \tag{A21}$$

$$C_7^{00} = \frac{4}{15\hat{k}^4\gamma^{7/2}}\left[\frac{1}{\hat{k}^2}(23\hat{k}^2+8k^4)E - 4(1+\hat{k}^2)K\right] \tag{A22}$$

$$C_7^{01} = \frac{4}{15k^2\hat{k}^4\gamma^{7/2}}\left[\frac{1}{\hat{k}^2}(-6+9k^2-19k^4+8k^6)E + 2(3\hat{k}^2+2k^4)K\right] \tag{A23}$$

$$C_7^{20} = \frac{16}{15\hat{k}^2k^4\gamma^{7/2}}\left[\frac{2}{\hat{k}^2}(\hat{k}^2+k^4)E - (1+\hat{k}^2)K\right] \tag{A24}$$

$$C_7^{03} = C_7^{01} - C_7^{20} + \frac{32}{15\hat{k}^2k^6\gamma^{7/2}}\left[-\frac{1}{\hat{k}^2}(8-13k^2+3k^4)E + (8-9k^2)K\right] \tag{A25}$$

$$C_p^{02} = C_p^{00} - C_p^{20} \tag{A26}$$

where

$$\hat{k}^2 = 1 - k^2.$$

(i) Small k expansions

A numerical difficulty arises when ρ and/or $\rho_\circ \longrightarrow 0$, because even in double precision arithmetic, terms in numerators do not cancel as fast as denominators go to zero. In reality, all of the elliptic integrals listed above approach constant values as $k \longrightarrow 0$, and to reflect this fact, it is necessary to do a generalized binomial expansion (Knopp 1956, p159) in k^2 on the integrand in Eq. (A11).

The result of the expansion is an infinite series in powers of k^2; we have truncated the series after the $O(k^2)$ term, under the assumption that the remainder is vanishingly small. Thus in the limit as $k \longrightarrow 0$, the integrals in Eqs. (A13)-(A26) reduce to the following:

$$C_1^{00} = \frac{2\pi}{\gamma^{1/2}}\left(1+\frac{1}{8}k^2\right) \tag{A27}$$

$$C_1^{01} = -\frac{\pi k^2}{4\gamma^{1/2}} \tag{A28}$$

$$C_3^{00} = \frac{2\pi}{\gamma^{3/2}}\left(1+\frac{3}{8}k^2\right) \tag{A29}$$

$$C_3^{01} = -\frac{3\pi k^2}{4\gamma^{3/2}} \tag{A30}$$

$$C_3^{20} = \frac{\pi}{\gamma^{3/2}}\left(1+\frac{3}{8}k^2\right) \tag{A31}$$

$$C_3^{03} = -\frac{9\pi k^2}{16\gamma^{3/2}} \tag{A32}$$

$$C_5^{00} = \frac{2\pi}{\gamma^{5/2}}\left(1+\frac{5}{8}k^2\right) \tag{A33}$$

$$C_5^{01} = -\frac{5\pi k^2}{4\gamma^{5/2}} \tag{A34}$$

$$C_5^{20} = \frac{\pi}{\gamma^{5/2}}\left(1+\frac{5}{8}k^2\right) \tag{A35}$$

$$C_5^{03} = -\frac{15\pi k^2}{16\gamma^{5/2}} \tag{A36}$$

$$C_7^{00} = \frac{2\pi}{\gamma^{7/2}}\left(1+\frac{7}{8}k^2\right) \tag{A37}$$

$$C_7^{01} = -\frac{7\pi k^2}{4\gamma^{7/2}} \tag{A38}$$

$$C_7^{20} = \frac{\pi}{\gamma^{7/2}}\left(1+\frac{7}{8}k^2\right) \tag{A39}$$

$$C_7^{03} = -\frac{21\pi k^2}{16\gamma^{7/2}} \tag{A40}$$

c. Derivation of the linear systems

This section gives, in much greater detail than §II of this chapter, the derivation of the linear system of equations, starting with the Green's function result from Ladyzhenskaya (1963) and applying the collocation approximation to the integral equations.

A solution to Stokes equation for the velocity of an element of fluid 2 on the interface S_I is

$$\begin{aligned}\frac{1}{2}\mathbf{u}_I(\mathbf{x}) = &- \int_{S_I} \boldsymbol{\Sigma}^j(\mathbf{x},\xi)\cdot\mathbf{u}_I(\xi)\cdot\mathbf{n}\,dS_\xi \\ &- \int_{S_I} \mathbf{v}^j(\mathbf{x},\xi)\cdot\mathbf{f}_I^{(2)}(\xi)\,dS_\xi \qquad\qquad \mathbf{x},\xi\in S_I.\end{aligned} \tag{A41}$$

A similar equation can be written for the velocity of an element of fluid 1 on S_I, and upon addition to Eq. (A41) we obtain

$$\begin{aligned}\frac{1}{2}\mathbf{u}_I(\mathbf{x}) = &\frac{\lambda-1}{\lambda+1}\int_{S_I} \boldsymbol{\Sigma}^j(\mathbf{x},\xi)\cdot\mathbf{u}_I(\xi)\cdot\mathbf{n}\,dS_\xi \\ &- \frac{\lambda}{\lambda+1}\int_{S_I} \boldsymbol{\Sigma}^j(\mathbf{x},\xi)\cdot\mathbf{u}_I^*(\xi)\cdot\mathbf{n}\,dS_\xi \\ &+ \frac{1}{\lambda+1}\int_{S_I} \mathbf{v}^j(\mathbf{x},\xi)\cdot\left[\hat{\mathbf{f}}_I(\xi) - \lambda\mathbf{f}_I^*(\xi)\right]dS_\xi \\ &+ \frac{1}{2}\frac{\lambda}{\lambda+1}\mathbf{u}_I^*(\mathbf{x}) \qquad\qquad \mathbf{x},\ \xi\in S_I.\end{aligned} \tag{A42}$$

These two vector equations are sufficient to determine the two vector unknowns $\mathbf{u}_I$ and $\mathbf{f}^{(2)}$. The process of solving for the two vector (or four scalar) unknowns is broken down into two parts: first Eq. (A42) is solved for $\mathbf{u}_I$, and then this velocity is used in Eq. (A41) to find the stress.

(i) The velocity

In the collocation approximation, the arc of the interface is divided up into N elements, or segments. It is assumed the elements are sufficiently small such that the values of the unknowns u_ρ, u_z, f_ρ, and f_z are constant in each

element. With this assumption, the velocity at the center of the ith element can be approximated as

$$\begin{aligned}\begin{pmatrix} u_\rho(\mathbf{x}_i) \\ u_z(\mathbf{x}_i) \end{pmatrix} \simeq\ & 2\frac{\lambda-1}{\lambda+1}\sum_{j=1}^{N}\left\{\left[\int_{s_{j-1}}^{s_j}\mathbf{P}(\mathbf{x}_i,\xi)\,d\hat{s}_\xi\right]\cdot\begin{pmatrix} u_\rho(\mathbf{x}_j) \\ u_z(\mathbf{x}_j)\end{pmatrix}\right\} \\ & - 2\frac{\lambda}{\lambda+1}\sum_{j=1}^{N}\left\{\int_{s_{j-1}}^{s_j}\mathbf{P}(\mathbf{x}_i,\xi)\cdot\begin{pmatrix} u^*_\rho(\xi) \\ u^*_z(\xi)\end{pmatrix} d\hat{s}_\xi\right\} \\ & + \frac{2}{\lambda+1}\sum_{j=1}^{N}\left\{\int_{s_{j-1}}^{s_j}\mathbf{Q}(\mathbf{x}_i,\xi)\cdot\begin{pmatrix} \hat{f}_\rho-\lambda f^*_\rho \\ \hat{f}_z-\lambda f^*_z\end{pmatrix} d\hat{s}_\xi\right\} \\ & + \frac{\lambda}{\lambda+1}\begin{pmatrix} u^*_\rho(\mathbf{x}_i) \\ u^*_z(\mathbf{x}_i)\end{pmatrix},\end{aligned} \tag{A43}$$

where ξ is the variable of integration, and $d\hat{s}_\xi = \rho\left[\dot{\rho}^2+\dot{z}^2\right]^{1/2} ds$. Note that only the unknown was pulled outside of the integral; the other integrals in Eq. (A43) have integrands which are known everywhere on the surface (through use of the spline functions), and it is more accurate to numerically integrate the entire integrand rather than assume part of it is constant. If we denote

$$\mathbf{A}_i^j \equiv \int_{s_{j-1}}^{s_j}\mathbf{P}(\mathbf{x}_i,\xi)\,d\hat{s}_\xi,$$

then, after combining the last term in Eq. (A43) with the result of the integration of the previous two terms, we obtain the linear equation

$$\begin{pmatrix} u_\rho(\mathbf{x}_i) \\ u_z(\mathbf{x}_i)\end{pmatrix} = 2\frac{\lambda-1}{\lambda+1}\sum_{j=1}^{N}\left\{\mathbf{A}_i^j\cdot\begin{pmatrix} u_\rho(\mathbf{x}_j) \\ u_z(\mathbf{x}_j)\end{pmatrix}\right\} + \begin{pmatrix} b_\rho(\mathbf{x}_i) \\ b_z(\mathbf{x}_i)\end{pmatrix}. \tag{A44}$$

This equation can be applied at any of the N nodes on the surface, and constructing the matrix

$$\hat{\mathbf{A}} = \begin{pmatrix} \mathbf{A}_1^1 & \mathbf{A}_1^2 & \cdots & \mathbf{A}_1^N \\ \mathbf{A}_2^1 & \mathbf{A}_2^2 & \cdots & \mathbf{A}_2^N \\ \vdots & \vdots & \ddots & \vdots \\ \mathbf{A}_N^1 & \mathbf{A}_N^2 & \cdots & \mathbf{A}_N^N \end{pmatrix} \tag{A45}$$

along with the vector

$$\mathbf{u} = \begin{pmatrix} u_\rho(\mathbf{x}_1) \\ u_z(\mathbf{x}_1) \\ u_\rho(\mathbf{x}_2) \\ u_z(\mathbf{x}_2) \\ \vdots \\ u_\rho(\mathbf{x}_N) \\ u_z(\mathbf{x}_N) \end{pmatrix}, \tag{A46}$$

leads to the linear system

$$\mathbf{u} = 2\frac{\lambda - 1}{\lambda + 1}\hat{\mathbf{A}} \cdot \mathbf{u} + \mathbf{b}. \tag{A47}$$

Rearranging Eq. (A47), the desired result may be obtained:

$$\mathbf{u} = \left(\mathbf{I} - 2\frac{\lambda - 1}{\lambda + 1}\hat{\mathbf{A}}\right)^{-1}\mathbf{b} \tag{A48}$$

(*ii*) The stress

Once the velocity has been found, application of the collocation approximation to Eq. (A41) yields the stress $\mathbf{f}^{(2)}$. Once again, the velocity at the center of the ith element on the interface is

$$\begin{aligned} \begin{pmatrix} u_\rho(\mathbf{x}_i) \\ u_z(\mathbf{x}_i) \end{pmatrix} \simeq & -2\sum_{j=1}^{N}\left\{\left[\int_{s_{j-1}}^{s_j}\mathbf{P}(\mathbf{x}_i,\xi)\,d\hat{s}_\xi\right]\cdot\begin{pmatrix} u_\rho(\mathbf{x}_j) \\ u_z(\mathbf{x}_j)\end{pmatrix}\right\} \\ & -2\sum_{j=1}^{N}\left\{\left[\int_{s_{j-1}}^{s_j}\mathbf{Q}(\mathbf{x}_i,\xi)\,d\hat{s}_\xi\right]\cdot\begin{pmatrix} f_\rho(\mathbf{x}_j) \\ f_z(\mathbf{x}_j)\end{pmatrix}\right\} \\ = & -2\sum_{j=1}^{N}\mathbf{B}_i^j\cdot\begin{pmatrix} f_\rho(\mathbf{x}_j) \\ f_z(\mathbf{x}_j)\end{pmatrix} - 2\sum_{j=1}^{N}\mathbf{A}_i^j\cdot\begin{pmatrix} u_\rho(\mathbf{x}_j) \\ u_z(\mathbf{x}_j)\end{pmatrix}, \end{aligned} \tag{A49}$$

where

$$\mathbf{B}_i^j \equiv \int_{s_{j-1}}^{s_j}\mathbf{Q}(\mathbf{x}_i,\xi)\,d\hat{s}_\xi.$$

In a manner analogous to Eqs.(A45) and (A46) we can construct a matrix $\hat{\mathbf{B}}$ and column vector $\mathbf{f}$. Then using the matrix $\hat{\mathbf{A}}$ and vector $\mathbf{u}$ from above, Eq. (A49) can be written for the system of equations as

$$\mathbf{u} = -2\hat{\mathbf{B}}\cdot\mathbf{f} - 2\hat{\mathbf{A}}\cdot\mathbf{u}. \tag{A50}$$

Rearranging Eq. (A50), the stress can be found by solving the system

$$\mathbf{f} = -\hat{\mathbf{B}}^{-1}\Big[\Big(\frac{1}{2}\mathbf{I} + \hat{\mathbf{A}}\Big)\cdot\mathbf{u}\Big]. \tag{A51}$$

d. The singular contributions

As mentioned in §II of this chapter, the numerical integration breaks down (blows up) when $\xi \longrightarrow \mathbf{x}$. To include the contribution from the integral over the small region surrounding the singular point, it is necessary to evaluate the integral analytically. This is accomplished by (1) expanding the terms shown in Eqs. (A3)-(A10) in the limit as $\hat{k} \longrightarrow 0$ (since $k \longrightarrow 1$ at the singular point) and (2) Taylor series expanding the resulting terms in ρ and z about the point $(\rho_\circ,\ x_3)$. The details involved in carrying out these expansions are the most tedious in implementing the entire scheme, so they will be left out and only the results presented. It is important to note, however, that only those terms in Eqs. (A3)-(A10) containing r must be considered, since $R \neq 0$ for $z > 0$.

(i) The single layer

Here we consider the integral

$$\begin{aligned}\mathbf{a} &= \int_{s_i-\epsilon/2}^{s_i+\epsilon/2}\int_0^{2\pi} \rho\big[\dot{\rho}^2 + \dot{z}^2\big]^{1/2}\Big\{\frac{\mathbf{f}}{r} + \frac{\mathbf{f}\cdot\mathbf{r}}{r^3}\mathbf{r}\Big\}\,d\theta\,ds \\ &= \int_{s_i-\epsilon/2}^{s_i+\epsilon/2} \rho\big[\dot{\rho}^2 + \dot{z}^2\big]^{1/2} ds\,\Big\{\mathbf{i}\Big[f_\rho C_1^{01} + (\rho^2+\rho_\circ^2) f_\rho C_3^{01} \\ &\quad + \rho\rho_\circ f_\rho(C_3^{00} + C_3^{02}) + f_z r_3(\rho C_3^{01} + \rho_\circ C_3^{00}\Big] \\ &\quad + \mathbf{k}\Big[f_z C_1^{00} + f_\rho r_3(\rho C_3^{00} + \rho_\circ C_3^{01}) + f_z r_3^2 C_3^{00}\Big]\Big\},\end{aligned} \tag{A52}$$

where s_i is the value of the arclength parameter of the ith node, and $\mathbf{i}$ and $\mathbf{k}$ are the cartesian base vectors. After carrying out the expansions, the $\mathbf{i}$ component of the integral is

$$\begin{aligned}a_i \simeq 2\epsilon\Big\{ & f_{z_\circ}\frac{\dot{\rho}_\circ\dot{z}_\circ}{\big[\dot{\rho}_\circ^2 + \dot{z}_\circ^2\big]^{1/2}} + f_{\rho_\circ}\Big[\frac{\dot{\rho}_\circ^2 + 2\dot{z}_\circ^2}{\big[\dot{\rho}_\circ^2 + \dot{z}_\circ^2\big]^{1/2}} \\ & - \big[\dot{\rho}_\circ^2 + \dot{z}_\circ^2\big]^{1/2}\ln\Big(\frac{\epsilon}{\rho_\circ}\big[\dot{\rho}_\circ^2 + \dot{z}_\circ^2\big]^{1/2}\Big)\Big]\Big\},\end{aligned} \tag{A53}$$

and the **k** component is

$$a_k \simeq 2\epsilon\Bigg\{f_{\rho_\circ}\frac{\dot\rho_\circ\dot z_\circ}{\left[\dot\rho_\circ^2+\dot z_\circ^2\right]^{1/2}}+f_{z_\circ}\Bigg[\frac{\dot z_\circ^2}{\left[\dot\rho_\circ^2+\dot z_\circ^2\right]^{1/2}} + \left[\dot\rho_\circ^2+\dot z_\circ^2\right]^{1/2}\Big(1-\ln\frac{\epsilon}{\rho_\circ}\left[\dot\rho_\circ^2+\dot z_\circ^2\right]^{1/2}\Big)\Bigg]\Bigg\}, \tag{A54}$$

where the subscript $\circ$ denotes evaluation at the singular point.

(*ii*) The double layer

The derivation of the contribution from the double layer (the fundamental stress) is significantly more involved than for the single layer. It is mainly for this reason that the double layer contribution has been left out of previous work on the boundary integral method under the argument, usually justifiable, that the effect is small. Nonetheless, we feel that for completeness the result should be presented. The singular contribution to the double layer takes the form

$$\mathbf{b}=\int_{s_i-\epsilon/2}^{s_i+\epsilon/2}\int_0^{2\pi}\rho\left[\dot\rho^2+\dot z^2\right]^{1/2}\left\{\frac{(\mathbf{n}\cdot\mathbf{r})\,\mathbf{r}\,(\mathbf{r}\cdot\mathbf{u})}{r^5}\right\}d\theta\,ds \tag{A55}$$

After carrying out the expansions, the **i** component of the integral is

$$\begin{aligned} b_i \simeq \epsilon u_\rho\Bigg\{&\frac{559\dot z_\circ}{384\rho_\circ}+\frac{1}{3\left(\dot\rho_\circ^2+\dot z_\circ^2\right)^2}\Bigg[\frac{\dot\rho_\circ^2}{\rho_\circ}\left(6\dot\rho_\circ^2\dot z_\circ+6\dot\rho_\circ\dot z_\circ^2-\dot\rho_\circ^2-\dot z_\circ^2\right)\\ &-2\dot\rho_\circ^2\ddot z_\circ\left(2\dot\rho_\circ+3\dot z_\circ\right)-2\dot\rho_\circ\dot z_\circ\ddot\rho_\circ\left(3\dot\rho_\circ+2\dot z_\circ\right)\Bigg]\Bigg\}\\ &+\frac{\epsilon u_z}{3\left(\dot\rho_\circ^2+\dot z_\circ^2\right)^2}\Bigg[2\dot\rho_\circ\left(\dot z_\circ\ddot\rho_\circ-\dot\rho_\circ\ddot z_\circ\right)-\frac{\dot\rho_\circ\dot z_\circ}{\rho_\circ}\left(\dot\rho_\circ^2-\dot z_\circ^2\right)\Bigg], \end{aligned} \tag{A56}$$

and the **k** component is

$$\begin{aligned} b_k \simeq{}& \frac{\epsilon\,u_{\rho_\circ}}{\dot\rho_\circ^2+zdsq}\Bigg\{\frac{\dot\rho_\circ\dot z_\circ}{3\rho_\circ}+\frac{\dot\rho_\circ\dot z_\circ^2}{3}\frac{2\ddot\rho_\circ+\dot z_\circ\ddot\rho_\circ+\dot\rho_\circ\ddot z_\circ}{\dot\rho_\circ^2+zdsq}\\ &+\frac{4\dot\rho_\circ\dot z_\circ}{3\left(\dot\rho_\circ^2+\dot z_\circ^2\right)^2}\Big[\dot\rho_\circ^2\left(\dot\rho_\circ\ddot z_\circ-\ddot\rho_\circ\dot z_\circ\right)+\dot z_\circ^2\left(\dot\rho_\circ^2\dot z_\circ-\dot\rho_\circ\dot z_\circ^2\right)\Big]\Bigg\}\\ &+\frac{\epsilon\,u_{z_\circ}}{3\left(\dot\rho_\circ^2+zdsq\right)}\Bigg\{\frac{\dot z_\circ^2}{\rho_\circ}+\frac{2\dot z_\circ^2\left(\ddot\rho_\circ\dot z_\circ-\dot\rho_\circ\ddot z_\circ\right)}{\dot\rho_\circ^2+\dot z_\circ^2}\\ &+\frac{4\dot z_\circ^2}{\left(\dot\rho_\circ^2+\dot z_\circ^2\right)^2}\left(\dot\rho_\circ^2-\dot z_\circ^2\right)\left(\dot\rho_\circ\ddot z_\circ-\ddot\rho_\circ\dot z_\circ\right)\Bigg\}. \end{aligned} \tag{A57}$$

e. The mass source

To model the injection through an orifice in the wall centered at the origin, an exact solution in oblate spheroidal coordinates (ξ, η, θ) is used. The solution for the streamfunction is

$$\begin{aligned} \psi^* &= -\frac{M}{2\pi}\left(1 - \cos^3\eta\right) \\ &= -\frac{M}{2\pi}\left\{1 - \left(\frac{1}{2c^2}\right)^{3/2} D^3\right\}, \end{aligned} \tag{A58}$$

where M is the dimensionless volumetric flow rate, c is the radius of the orifice, $\hat{R}_1 = \left[z^2 + (\rho - c)^2\right]^{1/2}$, $\hat{R}_2 = \left[z^2 + (\rho + c)^2\right]^{1/2}$ and $D = \left[c^2 - \rho^2 - z^2 + \hat{R}_1\hat{R}_2\right]^{1/2}$. Then, the components of velocity are

$$\begin{aligned} u_\rho^* &= \frac{1}{\rho}\frac{\partial \psi^*}{\partial z} \\ &= -\frac{3Mz}{2\pi\rho}\left(\frac{1}{2c^2}\right)^{3/2} D\left[1 - \frac{z^2 + \rho^2 + c^2}{D}\right] \end{aligned} \tag{A59}$$

and

$$\begin{aligned} u_z^* &= -\frac{1}{\rho}\frac{\partial \psi^*}{\partial \rho} \\ &= \frac{3M}{2\pi}\left(\frac{1}{2c^2}\right)^{3/2} D\left[1 - \frac{z^2 + \rho^2 + c^2}{D}\right]. \end{aligned} \tag{A60}$$

The corresponding pressure is given by

$$p = -\frac{3M}{\pi c^3}\left[\frac{\sinh\xi}{\sinh^2\xi + \cos^2\eta} + \tan^{-1}\left(\sinh\xi\right)\right]. \tag{A61}$$

		N = 10		N = 20		N = 30		N = 40	
z_{gap}	β (theoretical)	β (numerical)	Error*	β (numerical)	Error	β (numerical)	Error	β (numerical)	Error
100.	1.011263	1.01532	.401	1.01222	.095	1.01167	.040	1.01148	.021
75.	1.015024	1.01910	.402	1.01598	.094	1.01543	.040	1.01524	.021
50.	1.022553	1.02665	.401	1.02352	.095	1.02296	.040	1.02277	.021
25.	1.045196	1.04937	.399	1.04617	.093	1.04560	.039	1.0454	.020
10.	1.113503	1.11768	.375	1.11428	.067	1.11367	.015	1.11347	-.003
9.	1.126194	1.13032	.366	1.12688	.061	1.12627	.007	1.12606	-.012
8.	1.142068	1.14632	.372	1.14283	.067	1.14222	.013	1.14201	-.005
7.	1.162491	1.16688	.378	1.16334	.073	1.16271	.019	1.16249	-.0001
6.	1.189737	1.19428	.382	1.19065	.077	1.19001	.023	1.18980	.005
5.	1.227889	1.23264	.387	1.22889	.082	1.22823	.028	1.22800	.009
4.	1.285087	1.29008	.389	1.28618	.085	1.28548	.031	1.28525	.013
3.	1.380204	1.38558	.389	1.38140	.087	1.38066	.033	1.38041	.015
2.	1.569205	1.57532	.390	1.57057	.087	1.56974	.034	1.56946	.016
1.	2.125536	2.13369	.384	2.12730	.083	2.12620	.031	2.12584	.014
0.75	2.489273	2.49864	.376	2.49123	.079	2.48998	.028	2.48957	.012
0.5	3.205390	3.21674	.354	3.20751	.066	3.20603	.020	3.20558	.006
0.25	5.305324	5.31976	.272	5.30508	-.005	5.30405	-.024	5.30393	-.026
0.10	11.459157	11.79521	2.93	11.40327	-.488	11.41799	-.359	11.42883	-.265
0.05	21.585818	26.60858	23.3	21.56331	-.104	21.29163	-1.36	21.34026	-1.14

Table I. Comparison of C_D for a falling solid sphere between present work and analytical solution of Brenner (1961).

*Error is defined as

$$100 \times \frac{\beta(\text{numerical}) - \beta(\text{theoretical})}{\beta(\text{theoretical})}$$

References

Blake, J.R. 1971 *Proc. Phil. Soc.* **70**, 303.

Berdan, C. 1982 PhD Thesis, California Institute of Technology, Pasadena, California.

Boss, A.P. and Sacks, I.S. 1985 *Geophys. J. R. Astron. Soc.* **80**.

Brand, R.S. and Lahey, F.J. 1967 *J. Fluid Mech.* **29**, 305-315.

Brenner, H. 1961 *Chem. Eng. Sci.* **16**, 242.

Brown, R.A, Orr, F.M. and Scriven, L.E. 1980 *J. Colloid Interface Sci.* **73**, 76.

Chi, B.K. and Leal, L.G. 1987 *J. Fluid Mech*, submitted.

Coddington, E.A. and Levinson, N. 1955 *Theory of Ordinary Differential Equations*, McGraw-Hill, New York.

Foster, T.D. 1971 *Geophys. Fluid Dyn.* **2**, 201-217.

Geller, A.S., Lee, S.H. and Leal, L.G. 1986 *J. Fluid Mech.* **169**, 27.

Happel, J. and Brenner, H. 1983 *Low Reynolds Number Hydrodynamics*, Martinus Nijhoff Publishers, The Hague.

Higdon, J.J.L 1985 *J. Fluid Mech.* **159**, 195.

Knopp, K. 1956 *Infinite Sequences and Series*, Dover, New York.

Ladyzhenskaya, O.A. 1963 *The Mathematical Theory of Viscous Incompressible Flow*, Gordon and Breach, New York.

Lee S.H. and Leal, L.G. 1982 *J. Colloid Interface Sci.* **87**, 81.

Lee, S.H. and Leal, L.G. 1986 *J. Fluid Mech.* **164**, 401.

Morris, S. 1985 *J. Fluid Mech.*, submitted.

Olson, P. and Singer, H. 1985 *J. Fluid Mech.* **158**, 511.

Odqvist, F.K.G. 1930 *Math. Z.* **32**, 329.

Oseen, C.W. 1927 *Hydrodynamik*, Akademische Verlagsgesellschaft.

Pierson, F.W. and Whitaker, S. 1976 *J. Colloid Interface Sci.* **54**, 203-248.

Rallison, J.M. and Acrivos, A. 1978 *J. Fluid Mech* **89**, 91.

Richards, J.M. 1963 *Int. J. Air Wat. Pollut.* **7**, 17.

Roberts, G.O. 1977 *Geophys. Astrophys. Fluid Dyn.* **8**, 197-233.

Rouse, H., Yih., C.S. and Humphreys, H.W. 1952 *Tellus* **4**, 201.

Simmons, J. 1985 PhD Thesis, California Institute of Technology.

Spaulding, D.B. and Cruddace, R.G. 1961 *J. Heat Mass Transfer* **3**, 55-59.

Youngren, G.K. and Acrivos, A. 1975 *J. Fluid Mech.* **69**, 377.

Youngren, G.K. and Acrivos, A. 1976 *J. Fluid Mech.* **76**, 433.

Figure captions

Figure 1: Schematic of the geometry for an attached body.

Figure 2: Pendant drop shape at time $t = 1.32$ for $Ca = 10$, $Cg = 0.075$ and $\lambda = 0.1$. Each arrow represents the direction of the flow at a point, and its length is proportional to the magnitude of the velocity.

Figure 3: Diapiric plume shapes at constant time increments for $Ca = 5$, $Cg = 0.02$ and $\lambda = 1$

Figure 4: Experimental plume shapes from Olson and Singer (1985).

Figure 5: Pendant drop shapes for $Ca = 0.5$, $Cg = 0.05$ and $\lambda = 0.5$.

Figure 6: Pendant drop shapes for $Ca = 5$, $Cg = 0.02$ and $\lambda = 20$.

Figure 7: Comparison of static shapes obtained by boundary integral technique, and method of Brown *et al* (1980) for $Ca/Cg = 2.8$.

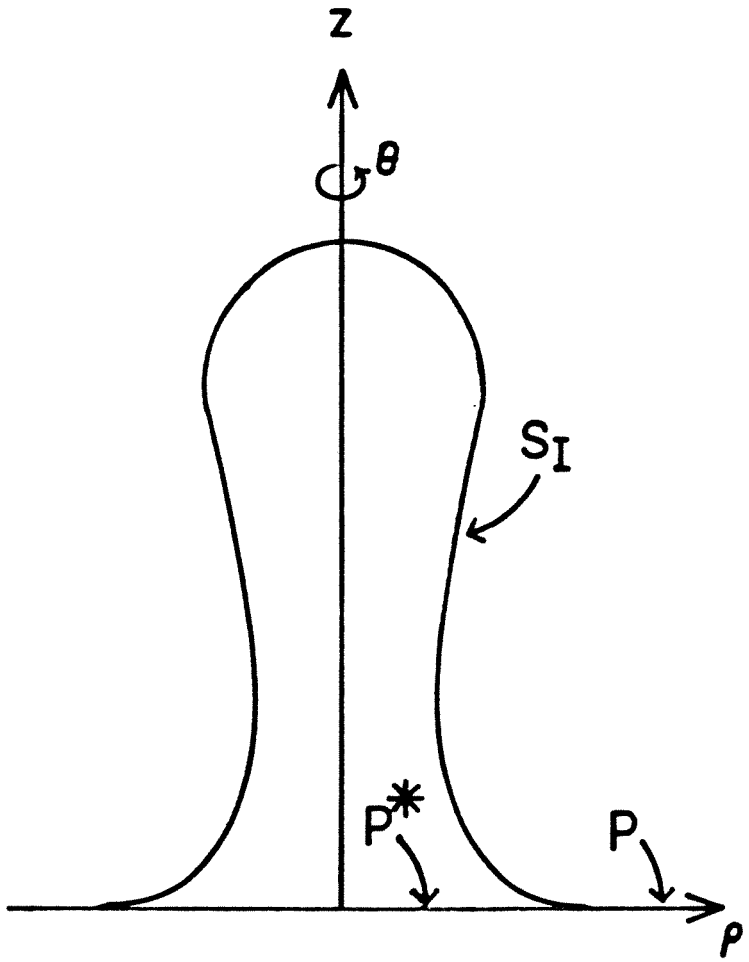

Figure 1.

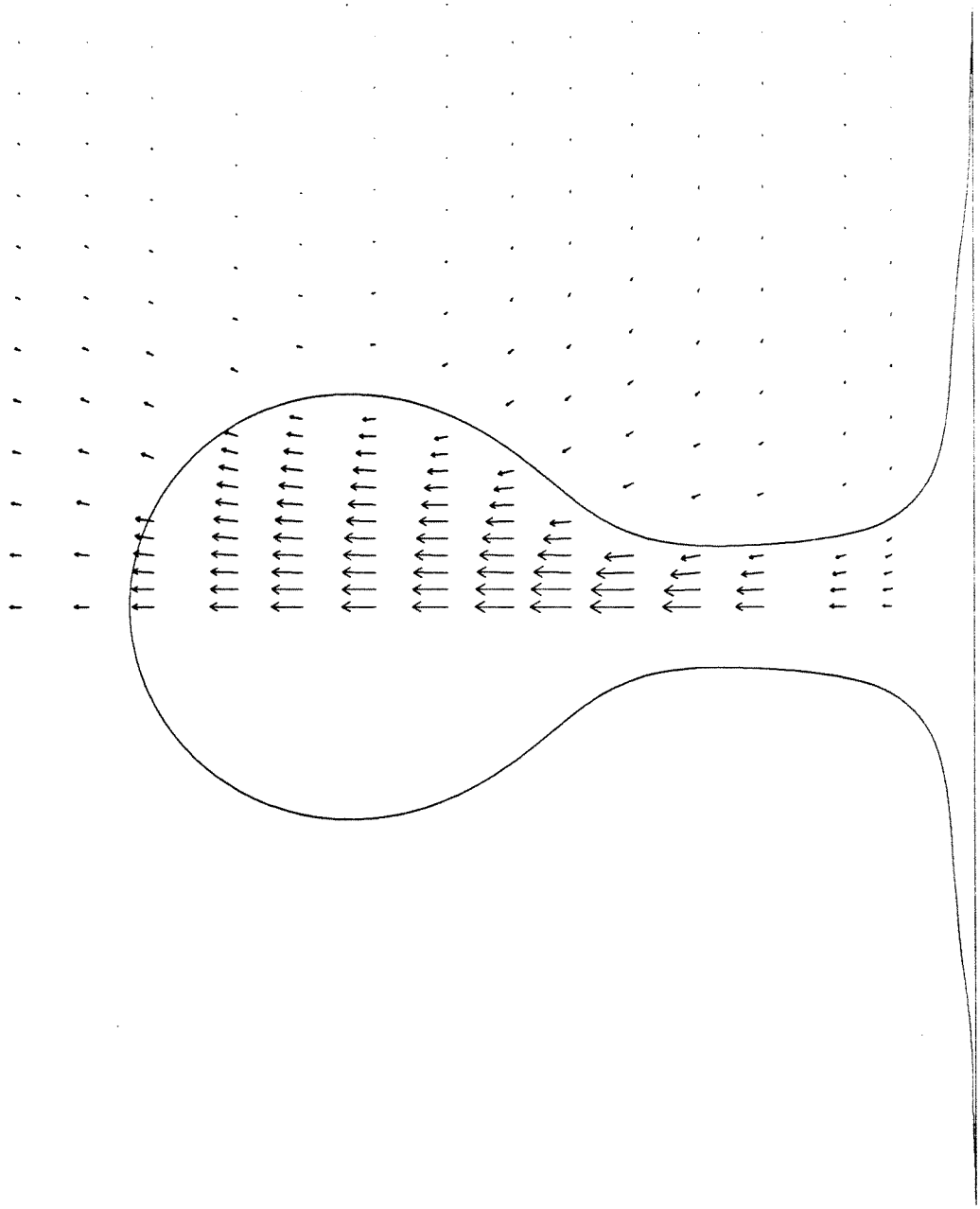

Figure 2.

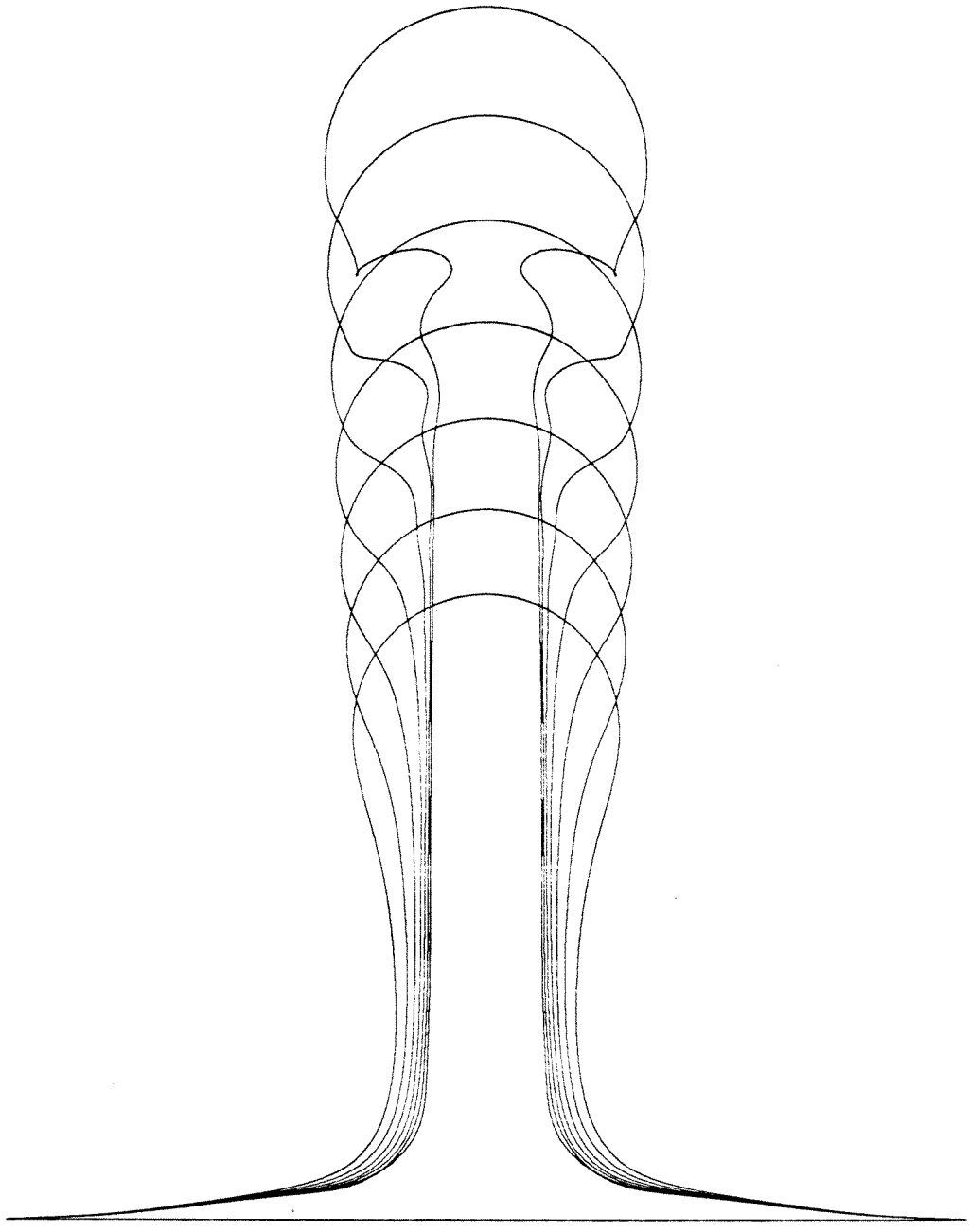

Figure 3.

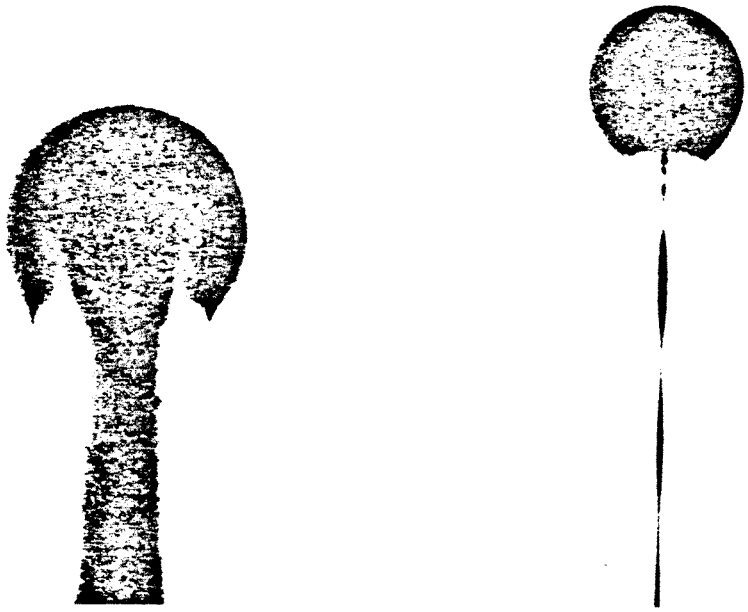

FIGURE 3. The leading edges of creeping plumes. Left is a diapiric plume, right is a cavity plume.

Figure 4.

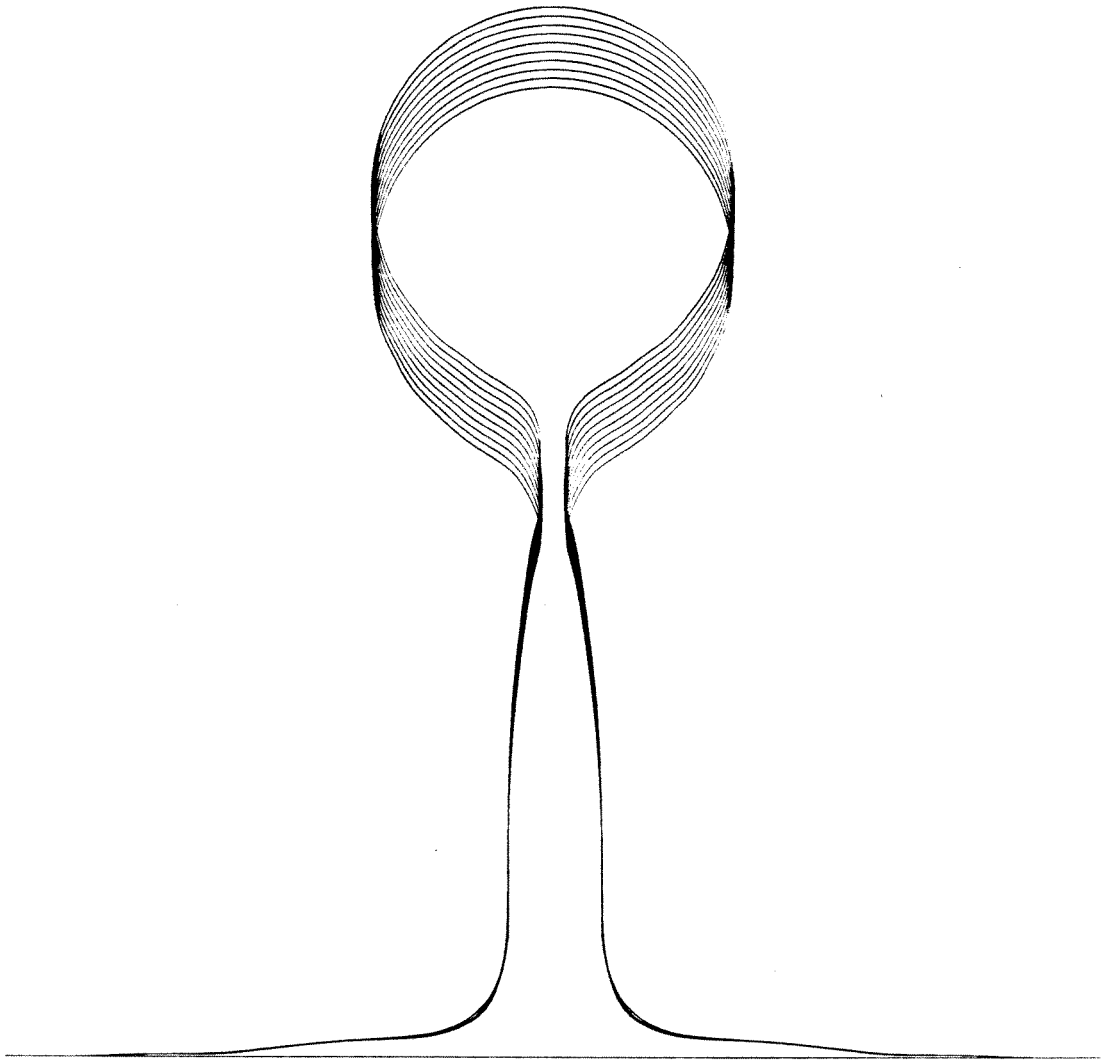

Figure 5.

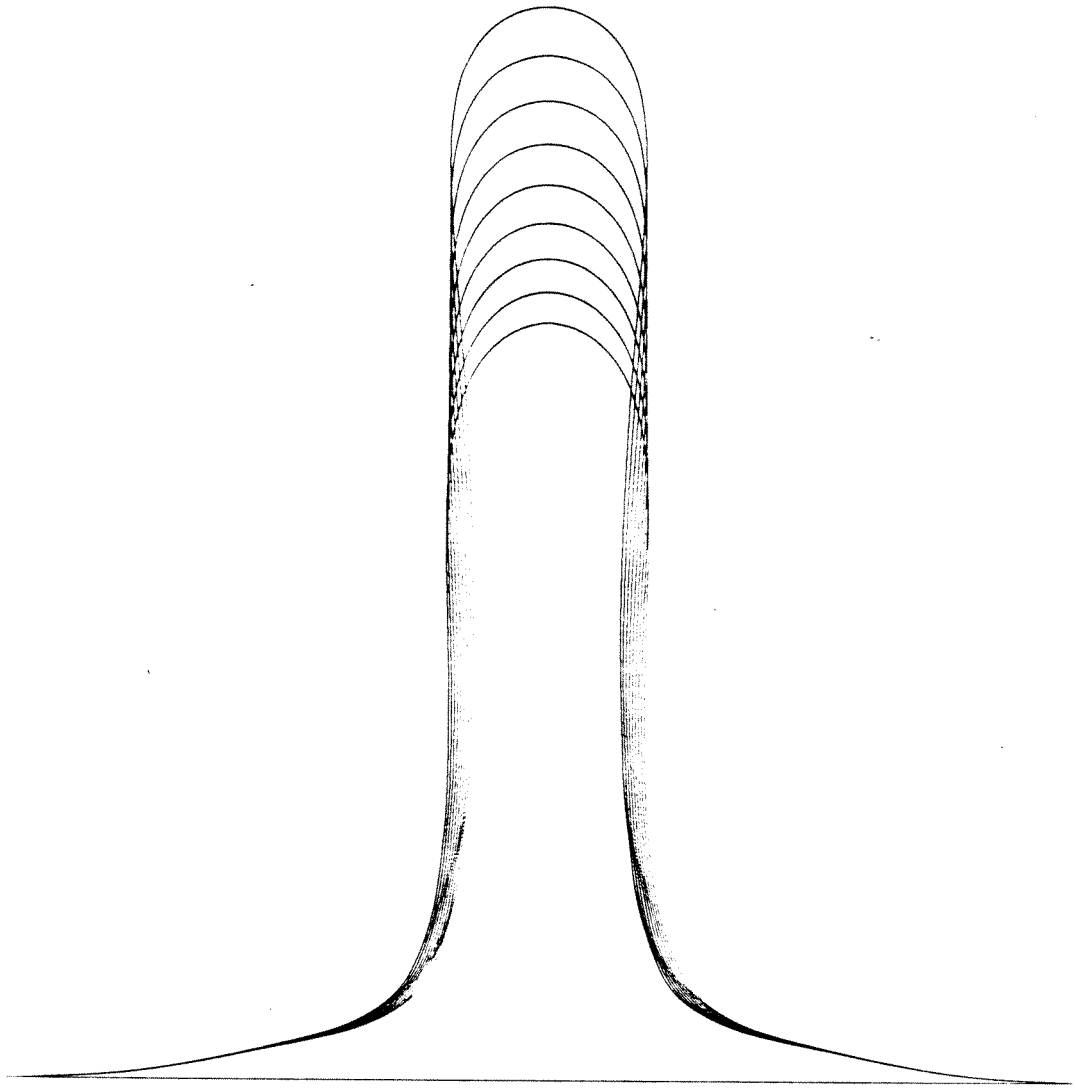

Figure 6.

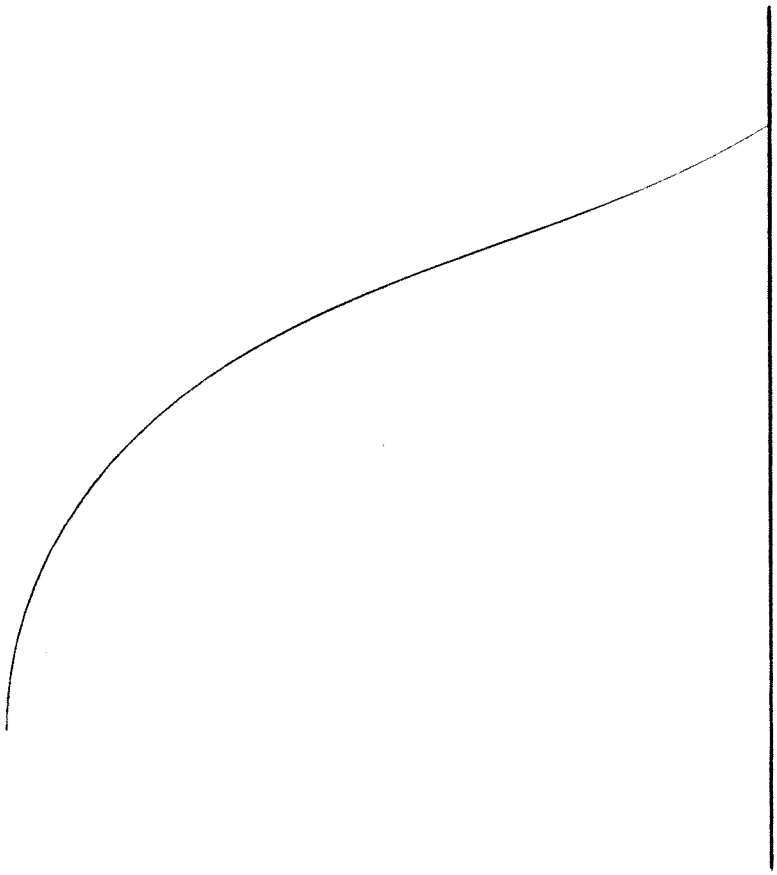

Figure 7.

Appendix III

New discoveries on the frontiers of fluid mechanics

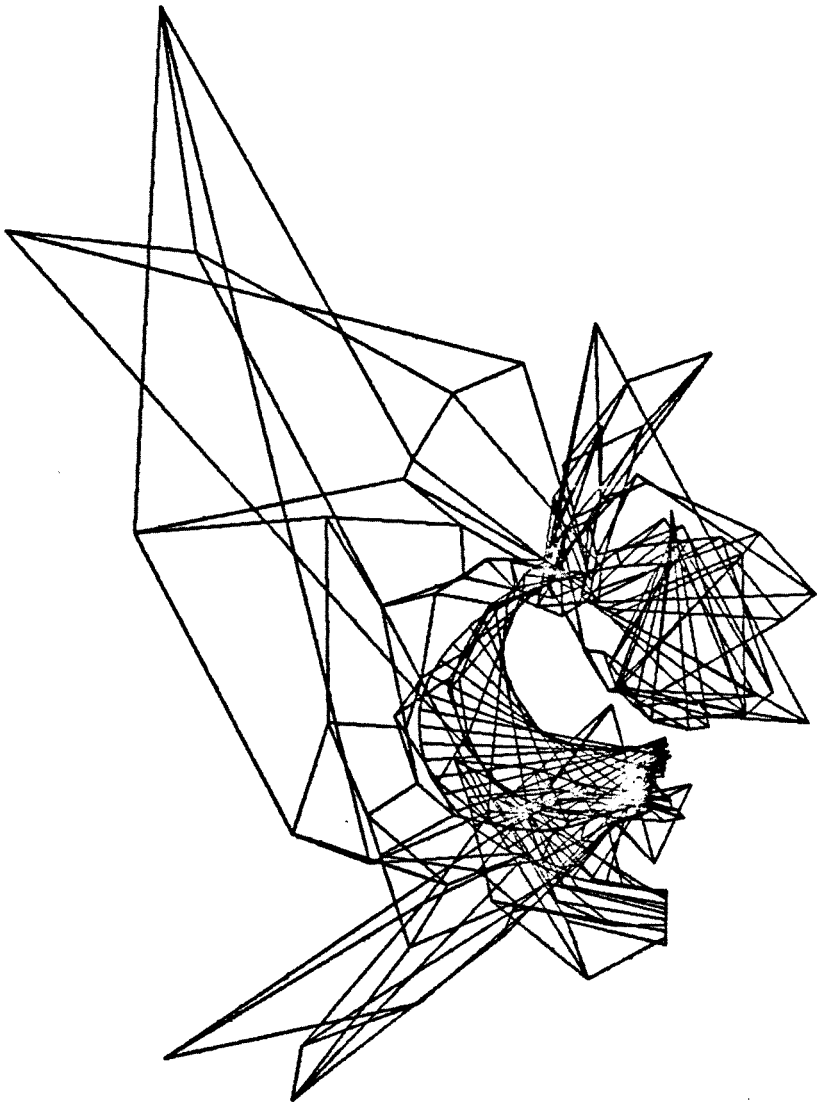

A deformable drop in uniform streaming flow,
as seen by an FPS-164 attached array processor.

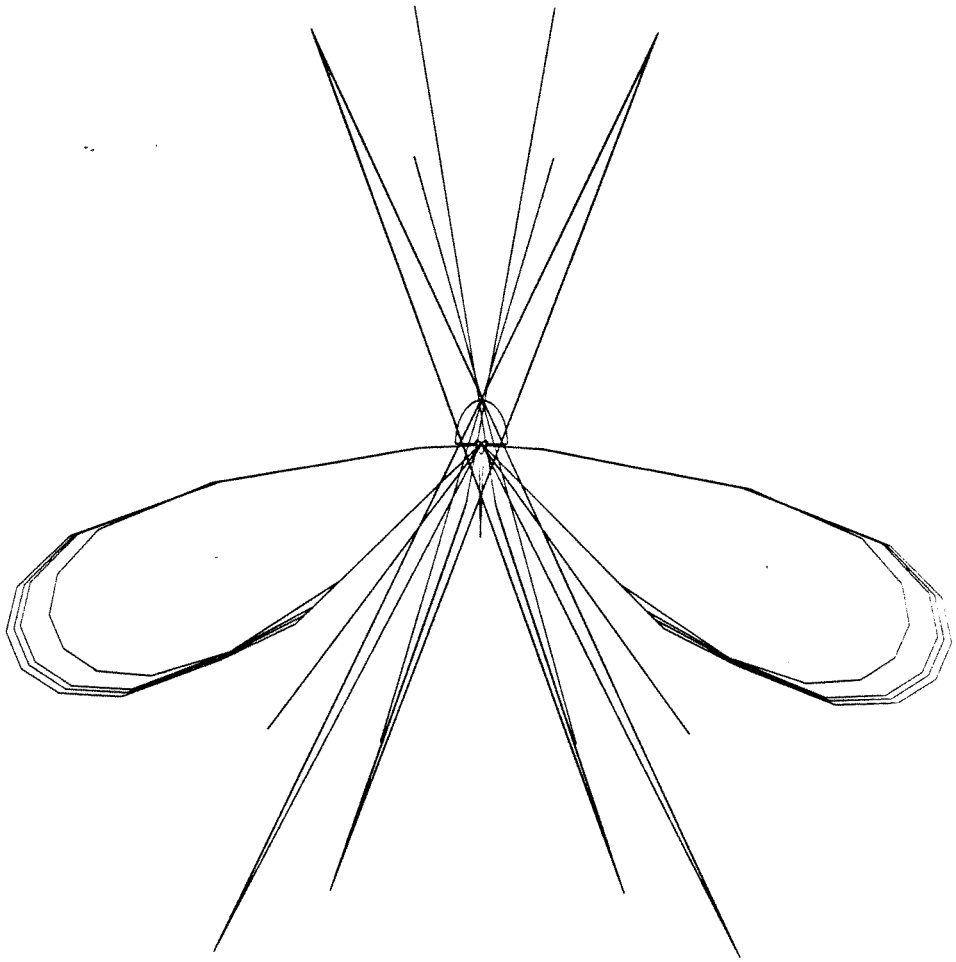

March 5, 1987. After months of searching, the bug in Newton's method program has been found.

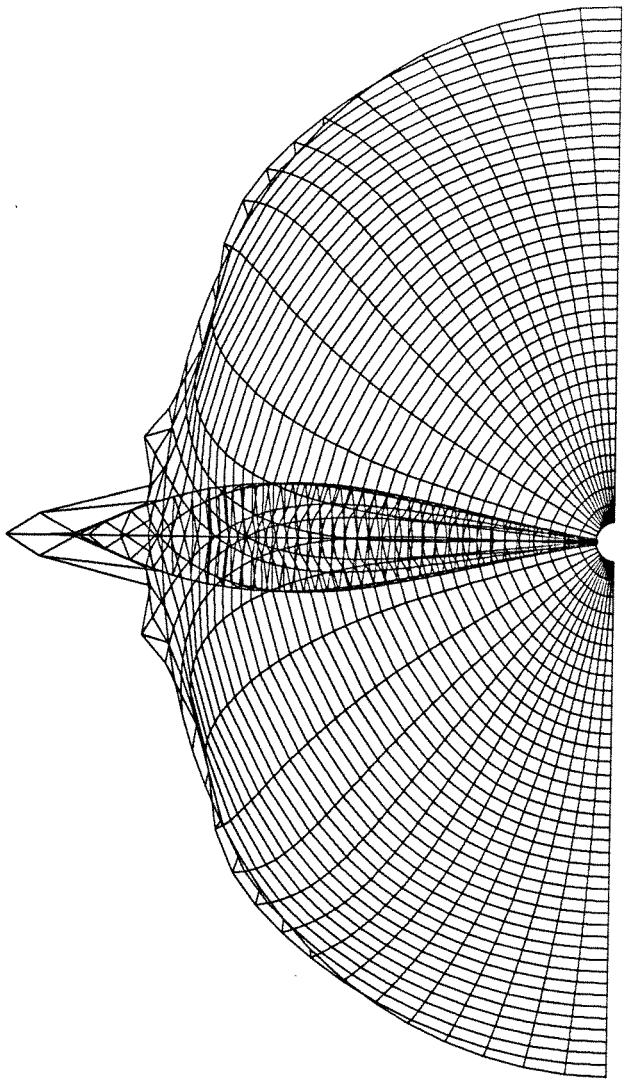

Contour plot of a pterodactyl in full flight.

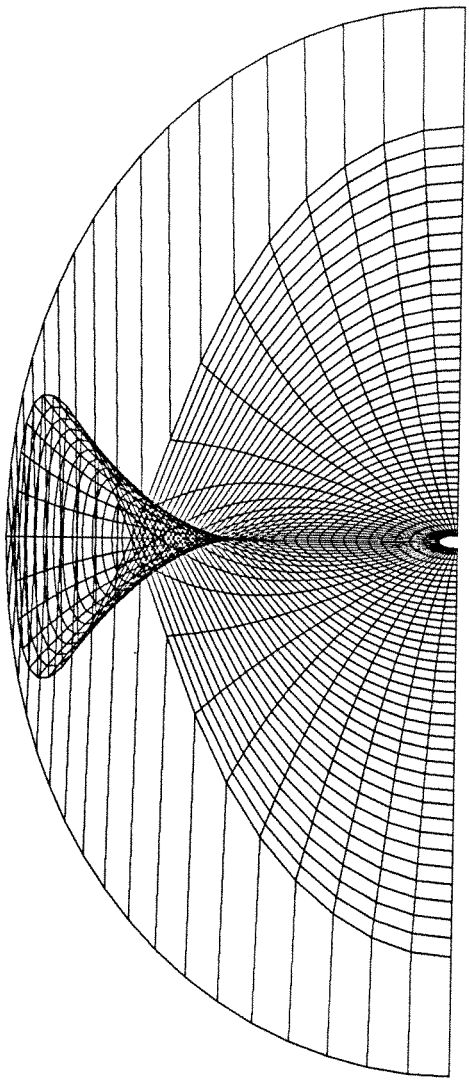

Lessons in non-euclidean geometry: the Dandy funnel.

—Pendant Drop—

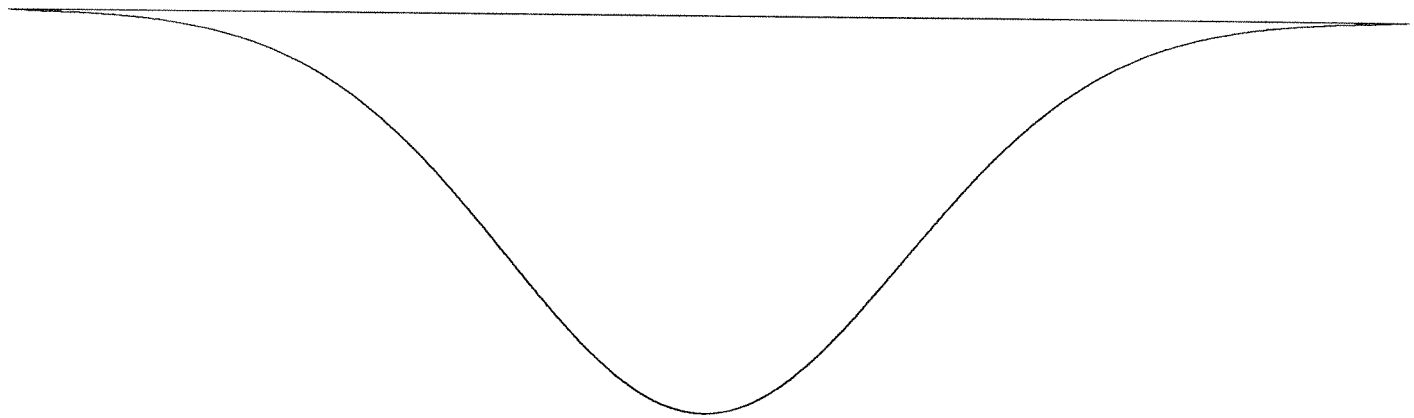

as seen by a Vax 11/780 ....

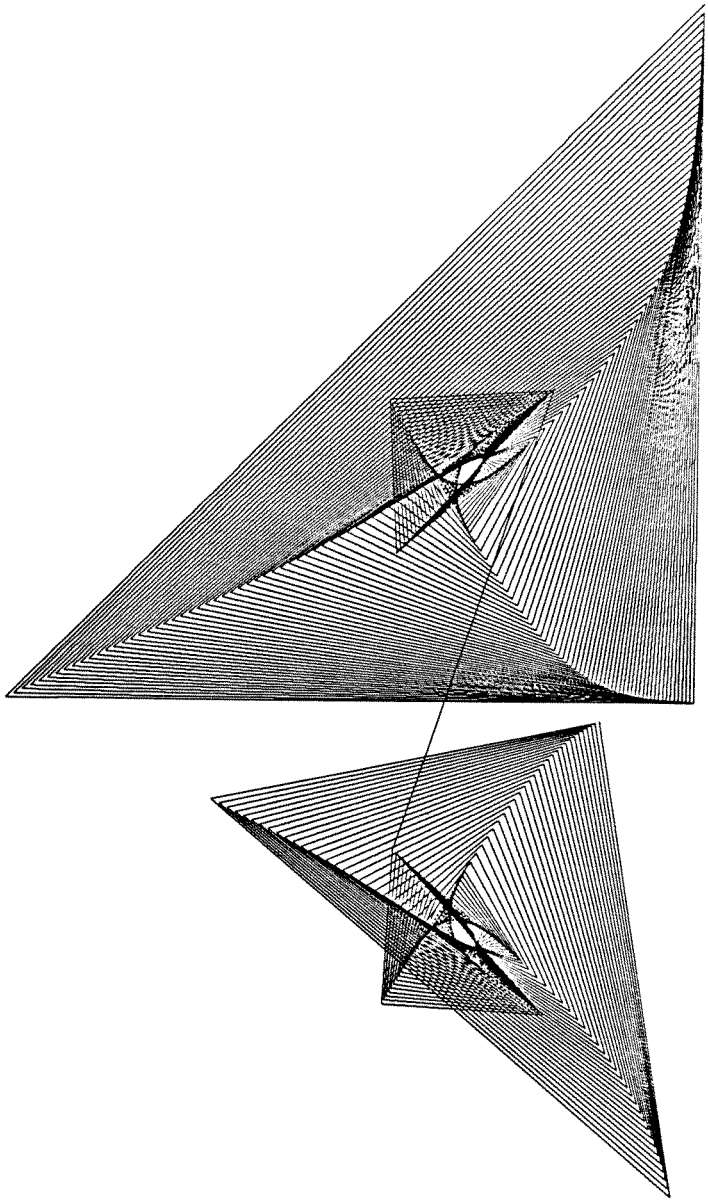

and as seen by a Sun 3/160 Workstation.

This sequence of three figures shows the eventual collapse of a poorly constructed boundary-fitted coordinate grid.

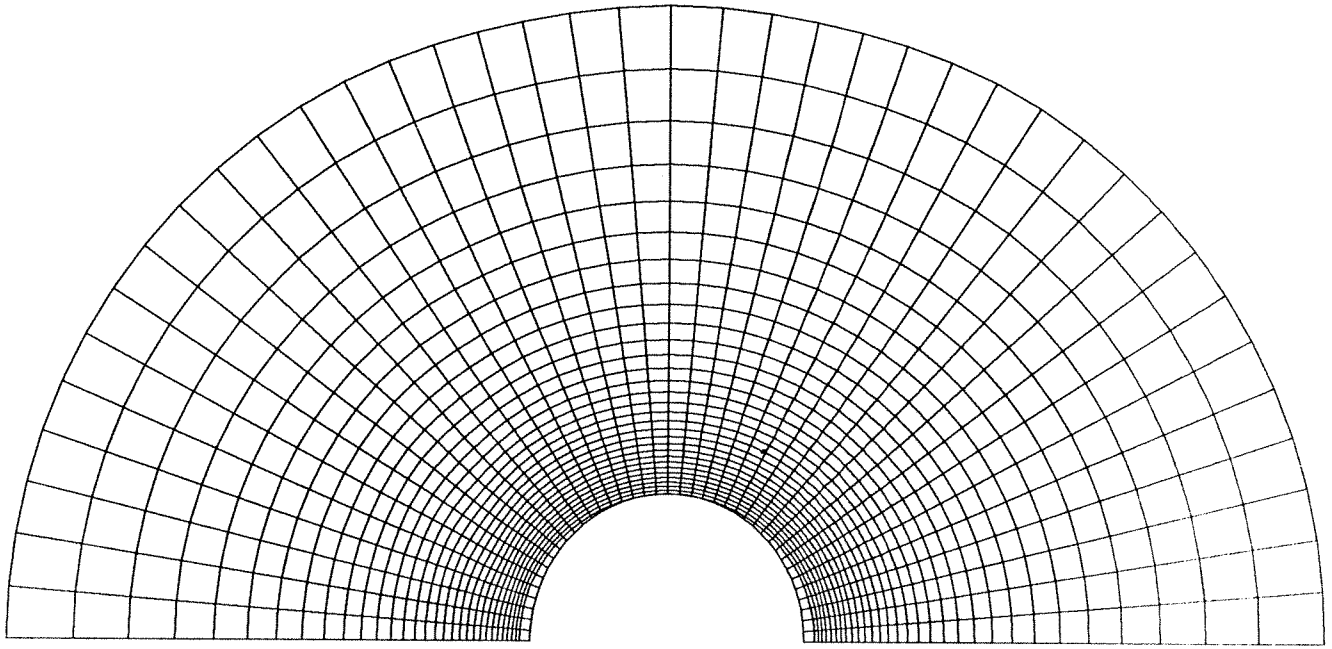

(a) The unsuspecting grid.

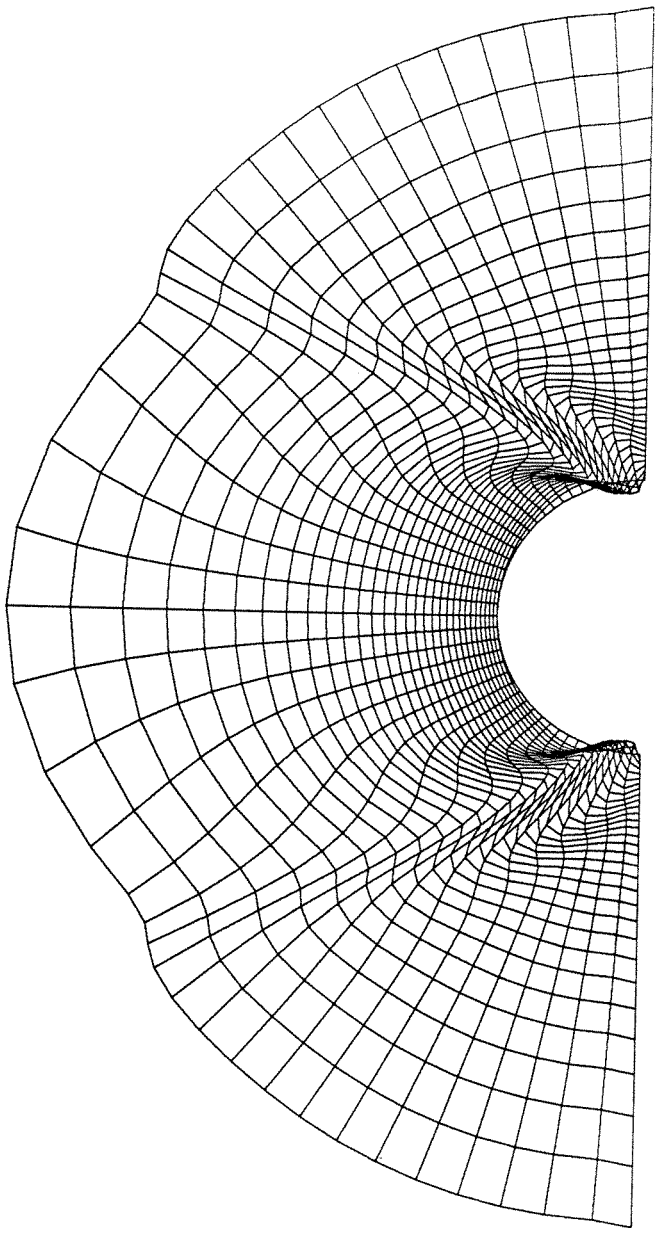

(b) Beginning of the end.

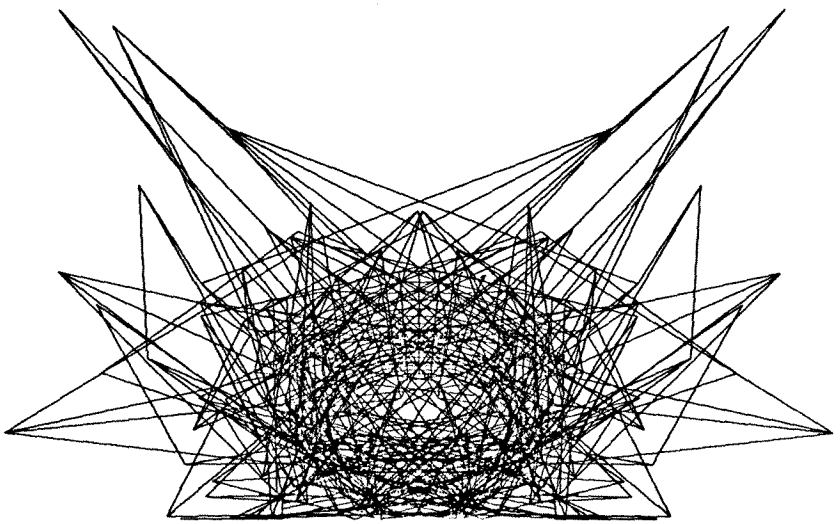

(c) Rubble. There were no survivors.

Remember—nonorthogonality kills.